2010

Investigation of PVD and CVD Coatings for Manufacturing, Fuel Cell and Biomedical Applications

Linlin Wang
University of Windsor

Recommended Citation

Wang, Linlin, "Investigation of PVD and CVD Coatings for Manufacturing, Fuel Cell and Biomedical Applications" (2010). *Electronic Theses and Dissertations.* Paper 470.

INVESTIGATION OF PVD AND CVD COATINGS FOR MANUFACTURING, FUEL CELL AND BIOMEDICAL APPLICATIONS

By

Linlin Wang

A Dissertation
Submitted to the Faculty of Graduate Studies and Research
through Engineering Materials
in Partial Fulfillment of the Requirements for
the Degree of Doctor of Philosophy at the
University of Windsor

Windsor, Ontario, Canada

2009

Investigation of PVD and CVD Coatings for Manufacturing, Fuel Cell and Biomedical Applications

By

Linlin Wang

APPROVED BY:

Dr. R. Wei, External Examiner
Southwest Research Institute

Dr. S. H. Eichhorn
Department of Chemistry and Biochemistry

Dr. A. T. Alpas
Department of Mechanical, Automotive & Materials Engineering

Dr. H. Hu
Department of Mechanical, Automotive & Materials Engineering

Dr. X. Nie, Advisor
Department of Mechanical, Automotive & Materials Engineering

Dr. R. Carriveau, Chair of Defense
Department of Civil & Environmental Engineering

25 November 2009

DECLARATION OF CO-AUTHORSHIP/PREVIOUS PUBLICATION

I. Co-Authorship Declaration

I hereby declare that this dissertation incorporates material that is result of joint research, as follows:

The Chapter 4.2 of this dissertation incorporates the outcome of a joint research undertaken in collaboration with J. Housden, E. Spain, J.C. Jiang, E.I. Meletis, A. Leyland and A. Matthews under the supervision of Professor Xueyuan Nie. The contribution of co-authors was primarily through the provision of commercial coatings and TEM test.

The Chapter 4.3 of this dissertation also incorporates the outcome of a joint research undertaken in collaboration with M.J. Lukitsch, J.C. Jiang, Y.T. Cheng and P. Zhang under the supervision of Professor Xueyuan Nie. The contribution of co-authors was primarily through the provision of coating deposition equipment, TEM and nano-indentation test.

In all cases, the key ideas, primary contributions, experimental designs, data analysis and interpretation, were performed by the author.

I am aware of the University of Windsor Senate Policy on Authorship and I certify that I have properly acknowledged the contribution of other researchers to my dissertation, and have obtained written permission from each of the co-authors to include the above materials in my dissertation.

I certify that, with the above qualification, this dissertation, and the research to which it refers, is the product of my own work.

II. Declaration of Previous Publication

This dissertation includes 3 original papers that have been previously published/submitted for publication in peer reviewed journals, as follows:

Dissertation chapter	Publication title/full citation	Publication status*
Chapter 4.2	Material transfer phenomena and failure mechanisms of a nanostructured Cr-Al-N coating in laboratory wear tests and an industrial punch tool application	*published*
Chapter 4.3	Effect of tribological media on tribological properties of multilayer Cr(N)/C(DLC) coatings	*published*
Chapter 4.3	Tribological properties of a-C/Cr(N) coatings in micro-and nano-scales	*published*

I certify that I have obtained a written permission from the copyright owners to include the above published materials in my dissertation. I certify that the above material describes work completed during my registration as graduate student at the University of Windsor.

I declare that, to the best of my knowledge, my dissertation does not infringe upon anyone's copyright nor violate any proprietary rights and that any ideas, techniques, quotations, or any other material from the work of other people included in my dissertation, published or otherwise, are fully acknowledged in accordance with the standard referencing practices. Furthermore, to the extent that I have included copyrighted material that surpasses the bounds of fair dealing within the meaning of the Canada Copyright Act, I certify that I have obtained a written permission from the copyright owners to include such materials in my dissertation.

I declare that this is a true copy of my dissertation, including any final revisions, as approved by my dissertation committee and the Graduate Studies office, and that this dissertation has not been submitted for a higher degree to any other University or Institution.

ABSTRACT

In this dissertation, wear and corrosion properties of hard coatings were characterized under simulated dry machining, fuel cell and biomedical application conditions. The test results were analyzed, and potentials of the coatings for the targeted applications were discussed.

To evaluate the effect of high temperature during the dry machining on the wear performance of various tool coatings, including TiN, TiAlN, CrN, CrAlN and DLC, the phase structurures as well as mechanical and tribological properties of un-annealed and annealed coatings were characterized. An industrial trial of CrAlN- and TiN-coated punches in an auto stamping plant was also conducted. The test results indicated that the CrN-based coating had a better thermal stability than the TiN-based and DLC coatings. The CrAlN coating exhibited the superior thermal stability and wear performance under both laboratorial pin-on-disc tests against ceramic Al_2O_3 and steel counterface materials and the industrial trial against high strength steel. DLC had a superior anti-sticking property when sliding against aluminum materials. A Cr(CrN)/C(DLC) coating system was also developed as a potential composite coating for dry machining of aluminum materials.

The contact resistance and electrochemical properties of uncoated, TiN-, CrN- and TiAlN-coated SS316L substrates were investigated in a simulated proton exchange membrane (PEM) fuel cell environment. Both TiN- and CrN-coated SS316L could potentially be used as bipolar plate materials in the PEM fuel cell environment. However, since the corrosion is likely initiated at pinholes in physical vapor deposition (PVD) coatings, more efforts are needed to eliminate the pinholes.

To exam the feasibility of those coatings for load-bearing medical devices and implants, the corrosion property of coatings was investigated in a simulated body fluid (SBF) environment, and the tribological property against polyethylene biomaterial was characterized. The results indicated that the CrN and DLC coatings had a high corrosion potential. TiAlN and CrAlN coatings had the least corrosion protection. TiN and DLC coatings presented a good wear resistance and chemical stability during the sliding tests with SBF. The uncoated and CrN-coated stainless steel samples were not compatible with polyethylene materials in the tested SBF condition.

DEDICATION

To

my dear parents Xiuen Wang and Lihua Song

my dear husband Xin Hu

for their devotion and support

ACKNOWLEDGEMENTS

I would like to express my sincere gratitude to my supervisor, Dr. Xueyuan Nie, for his excellent teaching, guidance and supervision throughout my study at the University of Windsor. His insightful knowledge and positive thinking on my research project have inspired me and helped me to overcome many difficulties and keep moving forward.

Dr. Y. T. Cheng, Dr. M. Lukitsch in GM R&D center and Dr. Jonathan Housden from Tecvac Ltd, UK are acknowledged for their help with coating deposition. Thanks go to Dr. J.C. Jiang (University of Texas Arlington), Dr. D.O. Northwood, Dr. A.T. Alpas and Dr. H. Hu for their technical supports on TEM analysis, corrosion test, optical surface profile measurement and thermal treatment.

I would like to sincerely thank my committee members Dr. A.T. Alpas, Dr. H. Hu and Dr. S. H. Eichhorn for their valuable advice and guidance to my research.

I would like to extend my thanks to the previous and current student fellows of plasma surface engineering and tribology laboratory for their help, encouragement and friendship. Mr. John. Robinson and Mr. Andrew Jenner’s technical assistance is also gratefully acknowledged. I am grateful to Ms. Barbara Tattersall for her administrative assistance during my study.

The financial supports from Natural Sciences and Engineering Research Council of Canada (NSERC) and Canada Graduate Scholarship are highly appreciated.

Last but not the least; I am deeply grateful to my husband Xin Hu for his support with his encouragement, patience and prayer, which helped me to reach the final step.

TABLE OF CONTENTS

LIST OF TABLES

LIST OF FIGURES

CHAPTER 1 INTRODUCTION

1.1 Background of this dissertation

Hard ceramic coatings produced by physical vapor deposition (PVD) and chemical vapor deposition (CVD) processes have been rapidly developed mainly for the anti-wear and decorative purposes. Among them, the commercially-available TiN, TiAlN, CrN, CrAlN and DLC coatings are predominantly used as universal wear protection for materials, tools and machine parts. The significance and the associated benefits of those coatings on tribological application are well documented.

However, to date, the machining manufacturers highly desire to eliminate or minimize cutting fluids by the movement from the fluid-assisted cutting toward a dry cutting in order to reduce the costs of production and make the processes environmentally benign. Generally, the use of cutting fluid in the fluid-assisted cutting process leads to an increase of tool life by the reduction of cutting forces (lubrication effect) and temperatures in the tool (cooling effect). The other important functions of the cutting fluids are to flush away the chips from the cutting zone (flushing effect). Elimination of coolants will result in the absence of above positive effects of the fluid on the metal cutting processes.

Another challenge comes from the change of engineering materials to be involved. Currently, there is a deliberate trend to use more lightweight materials especially aluminum alloys and advanced high strength steels, etc., to replace conventional ferrous materials for the powertrain and chassis components in automotive and aerospace industries. These materials would provide huge weight-saving advantages, hence improve fuel economy and reduce exhaust emissions. However, machining of apparently soft and ductile aluminum materials, for instance, is a real challenge especially for dry machining. The high chemical affinity towards various cutting tool materials and low melting point of aluminum cutting chips are roots of such difficulties. Development of built-up edge (BUE) is a main problem during the machining of those metals which leads to fluctuation of cutting force, deterioration in surface finish and drastic reduction in tool life etc.

Thus, the aggressive application conditions of the dry machining of lightweight metals require that the tool coatings should possess superior properties including not only high wear resistance but also good thermal stability, low friction, and chemical inertness to the sticky work materials at operation temperatures. Up to now, although some studies have been performed on the thermal stability of the TiN-based, CrN-based and DLC coatings, the researches on the effect of high temperature on the coating performance under dry machining of lightweight metals are still scarce and thus needed. With this goal in mind, the first part of experiments of this dissertation was to investigate the anti-wear performance of TiN, TiAlN, CrN, CrAlN and DLC coatings under dry sliding conditions after heating at different temperatures. An industrial trial of CrAlN- and TiN-coated punches in an auto stamping plant was conducted to study the wear property and failure mechanism of the coatings under extremely high contact stress conditions. A Cr(CrN)/C(DLC) coating system was also developed as a potential coating design model for dry machining of aluminum materials.

On the other hand, some non-cutting tool potential applications of the PVD and CVD hard ceramic coatings have increasingly gained an interest due to their high mechanical strength and chemical inertness. One of the potential applications is the coatings used for bipolar plates in fuel cells, especially in proton exchange membrane fuel cells (PEMFC). Commonly, the graphite and graphite composites are considered the standard material for PEMFC bipolar plates because of its low surface contact resistance and high corrosion resistance. Unfortunately, graphite and graphite composites are brittle and have poor cost effectiveness for high volume manufacturing processes. Metallic bipolar plates are explored as possible alternative materials which have good electrical conductivity, inexpensive material cost, versatile manufacturing process and high mechanical strength. However, the main issues of metals are relevant to degradation of PEMFC caused by corrosion of bipolar plates and the catalysts poisoning in membrane-electrode assemblies.

A new research direction on protective coatings on metallic bipolar plate produced by PVD or CVD technologies has emerged, although most of those studies are on TiN coatings with various N contents. More studies and reports on the performance of various PVD or CVD coated bipolar plates are still needed. To provide a better understanding of the coatings performance at simulated anodic and cathodic PEMFC environments, in the second part of experiments of this dissertation, the contact resistance and electrochemical properties of TiN-, TiAlN-, CrN-, CrAlN- and DLC-coated stainless steel in simulated PEMFC conditions were investigated and hence some important aspects of future efforts in research of the coatings deposition processes can be derived.

Recently, there has been an increasing interest in biomedical applications of hard ceramic coatings for implantation and surgical devices. Large-scale production of biomedical devices is based on materials such as austenitic stainless steels, titanium and cobalt-chromium alloys. Though these materials possess good corrosion resistance and biocompatibility, their wear resistance is relatively low. It is reported that life expectancy of an orthopedic implant with mobile parts as a hip implant, for instance, is of approximately 10 years. Such a short life span is due mainly to the mechanic wear and corrosion caused by the organisms on the mobile parts of the prosthesis, which demand their replacement. The research interests of the metal materials with PVD or CVD coatings in medical application have arisen. These coatings are used as protective coatings against wear and corrosion in order to increase the life expectancy of surgical implants and prosthesis. Most of the recent works are only limited to TiN and DLC coatings. More research on other coating systems is needed. Thus, in the last part of the experiment of this dissertation, the corrosion and wear properties of TiN, TiAlN, CrN, CrAlN and DLC coatings are investigated in a simulated body fluid environment to exam their feasibility for load-bearing medical devices.

1.2 Objectives of this research

The objectives of this research are to characterize TiN-, CrN- and C-based PVD and CVD coatings and to investigate their wear properties at dry and high contact stress conditions and their corrosion properties at fuel cell and biomedical conditions. The coatings include TiN, TiAlN, CrN, CrAlN, DLC and Cr(CrN)/C(DLC). The test results will be analyzed, and potentials of those PVD and CVD coatings for applications in dry machining of aluminum, die stamping of advanced high strength steels, fuel cell, and biomedical implants will be discussed.

1.3 Organization of this dissertation

This dissertation consists of seven chapters. Following this introduction, the relevant literatures regarding the fundamentals of PVD and CVD technologies and previous studies on characteristics and applications of TiN, TiAlN, CrN, CrAlN and DLC are reviewed in chapter 2. Chapter 3 describes the experimental procedures. Chapter 4 reports the investigation results of characterisation and performance of coatings under dry machining conditions. In chapter 4, there are three subsections. The first subsection is related to investigation into the effects of temperature (annealing) on the coating structure, and tribological properties using laboratorial testing methods. The second one is to illustrate the industrial trial results of CrAlN- and TiN-coated punches in an auto stamping plant. The third deals with a newly-developed coating system, Cr(CrN)/C(DLC), potentially for dry machining aluminum materials. Chapter 5 reports the performance of coatings under simulated PEM fuel cell applications and discusses the feasibility of coatings applied for bipolar plates of PEM fuel cell. In chapter 6, the comparative results of coatings' tribological and corrosion properties in simulated body fluid are presented. In the last chapter, chapter 7, conclusions of the present study are drawn and some future work is recommended.

CHAPTER 2 LITERATURE REVIEW

This chapter gives some introductions on the fundamentals of vapor deposition technologies and some overviews on previous studies on the formation and properties of PVD and CVD TiN, TiAlN, CrN, CrAlN and DLC coatings. The application trends of these coatings in cutting tools, bipolar plates of PEM fuel cells and biomaterials are also described in this chapter.

2.1 Fundamentals of Physical Vapor Deposition (PVD) and Chemical Vapor Deposition (CVD) technologies

2.1.1 Definitions of PVD and CVD processes

Physical Vapor Deposition (PVD) processes are those vapor deposition processes in which material is evaporated by various mechanisms (heating, high-energy ionized gas bombardment (sputtering), or electron gun) under vacuum or low pressure gaseous or plasma environment. The vapor phase is transported to the substrate forming a coating [1]. PVD is a line-of-sight process in which atoms or molecules travel from the source material to the substrate in a straight path [1]. PVD processes can be used to deposit films of elements and molecules and also of compound materials by the reaction of depositing material with the ambient gas environment (e.g. TiN) or with a co-depositing material (e.g. TiC) [1-3].

Chemical Vapor Deposition (CVD) may be defined as a deposition process whereby a reactant gas mixture is passed in a high-temperature reactor to form a solid product in the form of a thin film at the substrate surface [1, 2].

2.1.2 Classification of PVD and CVD processes

PVD and CVD techniques have evolved considerably over time with the requirements of new applications. To date, some hybrid and combination processes with PVD and CVD processes used in the same or connected processing chambers have emerged. It is difficult to classify the PVD and CVD processes due to some amounts of overlap between the two categories and a variety of terms have been used to describe essentially the same technique. In this review, PVD and CVD processes are attempted to be classified based on the coating deposition mechanisms and the energy sources. The classification of some typical PVD and CVD processes is illustrated by Fig. 2.1.

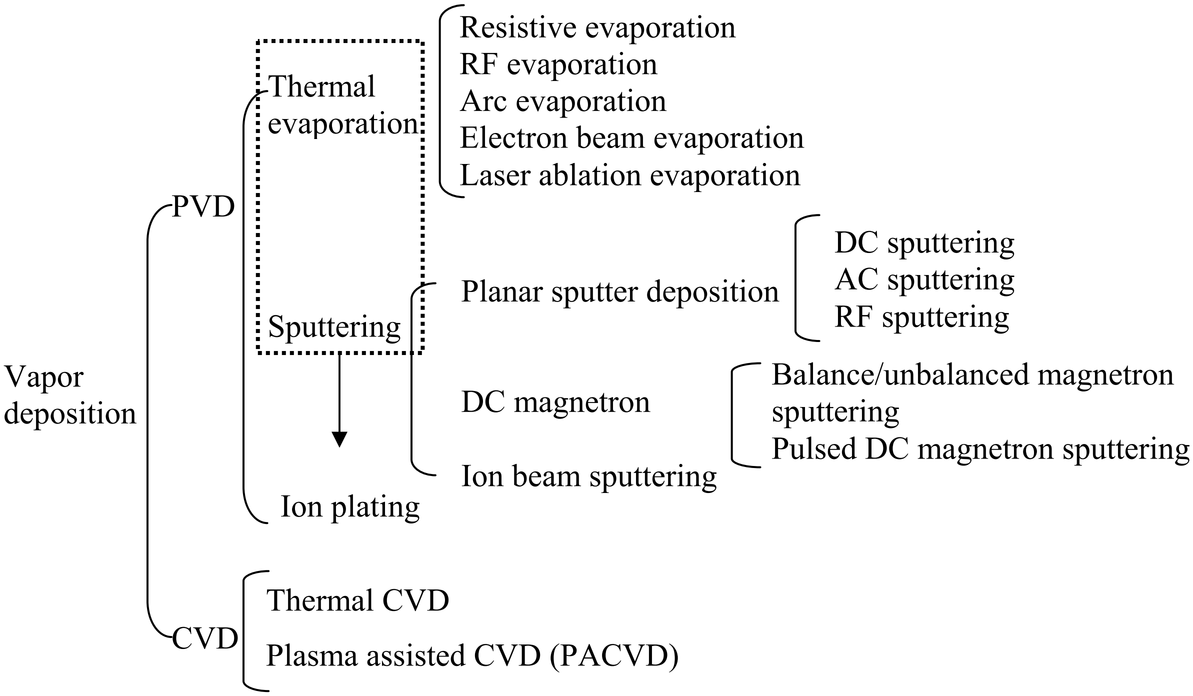

Fig. 2.1 Classification of PVD and CVD processes.

The PVD process is divided into two categories: (1) thermal evaporation and (2) sputter deposition.

The thermal evaporation is also called vacuum deposition or vacuum evaporation in which the atoms or molecules from a thermal vaporization source reach the substrate in a vacuum chamber without collisions with residual gas molecules and then condense the evaporated particles on the substrate. According to the heat sources of thermal vaporization source, the thermal evaporation can be sub-classified as resistive, inductive (RF), arc, electron beam, or laser evaporation deposition etc. Two types of thermal evaporation processes are shown in Fig. 2.2.

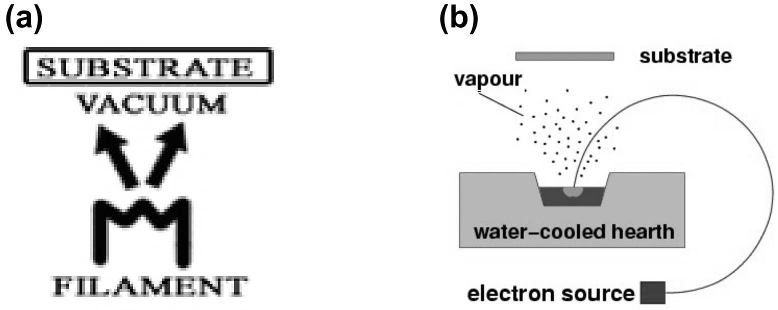

Fig. 2.2 (a) Resistive [3] and (b) electron beam evaporation processes [1].

Sputter deposition, which is often called just sputtering, is the deposition of the physical (not thermal) vaporization of atoms from a cathodic surface (target) by momentum transfer from bombarding energetic atomic sized particles. The energetic particles are usually ions of a gaseous material accelerated in an electric field [3]. Typically the use of the term sputter deposition only indicates that a surface being sputtered is the source of the deposited material. In some cases, the main sputtering configurations include simple diode planar sputter deposition, balanced magnetron and unbalanced magnetrons sputter deposition and ion beam sputter deposition [3]. Fig. 2.3 is the schematics of some sputter deposition processes (a) planar diode sputter deposition (b) ion beam sputter deposition (c) balanced and (d) unbalanced magnetron sputter deposition.

Ion plating is a hybrid PVD process of evaporation and sputtering (Fig. 2.4 [3]), which is sometimes called ion assisted deposition (IAD) or ion vapor deposition (IVD). The depositing material may be vaporized either by evaporation, sputtering, arc erosion or by decomposition of a chemical vapor precursor. The energetic particles used for bombardment are usually ions of an inert or reactive gas, or, in some cases, ions of the condensing film material ("film ions"). Ion plating can be done in a plasma environment where ions for bombardment are extracted from the plasma or it may be done in a vacuum environment where ions for bombardment are formed in a separate "ion gun" [4].

(a) Planar diode sputter deposition (b) ion beam sputter deposition

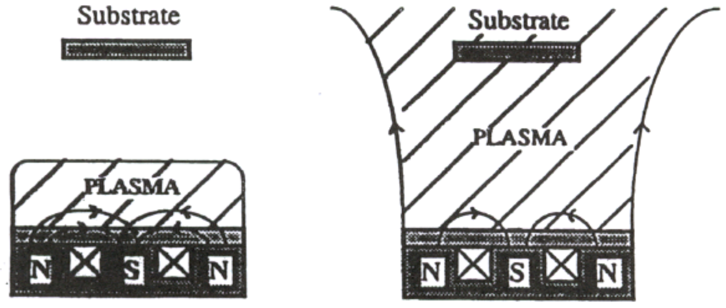

(c) Balanced Magnetron (d) Unbalanced Magnetron

Fig. 2.3 Some sputter deposition processes (a) planar diode sputter deposition, (b) ion beam sputter deposition [3], (c) balanced and (d) unbalanced magnetron sputter deposition [5].

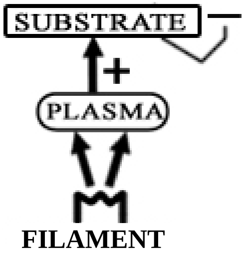

Fig. 2.4 Ion plating [3].

In recent years, a significant number of specialized PVD processes based on the basic PVD processes above have been developed and extensively used, e.g., reactive ion plating, activated reactive evaporation, reactive sputtering, etc [6]. In those reactive PVD processes, thin films of compounds are deposited on substrates by sputtering or evaporation from metallic targets in the presence of a reactive gas usually mixed with an inert working gas (invariably Ar) [6, 7]. The most common compounds and the reactive gases employed are briefly listed [7]:

1. Oxides (oxygen)-Al_2O_3, In_2O_3, SnO_2, SiO_2, Ta_2O_5.
2. Nitrides (nitrogen, ammonia)-TaN, TiN, AlN, Si_3N_4, CN_x
3. Carbides (methane, acetylene, propane)-TiC, WC, SiC.
4. Sulfides (H_2S)-CdS, CuS, ZnS.
5. Oxycarbides and oxynitrides of Ti, Ta, Al, and Si

CVD processes are divided into conventional CVD (CCVD) and plasma assisted CVD (PACVD).

In conventional CVD (CCVD), also called thermal CVD, the gaseous reactants are activated thermally in the vicinity of the heated substrate, and then react to form a film on the substrate. This technique is referred to simply as CVD in many cases. A simple schematic representation of CVD is shown in Fig. 2.5 [8]. However, the CVD reactions can also be initiated using different energy sources. This has given rise to other variants of CVD methods such as plasma assisted CVD (PECVD) and photo-assisted CVD which use plasma and light, respectively, to activate the chemical reactions [9].

Plasma assisted CVD (PACVD) is also called plasma enhanced CVD (PECVD). PACVD can be defined as a process, in which the constituents of the vapor phase react to form a solid film assisted by an electric discharge. In the PACVD technique, the gas molecules are mainly dissociated by electron impact generating very reactive neutral, radical, and ion species. These reactive species arrive on a surface and react with each other via an ionic or free radical mechanism in the film forming process. Since the gas molecules are activated by the energetic electrons instead of thermal energy, the reaction temperature can be easily reduced.

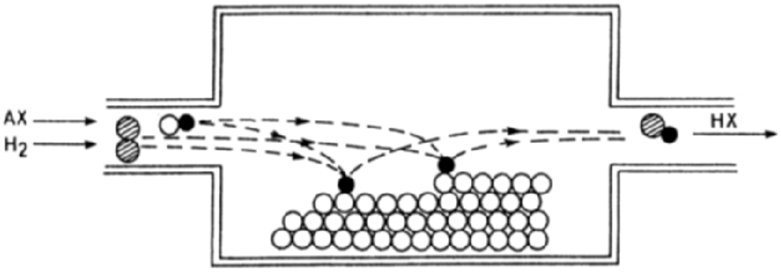

Fig. 2.5 A simple schematic representation of CVD [8].

2.1.3 Microstructural evolution during film growth

Petrov et al. [10] reviewed the present progress in understanding of microstructural evolution in thin films synthesized by low-temperature PVD on amorphous and polycrystalline substrates.

The growth processes controlling microstructural evolution, are presented schematically in Fig. 2.6 [10], include nucleation, island growth, impingement and coalescence of islands, formation of polycrystalline islands and channels, development of a continuous structure, and film growth. The typical product of today's coating processes of ceramic materials exhibits a columnar microstructure with elongated grains. Fig. 2.7 [10] shows a typical example of the columnar microstructure of TiN film deposited by reactive magnetron sputter deposition.

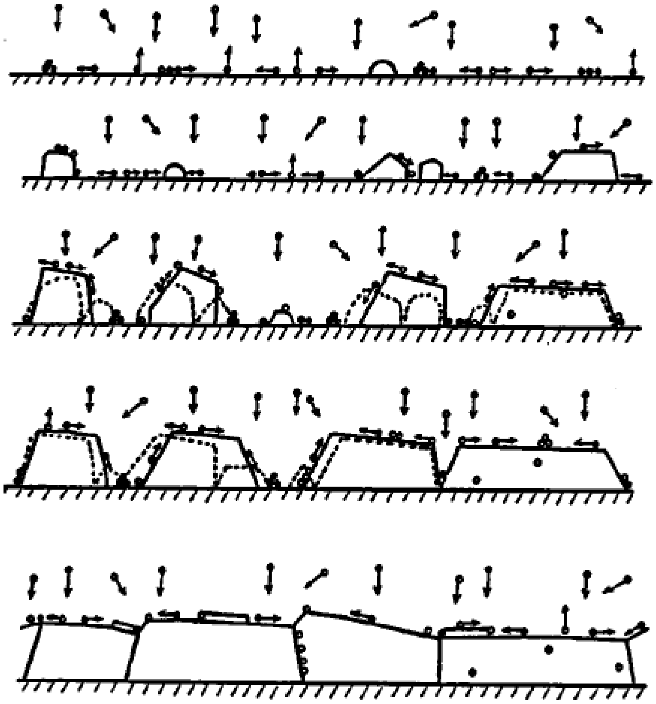

Fig. 2.6 Schematic diagram illustrating fundamental growth processes controlling microstructural evolution: nucleation, island growth, impingement and coalescence of islands, grain coarsening, formation of polycrystalline islands and channels, development of a continuous structure, and film growth [10].

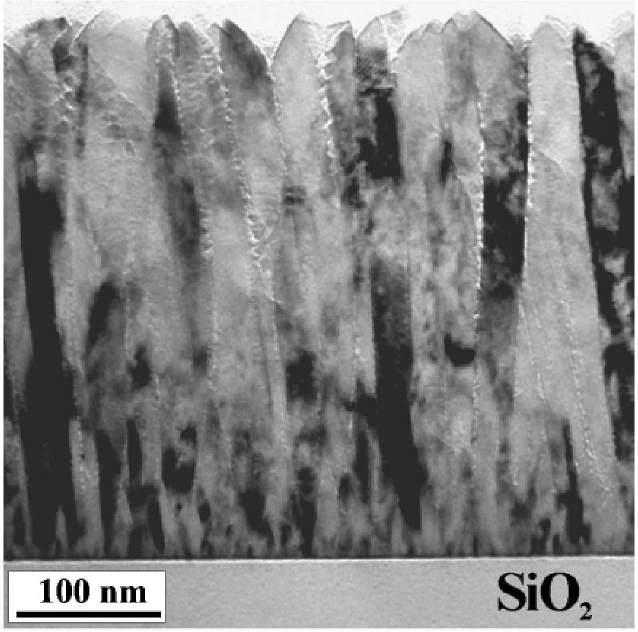

Fig. 2.7 Bright-field XTEM micrograph from a TiN film deposited on amorphous SiO_2 at 300 °C with a total pressure P_t=5 mTorr. The ion-to-Ti flux ratio J_i /J_{Ti} incident at the growing film was ~1 with an ion energy E_i=20 eV [10].

2.2 TiN, TiAlN, CrN, CrAlN and DLC coatings

TiN, TiAlN, CrN, CrAlN and DLC coatings are commonly used and technically matured PVD or CVD coatings. Those coatings are widely studied and applied for wear and corrosion protective coating, as well as some diffusion barrier, the solar energy absorber and IR reflector. In this section, the reviews of previous studies are restricted to coatings' structural, mechanical, tribological, corrosion properties and thermal stability, whereas other characterizations such as optical properties are not included.

2.2.1 TiN coating

The equilibrium phase diagram of Ti-N binary system (Fig. 2.8 [11]) shows that if some nitrogen is dissolved in titanium, the Ti(α) can be stable up to the melting point, which is then raised to about 2350 ^{o}C and the maximum N containing is reached at about

25 at.%. An ε-phase occurs when adding more nitrogen to the binary system until the content of N increases to 33.7 at. % and the stoichiometric formula Ti_2N is formed, which has a tetragonal structure. Adding further nitrogen to the system, a δ-phase appears which has a Ti riched composition (TiN_x, $x \leq 1$) with a NaCl type structure. In conventional TiN films, titanium nitride crystallizes mainly in the B1 NaCl structure [12] containing nitrogen in the range 33.7-50 at.% (Fig. 2.8) [11] and also contains some Ti_2N and Ti phases in some cases. Fig. 2.9 shows lattice structure of NaCl type TiN crystal where the center of f.c.c lattice is formed by Ti atoms and the corner of the f.c.c lattice formed by N atoms is located at the point (1/2, 0, 0) [13].

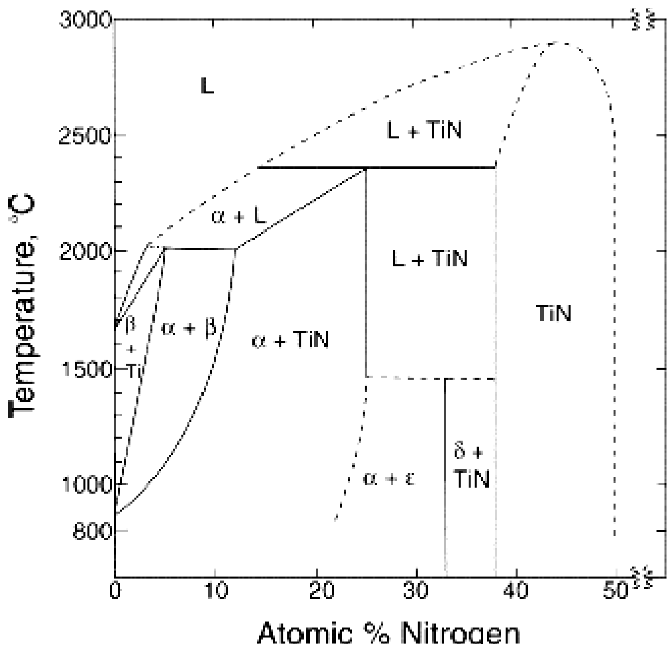

Fig. 2.8 Equilibrium phase diagram of Ti-N binary system [11], where the stoichiometric formulas of ε and δ phases are Ti_2N and TiN_x ($x \leq 1$).

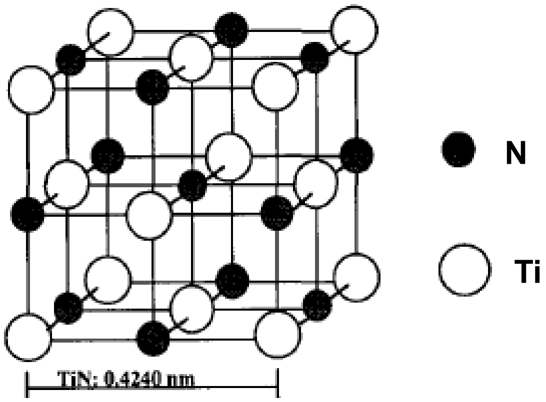

Fig. 2.9 Illustration of lattice structure of TiN [13].

The deposition of hard materials in the TiN systems with CVD processes was described in the German patent literature in 1953 for the first time [14]. However, the CVD deposition would require high temperatures (>800 ^{o}C), which is above the tempering temperature of most steels. Thus, high-temperature CVD is less suitable for tool applications because tool steel has a low austenising temperature (450–550 ^{o}C). Currently, low-temperature magnetron sputtering[15-17], cathode arc deposition [18, 19], electron beam evaporation [20] and plasma CVD [21] techniques have been applied to deposit TiN coatings on steel substrates. Especially, the plasma techniques provide, besides the low deposition temperature, the possibility to control the ion bombardment of the growing film which results in a smaller grain size, a less columnar structure and a controllably adjustable compressive stress and thus provide high hardness for the films formed.

Electrical properties

According to the band structure, strongly hybridized N 2*p* and Ti 3*d* orbitals contribute nine valence electrons to the electrical conductivity. Single-crystal TiN is a metallic conductor with an electrical resistivity of 23 μΩ.cm at room temperature [19]. However, TiN films rarely achieve the low resistivity of single-crystal TiN.

In the previous works [19, 22, 23], some studies were conducted on the influence of deposition parameters, i.e., deposition pressure, substrate bias, and deposition temperature, on the structure and electrical resistivity. It was concluded that the electrical resistance was significantly affected by the N content, phase structure, and defect density. The grain size played only a minor role in the electrical resistivity of TiN films. The structure of the films developing from hexagonal a-$TiN_{0.30}$ to cubic TiN, led to a drastic decrease in the electrical resistivity. A great decrease in the grain size contributed to the slight increase in the electrical resistivity of TiN films. The increase in the deposition temperature resulted in a drastic decrease in the defect density and an increase in the grain size of TiN films, which accounted for a linear decrease in the electrical resistivity of TiN films.

Mechanical properties

The mechanical properties of TiN coating correspond to the deposition conditions where stoichiometric TiN is formed. Studies on the microhardness of TiN_x films have been reported in the literature with widely varying results. The hardness values of Ti-N coatings deposited by various PVD or CVD processes as foundation of composition are summarized and shown in Table 2.1 here according to the review of Sundgren [24].

It has been concluded that the microstructure was of great importance for the physical properties of TiN coatings and because of the specific microstructures, values of hardness and resistivity far from the equilibrium bulk values could be obtained. One frequently observed microstructural feature is that of voids located in grain boundaries.

Such voids lower the hardness and increase the resistivity. For dense stoichiometric TiN films, hardness values are between 2000 and 2500 kgfmm^{-2} and resistivities range between 20 and 30 μΩ.cm.

Table 2.1 Hardness of Ti-N films [24]

Hardness (kgf mm^{-2})			
$Ti + Ti_2N$	$Ti + Ti_2N + TiN$ or $Ti + TiN$	$Ti_2N + TiN$	TiN
1160–1270		2550–2800	465, 750
		1300–2800	340–1900
1000		2000–2300	1700–2200
600–700		2000–2800	1200–2000
1100–1400		1700	1700–2200
	2800–3100		400–4000
		2500	1800
			1300–3500
			2400
			2500
			< 2000
			700–3100
1400–2800		1800–2500	1400–1800
		2400–3150	2100–2800
			1800–2600
			2300

2.2.2 CrN coating

CrN coatings produced by PVD processes on machine parts and tools for tribological applications have been well established. In the 1980s and the beginning of the 1990s, new coating materials were needed in order to improve the so far known properties of hard coatings [25]. Since the early 1980's, CrN became the promising coatings for tribological use as an alternative to TiN [25, 26]. To date, it has been applied on a large scale as an industrial coating on combustion engine components and metal machining tools, owing to its beneficial friction properties and oxidation resistance. The technologies used for CrN depositions include reactive sputter deposition [25, 27-30], magnetron sputtering process [27-29], plasma beam sputtering process [30, 31], arc-evaporation [32-37] and electron beam PVD [38] etc.

Depending on the choice of deposition techniques and parameters, the microstructure, phase compositions and mechanical properties of CrN coatings can be different. Typically, CrN coatings have a columnar structure as seen in Fig. 2.10 which shows some examples of the structure of CrN coatings produced by PVD processes [39].

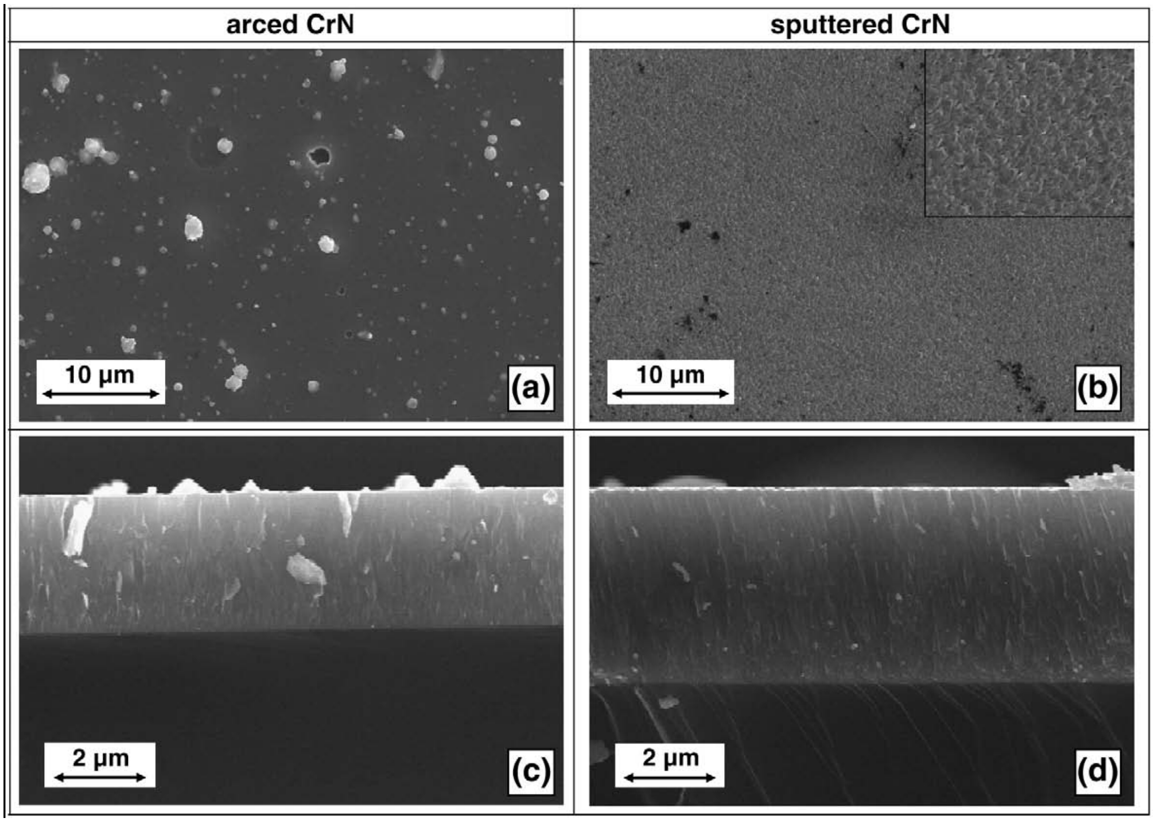

Fig. 2.10 SEM micrographs of the surface (a, b) and fracture cross-sections (c, d) of CrN coatings synthesized by reactive arc evaporation and magnetron sputtering on Si. The inset in (b) is 4× magnified to show the faceted surface of the sputter deposited coating [39].

Mechanical properties

Tu *et al.* [40] systematically investigated the correlation between the gas flow rate during reactive sputtering deposition and the composition and crystal structure of the deposited films. Table 2.2 shows the effect of N_2 flow rates on the compositions and phases [40] and Fig. 2.11 shows the microhardnesses of various CrN coatings with various N at.%. With N content increased, the phase transmitted from hexagonal (Cr_2N) to cubic CrN. The microhardness of the deposited CrN films at a load of 3 gf ranged from 1482 to 1771 HK. The hardness of these films can be related to stress, grain size, and defect density in the deposited films. Coating A in Table 2.2 with most dense and fine-grained structure exhibited the highest hardness value. On the other hand, with the largest grains and the roughest surface, coating B possessed the lowest hardness.

Table 2.2 Compositions and phases of CrN films deposited at various N_2 flow rates [40]

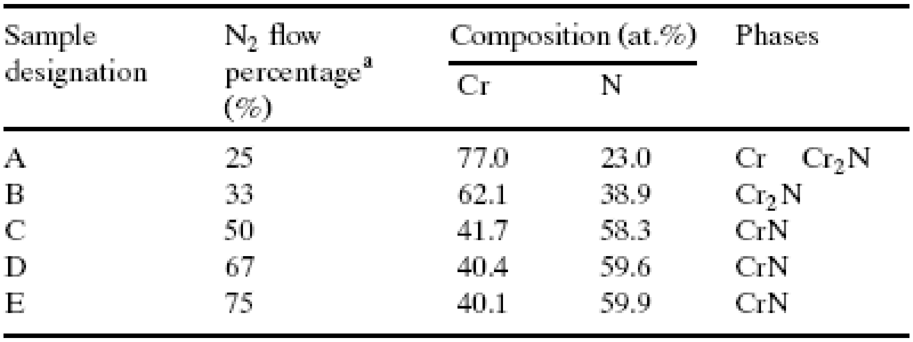

Sample designation	N_2 flow percentage[a] (%)	Composition (at.%)		Phases
		Cr	N	
A	25	77.0	23.0	Cr Cr_2N
B	33	62.1	38.9	Cr_2N
C	50	41.7	58.3	CrN
D	67	40.4	59.6	CrN
E	75	40.1	59.9	CrN

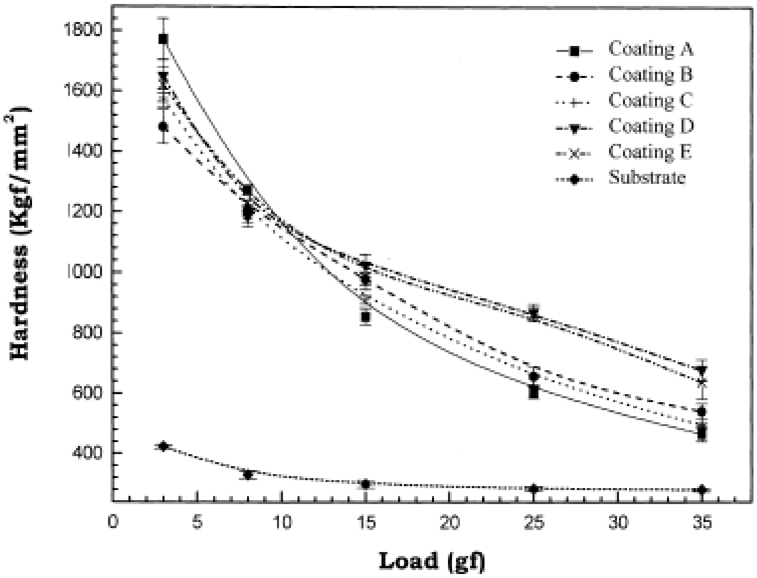

Fig. 2.11 The hardness of various CrN coatings as a function of load [40].

Rebholz *et al.* [41] also did the study similar to Tu and his coworkers. In Rebholz's study, the influence of nitrogen content (0-40 at.%) during the magnetron sputtering on the structural, composition, mechanical and tribological properties of the CrN coating has been studied. Dependent on the chemical composition of the coatings, cubic Cr, hexagonal Cr_2N, cubic CrN (and/or mixtures) could be detected. The phase's transmit with the increasing of N content in the coating is shown in Fig. 2.12 [41]. The results were similar to those of Tu's work and agreed with the equilibrium phase diagram of Cr-N system (Fig. 2.13 [42]). In Rebholz's work, a progression towards a denser microstructure was found with increasing nitrogen content up to x=0.29, associated with an increase in hardness from 700 up to 2400 $HK_{0.025}$. $Cr_{1-x}N_x$ coatings with x=0.10–0.16 showed good adhesion and the best abrasive and pin-on-disc sliding wear resistance, together with less crack development around the indentation area (and thus improved toughness) in impact tests after 50, 000 impacts against both steel and cemented tungsten carbide balls. The hardest coating ($Cr_{0.71}N_{0.29}$) was found to perform best (Fig. 2.14 [41]) in terms of reducing the resulting impact indentation volume.

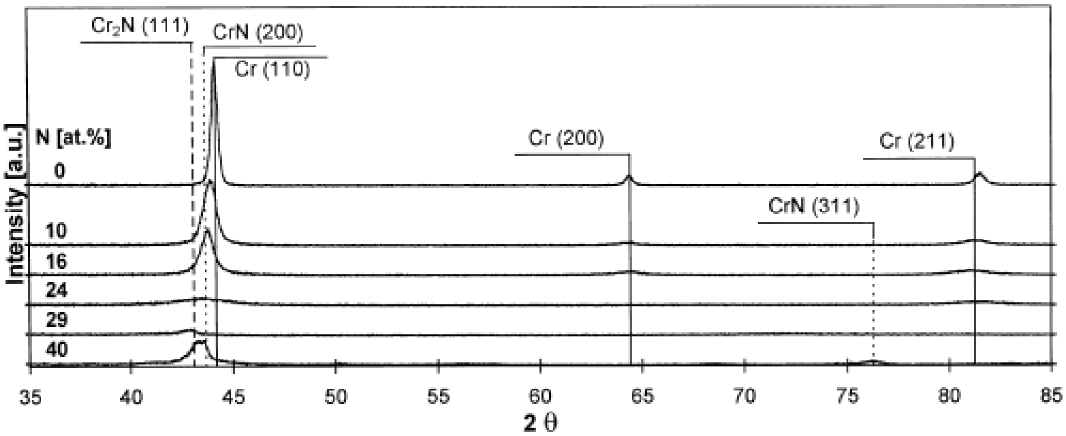

Fig. 2.12 XRD patterns of $Cr_{1-x}N_x$ coatings with x=(0, 0.1, 0.16, 0.24, 0.29 and 0.4) [41].

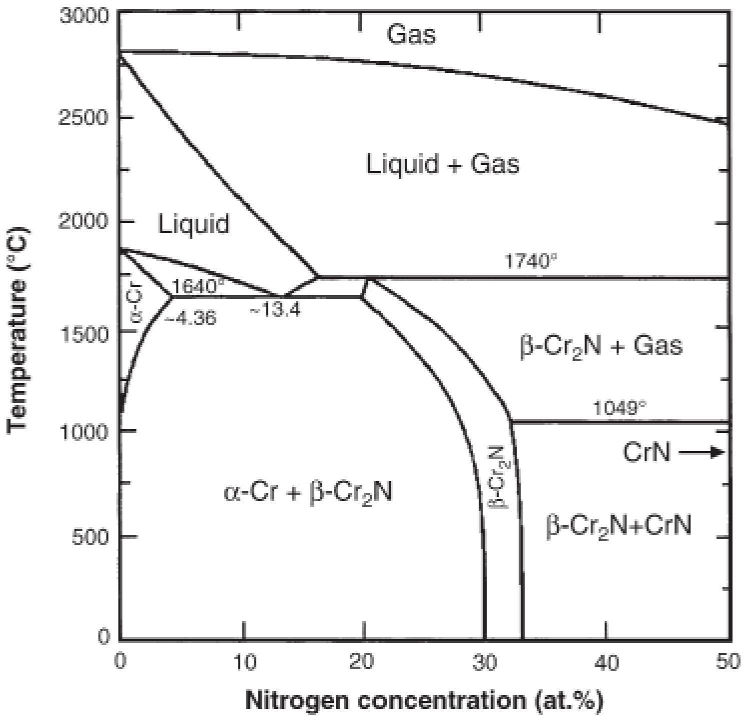

Fig. 2.13 Equilibrium phase diagram of the Cr–N system [42].

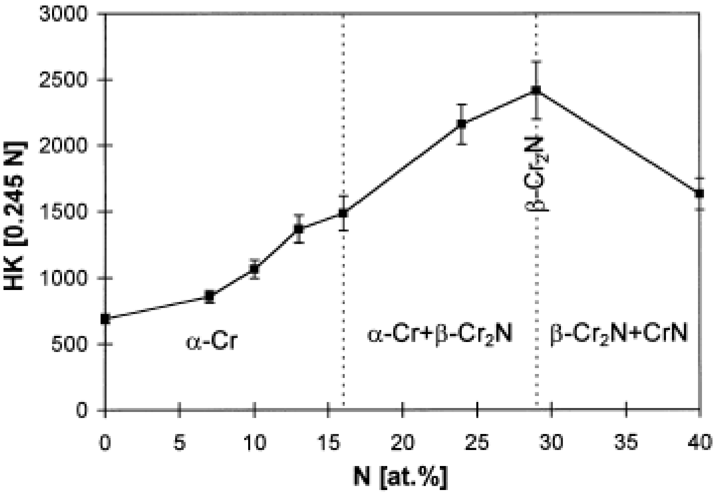

Fig. 2.14 Knoop microhardness (0.245 N) versus nitrogen concentration [41].

2.2.3 TiAlN and CrAlN coatings

In order to improve the oxidation resistance and the thermal stability of TiN films, the efforts to develop ternary compounds of (Ti,X)N have been demanded by incorporation of X in TiN film. Since last decades, TiAlN coatings have been attracting a lot of attentions.

In (Ti,Al)N films, Ti-atoms of the TiN-grid are partly substituted by Al-atoms. Due to the smaller atomic diameter of aluminum compared to titanium, the coating structure becomes deformed and strengthens the grid structure. In different investigations a higher oxidation resistance of (Ti,Al)N compared to TiN has been proven. Oxidation of TiN starts at temperatures slightly higher than 600 ^{o}C, whereas (Ti,Al)N shows a much higher oxidation resistance up to 800°C (Fig. 2.15 [43]). The formation of a dense Al_2O_3 top layer increases diffusion and oxidation resistance of the (Ti,Al)N film. Compared to TiN, the ternary coating system (Ti,Al)N shows an increasing hardness even at elevated temperatures. In dry drilling tests, an improved wear behavior was found compared to TiN, which was due to the superior high temperature properties of (Ti,Al)N films.

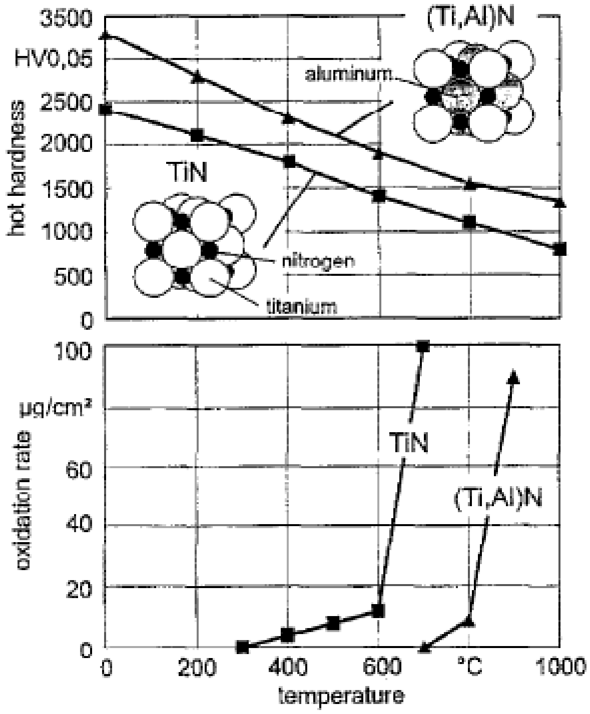

Fig. 2.15 Comparison of properties of TiN and (Ti,Al)N coatings [43].

Couple of publications [44, 45] reported on a successful coating process for the coating of (Ti,A1)N films by plasma-assisted chemical vapor deposition (PACVD) technique using a $TiCl_4/A1Cl_3/N_2/H_2/Ar$ gas mixture, whereas PVD processes such as cathodic arc vapor (plasma or arc ion plating) deposition, magnetron sputtering (or sputter ion plating), and combined magnetron and arc processes were the most widely used techniques to deposit titanium-aluminum based coatings.

As the addition of Al improves the mechanical properties and oxidation resistance of TiN coatings, a similar effect of Al in CrN coatings could also be expected. For these coatings, intrinsic hardening and solid solution hardening effects play an important role. Incorporating Al into CrN results in enhanced properties like hardness, oxidation resistance, and thermal stability.

Mechanical properties

The structures and properties of TiAlN and CrAlN coatings were affected by varieties of PVD techniques, different types of targets materials (e.g. alloyed or single metal) and the ratio of Al/Ti. It has been reported that the $Ti_{1-x}Al_xN$ [46] and $Cr_{1-x}Al_xN$ [47] films' crystal structure changed from the NaCl (TiN or CrN) into wurtzite type (AlN) at x=0.6 to 0.7 (Figs. 2.16-2.17). The hardness increased with increasing of Al content until the maximum value of ~2700 HV for $Ti_{1-x}Al_xN$ and ~3200 for $Cr_{1-x}Al_xN$ were obtained at x=0.6 (Fig. 2.18). Further increasing the content of Al resulted in the decrease of hardness to ~1400 HV for $Ti_{1-x}Al_xN$ and ~1700HV for $Cr_{1-x}Al_xN$ at x=1, respectively. However, the lattice parameter of two coatings decreased with increasing of Al content.

Thermal stability

In the research of Chim *et al.* [48] , the TiN, CrN, TiAlN and CrAlN (with Al/Ti or Al/Cr atomic ratio around 1:1) were deposited on stainless steel substrates by a lateral rotating cathode arc technique and the oxidation behavior and its influence on overall hardness of those four PVD coatings were investigated. The conclusions are summarized as follows. TiAlN and CrAlN coatings showed better oxidation resistance as compared to TiN and CrN. Particularly, the TiN coating was evidently oxidized and became soft at 500 °C, and completely delaminated from the substrate at 800 °C. TiAlN coating started to oxidize at 600 °C and its hardness decreased significantly at 700 °C. Among the four coatings studied in that work, CrAlN showed the best oxidation resistance. Its hardness was stable (between 33 and 35 GPa) up to an annealing temperature of 800 °C and still kept at a relatively high value of 18.7 GPa after annealing at 1000 °C.

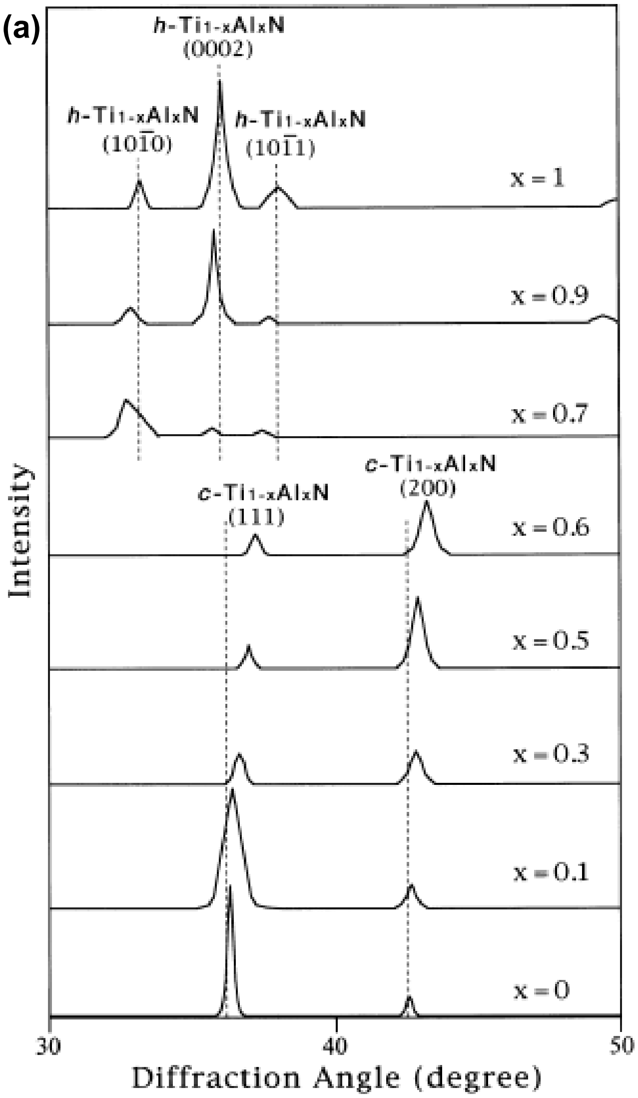

Fig. 2.16(a) X-ray diffraction patterns from $Ti_{1-x}Al_xN$ films with x=0, 0.1, 0.3, 0.5, 0.6, 0.7, 0.9, 1 respectively: $Ti_{1-x}Al_xN$ films with $x \leq 0.6$ had NaCl structures and those with $x \geq 0.7$ had wurtzite structures. Here, c- and h- represent cubic and hexagonal phase, respectively [46].

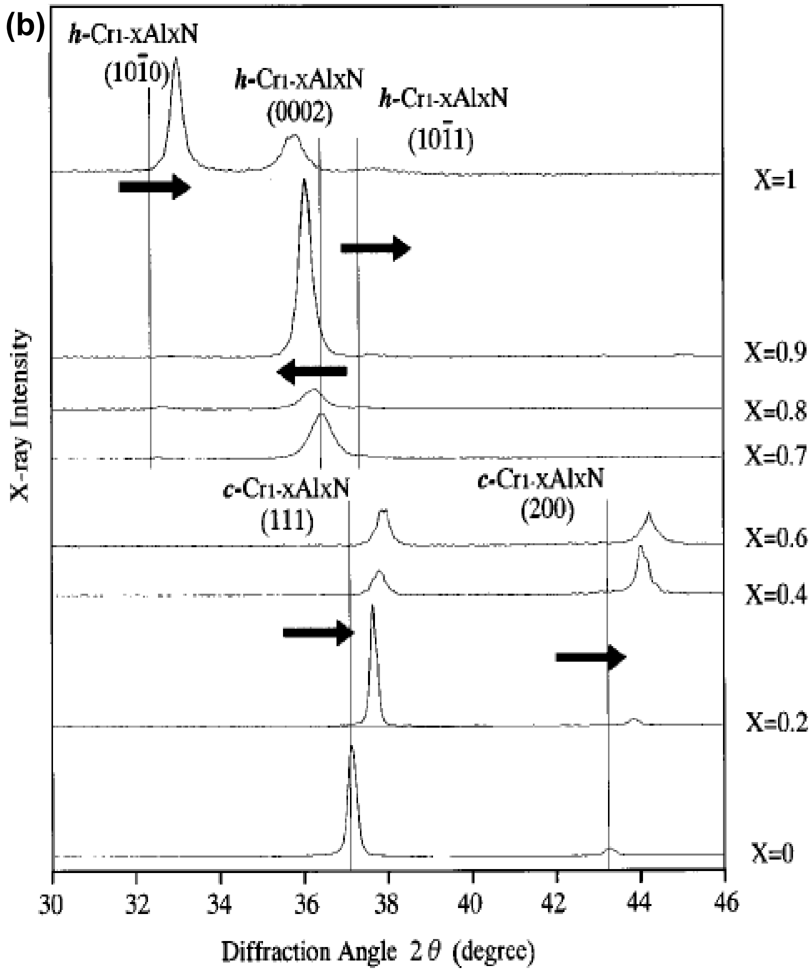

Fig. 2.16(b) XRD patterns from $Cr_{1-x}Al_xN$ [47] films with x=0, 0.2, 0.4, 0.6, 0.7, 0.8, 0.9, and 1, respectively. Crystal structures of $Cr_{1-x}Al_xN$ films were changed from the NaCl type for x<0.6 to the wurtzite for x>0.7. Here, c- and h- represent cubic and hexagonal phases, respectively. Arrows indicated the gradual shift of peaks against CrN or $Cr_{0.3}Al_{0.7}N$, respectively.

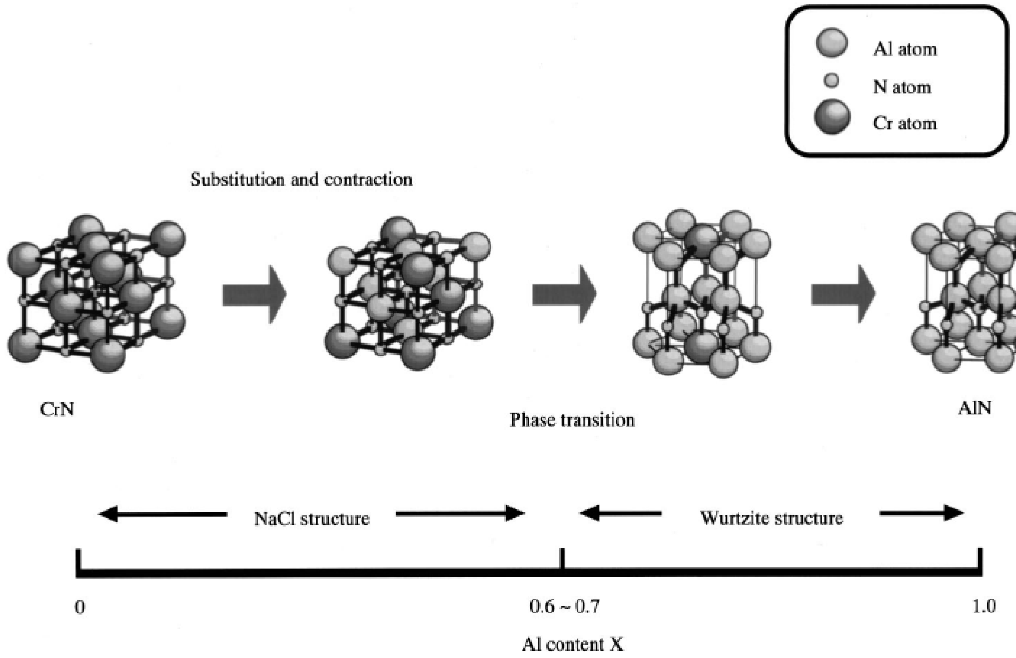

Fig. 2.17 Change in the crystal structure of $Ti_{1-x}Al_xN$ [46] or $Cr_{1-x}Al_xN$ [47] against Al content. The crystal structure changed from NaCl into wurtzite type at x=0.6-0.7, and the lattice parameter decreased with Al content.

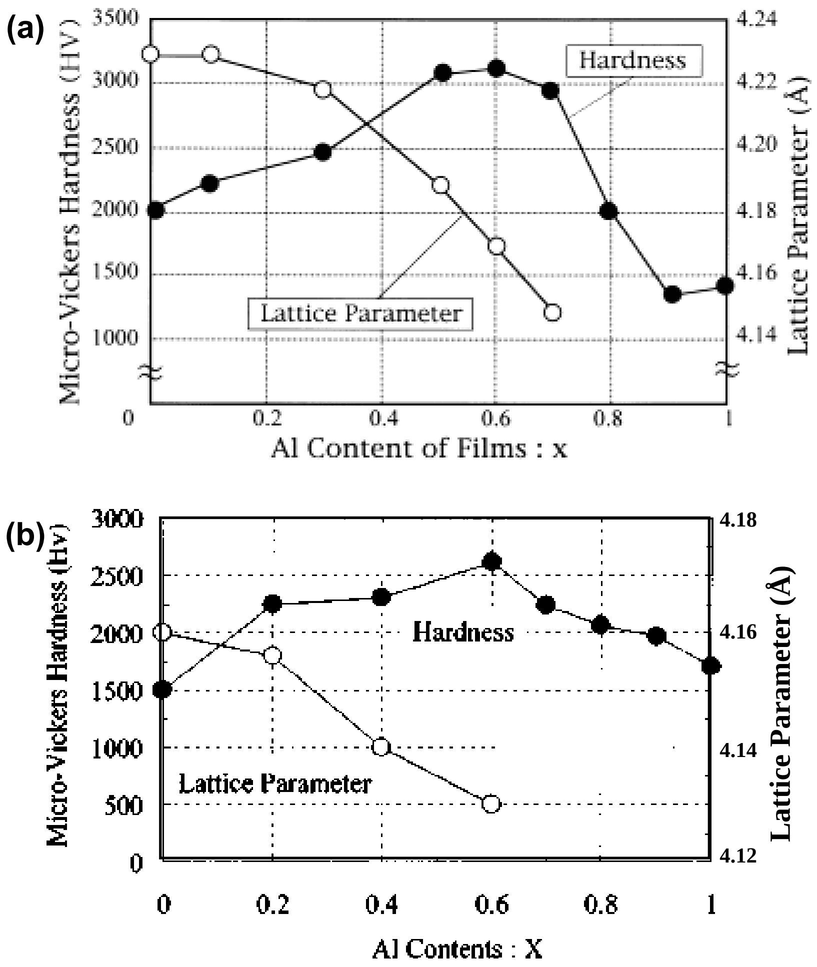

Fig. 2.18 Changes in the lattice parameters of (a) $Ti_{1-x}Al_xN$ [46] and (b) $Cr_{1-x}Al_xN$ [47] films with the NaCl structure (open circles) and micro-Vickers hardness (closed circles) against Al content.

2.2.4 DLC coating

The first DLC films were prepared by Aisenberg and Chabot in 1971 using ion beam deposition. Currently, a wide range of PVD and CVD deposition methods have been used to produce DLC coatings such as ion beam, sputtering, cathodic arc, pulsed laser deposition, and plasma assisted CVD [49, 50].

Diamond-like carbon (DLC) is a metastable form of amorphous carbon containing a significant fraction of sp^3 bond. DLC has some extreme properties similar to diamond, such as the hardness, elastic modulus and chemical inertness, but these are achieved in an isotropic disordered thin film with no grain boundaries. In addition, it is much cheaper to be produced than diamond itself. There are several different types of DLC films such as hydrogen free DLC (a-C), hydrogenated DLC (a-C:H), tetrahedral amorphous carbon (ta-C), hydrogenated tetrahedral amorphous carbon (ta-C:H), and those containing silicon or metal dopants, such as Si-DLC and Me-DLC. Jacob and Moller [51] used a ternary phase diagram (Fig. 2.19) to display the compositions of the various forms of amorphous C-H films.

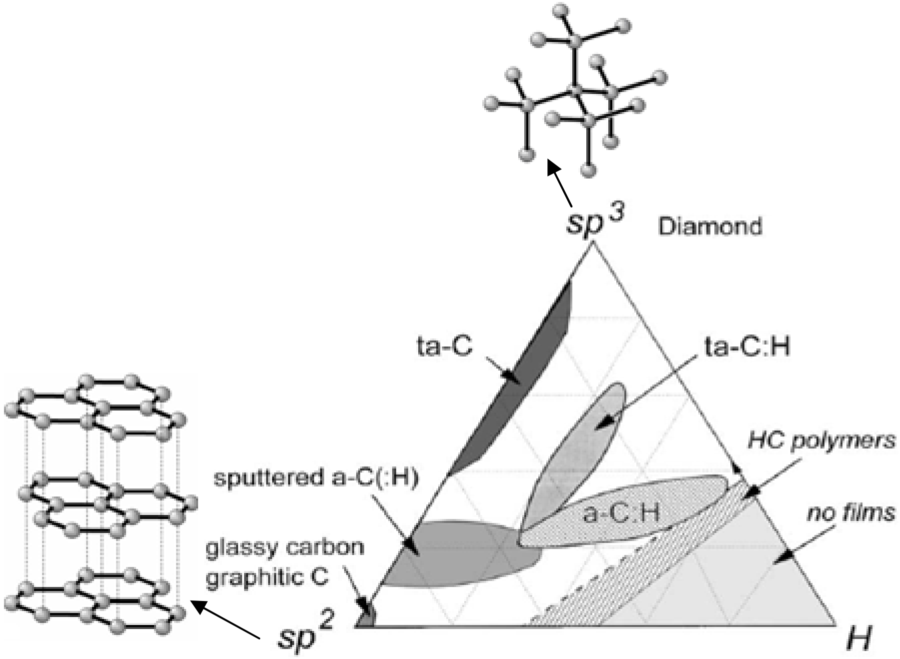

Fig. 2.19 Ternary phase diagram of bonding in amorphous carbon-hydrogen alloys [51].

Mechanical properties

Hainsworth and Uhure in their review [50] summarized a selected range of properties for the various DLC films, along with the properties of diamond and graphite, which are presented in Table 2.3. With the increasing of sp^3 content, the hardness of DLC coating increased. The hardness of a-C:H can reach up to 20 GPa and for ta-C DLC, the maximum hardness ever reported is 90 GPa.

Tribological properties

DLC coatings have high hardness, low frictional coefficient, high wear resistance, high chemical inertness, good biocompatibility and high electrical resistance. Among these properties, the tribological properties of DLC coatings were most widely investigated. It was generally believed that the good tribological behavior is due to the ability of DLC to form lubricative interface layer under most tribological conditions. Liu *et al.* [52] have introduced one mechanism of DLC's low coefficient of friction (cof) which is so called 'wear-induced surface graphitization' mechanism. In this mechanism, it has been proposed that graphitization occurs following a hydrogen evolution stage due to thermal and strain effects from the repeated friction at the asperities, which causes the destabilization of the sp^3-hybridized carbon structure and thus a graphite interface layer with a critical thickness is formed. The low cof of DLC can be attributed to this graphite layer [52, 53]. Grill proposed [53] another explanation about the low cof of DLC, which was due to the existence of the hydrogen-contained tribochemcial layer at the interfaces. The hydrogen (chemisorbed from the application environment and/or existing in the a-C:H structure) passivated the dangling bonds in the hydrogenated DLC films and permitted only weak interactions between coating and the sliding partner, therefore resulting in the reduced friction [53]. The self-lubricating characteristic of DLC coating has made it a promising candidate of tool coating used for high speed and dry machining (machining without coolants) lightweight metals (Al, Zn, and Mg etc.), which is a significant goal in environmentally conscious manufacturing.

Thermal stability

In the past, the unsatisfying thermal stability limited the further exploitation of DLC since high temperature caused irreversible changes in the structure leading to the loss of hydrogen and graphitization (sp^3 to sp^2 transition). The coating structure variation with the temperature has been well documented. Depending on the deposition conditions and the dopants contained in the films, the trigger temperatures of sp^3 to sp^2 transition and hydrogen loss were variously reported [54-60]. The previous works revealed that, at temperature up to the low trigger temperature (which was reported as 200 [57], 250-300 [54, 56, 59] and 400 °C [60]), the DLC coating only slightly released its bonded hydrogen and had no obvious changes in their structure, mechanical and tribological properties [57]. While above the trigger temperature, a structural transition occurred accompanying with the drastic loss of hydrogen and CH_x species and sp^3 to sp^2 transformation, which leaded to the more graphite-like structure with poorer mechanical properties. Thus, the high temperature changed the dimensions and properties of the material and limited the use of DLC in applications involving a high temperature.

Table 2.3 Comparison of properties of various amorphous carbon films with those of diamond and graphite [50]

	sp^3 content, %	Hydrogen content, %	Density, g cm^{-3}	Poisson's ratio	Young's modulus, GPa	Fracture toughness, MPa $m^{1/2}$	Residual stress, GPa	Hardness GPa
Diamond	100	0	3.515	0.07	1144	3.4	-	100
Graphite	0	0	2.267	0.2	9-15	-	-	0.2
a-C:H (hard)	40	30-40	1.6-2.2	0.4	140-170	1.2-1.6	1-3	10-20
a-C:H (soft)	60	40-50	1.2-1.6	0.25	50	2.9-3.3	~1	<10
ta-C	80-88	0	3.1	0.12	757±47.5	-	<12	40-90
ta-C:H	70	30	2.35	0.3±0.09	300±49	-	8.4	?50

2.3 Applications of TiN-based, CrN-based and DLC coatings

2.3.1 Applications in cutting tools for dry machining

Introduction to dry machining

During machining processes such as drilling, turning, milling, grinding, shaping (forming), planning and saws, the use of cutting fluid leads to an increase of tool life by the reduction of cutting forces (lubrication effect) and temperatures in the tool (cooling effect). Another important function of the cutting fluids is to flush away the chips from the cutting zone (flushing effect) [61].

A process carried out in absence of these fluids is called dry machining or green machining. In another situation, i.e. high cutting speeds, the lubrication in the cutting zone is not evident and not really effective since high speed machining leads to lower cutting forces, higher removal rates and therefore lower energy consumption. Thus, high speed machining and dry machining are often associated [62].

The advantages of the dry machining include non-pollution of the atmosphere and water, reduced disposal, less danger to human health and no residue on the swarf, which can significantly reduce the cost of disposal and cleaning cost. Moreover, it offers cost reduction in machining. It has been reported [63] that the cost associated with cutting fluids use was approximately 7 to 17% of total manufacturing cost, which is very high. Thus, dry machining is not an option but a necessity of sustaining competitiveness and ecologically desirable for manufacturing enterprises in the near future [62, 64].

Elimination of coolants involves the absence of their positive effects on the metal machining cutting processes. That means that there is a higher friction between tool and workpiece, between the chip and the tool and, consequently, higher temperatures. The tool is subjected to larger thermal load, which can result in higher levels of abrasion, diffusion and oxidation and thus reduction of its life. The workpiece, when receiving a larger amount of heat, expands, hindering the attainment of tight tolerances and, in some cases, causing metallurgical damage to its superficial layer [65]. Moreover, due to absence of flushing effect and temperature rise under dry machining, the chip are readily picked up and form built-up edge (BUE). BUE is one of damage mechanisms of tools and leads to worsen the cut surface finish and accuracy [66].

Dry machining of some difficult-to-machine non-ferrous metals such as Al [67-69], Ti [70-72] and Ni [61, 73] alloy is one of the main challenges of manufacturers. Currently, the growing demand to reduce energy consumption has stimulated an urgent need for weight reduction in the engineering components, especially in automotive and aerospace industries. Among the light weight materials, Al and its alloys have been widely applied due to their low cost, high strength to weight ratio, good formability and recycling potential, and high thermal and electrical conductivity [74, 75]. Emerging trend of dry machining environment of materials has given a real challenge in machining of aluminum and its alloys, since aluminum are easily welded and stuck to the tool surface and form BUE due to their relatively low melting temperature (500-600 ºC) and chemically activity [76]. Carrilero [68] reported the microstructural features of built-up edge (BUE) and built-up layer (BUL) (illustrated by Fig. 2.20) by a study using the SEM and EDS to observe the formation of BUE and BUL over TiN turning inserts in machining of an Al–Cu alloy.

PVD or CVD coatings used for dry machining

Besides the optimization of machining process such as tool geometry and cutting parameters, widely studies have recently been attempted to improve the nature of contact surface between tools and workpieces by applying coatings on tools to achieve dry machining. The goals of those studies are to achieve low wear and friction and anti-sticking between the contact surfaces so as to overcome the BUE, prolonged tool life and lower down time. The aggressive application conditions during dry machining processes require the coatings having properties such as good thermal stability, low friction, high wear resistance, and good anti-sticking properties while against the counter materials. The following description will review the previous research on the performance of TiN-based, CrN-based and DLC coatings applied in dry machining of common metals and aluminum alloys.

TiN-based and CrN-based PVD coatings

TiN, TiAlN, CrN and CrAlN are commercial PVD coatings used in tools industry and they are successful particularly for dry machining of some ferrous materials [43, 69, 77].

Roy *et al.*'s study [69], which investigated machinability of pure aluminum and Al–12% Si alloys against uncoated and coated carbide inserts, indicated that WC based uncoated tools and coated tools with coating of TiC, TiN, TiB_2, Al_2O_3, and AlON ,which are capable of dry machining of ferrous materials, could not succeed in dry machining of aluminum because work material built-up both in face and flank covering the cutting edge.

Leyendecker *et al.* [78] reported the performance of PVD (Ti,Al)N as a commercial coating on cutting tools. The coating exhibited superior wear resistance in the machining of cast iron. Derflinger *et al.* [79] applied different PVD hard layers on high speed steel drills, with or without a WC/C lubricant layer on top of the coating, and investigated their performance in dry drilling tests on cast iron and alloy steels. They observed that the performance of (Ti,Al)N coated tools were superior to both TiN and TiN-WC/C coated tools. Similar results can be obtained from many reports. However, the TiAlN coating used for dry machining of aluminum alloys has been scarcely reported.

Konca *et al.* [80] investigated the material transfer and adhesion phenomena between 319 Al alloy and different TiN based and CrN-based coatings deposited on M2 type steel substrates using a pin-on-disc test. The amount of aluminum transferred on the coating surface was in the order of TiAlN, TiN and CrN. The material transfers can reflect the trend of BUE formation.

Similar to the TiAlN coating system, the incorporation of Al into the cubic CrN crystalline structure greatly enhances the hardness of the CrAlN coating system (as descried in section 2.2). A better abrasive wear resistance, which is believed to be the major wear mechanism in machining and forming applications, of the CrAlN coatings (particularly with higher Al-content) than the TiAlN coatings was also reported [81]. Also due to the superior thermal stability, CrAlN coating is very promising for high speed dry machine and other high temperature applications [48]. However, as a newly merged coating system, the reports on the actual application on dry machining, especially the machining of aluminum alloy, are still few.

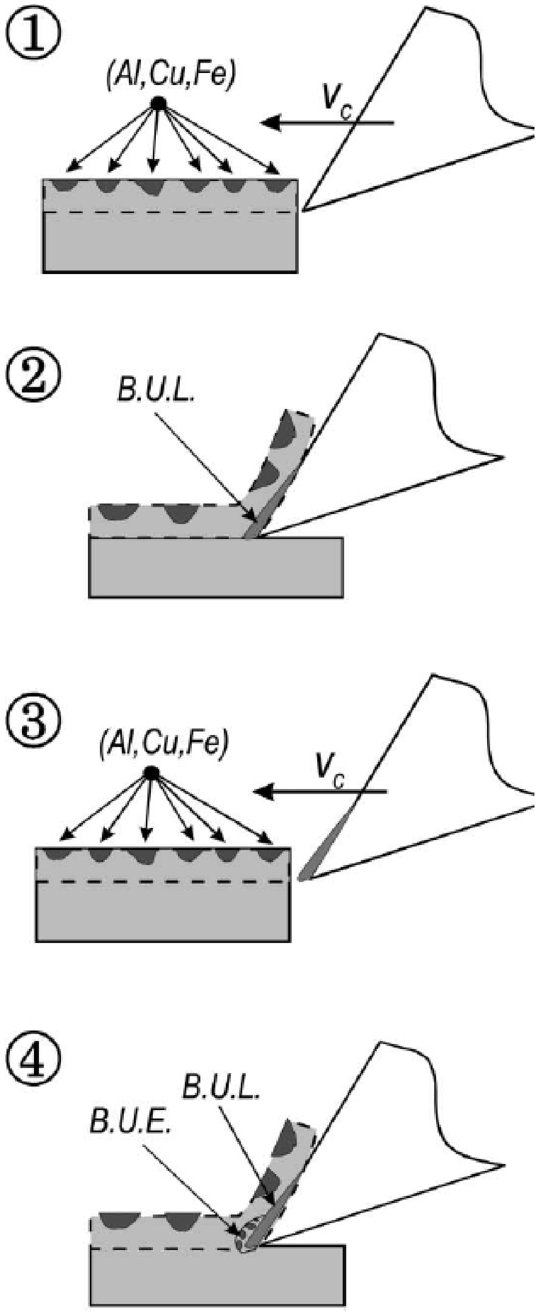

Fig. 2.20 Scheme of the BUL (1 and 2) and BUE (3 and 4) formation [68].

DLC coatings

CVD diamond coated tools have been used for dry machining of aluminum, copper or magnesium and also in the machining of wood, semi-sintered ceramics, hard rubbers, graphite composite materials and fiber reinforced polymers because of their high thermal coefficient, fast heat diffusion and no affinity for most counterface materials. The thermal degradation of diamond starts at temperatures around 700~800°C [82]. The size of diamond crystal grains grown by CVD is not so fine, which results in the rough surface of diamond coating (Fig. 2.21). When coated tools are used in finishing process, however, they could not achieve the finished surface fine enough as usually required. The sharp pointed apices of diamond crystals with the height of normally several microns put scratch traces of the same depth on the surface of workpiece when the coated tools are used for machining, whereas in the case of machining aluminum alloy, for example, the required roughness of finished surface is normally less than 1 μm [83]. Additionally, the relatively high price of diamond coatings further limits the use of diamond tools.

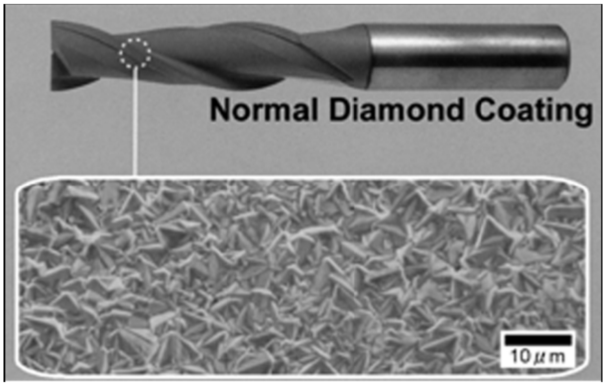

Fig. 2.21 Appearance of diamond coated endmills and diamond crystal grains on the surface of coating [83].

Diamond-like carbon (DLC) coatings have relatively smooth surface and low cost compared to diamond coatings, therefore are considered as alternative coating materials. Dasch *et al.* [67] conducted a comparative research of five categories of DLC coatings (shown in Table 2.4) where both pin-on-disc at three temperatures from 120 to 400 ^{o}C, and actual drilling tests were performed on each coatings.

Table 2.4 Coatings tested in study [67]

Coating type	Category	Designation	Hydrogen H/C atom ratio
Metal-containing	Me-a-C:H	Me-DLC	0.038 to 0.14
Graphitic	a-C	Graphitic	0.013
Blend	a-C/ a-C:H	Blend	0.27
Hydrogenated DLC	a-C:H	HDLC1	0.34
		HDLC2	ND
Nonhydrogenated DLC	ta-C	HDLC1	<0.01
		HDLC2	ND
CVD diamond	t-C	Diamond	0.016

The results from the five coating categories are summarized below: The Me-DLC coating (WC/C) failed at 120 ^{o}C and performed the worst of all coatings on the pin-on-disc and drilling tests. The non-hydrogenated DLC coating performed poorly on both pin-on-disc and drilling tests. The graphitic-type coating failed at 260 ^{o}C during pin-on-disc testing due to wear. Even this coating showed improved performance over an uncoated drill, but eventually failed after a few hundred holes. The blend coating which have properties of both the graphitic and the HDLC (hydrogenated DLC) coatings performed the best during the drilling test and the HDLC coating performed the best during pin-on-disc testing, yielding good results even at 400 ^{o}C. However, the HDLC coating did not show good performance at the drilling test, possibly due to the coating delamination during the higher forces of drilling. The results above indicated that hydrogenated DLC or the coatings with incorporated hydrogen were the most successful coatings and performed best in dry environments.

Bhowmick *et al.* [84] investigated the dry drilling performance of hydrogenated (H-DLC) and non-hydrogenated diamond-like carbon (NH-DLC). Tool coatings were tested against 319 grade cast aluminum alloy using the performance of uncoated HSS drills as a baseline. The study concluded that DLC-coated drills were superior to HSS drills when drilling 319 Al under ambient conditions without any fluids. Under the same conditions, among the DLC coatings, the H-DLC had advantages over the NHDLC grade coatings in keeping the cutting forces low and limiting adhesion.

Some other previous works also indicated that DLC coatings, especially hydrogenated DLC, were suitable for dry machining of aluminum alloys in the term of avoiding aluminum-adhension, but the relatively low hardness and coating degradation over 400 ^{o}C limited their further applications.

2.3.2 Applications in the bipolar plates of PEM fuel cell

Fuel cells

With depleting oil reserves and increasing environmental concerns, a number of manufacturers - including major auto makers - and various federal agencies have supported ongoing research into the development of fuel cell technology to replace traditional power sources for use in fuel cell vehicles (FCV) and other applications in the coming years [85-87].

A fuel cell is an electrochemical conversion device, in which hydrogen and oxygen react electrochemically and convert the chemical energy of a fuel directly into electrical energy producing electricity, heat and water. Therefore, a fuel cell is a high efficiency, low pollution energy source [88]. There are several types of fuel cells currently under development, and they are classified primarily by the kind of electrolyte they employ. Some of the most promising types include proton exchange membrane, phosphoric acid, direct methanol, alkaline, molten carbonate, and solid oxide fuel cells [88, 89].

Proton exchange membrane fuel cell (PEMFC) and bipolar plates (BPs) in PEMFC

Among of the fuel cell types, the proton exchange membrane fuel cell (PEMFC) is gaining worldwide interest [85, 87, 89-104] due to its advantages over other fuel cells such as delivering high power density, a low weight and volume. Moreover, PEM fuel cells operate at relatively low temperatures (<100 °C), resulting in a better durability of system components, and therefore lower material costs. A typical PEM fuel cell (Fig. 2.22 [90]) essentially consists of an anode backing, membrane electrode assembly (MEA) and cathode backing sandwiched between two bipolar plates (anode and cathode). In a PEMFC, a stream of hydrogen is delivered to the anode side of the MEA, and then hydrogen is catalytically split into protons and electrons at the anode side. This oxidation half-cell reaction is represented by:

$$H_2 \rightarrow 2H^+ + 2e^- (E^0 = 0V_{SHE})$$

The newly formed protons permeate through the polymer electrolyte membrane to the cathode side. The electrons travel along an external load circuit to the cathode side of the MEA, thus creating the current output of the fuel cell. Meanwhile, a stream of oxygen is delivered to the cathode side of the MEA. These oxygen molecules then react with the protons permeating through the polymer electrolyte membrane and the electrons arriving through the external circuit to form water molecules at the cathode side. This reduction half-cell reaction is represented by:

$$4H^+ + 4e^- + O_2 \rightarrow 2H_2O(E^0 = 1.229V_{SHE}).$$

In term of weight, volume and cost, bipolar plates are one of the most significant parts of a fuel cell stack [90, 91, 105]. Tsuchiya *et al.* [106] reported that bipolar plates accounted for about 80% of total weight and 45% of stack cost and in another study, Cunningham *et al.* [105] claimed that bipolar plates represented about a third of the overall cost of a fuel cell. The performance functions of the bipolar plates are listed in the follows [90]:

(1) To distribute the fuel and oxidant within the cell.

(2) To facilitate water management within the cell.

(3) To separate individual cells in the stack.

(4) To carry current away from the cell.

(5) To facilitate heat management.

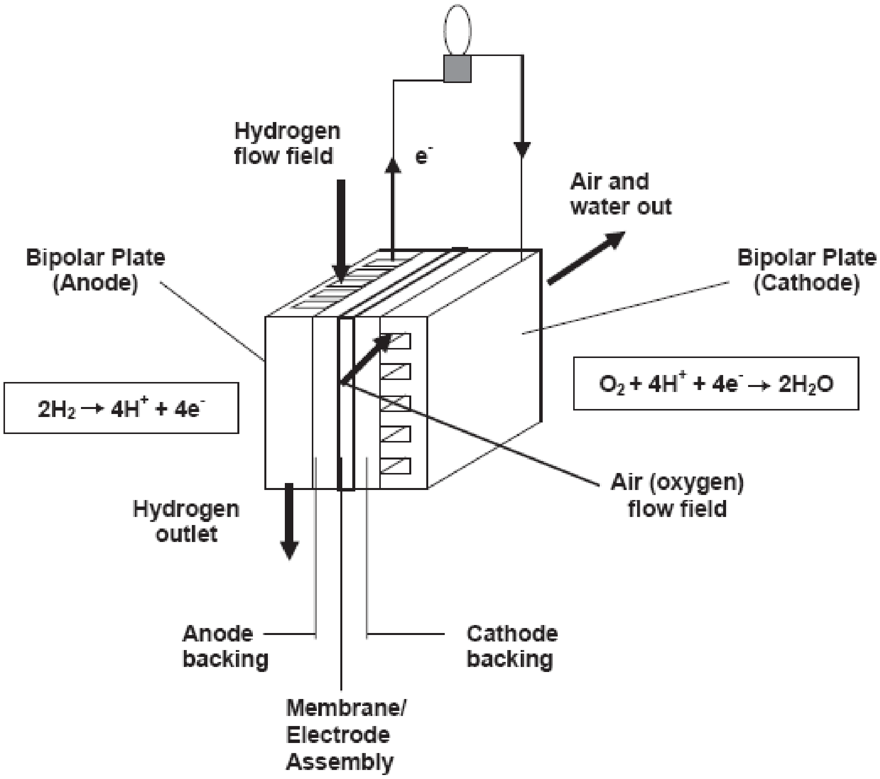

Fig. 2.22 Schematic diagram of a polymer electrolyte membrane fuel cell [90].

Typical work conditions of bipolar plates in PEMFC

The bipolar plates of a PEMFC are operated in an acidic environment of pH 3–5 in the presence of SO_4^{2-}, NO_3^-, Cl^-, F^- ions arising from the Nafion membrane at the temperature >100 ˚C [91] , with direct contact with oxidizing gases such as pure O_2 or air on the cathode side, and reducing gases such as H_2 on the anode side. The PEMFC separator plates are also typically exposed to potentials of -0.5 to 0.1 V due to the contact with the electrodes, and potentials at the cathode can be as high as 0.6-0.8 V [107].

Materials for BPs used in PEM fuel cells

Non-porous graphite

Traditionally, graphite sheet is one of the most commonly used BP materials because it has excellent chemical stability to survive in the fuel cell environment. It also has very low resistivity, resulting in highest electrochemical power output [108, 109]. However, due to the brittleness of graphite, the bipolar plates need to have a thickness in the order of several millimeters, which makes a fuel cell stack heavy and voluminous. Moreover, graphite are costly and difficult to machine to form the flow channels [90, 109].

Metals

In the review of Hermann *et al.* [90] and some previous reports, the performance of titanium, aluminum, nickel, copper alloys and stainless steels [87, 96, 110] in an operation conditions similar to PEM fuel cells were studied as potential candidates for BP materials. The results indicated that they offered some advantages over graphite and composite materials. Those alloys can be manufactured as thin sheets at a lower cost. In addition, the electrical conductivity of some metallic materials such as iron alloy and titanium was superior to graphite. Thus, taking into account the bulk cost, density and typical plate thickness, the material costs for metallic bipolar plate were significantly less than a graphite plate [91, 95]. In particular, stainless steels (SSs) are the material in this category to have received considerable attention due to their relatively high strength, high chemical stability, low gas permeability, wide range of alloy choice, and applicability to mass production and low cost. The recent research results concluded that both austenitic (349TM) and ferritic (AISI446) SS with high Cr content can be suitable for BP, although AISI446 requires some improvement in contact resistance [96, 110]. In spite of these advantages, the surface oxide layer of metals such as Al, Ti, Ni and stainless steels similarly forms a surface passive layer that has good corrosion resistance but poor surface contact resistance. Moreover, the metal ions produced by corrosion, will migrate to the membrane and displace H^+ ions of the membrane, thereby, reducing the conductivity of the membrane and the overall efficiency of the fuel cell [111].

Coated metals

Various protective coatings have been employed to overcome oxide formation and ion dissolution for metal plate materials such as Al, Ti, SS alloys. Those coatings include conducting polymers, noble metals (Gold) and some hard coatings produced by vapor deposition (nitride and carbon based coatings). For conducting polymers, although corrosion resistance could be increased with these polymer-coated plates, it has been reported that electrical resistance is 10 times higher than the value for graphite at the same compaction force [95, 112]. Thin gold coatings with various thickness (10 nm-10 μm) on various metal substrates have been studied [87, 95]. Those studies showed that a very thin layer of gold was sufficient to prevent corrosion and to improve electrical conductivity. However, despite the fact that gold coatings can offer excellent results when performing in the fuel cell environment, its high price is a major disadvantage for economies of mass production.

PVD or CVD hard coatings

Thus, to meet the PEMFC cost targets, as well as meeting the fundamental characteristics such as high electrical conductivity, mechanical and chemical stability, PVD or CVD carbon based and nitride based coated bipolar plates have gained many attentions recently.

Show *et al.* [99] investigated the effect of growth temperature on the electrical conductivity of a-C coatings on Ti bipolar plate by RFPECVD method. The a-C film was electrically conductive (10−3 Ωcm) when it was deposited at a high growth temperature (above 550 °C). The electrically conductive a-C film effectively reduced the contact resistance between its surface and the membrane electrode assembly (MEA). Therefore, the use of this a-C coating technique for metal bipolar plates improved the efficiency of fuel cells for the generation of electric power.

Lee *et al.*[113] investigated the corrosion properties of multi-layered TiN, TiCN and TiC PVD coatings on aluminum substrates. The corrosion rates of all materials were tested in a simulated fuel cell environment. The linear polarization curve of electrochemical method measured by potentiostat instrument was employed to determine the corrosion current. Results of the corrosion tests indicated that all of the coating materials had good corrosion resistance and were stable in the simulated fuel cell environment. The conductivities of the coated layers were even better than that of substrate and the resistances changed very little after the corrosion test. The single cell test results indicated that metallic bipolar plates with PVD coating could be used in PEM fuel cells.

In the work of Fukutsuka *et al.* [98], carbon-coating (DLC) was prepared by using plasma-assisted chemical vapor deposition on SUS304 stainless steel substrates. Anodic polarization behavior under PEMFC operating conditions (H_2SO_4 solution bubbled with H_2 (anode)/O_2 (cathode) containing 2 ppm HF at 80 °C) was examined. It was concluded that the carbon-coating on SUS304 might be a candidate technique for the improvement of metal bipolar plates.

In the works of Wang [101, 102], TiN was coated on an austenitic stainless (316L) and martensitic stainless steel (SS410) using a PVD technology and the electrochemical characteristics were determined in simulated PEM fuel cell environments. The results indicated that TiN coated SS410 and 316L were a potential material for bipolar plates of PEM fuel cells. However, improved TiN coatings, which do not contain defects such as pinholes, were required and further research on interfacial contact resistance and actual fuel cell performance were needed before TiN coated steel alloys can be considered as a commercial bipolar plate material.

Li and his coworkers [100] investigated the performance of the TiN-coated 316 SS in simulated PEMFC environments, i.e., 0.01 M HCl + 0.01 M Na_2SO_4 solutions bubbled with O_2 or H_2, since TiN coated 316SS had high corrosion resistance and passivity. The results indicated that TiN coating may offer 316SS higher corrosion resistance and electric conductivity. The operation potentials of fuel cell had no significant effect on TiN coating properties. Although the results in this study have indicated that TiN coatings are full of promise to be used on 316SS bipolar plates, it is necessary to investigate the electrochemical stability of TiN coatings in much longer times.

From above reviews, the PVD or CVD hard coatings are promising for coated-metallic bipolar plates in PEM fuel cell. However, only a few of research works are conducted on TiN and DLC coatings. Further studies on the potential application of some other ceramic hard coatings are needed, for examples, TiAlN, which is reported to have improved corrosion protective properties in salt solutions compared to TiN coating [114]. The performance of TiAlN in solid oxide fuel cell (SOFC) has been studied and reported and the study concluded that (Ti,Al)N coatings were good candidates for the SOFC interconnect applications at 700°C [115]. However, few reports have been presented on the possibility of the coating used for PEM fuel cells.

2.3.3 Applications in biomedical devices

A biomaterial is here defined as any synthetic material that is used to replace or restore function of a body tissue and materials used for devices such as surgical or dental instruments which are continuously or intermittently in contact with body fluids [116, 117]. The definition used in this dissertation excluded the materials used for external prostheses such as artificial limbs or devices such as hearing aids. These materials are not exposed to body fluids. There are several most prominent application areas for biomaterials including orthopedics, cardiovascular, ophthalmics, dental applications, wound healing and drug-delivery systems [116]. In this dissertation, the research was restricted to the area of biomaterials for load-bearing medical devices such as orthopedic purpose-hip stems, balls and knee, and so on, where hard tissue (bony structures) must be repaired or replaced.

Chemical and mechanical requirements for medical device materials

The physiological environment applied on biomaterials normally has a pH level of 7.4 and a temperature of 37 °C (98.6 °F). Physiological solutions are oxygenated and contain organic components in addition to various salts. These solutions are electrical conductors [116]. The nominal inorganic chemical composition in a human body, including physiological elements in the body fluid is shown in Table 2.5 [118].

Table 2.5 Inorganic composition in a human body, including physiological elements in the body fluid [118]

Basic Elements [a]	Conc. % (Aver.)	**Trace elements**[a]	Conc. (Aver.)
Oxygen	61.4	Magnesium	271 ppm
Carbon	22.9	Iron	61.4 ppm
Hydrogen	10.0	Zinc	33 ppm
Nitrogen	2.6	Iodine	1.9 ppm
Total	96.9	Copper	1.0 ppm
Physiological[a] **elements**	Conc. % (Aver.)	Aluminium	0.9 ppm
Calcium	1.43	Vanadium	260 ppb
Phosphorus	1.11	Selenium	<190 ppb
Potassium	0.20	Manganese	170 ppb
Sulfur	0.20	Nickel	140 ppb
Sodium	0.14	Molybdenum	<136 ppb
Chlorine	0.14	Titanium	130 ppb
Total	3.22	Chromium	<94 ppb
[a] **Total of concentrations exceeds 100% due to variety of primary sources and experimental error in individual values.**		Cobalt	<21 ppb
		Total	<0.37%

The material release (ions or particles) from implants will cause the change of the intrinsic physicochemical composition of the body and therefore might lead to acute or chronic adverse biological reaction. Thus, the biomaterial should have an ion release rate as small as possible in biomedical environments. Although it may not be easy to exactly measure the ion content released into the body fluid environment, electrochemical corrosion tests can conveniently be conducted to study corrosion rate of a biomaterial. Since the corrosion rate is relevant to the ion releasing rate, the lower corrosion rate of a biomaterials the less invasion to human body.

Moreover, there can be very great mechanical loading demands on biomaterials used for structural purposes. For instance [116], for structural implants used to repair the hip, it is estimated that the average nonactive person may place 1 to 2.5×10^6 cycles of stress on his or her hip in a year. For a person 20 to 30 years of age, with a life expectancy of 70 to 80 years, that is the equivalent of approximately 10^8 cycles of loading in a lifetime. The actual loads and cycles are a function of the weight and activity level of the person, but the need for longtime cyclic capability in fatigue is obvious. Other applications in the body also impart many millions of fatigue cycles to the device or component implanted. Many structural applications of materials in the body require the replacement materials fit into a space perhaps only one-fourth the area of the part being permanently or temporarily replaced or assisted. Consequently, the implant may have to withstand loads up to 16 or more times than which the human bone must withstand [116].

Additionally, the majority of joint replacement designs utilize metal- or ceramic-on-plastic bearing couple. For example, the most commonly used material combination for an artificial hip joint consists of a femeoral component made of a metal stem with a polished metallic or ceramic ball, which articulates against a metal shell with a plastic inner socket. Generally, high density polyethylene (HDPE) and ultra high molecular weight polyethylene (UHMWPE) have been used as the plastic material in those bearing couples due to its toughness, durability, and biological inertness. The wear debris generated during normal wear of polyethylene may cause substantial negative biological effects. Wear debris is transported to the soft tissue surrounding the implant and causes chronic inflammation. Thus, besides corrosion and wear protection properties, the compatibility of coatings with polyethylene material is another important characteristic.

As described above, the application conditions of biomaterials required some unique properties. First, a biomaterial must be biocompatible - it should not elicit an adverse response from the body and vice versa. Additionally, it should be nontoxic and noncarcinogenic. Next, the biomaterial should possess adequate physical and mechanical properties to serve as augmentation or replacement of body tissues. For practical use, a biomaterial should be amenable to being formed or machined into different shapes, have relatively low cost and be readily available.

The ideal material or material combination should exhibit the following properties:

- A biocompatible chemical composition to avoid adverse tissue reactions.
- Excellent resistance to degradation (e.g. corrosion resistance for metals or resistance to biological degradation in polymers).
- Acceptable strength to sustain cyclic loading endured by the joint.
- A low modulus to minimize bone resorption.
- High wear resistance to minimize wear debris generation.

Types of biomaterials used for load-bearing medical devices

In general, these materials can be divided into the following categories: metals, polymers, ceramics and composites. As a class of materials, metals are the most widely used for load-bearing implants [1]. For instance, some of the most common orthopedic surgeries involve the implantation of metallic implants. Although many metals and alloys are used for medical device applications, the most widely used metallic biomaterials for implants devices are 316L stainless steels, cobalt alloys, commercially pure titanium and Ti-6Al-4V alloys [117, 119-122]. These materials suffer from some drawbacks, in case of sustained and long-term use, such as cytotoxicity, release of metal ions, corrosion, and wear. For example, though stainless steel has been successfully used in many biomedical applications, it can become corroded and releases Cr, Ni, Mn, and Mo ions when the metal is placed in coronary vessels. Because the metal ions and other particles released from implants are suspected to trigger allergic reactions, as in the case of Ni, or to cause tumors, there is a growing interest searching for less corrosive and better inert biomaterials for their wide use in clinical applications.

Balamurugan *et al.* [123] summarized that the corrosion mechanisms of metallic implant materials were induced by electrochemical processes and mechanical processes. Electrochemical processes may include generalized corrosion, uniformly affecting the entire surface of the implant, and localized corrosion, affecting either regions of the device that are shielded from the tissue fluids (crevice corrosion) or seemingly random sites on the surface (pitting corrosion). Electrochemical and mechanical processes (e.g. stress corrosion cracking (SCC), corrosion fatigue and fretting corrosion) may interact, causing premature structural failure and accelerate the release of metal particles and ions.

PVD and CVD hard coatings for biomaterial

Previously, medical devices were selected based on its material and bulk properties. However, it is now recognized that the surface properties of the device mainly govern its biomedical applications. In most cases, a surface modification is considered to be a prerequisite for better biocompatibility.

PVD and CVD hard ceramic coatings are expected to be the new biomaterials for load-bearing devices including orthopedic implants, pacemakers, surgical instruments, orthodontic appliances and dental instruments. So far, two kind of PVD and CVD hard ceramic coatings, i.e., TiN and amorphous carbon (DLC) coatings are under development for biomedical applications.

TiN-coated biomaterials

TiN is a hard ceramic coating applied as biomaterials. TiN is biocompatible with most of biomedical environments i.e. exhibits no cytotoxicity, dermal irritation, or acute systemic toxicity response [124, 125]. It was reported that TiN coatings had been used for orthopaedic prostheses, cardiac valves, and dental prostheses [126, 127], concluding that TiN is well tolerated by the human body in interactions with the blood system. However, it has also been reported that the corrosion resistance of TiN-coated prostheses is strongly dependent on the porosity of the coating, thereby limiting the coating's protective qualities, and leaching of the metal ions from metal prostheses can accumulate in the body to toxic levels [128]. In other studies, TiN coatings have been compared with Co-Cr [129] and stainless steel [130] and it is concluded that TiN coatings can achieve high wear resistance under some medical application environments.

DLC-coated biomaterials

Several reviews have reported [131-135] the biocompatibility and performances of DLC-coated biomaterials in actual applications. The biocompatibility of a material is determined by some in vitro and in vivo tests, involving the interaction of the material with biological cells. Hydrogenated amorphous carbon (a-C:H) films are most widely investigated among DLC films in the previous works on the biocompatibility. The biocompatibility test results [131-134] indicated that no toxicological or cytotoxic effects on the cells in culture were observed and cells grew on a-C:H film without any inflammation, revealing good surface biocompatibility of the coatings. Some metal doped DLC coatings, Ti-a-C:H, Si(O)-a-C:H and CaO-a-C:H were studied in vitro studies. The results showed that a-C:H films tended to promote the growth and adhesion of cells without any toxilogical effect [132, 136]. However, it has been observed that the addition of toxic elements Cu, Ag or V to DLC films inhibited the growth and spreading of cells on the DLC surfaces [132, 137].

For DLC-coated load-bearing biomedical applications, some contradicting results were reported [132] by different research groups in vitro experiments since those examinations used different experimental setups (pin-on-disk, hip or knee simulator, different surface roughness) and different liquids were used as lubricants. The low wear properties known from the tribological behavior of DLC in air could not be adapted to load bearing joints operated in a biological fluid.

There are many papers [138, 139] reporting on experiments using a hip simulator to determine friction and wear of DLC-coated hip joint balls sliding against UHMWPE (ultra high molecular weight polyethylene). From the literature presented above, it can be indicated that the superior properties, which DLC shows in air or vacuum, can probably not be easily transferred to hip joints and other load bearing implants. The build up of a transfer layer does not seem to take place, and the UHMWPE counterpart still shows wear. However, the corrosion resistance of the Co–Cr–Mo is enhanced to a greater extent by the DLC coating. Sheeja *et al.* [138, 139] investigated the wear performances of DLC on various metal substrates, which were commonly used in total joint replacements (Ti, Ti-6Al-4V, stainless steel 316L and Co–Cr–Mo) against UHMWPE in a simulated body fluid. The study showed that the adhesion of the coating to the substrate was the main parameter that determined the long-term tribological application of the coating and stainless steel was a better substrate for depositing DLC films compared to titanium and titanium alloy Ti6Al4V. Very few in vivo experiments on DLC coated load bearing implants could be found in the literature. In 2001, a company produced and sold artificial joints with a DLC-coated femur part. Within a short time, some of these implants became failure due to increased wear and coating delamination. Consequently, the implantation of this coated knee joint was forbidden [132].

Other coatings

Only very few works have reported on other PVD or CVD hard ceramic coatings used for biomaterials. TiAlN, TiN/TiAlN, TaN and ZrN [140-142] prepared by cathodic arc method, reactive magnetron sputtering etc. were studied on their corrosion resistance and biocompatible characteristics. It was concluded that those coatings presented a good biocompatibility (in terms of cell density, cell morphology and cell viability) and improved the biocompatibility of Ti5Al2.5Fe and especially, CoCr substrate. Further research on the corrosion and wear performance for biomaterial applications is needed.

2.4 Summaries of Chapter 2

This chapter gives some introductions on the fundamentals of vapor deposition technologies and some overviews on previous studies on the formation and properties of PVD and CVD TiN, TiAlN, CrN, CrAlN and DLC coatings.

The application trends of these coatings in manufacturing, bipolar plates of PEM fuel cells and biomaterials applications are also described in this chapter. It was revealed that the conventional TiN, TiAlN, CrN and DLC coatings could not satisfy the more aggressive working conditions in the dry machining processes. The CrAlN coating is a promising candidate material used for dry machining due to its superior thermal stability. So far, no actual application of CrAlN coating has been reported. In the previous studies, some mechanisms of the coating failure have been investigated to provide useful information for designing of new applicable coatings. In addition, there were some reports on the thermal stability of coatings such as oxidation behaviors and structure changes with various temperatures. However, comprehensive studies on effects of those oxides and structure transformation resulting from high temperature of dry machining processes on the wear performance of coatings against various types of counterface material are still scarce and needed. Thus, this dissertation will conduct systematical and comparative studies on all those Ti-based (TiN and TiAlN), Cr-based (CrN and CrAlN) and C-based (DLC) coatings with respect to coating morphology, phase structure, thermal stability, hardness, elastic modules, wear and tribological properties.

The previous investigations of PVD and CVD coatings for applications in bipolar plates of PEM fuel cells and biomedical materials were mainly focused on TiN and DLC coatings. It was revealed that these two coating systems could supply corrosion and wear protection to metal substrates to some extent. However, reports on other coating materials for PEM fuel cell and biomedical applications are limited. In this dissertation, the potentials of more coating materials, i.e., CrN, TiAlN and CrAlN, besides TiN and DLC, will be also investigated in the simulated conditions of PEM fuel cells and biomedical applications, respectively.

CHAPTER 3 EXPERIMENTAL DETAILS

In this chapter, the experimental procedures are described. There are three main parts of experiments in this project.

3.1 Performance of tool coatings for manufacturing applications

3.1.1 Effects of annealing temperatures on the tribological properties and material transfer phenomena under pin-on-disc testing conditions

3.1.1.1 Preparation and characterization of substrate materials and coatings

Substrate preparation and coating deposition. In this part of experiments, AISI M2 steel was chosen as a substrate material. M2 steel is a preferred high speed tool steel type for the manufacture of general-purpose lathe tools like milling cutters, taps, dies, reamers, and form tools. Steel discs of 30 mm diameter and 3 mm in thickness were cut from commercial AISI M2 rods with HRC=62-63. All the discs were polished then cleaned to obtain a uniform surface roughness of 0.1±0.02 μm. The composition of AISI M2 steel is presented in Table 3.1.

Table 3.1 Nominal composition of AISI M2

	Composition, wt%						
	C	Cr	W	Mo	V	Si	Fe
AISI M2	1.00	4.15	6.40	5.00	2.00	0.27	The balance

TiN, CrN, TiAlN, CrAlN and hydrogenated DLC coatings were produced by coating suppliers Tecvac Ltd., UK on the well prepared AISI M2 steel discs. The TiN and CrN coatings were deposited using a single electron beam PAPVD system (Tecvac IP70L). The TiAlN and CrAlN coatings were deposited using a twin electron beam

PAPVD system (Tecvac IP35L). The DLC coating (Diamolith®), which is a-C:H in nature, was deposited by using plasma enhanced chemical vapor deposition (PECVD).

Coating thickness and surface roughness. The cross-sectional morphology observation and thickness measurement of the coatings were conducted using a JEOL Scanning Electron Microscope (SEM) with Kevex 5100C energy dispersive X-ray analysis (EDX) (Fig.3.1). Before the examination of the cross-sections, the cross-sectional samples were mounted with resin and polished first with a series of SiC abrasive papers of gradually decreasing grit sizes, then with an alumina suspension for the final polishing. Because of the low electrical conductivity of the resin, the samples were sputter-coated with gold prior to SEM examination.

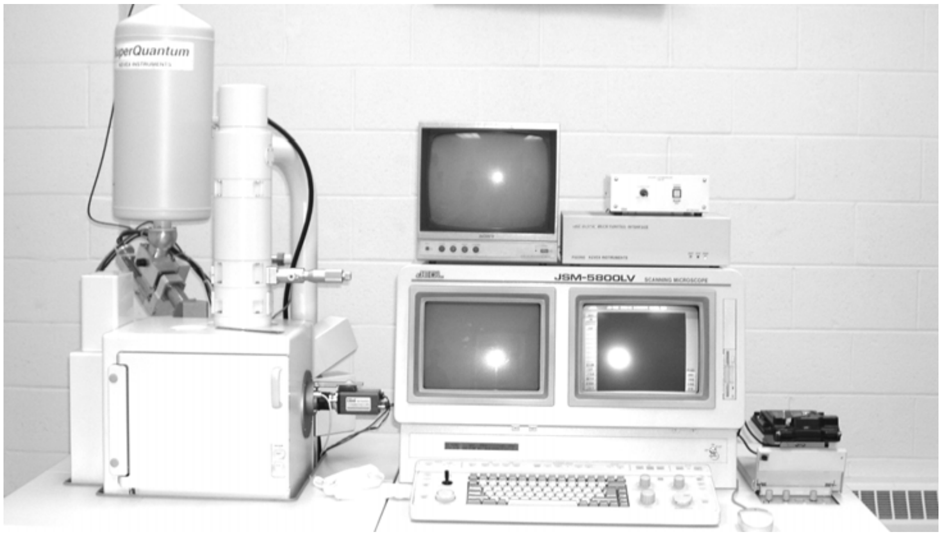

Fig. 3.1 A JEOL Scanning Electron Microscope (SEM) with Kevex 5100C energy dispersive X-ray analysis (EDX).

The surface roughness (R_a) of as-deposit coatings was measured using the Mitutoyo SJ-201P surface profilometer (Fig. 3.2)

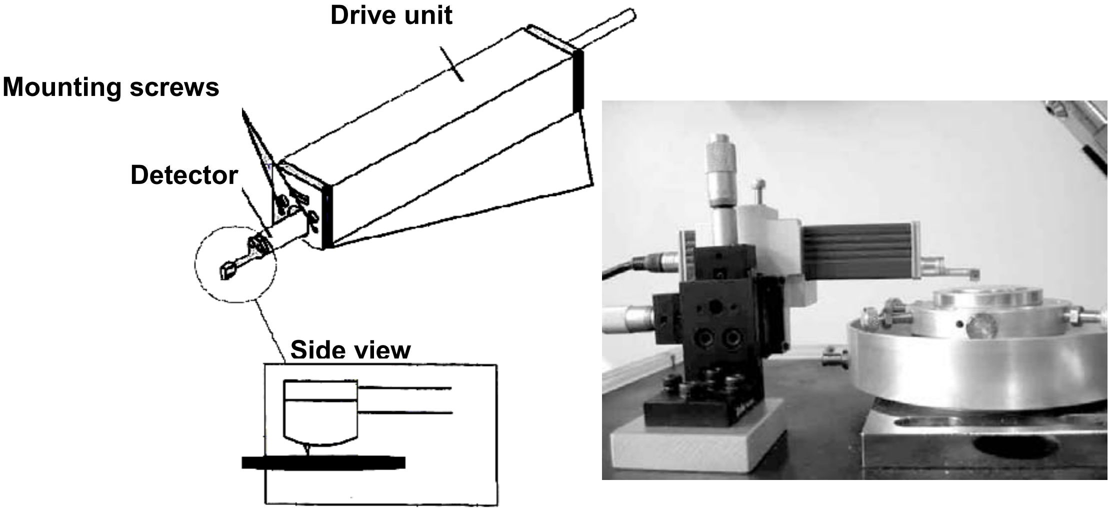

(a) (b)

Fig. 3.2 (a) The schematic of detector unit and (b) a photograph of Mitutoyo SJ-201P surface profilometer.

3.1.1.2 Effects of annealing temperatures on the coating structures and hardness

As described in chapter 2, the effect of high temperature arising from dry machining process is one of the critical causes of tool fail. In this part of experiment, the coating structural and mechanical properties were investigated on annealed coated and uncoated M2 steel samples to simulate the effect of high temperature during dry machining.

Annealing processes. The annealing processes were conducted in a Lindberg BF51866C Moldatherm Box Furnace (Fig. 3.3). The annealing treatments were performed on the TiN, TiAlN, CrN and CrAlN coating samples at 500-1000 °C and on the DLC coatings at 200-600 °C at a 100 °C interval in air for 1 hour with a heating rate of 10 °C/s followed by natural cool down to room temperature in the furnace before taking the samples out for different analysis. These samples are designated as those in Table 3.2.

Table 3.2 Samples treated at various annealing temperatures

Anneal. Temp.(^{o}C) Coating	500	600	700	800	900
TiN	T500	T600	T700	T800	T900
TiAlN	TA500	TA600	TA700	TA800	TA900
CrN	C500	C600	C700	C800	C900
CrAlN	CA500	CA600	CA700	CA800	CA900
Anneal. Temp.(^{o}C) Coating	200	300	400	500	600
DLC	D200	D300	D400	D500	D600

Fig. 3.3 Lindberg BF51866C Moldatherm Box Furnace.

Hardness and elastic modulus. Hysitron Ub1 nanomechanical test system (Fig. 3.4 (a)) was employed to measure the hardness (H) and reduced elastic modulus (E_r) of the coated discs at a normal load of 4 mN using the Oliver and Pharr analysis method

[143]. The indenter used was a three-sided pyramid Berkovich diamond with a tip radius of curvature of ~100 nm (Fig. 3.4 (b)).

Phase structure. The crystalline structures of the annealing treated and original coatings were analyzed by x-ray diffraction (XRD), which was performed on a Rigaku D/max 1200 X-ray diffractometer in a θ-2 θ scan mode using CuKα radiation (30 KV, 30 mA). Samples were scanned from 10 to 100 degree in 2θ, and the scanning step was 0.02 degree in 2θ.

(a) **(b)**

Fig. 3.4 (a) Hysitron Ub1 nanomechanical test system and (b) a three-sided pyramid Berkovich diamond.

3.1.1.3 Effects of annealing temperatures on the tribological properties

Pin-on-disc tests. Tribological behaviors of original coatings and the ones after annealing were characterized by a pin-on-disc tribometer under dry sliding test conditions at ambient environment (25±5 °C and 47±2% relative humidity). Three types of counterface materials were used to investigate the tribological properties of coatings against various counterface materials. The counterface balls were ceramic alumina, aluminum 6061 and steel AISI 52100 balls (Ø= 5.5 mm, Salem Specialty Ball company). Sliding speed was 0.1 m/s; the sliding distance was 125 m (i.e., 10000 revolutions) with the normal load of 1 N.

Surface morphology of wear tracks. SJ-201P surface profilometer was used to scan the cross-section of wear tracks. The wear loss or material transfer were observed and the wear rate (*k*) was calculated and determined by the expression: $k = \frac{A \times L}{N \times l}$. A and L are the cross-sectional area and circumference of wear track, respectively. *N* and *l* are the normal load and sliding distance, respectively. The details of material transfer phenomena between coatings and counterface balls were observed by optical microscope and SEM.

3.1.2 An industrial trial of TiN and CrAlN coatings in an actual stamping plant

Coating deposition. TiN and CrAlN coatings were deposited on the industrial AISI M2 tool steel punch tools (Fig. 3.5) using the same process parameters as on AISI M2 test discs. The punch size was 25 mm in diameter.

Stamping trials. CrAlN- and TiN-coated punches were installed into a stamping die in an automotive manufacturer's stamping plant (Fig. 3.6). Instead of applying the punches at a 90-degree angle, angled tools were used (Fig. 3.7), which came in contact with a steel sheet gradually during the piercing. In the stamping process, coils of hot-dip Zn-coated high strength low alloy steel (HSLA) sheet of thickness of 1.8 mm were fed through the punch station at a feed pitch of 375 mm. The punches operated at 8 strokes per minute. Prior to piercing, a thin film of Quaker 61AUS mill oil was put on the coils as a lubricant. Whenever severe burrs occurred on the perforated sheet, punches were judged as failed and the number of holes blanked prior to failure was used to express their lifetimes.


(a) **(b)** **(c)**

Fig. 3.5 (a) uncoated-, (b) TiN- and (c) CrAlN-coated industrial AISI M2 tool steel punches.

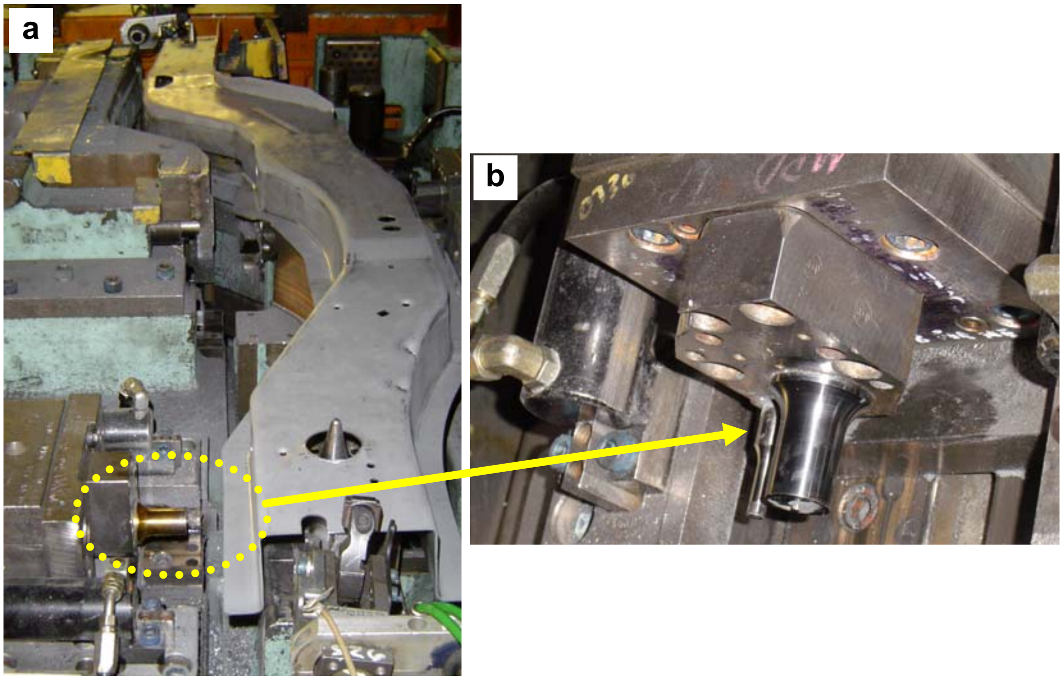

Fig. 3.6 (a) An automotive manufacturer's stamping die and (b) the coated punch installed on the stamping die.

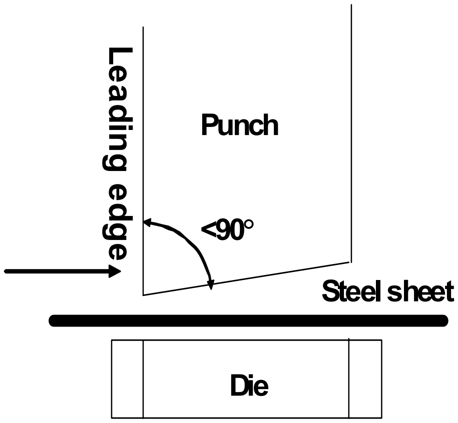

Fig. 3.7 Schematic of angled punch installation.

Failure observation of punches. The failure mechanisms of punches were investigated using optical microscopy and SEM with EDX.

3.1.3 Development and characterization of Cr(CrN)/C(DLC) multilayered coating system used for dry machining of aluminum alloys

In this part of experiments, a Cr(CrN)/C(DLC) nanoscaled multilayered coating as a model coating system was developed with intention of making the coating to have both good anti-wear and anti-sticking properties against aluminum under a pin-on-disc testing condition.

3.1.3.1 Deposition of Cr(CrN)/C(DLC) multilayered coating system.

Cr(CrN)/C(DLC) multilayered coatings were deposited on both Si wafer and M2 steel substrates by an unbalanced magnetron sputtering technique (Teer UDP 450 PVD coater). Two C targets and one Cr target were used as sputtering sources (Fig. 3.8). The target current was 3 A for each C target and 2.5 A for the Cr target. Nitrogen gas with working gas argon was introduced into the deposition chamber for nitrogen doping. The chamber working pressure was 1.33 Pa. Flow rates of argon and nitrogen gases were 30 sccm and 8 sccm, respectively. The substrate bias voltage was −100 V, and the deposition temperature was about 200 °C. Four substrate rotation speeds in revolutions per minute (rpm), i.e., 1 rpm, 2 rpm, 3 rpm, and 4 rpm, were chosen to produce four multilayered coatings with different bilayer thickness (designated as R1, R2, R3 and R4, respectively). The deposition rate was set at approximately 2 μm/h. The total thickness of each coating was 3 μm.

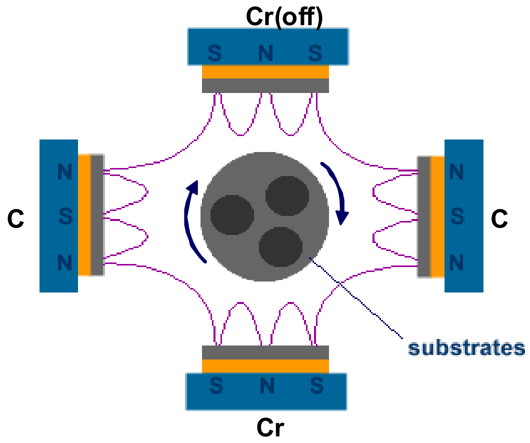

Fig. 3.8 Schematic of an unbalanced magnetron sputtering deposition with two C targets and one Cr target were used as sputtering sources.

3.1.3.2 Coating bilayer thickness determination and mechanical properties

Bilayer thickness and structure of multilayered coatings were characterized by three methods, i.e., low angle XRD (Siemens D3000), X-ray photoelectron spectroscopy (XPS) depth profile based on standard Ta_2O_5 etch (etching rate 11.1 nm/min), and cross-section transmission electron microscopy (TEM Joel 2010) analysis.

A low angle ($2\theta \leq 15°$) XRD pattern, as an example in Fig. 3.9, results from the reflection of X-rays off the interfaces between layers and it is not affected by the crystalline quality within each layer. Thus, the low-angle XRD pattern was used to calculate the bilayer thickness [144, 145] according to the Bragg's Law Equation [146]:

$\sin^2\theta = (\frac{n\lambda}{2\Lambda})^2 + 2\delta$, where 2θ is the peak position of the *n*th order to reflection, λ is the X-ray wavelength (0.156 nm), δ is the deviation of the average refractive index of the film, and Λ is the bilayer period. By plotting $Sin^2\theta$ as function of n^2, the almost constant slope $\left(\frac{\lambda}{2\Lambda}\right)^2$ of the linear curve was gained and therefore the average Λ was determined.

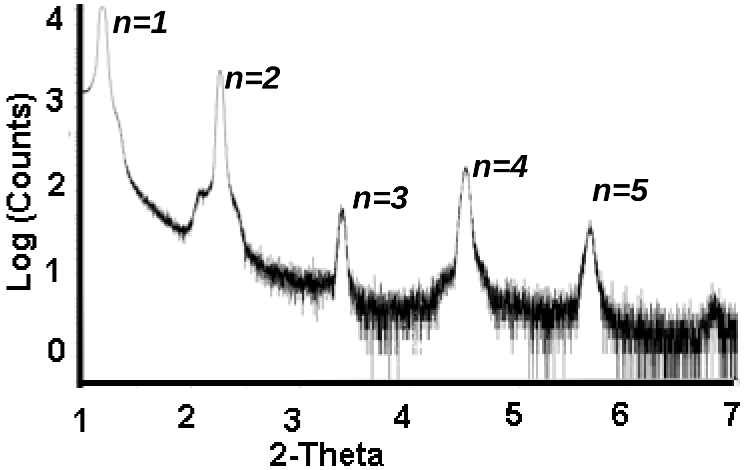

Fig. 3.9 An example of low angle (2θ ≤ 15°) XRD pattern of a multilayered coating.

Nanomechanical properties were measured using a Hysitron Ub1 nanomechanical test system (Berkovich diamond tip) with maximum load of 1 mN.

3.1.3.3 Tribological properties in nano-scale

Scanning nanowear tests were conducted also by using nanomechanical test system (Berkovich diamond tip) with normal load 150 μN and scanning wear size 1.5×1.5 μm^2. The tip velocity and the cycle time were 9 μm/s and 80 s, respectively. The wear scar depth and images were obtained by the measurement of average height of worn surface by the Ub1 software. The wear rate was calculated by equation:

$k = \frac{h}{n}$, where h is the wear scar depth; n is the number of scanning passes.

3.1.3.4 Tribological properties of Cr(CrN)/C(DLC) multilayered coatings in microscaled pin-on-disc sliding wear tests

For better understanding of coating performance difference in dry and wet testing conditions, a pin-on-disc tribometer with a tribological medium container was used to investigate the wear behaviors of the four multilayered coatings under dry and boundary lubricated (S500 coolant) sliding conditions. The counterface material was Al 319 alloy pin (diameter of spherical pin tip: 5.5 mm) and the nominal composition of the alloy (in wt. %) was 5.5-6.5 Si, 1 % Fe, 3-4 % Cu, 0.1 % Mg, 0.5 % Mn, 0.35 % Ni, 1 % Zn, and the balance Al. Sliding speed was 0.1 m/s, normal load 1 N, sliding distance 125 m (10000 revolutions), and relative humidity 47 %. A Stylus surface profilometry were used to measure wear rate. The investigations of wear tracks and wear mechanism were performed using SEM.

3.2 Performance of coatings in simulated PEM fuel cell conditions

3.2.1 Coating deposition

TiN, TiAlN, CrN, CrAlN and DLC coatings supplied by Tecvac Ltd. were deposited on mirror polished (Ra<0.1μm) AISI 316L stainless steel discs of 30 mm diameter and 3 mm in thickness. Uncoated AISI 316L stainless steel discs were also polished and cleaned for use as a reference material. The nominal compositions of AISI 316L stainless steel are presented in Table 3.3.

Table 3.3 Nominal composition of AISI 316L

	Composition, wt %								
	Cr	Ni	Mo	Mn	Si	P	S	C	Fe
AISI 316L	17	12	2.5	2	1	0.045	0.03	0.03	The balance

Except for substrate materials, the coatings, in nature, are the same as those on M2 steel testing discs described in the early part of this chapter. Thus, coating structural and mechanical properties are the same as those of original (non-annealed) coatings on M2 steel.

3.2.2 Contact resistance (CR) screening test

The CR measurements were conducted on all coated and uncoated stainless steel samples. The CR measurement method used in this study was similar to that reported by Cho *et al.* [103, 147]. In this setup (Fig. 3.10), two pieces of conductive carbon paper (Electrochem Inc.) were sandwiched between the steel sample and two copper plates. A GOM-802 DC Mill-ohm Omega meter was used in a 4-wire measurement mode to measure the total resistance drop through this setup with increase in compaction force. The compaction force was applied using a manual test stand (Rima Spring tester). Before each measurement, the copper plates were polished to remove the natural oxide film using # 1200 ANSI grit SiC abrasive paper. The carbon paper was only used once for each measurement test. The maximum compaction pressure applied in the CR test was 300 N/cm^2 (3.0 MPa). With this approach, the measured resistance (R_{totl}) consisted of (a) the bulk resistance of two flat carbon papers, $2R_{cp}$; (b) the bulk resistance of specimen (stainless steel substrate with/without coatings), R_S + (R_{film}); (c) two interfacial contact resistances between flat carbon paper and test specimen, $2R_{cp}/_{Rs}$; (d) two interfacial contact resistances between copper plate and flat carbon plate, $2R_{Cu}/_{cp}$. Thus, the measured resistance is expressed as $R_{totl}= 2R_{cp}+ Rs+ (R_{film}) +2R_{cp}/_{Rs}+2R_{Cu}/_{cp}$.

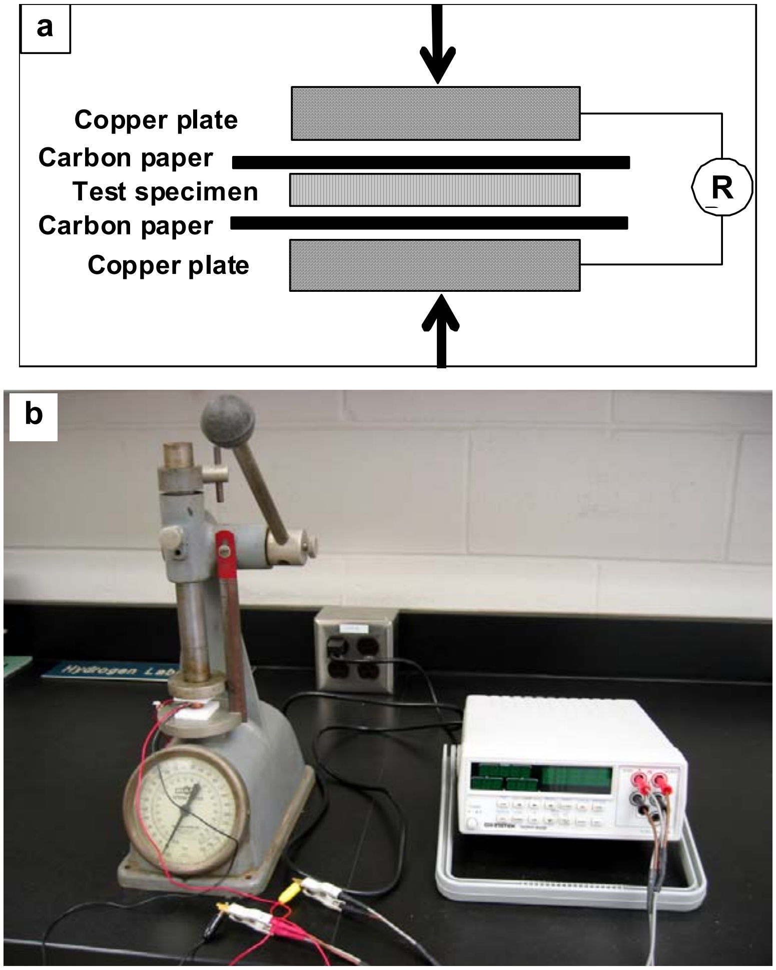

Fig. 3.10 (a) Schematic diagram and (b) a picture of the interfacial contact resistance test setup.

3.2.3 Corrosion properties in simulated PEM Fuel Cell environments

Potentiodynamic and potentiostatic tests were conducted in a three-electrode system test unit (Fig. 3.11) with a platinum counter electrode of 1 cm^2, an Ag/AgCl, 3 M KCl electrode as the reference electrode and a testing specimen as work electrode using a SP-150 Potentiostat (Biologic Science Instruments) controlled by a computer (Fig. 3.11). Additionally, a rod immersion heater with glass sheath was immerged into the solution. The heater was controlled by a temperature controller. Gas was fed into the solution by a plastic gas tube connected to gas supply cylinders. To simulate the aggressive PEMFC environment, all the electrochemical characterizations were performed in a 1 M sulphuric acid solution at 70±5 ^{o}C with H_2 or O_2 purging to simulate the anodic and cathodic environments, respectively.

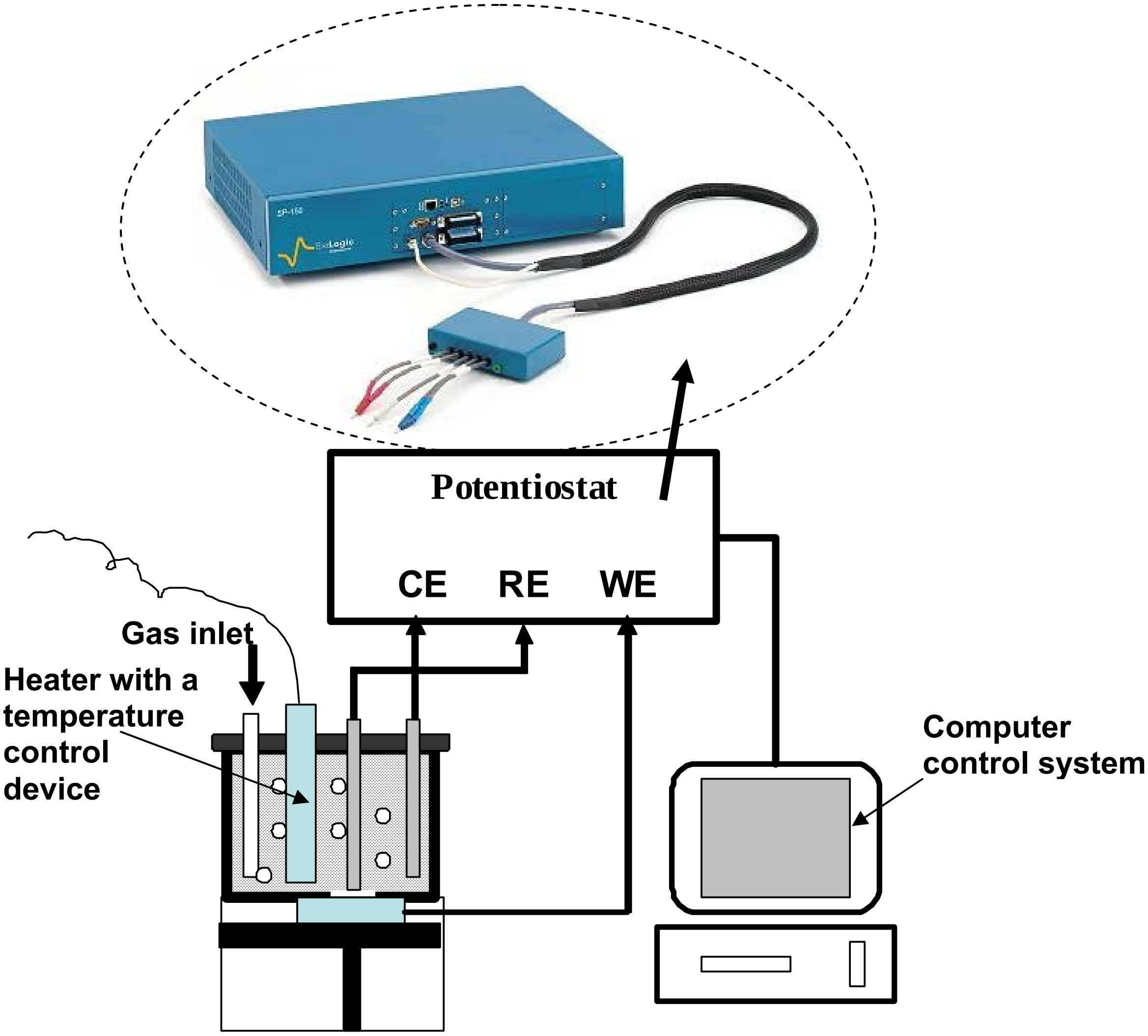

Fig. 3.11 Schematic diagram of the polarization testing equipment. CE: counter electrode, RE: reference electrode, WE: working electrode.

Potentiodynamic polarization corrosion test. In this dissertation, polarization resistance method was adopted to evaluate the corrosion rate since the measured polarization resistance was inversely related to the corrosion rate. In the polarization resistance technique the sample potential was scanned over a very small range (Tafel range) relative to the open circuit potential and the resulted current was measured. Over Tafel range, the current vs. voltage curve was roughly linear (Fig. 3.12). The polarization corrosion resistance (R_p) was calculated according to Tafel-extrapolation method. The Tafel region was extrapolated to the corrosion potential, as shown in Fig.3.13. The polarization resistance, R_p, was calculated using Stern-Geary equation: $R_p = \frac{\beta_a \beta_c}{2.3.i_{corr}(\beta_a + \beta_c)}$, where β_a and β_c are the anodic and cathodic Tafel slopes (Fig. 3.13), respectively, and i_{corr} is the corrosion current.

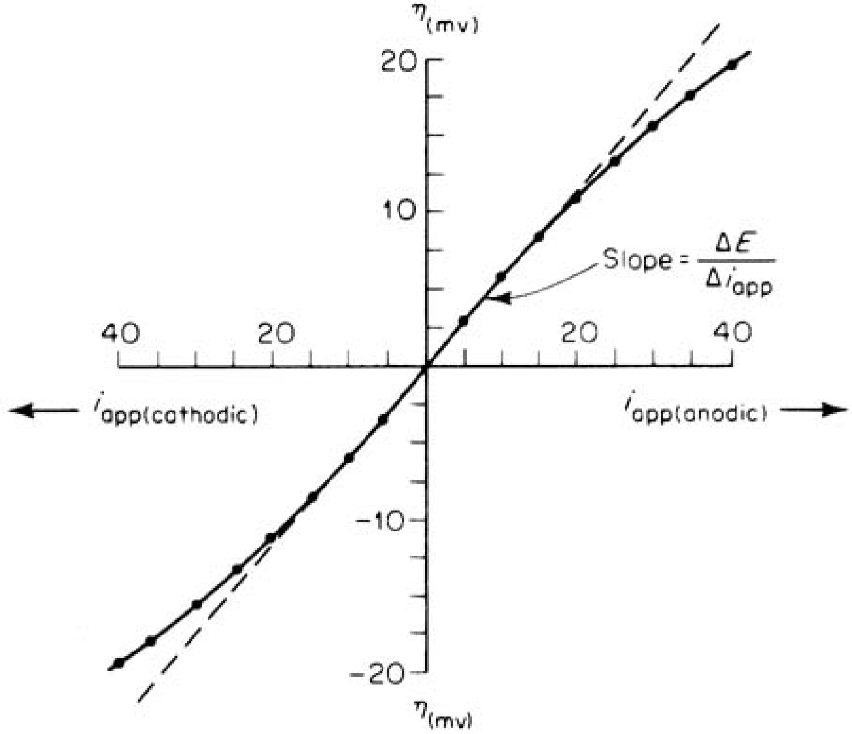

Fig. 3.12 Applied-current linear-polarization curve [148].

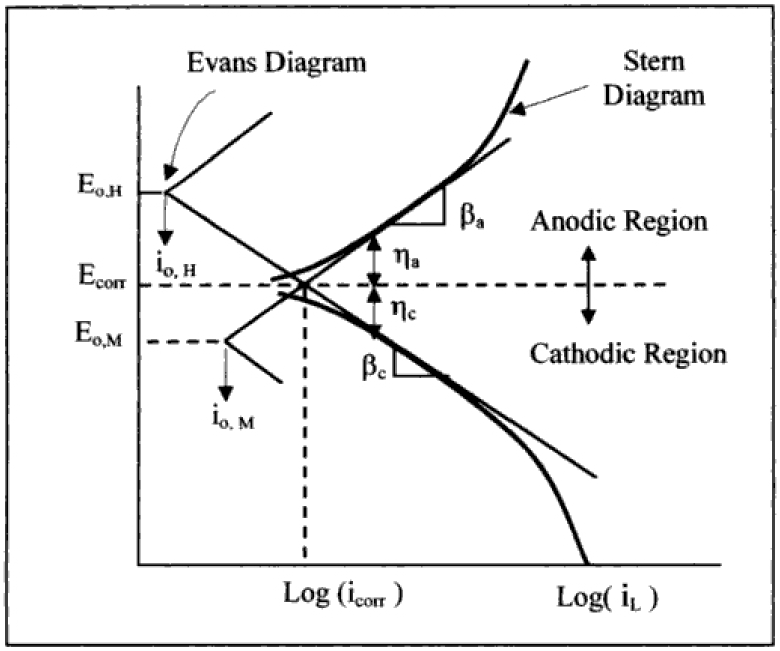

Fig. 3.13 Corrosion measurement by the Tafel-extrapolation method [149].

In the potentiodynamic tests, the initial potential was -0.1 V vs. open circuit potential (OCP), and the final potential was 1.2 V vs. Ag/AgCl electrode. The scan rate was 1 mV/s.

Potentiostatic corrosion tests. Potentiostatic corrosion tests were conducted for 4 hours at the anodic and cathodic conditions: the applied potential was -0.1 V vs. Ag/AgCl electrode with H_2 purging (anodic) and +0.6 V vs. Ag/AgCl electrode with O_2 purging (cathodic).

The surface morphologies of samples after corrosion testing were observed using SEM with EDX.

3.3 Corrosion and tribological properties of coatings in simulated biomedical environments

To evaluate the possibility of coatings applying for bio-devices and implant, the corrosion performance of coatings in simulated body fluid and their tribological properties against a polyethylene biomaterial were conducted in a simulated biomedical environment. The electrolyte used for simulating human body fluid conditions was Hank's solution, prepared using commercial Hanks' Balanced Salt (Sigma-Aldrich$^{®}$). The pH of the solution was precisely adjusted at 7.4. Freshly prepared solution was used for each experiment. The composition of the Hanks solution used was (in g/l) 8 NaCl, 0.4 KCl, 0.185 $CaCl_2.2H_2O$, 0.09767 $MgSO_4$, 0.35 $NaHCO_3$, 1.00 Glucose, 0.06 KH_2PO_4 and 0.04788 NaH_2PO_4 [150].

3.3.1 Coating deposition

TiN, CrN, TiAlN, CrAlN and hydrogenated DLC coatings were produced by coating supplier, Tecvac Ltd., UK. The substrate materials were mirror polished (Ra<0.1 µm) stainless steel AISI 316L steel discs (Ø 30 mm ×3 mm).

3.3.2 Corrosion tests in simulated body fluids

Potentiodynamic polarization corrosion tests and corrosion potential monitoring were conducted in a three-electrode system test unit (Fig. 3.11) with Hanks' balanced salt solution, at 37±2 ^{o}C.

The initial potential was -1.5 V vs. open circuit potential (OCP), and the final potential was +1.5 V vs. Ag/AgCl electrode. The scan rate was 1 mV/s.

E_{corr} vs. time testing. The corrosion potential (E_{corr}) measurement was maintained up to 12 h using the corrosion test unit same as descripted in section 3.2.3 and Fig. 3.11 in Hanks solution at 37±2 ^{o}C.

The surface morphologies of samples after corrosion testing were observed using SEM with EDX.

3.3.3 Tribological properties against polyethylene biomaterial

Pin-on-disc tests. Tribological behaviors of coatings were characterized by a pin-on-disc tribometer against high density polyethylene(HDPE) (Ø= 5.5 mm) under dry and lubricated conditions with distilled water and Hanks solution dripping on the coating surface (0.5 ml/2000 revolutions). The sliding distance was 500 m i.e., 40000 revolutions with the normal load of 10 N.

Observation of wear tracks and wear debris. The details of material transfer phenomena between coatings and counterface balls and morphology of wear chips were observed using FEI Quanta 200F SEM with EDX (Fig. 3.14). Since the polyethylene balls are electrically inductive, the low vacuum (70 Pa) mode was used to observe the worn HDPE ball surface.

Fig. 3.14 A FEI Quanta 200F Scanning Electron Microscope (SEM) with energy dispersive X-ray analysis (EDX).

CHAPTER 4 PERFORMANCE OF COATINGS FOR MANUFACTURING APPLICATIONS

4.1 Effects of annealing temperature on the tribological properties and material transfer phenomena under pin-on-disc testing conditions

4.1.1 Original coating thickness, surface roughness and chemical composition

Figs. 4.1 (a-e) are the cross-sectional SEM micrographs of TiN, CrN, TiAlN, CrAlN and DLC coatings, respectively. The coatings' surface roughness and thickness which was obtained from the cross-sectional SEM observation, are listed in Table 4.1.

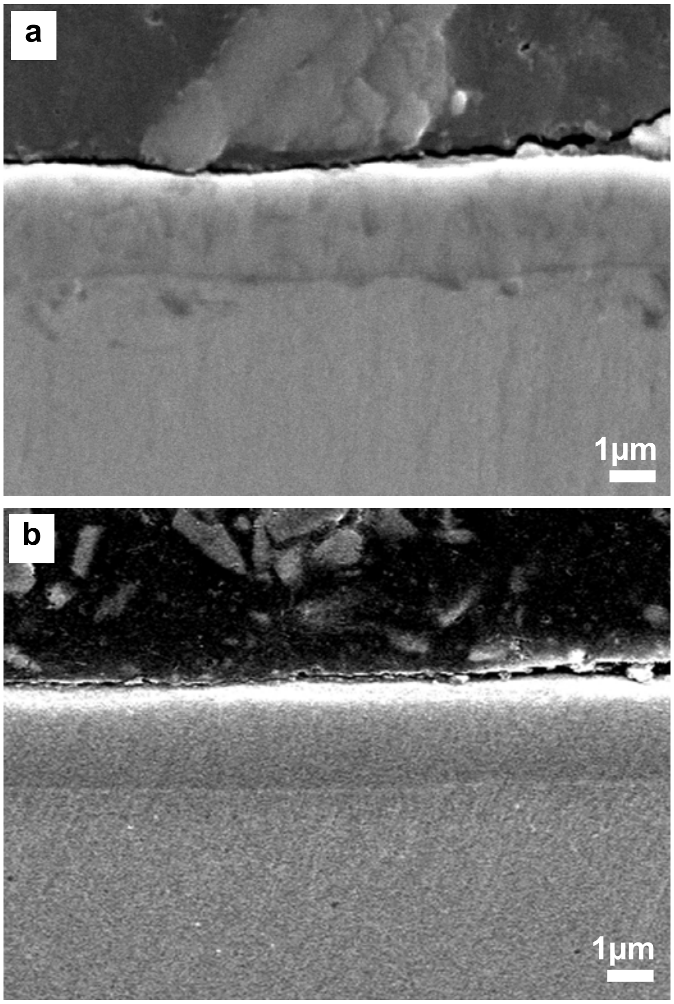

Figs. 4.1 (a) and (b)

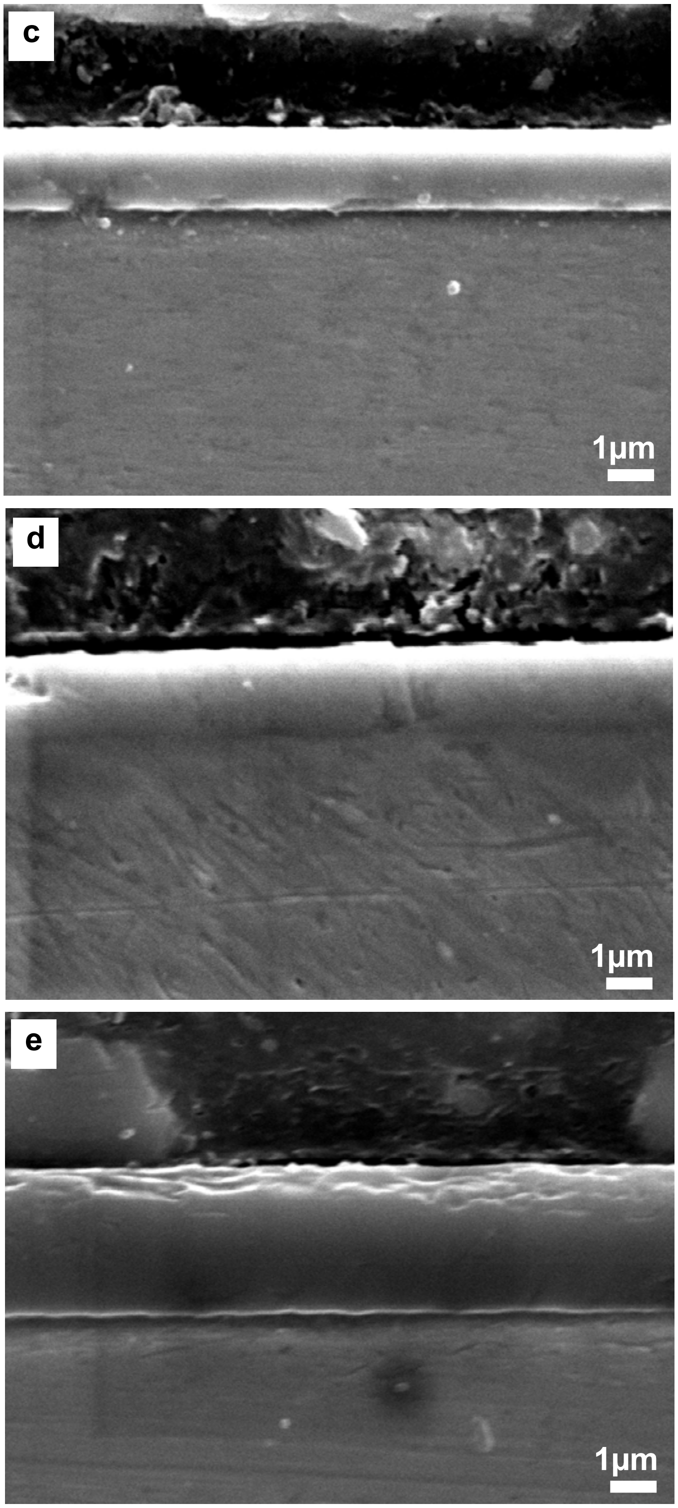

Fig. 4.1 SEM micrographs of cross-sections of (a) TiN, (b) CrN, (c) TiAlN, (d) CrAlN and (e) DLC coatings.

Table 4.1 Coating roughness and thickness

Coatings	TiN	CrN	TiAlN	CrAlN	DLC
Thickness (μm)	2.0 ±0.2	2.0±0.1	1.9±0.05	1.9 ±0.05	3.3±0.05
Roughness (R_a/μm)	0.09±0.01	0.07±0.1	0.07±0.1	0.07±0.1	0.06±0.1

The PVD TiN, CrN, TiAlN and CrAlN coatings have a similar coating thickness around 2.0 μm and the CVD DLC coating is thicker and about 3.3 μm. The surface roughness of all coatings is <0.1 μm. The TiN has the highest roughness 0.09 μm, and the DLC has the lowest R_a 0.06 μm.

It should be mentioned that, unlike the other coatings which have a monolayered structure with one ~100 nm-thick Ti or Cr interlayer, CrAlN coating produced by our supplier (Tecvac Ltd., UK) has a multilayered structure. Figs. 4.2 (a) and 4.2 (b) show an XPS compositional depth profile and a cross-sectional TEM image of the CrAlN coating, respectively. Fig. 4.2 illustrates that the CrAlN coating has a multilayered nanostructure with alternating CrN (dark layers shown in Fig. 4.2(b)) and $Cr_{1-x}Al_xN$ layers (bright layers in Fig. 4.2(b)) and the outermost layer is a Cr-Al-N layer. Each individual layer has an even, uniform thickness throughout its layer. However, different layers has a different thickness; the $Cr_{1-x}Al_xN$ and CrN layer thickness vary from layers to layers, ranging from 350 to 400 nm for the former and from 150 to 350 nm for the latter. In addition, a chromium (Cr) interlayer between the M2 steel substrate and the top layers was deposited to improve the coating adhesion as seen in Fig. 4.2(b). The coating has no columnar structure and the interfaces between the layers are sharp.

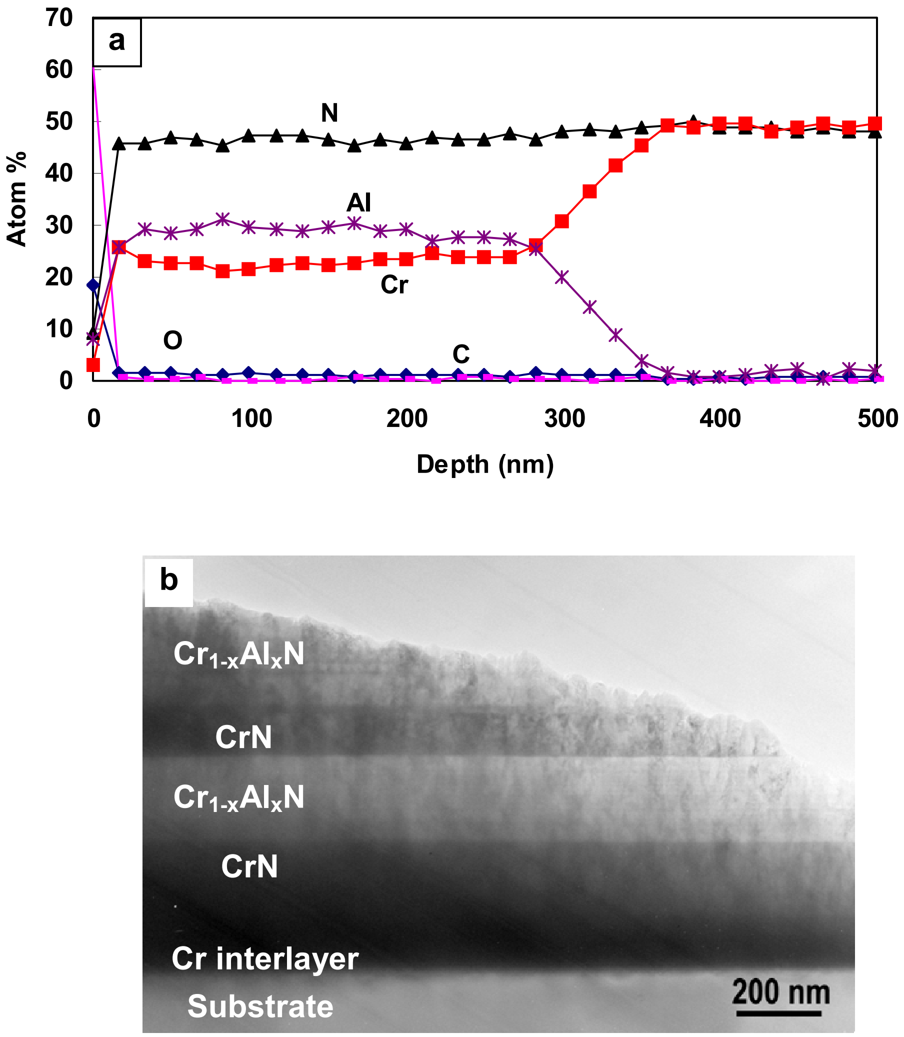

Fig. 4.2 (a) XPS compositional depth profile and (b) TEM image of cross-section of the CrAlN coating.

The data of composition of each coating were supplied by the coating supplier and listed in Table 4.2. The average Cr/Al ratio in the entire CrAlN coating is 35/15 but from XPS analysis, the Cr/Al in the CrAlN outmost layer is 22/27 where Al has a higher proportion than Cr. The commercial DLC coating, Diamolith (Tecvac Ltd.), used in this dissertation is a-C:H in nature.

Table 4.2 Chemical compositions for of TiN, CrN, TiAlN, CrAlN and DLC coatings

Coating	Composition (at. %)			
	Ti	Cr	Al	N
TiN	50±3	-	-	50±2
CrN	-	70±3		30±2
TiAlN	35±3	-	15±2	50±2
CrAlN	-	35±3	15±2	50±2
DLC	a-C :H; I (D)/I (G) ratio of 0.35 by Raman spectroscope with a Laser Physics Ar+514 nm wavelength laser [151].			

4.1.2 Effects of annealing temperature on the coating structure and hardness

Surface morphology change. Tables 4.3 (i/ii and ii/ii) describe the coating color and surface morphology change after annealing process. The coating damage resulting from the annealing occurred at 800 °C, 1000 °C and 900 °C for TiN, CrN and TiAlN coatings, respectively. CrAlN coating kept an intact surface morphology though some oxidization occurred after annealed at 1000 °C. Delamination of the DLC coating occurred beyond annealing temperature of 400 °C. After annealing at 500 °C, the DLC coating delaminated from its substrate completely. The DLC coating after 600 °C annealing was partially delaminated.

Phase structure. Figs. 4.3-4.6 are the XRD patterns of original and annealed coatings of TiN, CrN, TiAlN and CrAlN, respectively, in which the ones designated as (b) show the patterns zoomed into relatively narrow angle ranges to give more clear views of overlapped peaks in the corresponding patterns designated as (a).

Table 4.3 Changes in color and surface morphology of coatings (i/ii)

		Coating color	Surface morphology
TiN	T0	Golden yellow	Intact
	T500	Grey yellow	Intact
	T600	Brown	Intact
	T700	Brown	Intact
	T800	Grey black	Delaminated partially
	T900	Grey black	Delaminated completely
CrN	C0	Grey black	intact
	C500	Grey black	intact
	C600	Dark blue	intact
	C700	Blue	intact
	C800	Blue	intact
	C900	Grey blue	Intact
	C1000	black	Delaminated partially
TiAlN	TA0	Brown	Intact
	TA500	Dark blue	Intact
	TA600	Blue	Intact
	TA700	Brown blue	Intact
	TA800	brown	Intact
	TA900	black	Delaminated completely

Table 4.3 Changes of color and surface morphology of coatings (ii/ii)

CrAlN	CA0	Black	Intact
	CA500	Black	Intact
	CA600	Dark blue	Intact
	CA700	Dark blue	Intact
	CA800	Brown	Intact
	CA900	Bright blue	Intact
	CA1000	Bright blue	Intact
DLC	D0	Black	Intact
	D200	Black	Intact
	D300	Black	Intact
	D400	Black	Intact
	D500	-	Delaminated
	D600	Rainbow color	Delaminated

Fig. 4.3 is the patterns of the TiN coating after annealed at different temperatures. The original TiN is well crystallized in a cubic structure with a strong (111) preferential orientation. The rutile structure TiO_2 in (111) orientation begins to be detected after annealing at 600 ^{o}C. After annealing at 800 ^{o}C, little TiN-related phases can be detected excepted for the very weak TiN (111) peak since large pieces of the coating have peeled off from substrate. After annealing at 900 ^{o}C, the main phase compositions are only some iron oxides as the coating has completely delaminated from the substrate.

Fig. 4.4 shows the XRD patterns of the CrN coating after annealed at different temperatures. The original CrN coating is also well crystallized in an orthorhombic CrN structure and a very week β-Cr_2N phase (Fig. 4.4(a)). Phase transformation from CrN to Cr_2N occurred after annealing at 500 ^oC. The reaction of the phase transformation between CrN and β-Cr_2N can be written as: $2CrN_{(s)}= Cr_2N_{(s)}+1/2\ N_{2\,(g)}$ [152]. According to Lu et al.'s study [152], the thermodynamic analysis by Gibbs free energy calculation has indicated that Cr_2N is not thermodynamically stable at the low temperatures <1010 ^oC. Such phase transformation between CrN and β-Cr_2N is possibly due to a non-thermodynamic factor, i.e., the large stress relaxation occurring in this similar temperature range [152]. Thus, for the deposition processes of CrN based coatings, the control of coating internal stress is an important factor since it not only significantly affects the mechanical and chemical properties but also governs the phase transformation at the temperatures lower than <1010 ^oC. When annealing temperature ≤ 700 ^oC (i.e., C0, C500, C600), no obvious Cr oxides can be detected from the XRD patterns. The Cr_2O_3 phase can be detected above 700 ^oC and the phase compositions of coatings are CrN, Cr_2O_3 and Cr_2N. Relative intensity of Cr_2O_3 generally increases with rising the annealing temperature.

The evolution of the XRD patterns of the TiAlN coating annealed at different temperatures is shown in Fig. 4.5. The as-deposited TiAlN coating is also crystallized in the cubic structure with a significant (111) preferential orientation. A tetragonal rutile TiO_2 structure (t-TiO_2) begins to exist in the TiN coating after 700 ^oC annealing. Besides the t-TiO_2, an aluminum titanium oxide nitride compound, $Al_{0.54}Ti_{2.46}N_{0.28}O_{4.58}$ (marked as ATNO in Fig. 4.5), is detected on the TiAlN coating after annealing at 800 ^oC. After annealing at 900 ^oC, the coating peeling off has occurred, and the phase compositions are mainly iron oxides. In the study of Chung Wan Kim and Kwang Ho Kim on the oxidation mechanism of TiN and TiAlN [44], the roles of Al in TiAlN coating have been summarized. Since Al has a very strong affinity to oxygen and the standard Gibb's free energy of formation for aluminum oxide has a very large negative value ($\Delta G_f^0 = -954 KJ/mol$), the driving force for Al ions to move to the surface and to form aluminum oxide is high. Small aluminum ions in the TiN lattice can easily diffuse through the grain boundaries. Thus, at the initial stage of oxidation, Al ions diffuse to the surface and form solid $Al_xTi_yO_z$ which is not crystalline and can not be detected by XRD (Fig. 4.5). The $Al_xTi_yO_z$ phase then acts as a passive layer against further oxidation. Because the oxidation was proceeded by continual oxygen diffusion through oxidized surface layer, the passive layer of the $Al_xTi_yO_z$ formed on the TiAlN coating played an effective role as a diffusion barrier against oxygen.

The evolution of the XRD patterns of the CrAlN is shown in Fig. 4.6. The main phase composition of original CrAlN coating is CrN and Cr_2N. After annealing at 600 ^oC, a weak Al_2O_3 peak is observed. No other evident oxide peaks can be detected. When the annealing temperature is increased up to 900 ^oC, the XRD intensity of CrAlN phase is still very strong. Compared with the TiAlN coating, Al_2O_3 phase is formed more readily in CrAlN at a relatively low temperature (700 ^oC) which agrees with the description in the reference [48] that the presence of Ti would perturb the formation of the protective Al_2O_3. It is well known that in an oxidation or corrosive environment Ti element often forms a porous non-protective oxide scale, and therefore the oxidation and corrosion resistance of titanium-based coatings are limited [153, 154].

It can be concluded that, among these four hard coatings, TiN has the worst oxidation resistance while CrAlN has the best oxidation resistance. Although the TiAlN coating has an improved thermal stability with Al introduction into TiN crystalline, its thermal stability is still worse than that of CrN and CrAlN.

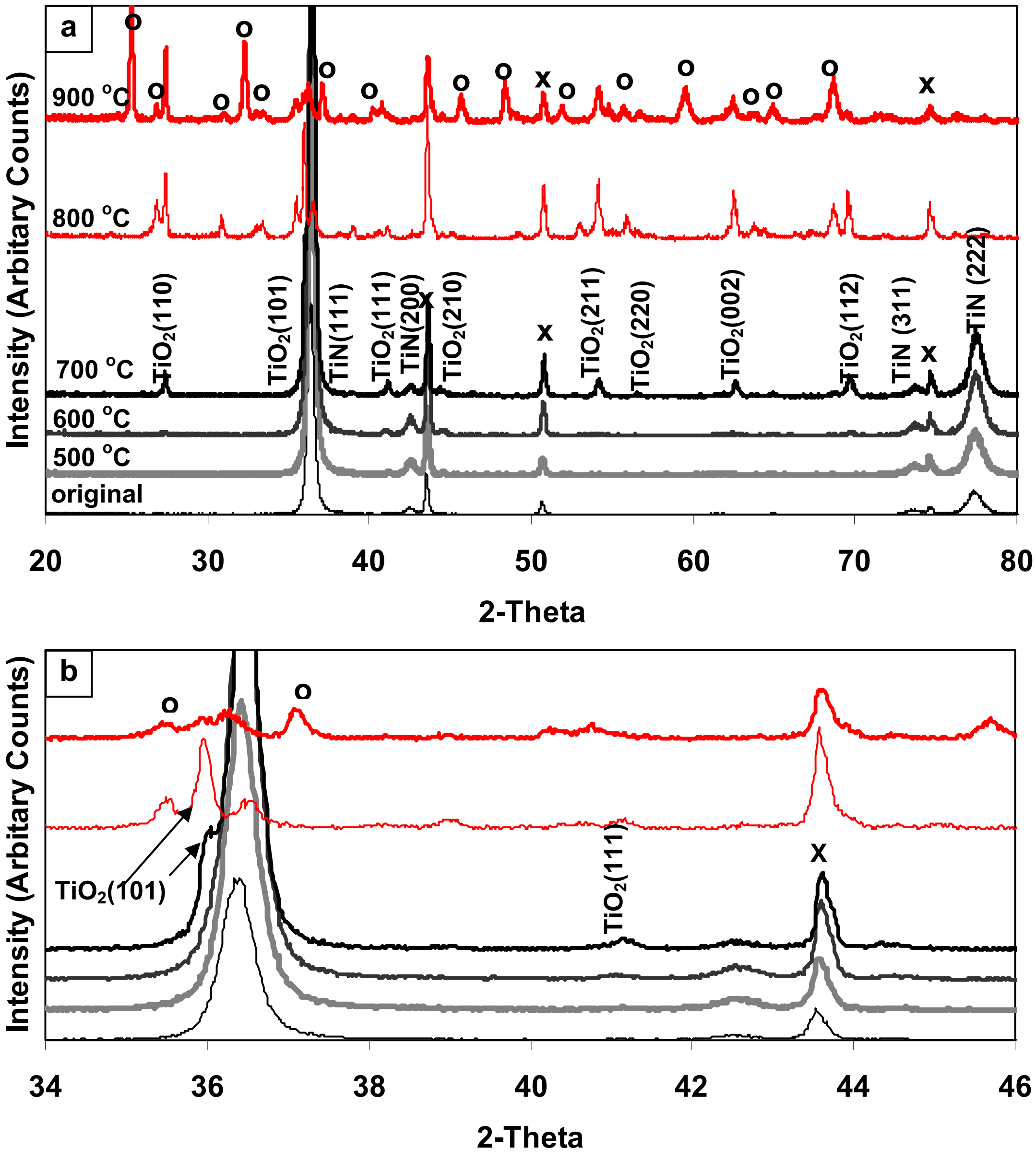

Fig. 4.3 XRD patterns of the TiN coatings before and after annealed at different temperatures marked on the curves and the peaks marked with “X” and “O” belong to the M2 substrate and iron oxides, respectively. (a) shows the patterns at the range of 20-80^{o} in 2θ and (b) gives a magnified image of the corresponding patterns at the range of 34-46 ^{o} in 2θ to show the overlapped peaks.

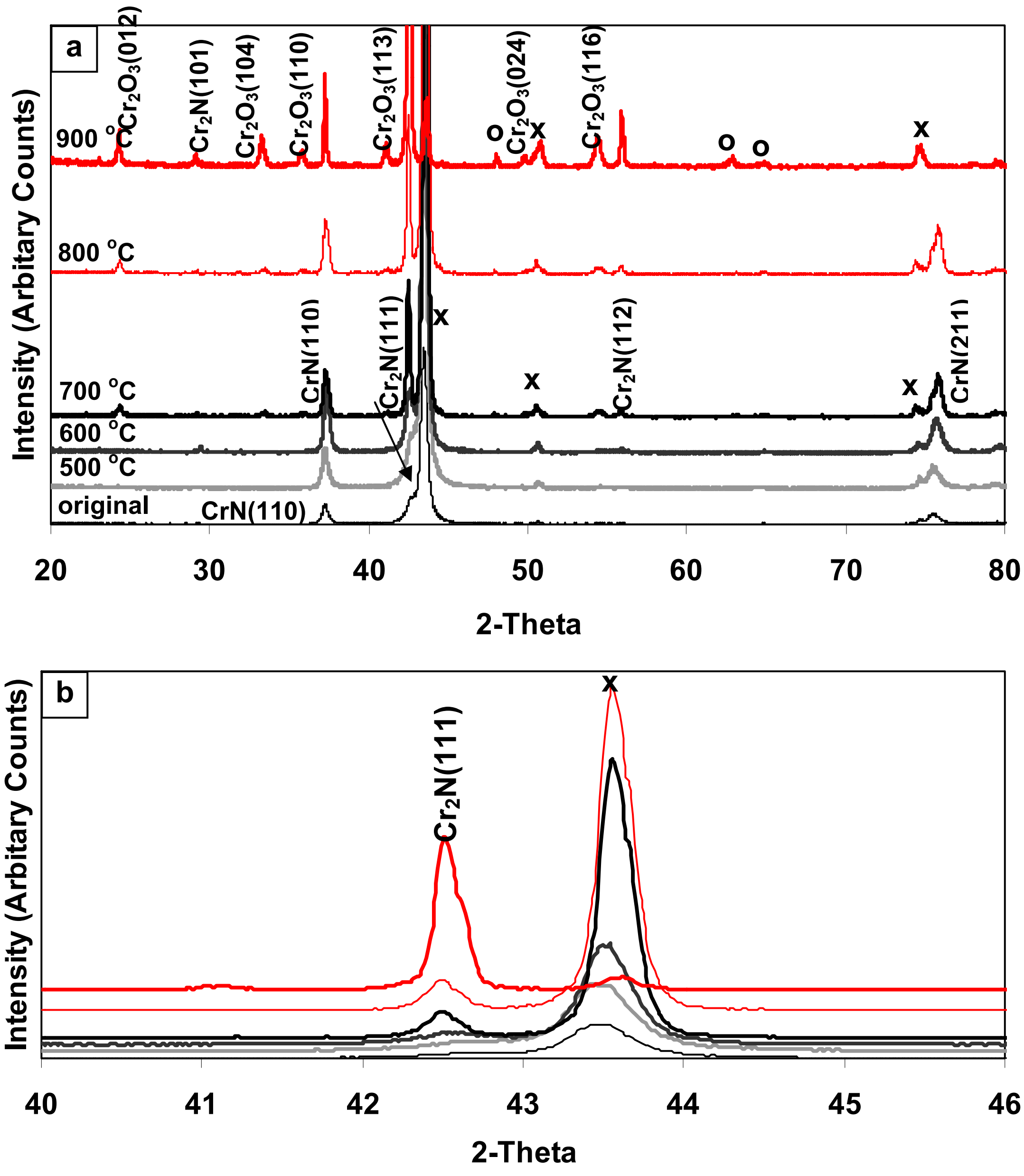

Fig. 4.4 XRD patterns of the CrN coatings before and after annealed at different temperatures marked on the curves and the peaks marked with “X” and “O” belong to the M2 substrate and iron oxides, respectively. (a) shows the patterns at the range of 20-80^{o} in 2θ and (b) gives a magnified image of the corresponding patterns at the range of 40-46 ^{o} in 2θ to show the overlapped peaks.

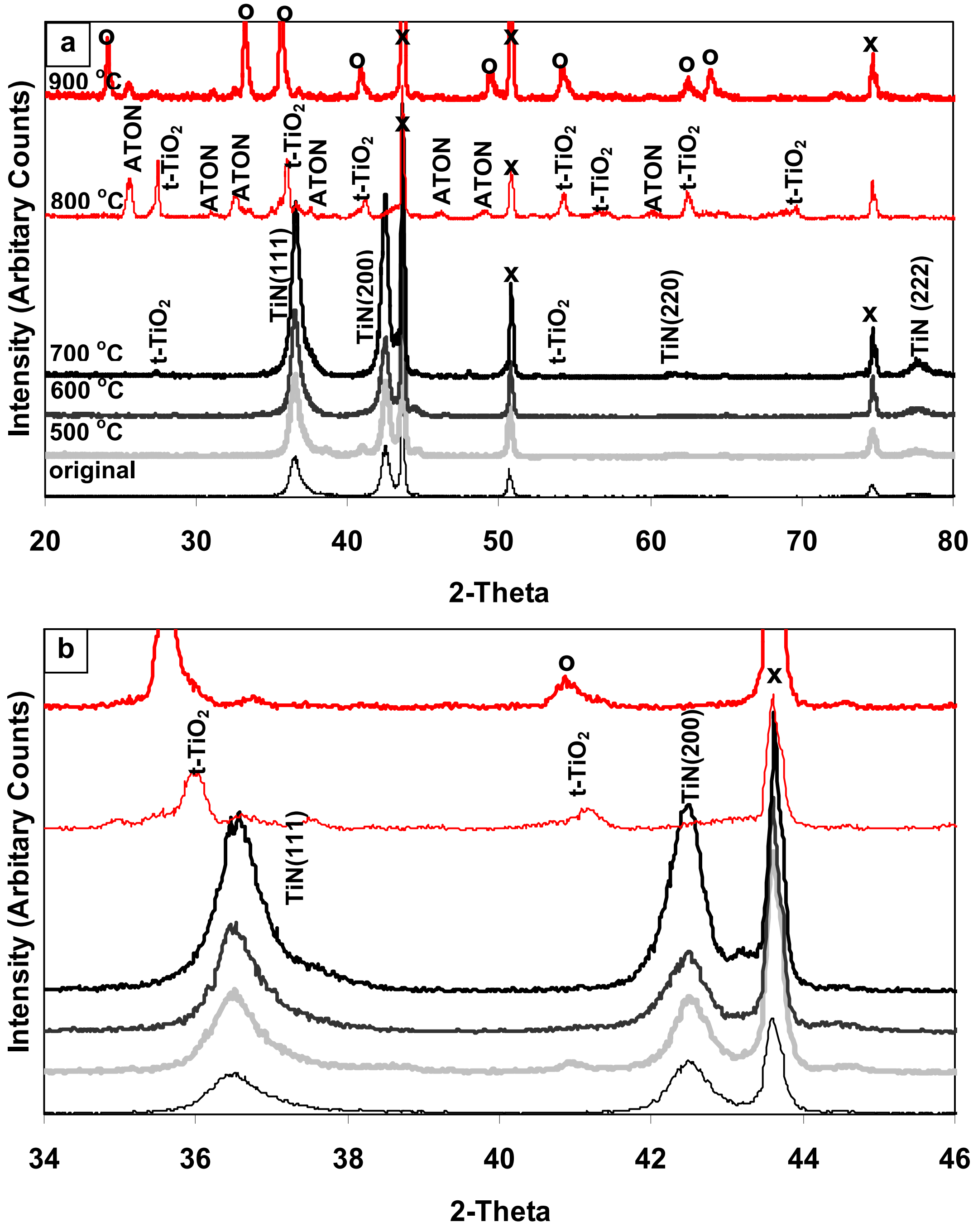

Fig. 4.5 XRD patterns of the TiAlN coatings before and after annealed at different temperatures marked on the curves and the peaks marked with "X" and "O" belong to M2 substrate and iron oxides, respectively. (a) shows the patterns at the range of 20-80° in 2θ and (b) gives a magnified image of the corresponding patterns at the range of 34-46° in 2θ to show the overlapped peaks.

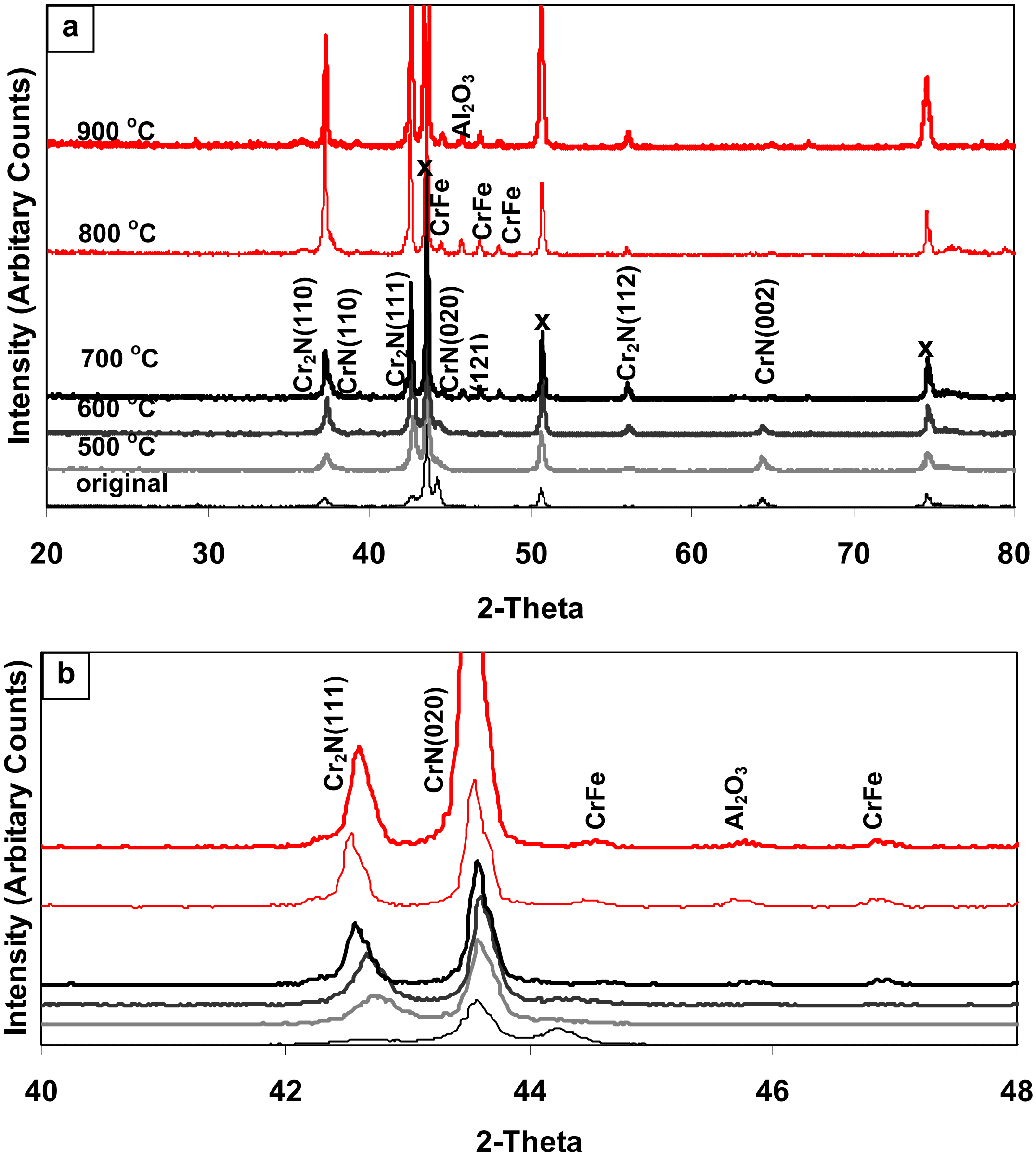

Fig. 4.6 XRD patterns of the CrAlN coatings before and after annealed at different temperature marked on the curves and the peaks marked with “O” and “X” belong to M2 substrate and iron oxides, respectively. (a) shows the patterns at the range of 20-80^o in 2θ and (b) gives a magnified image of the corresponding patterns at the range of 40-48 ^{o} in 2θ to show the overlapped peaks.

Hardness (H) and Reduced elastic modulus (E_r). Fig. 4.7 shows the load-depth displacement nanoindentation curves of original and annealed coatings. Table 4.4 summarizes the average values of hardness and reduced elastic modulus.

The hardness of the as-deposited TiN coating is about 25.5 GPa (Table 4.4(i)). After annealing at 500 ^{o}C, the coating hardness drops to 12.4 GPa. No remarkable changes have been observed in the XRD pattern after annealing at 500 ^{o}C (Fig. 4.3); however, it is found from the color change of the coating, from gold yellow to grey (Table 4.3) that TiN has been oxidized at a temperature of above 500 ^{o}C. With an increase of annealing temperature to 700 ^{o}C, the hardness gradually drops to 10.7 GPa. When annealing temperature increases to 800 ^{o}C and 900 ^{o}C, the coating delaminating occurs and the hardness is ~7 GPa and ~2 GPa, respectively. These hardness values can be attributed to the oxidized substrate surface but not the coating itself. The elevated annealing temperature also decreases the reduced elastic modulus (E_r) of TiN coatings from about 350 GPa for the un-annealed coating condition (T0) to about 170 GPa for the annealed coating condition at 900 ^{o}C (T900).

The values of H and E_r of CrN coating decrease with increasing annealing temperature (Table 4.4(i)). The hardness of the as-deposited CrN coating is about 24.8 GPa which is softer than that of TiN coating. After annealing at 500 ^{o}C, the hardness does not drop significantly with a value of ~21 GPa. After annealing at 600 ^{o}C, the hardness decreases significantly to ~16 GPa. Although a high hardness up to 30 GPa of Cr_2O_3 coating has been reported before [155, 156], even with the evident emergence of Cr_2O_3 at the annealing temperature beyond 700 ^{o}C, the coating hardness is still low, about 9 GPa at 900 ^{o}C. That implies that Cr_2O_3 in the annealed CrN coating does not form a thick top layer serving as a load-bearing layer.

The values of H and E_r of TiAlN coating also decrease with increasing annealing temperature (Table 4.4(ii)). The hardness of the original TiAlN coating is ~26 GPa which is higher than TiN and CrN coatings. After 500 ^{o}C annealing, the coating (TA500) has a hardness of 15.6 GPa which is higher than the corresponding TiN coating annealed at 500 ^{o}C (T500) but lower than the corresponding CrN coating (C500). When annealing at 800 ^{o}C, an $Al_{0.54}Ti_{2.46}N_{0.28}O_{4.58}$ phase emerges together with t-TiO_2 phase in the TiAlN coating (TA800) and its hardness drops to 8.3 GPa. When the annealing temperature is increased to 900 ^{o}C (TA900), the coating still has a hardness of ~5 GPa. During the evolution of hardness with annealing temperature, the E_r decreases from ~290 to 157 GPa.

The original hardness of CrAlN is about ~30 GPa and after 600 ^{o}C annealing, the hardness is still 21.6 GPa (Table 4.4(ii)). After 700 ^{o}C annealing, H and E_r drops to ~17 and ~166 GPa but recovers to ~20 and ~180 GPa after annealing at 800 ^{o}C, respectively. That implies that the Al_2O_3 film on the CrAlN surface not only retards the coating oxidation but also contributes to the hardness recovery. After 900 ^{o}C annealing, the CrAlN coating hardness drops at a great extent to 12.6 GPa, whereas this value is still much higher than those of the other three coatings at the corresponding annealing temperature.

The hardness changing trend of DLC coating (Fig. 4.7(e) and Table 4.4 (ii)) indicates that before 400 ^{o}C, the hardness drops slowly from 21.9 to 15.1 GPa with increasing annealing temperature. After annealing at above 500 ^{o}C, the hardness drops to <2 GPa due to the severe coating delaminating and peeling.

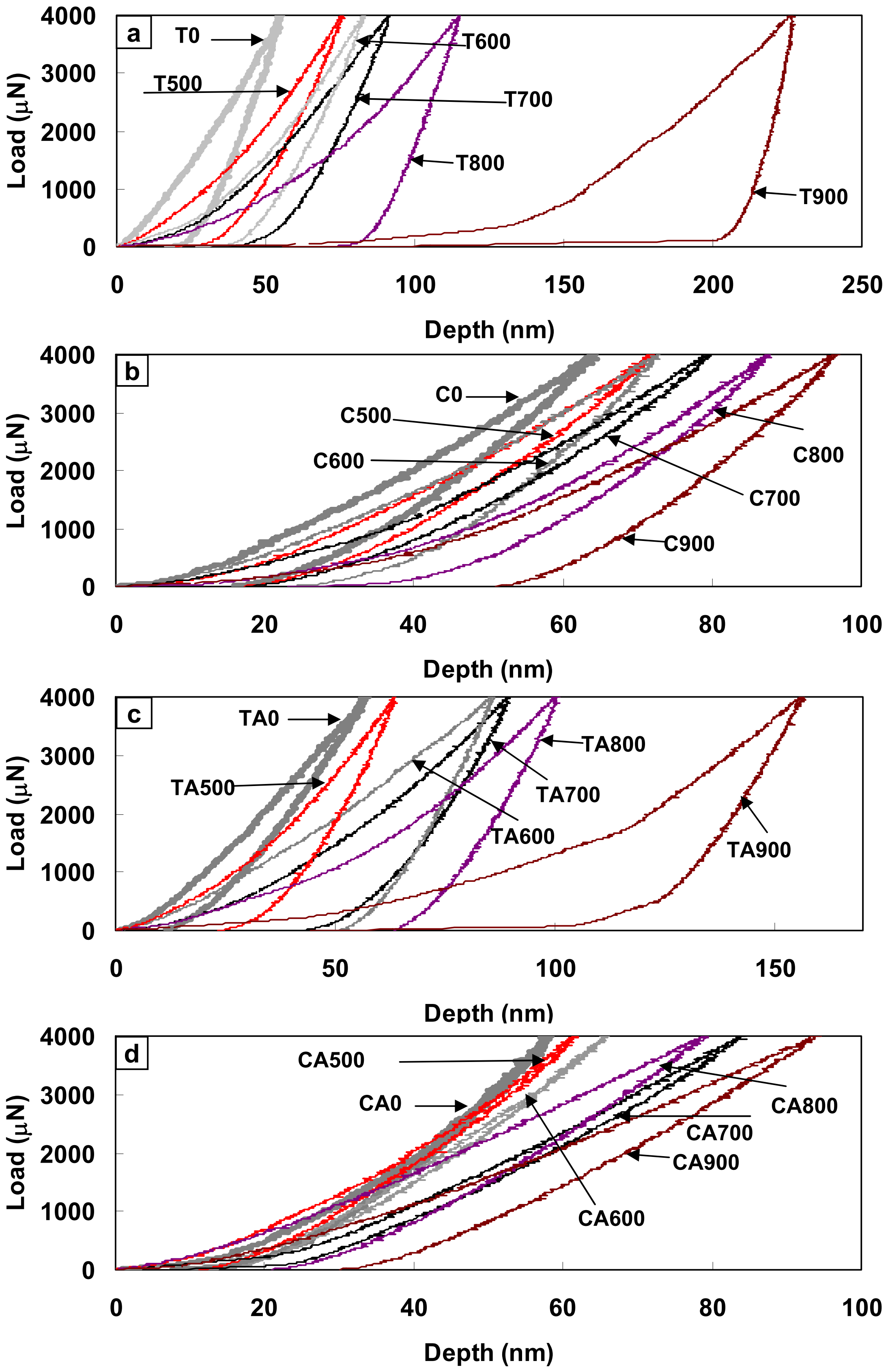
a
T0
T500
T600
T700
T800
T900
Load (μN)
Depth (nm)
0
1000
2000
3000
4000
0
50
100
150
200
250
b
C0
C500
C600
C700
C800
C900
Load (μN)
Depth (nm)
0
20
40
60
80
100
c
TA0
TA500
TA600
TA700
TA800
TA900
Load (μN)
Depth (nm)
0
50
100
150
d
CA500
CA0
CA600
CA700
CA800
CA900
Load (μN)
Depth (nm)
0
20
40
60
80
100

Fig. 4.7 (a-d)

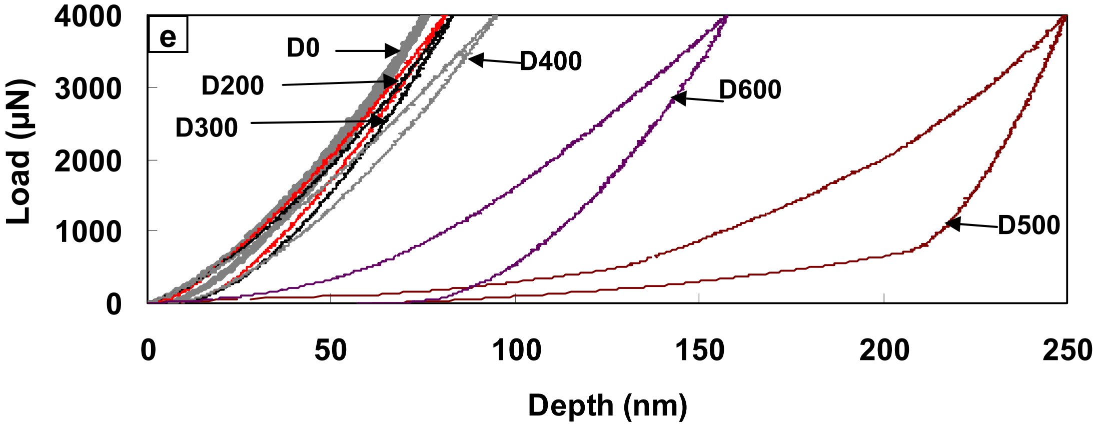

Fig. 4.7 Load-depth displacement nanoindentation curves of original and annealed coatings (a) TiN, (b) CrN, (c) TiAlN, (d) CrAlN and (e) DLC.

Table 4.4 Hardness (H) and reduced elastic modulus (E_r) of un-annealed and annealed coatings (i/ii)

		Hardness (H/GPa)	Reduced elastic modulus (E_r/GPa)
TiN	T0	25.5±0.5	355.1±30.5
	T500	12.4±3.0	215.7±6.3
	T600	11.4±3.8	194.9±19.7
	T700	10.7±2.5	193.0±20.3
	T800	7.1±1.2	197.6±9.2
	T900	1.7±0.3	173.5±4.0
CrN	C0	24.8±1.0	278.1±5.1
	C500	21.4±1.8	237.5±22.2
	C600	16.5±2.9	236.1±23.2
	C700	12.8±3.2	197.3±12.1
	C800	10.4±1.5	186.3±1.5
	C900	9.1±0.6	166.4±18.5

Table 4.4 Hardness (H) and reduced elastic modulus (E_r) of un-annealed and annealed coatings (ii/ii)

		Hardness (H/GPa)	Reduced elastic modulus (E_r/GPa)
TiAlN	TA0	26.3±2.8	292.4±5.2
	TA500	15.6±0.5	280.4±30.0
	TA600	13.3±0.7	235.5±50.0
	TA700	11.4±0.8	205.7±10.0
	TA800	8.3±1.8	186.8±0.20
	TA900	5.2±1.5	157.2±30.6
CrAlN	CA0	29.8±2.2	328.8±25.4
	CA500	22.5±2.5	256.1±14.2
	CA600	21.6±1.3	280.4±22.6
	CA700	17.5±0.7	166.4±9.4
	CA800	20.2±2.1	184.2±16.2
	CA900	12.6±1.1	126.1±11.4
DLC	D0	21.9±0.2	180.0±3.0
	D200	19.52±0.2	163.7±3.5
	D300	17.8±0.3	162.1±5.0
	D400	15.1±0.7	112.9±13.4
	D500	1.56±0.2	68.65±5.0
	D600	1.7±0.2	48.7±5.4

4.1.3 Effects of annealing temperature on the tribological property of TiN, CrN, TiAlN and CrAlN coatings

In this part of experiment, pin-on-disc sliding tests were conducted on the original and annealed at 500, 700 and 800 °C TiN, CrN, TiAlN and CrAlN coatings against ceramic alumina, steel and aluminium counterface materials.

4.1.3.1 Wear behavior of coatings against ceramic Al_2O_3 balls

Fig. 4.8 shows the coefficient of friction (cofs) curves of original and annealed TiN, CrN, TiAlN and CrAlN coatings during the dry sliding tests against ceramic Al_2O_3 balls under 1 N normal load. Figs. 4.9-4.12 are the SEM micrographs of the wear tracks on the TiN, CrN, TiAlN and CrAlN coatings. Fig. 4.13 shows the optical micrographs of surface morphologies of corresponding Al_2O_3 balls after the wear tests.

Fig. 4.8(a) shows the cof curves of original and annealed TiN coatings and Fig. 4.9 is the SEM micrographs of wear tracks of (a, b) T0, (c, d) T500, (e, f) T700 and (g) T800 during the dry sliding tests against ceramic Al_2O_3 balls under 1 N normal load. Fig. 4.9 (b, d, f) are the corresponding magnified images of Fig. 4.9 (a, c, e). The original TiN coating (T0) has a cof of 1.1 when against Al_2O_3 ball. At the early test stage (<4000 revolutions), the average cofs of T500 and T700 are similar, which is about 1.1 and after 4000 revolutions, the curves fluctuate severely with a reduced average cofs of ~0.7. T800 has a relatively low cof of about 0.5. After the dry sliding test against Al_2O_3 ball, abrasive wear and partially spallation occur on the coating T0 (Figs. 4.9(a, b)). For coating T500, due to the reduced hardness, this coating has been penetrated at the central wear track (Figs. 4.9(c, d)). After wear test, the coating T700 has been worn out after about 4000 revolutions and the sliding is actually between Al_2O_3 ball and M2 steel substrate where the cof decreases to about 0.7. Since coating peeling has already presented after annealing at 800 ^{o}C, coating T800 is damaged and not suitable for use as a tool coating. From SEM micrograph of wear track on T800 (Fig. 4.9(g)), coating has worn out completely and partial coating peeling can be observed. No material transfer occurs on the ball against T0 coating (Fig. 4.13(a)) and with the increase of annealing temperature, more material transferred from relatively soft annealed TiN coatings to the Al_2O_3 balls can be observed (Figs. 4.13(a)).

Compared to the corresponding TiN coatings (Fig. 4.8(a)), CrN coatings (Fig. 4.8(b)) after annealing at various temperatures have lower cofs. After a short running-in stage, the cof of original CrN coating (C0) is about 0.6 and then decreases with increasing annealing temperature. For coating C800, the cof is about 0.4. It is believed that the lubrication effect of Cr-O on the coating surface contributes to the decrease of cof [157]. SEM micrographs (Fig. 4.10) of wear tracks on original and annealed CrN coatings against Al_2O_3 balls show that no obvious abrasive or coating spallation but some slightly coating polishing can be observed. Even for C700 and C800 which have relatively low hardness, <13 GPa, no visible coating wear can be detected. The surface morphology of Al_2O_3 balls against CrN coatings (Fig. 4.13(b)) shows that a little material transferring from CrN coating to the ball occurs on the ball against C0 coatings. However, no ball wear and material transferring can be observed on the balls against other CrN coatings.

The cof curves of TiAlN coatings against Al_2O_3 balls are shown in Fig. 4.8(c). Coatings TA0 has a cof of about 0.7 which is slightly lower than the coating T0. TA500 and TA700 have a similar cof of about 1.1. For TA800, the cof is increasing gradually during the first 3000 revolutions then increases suddenly to about 1. The lower cof of original TiAlN coating could be due to the natural oxide top layer (Ti-O and Al-O) on the TiAlN coating surface, but the Ti-Al-N-O compounds formed at high temperature did not lead to low friction. From the SEM micrographs of wear tracks on TiAlN coatings (Fig. 4.11), no detectable coating wear can be observed on the coating TA0 (Figs. 4.11(a, b)) but some abrasive wear and plastic deformation on TA500 ((Fig. 4.11(d)) and TA700 (Fig. 4.11(f)) can be found. On TA800 coating (Fig. 4.11(g, h)), in the wear track, some small sized coating chipping can be observed (Fig. 4.11(h)). Comparing the surface morphology of Al_2O_3 balls against the various TiAlN coatings (Fig. 4.13(c)), it is easily seen that the counterface wear decreases with increasing annealing temperature.

The CrAlN coatings have higher cofs than the corresponding CrN coatings annealed at the same temperature (Fig. 4.8(d)). Coating CA500 has a cof of 0.55 which is lower than the original CrAlN (cof=0.75), then the cof increases to around 0.6 for CA700 and CA800 coatings. Since the Al_2O_3 layer on the CrAlN coatings serves as a barrier layer to prevent coatings from further oxidation, there are less lubricate oxides such as Cr_2O_3 or Cr-Al-O compound in the CrAlN than CrN coatings. Thus, the CrAlN presents higher cofs than CrN but still lower than TiN and TiAlN coatings. The SEM micrographs (Fig. 4.12) of wear tracks on CrAlN coatings show some slightly plastic deformation and surface polishing on the coatings. The counterface Al_2O_3 ball against CA0 has been worn and no ball wear can be observed on the balls against CA500 and CA700. On the Al_2O_3 ball against CA800, no ball wear can be found but a little material transfers from CA800 coating and attaches on the ball (Fig. 4.13(d)).

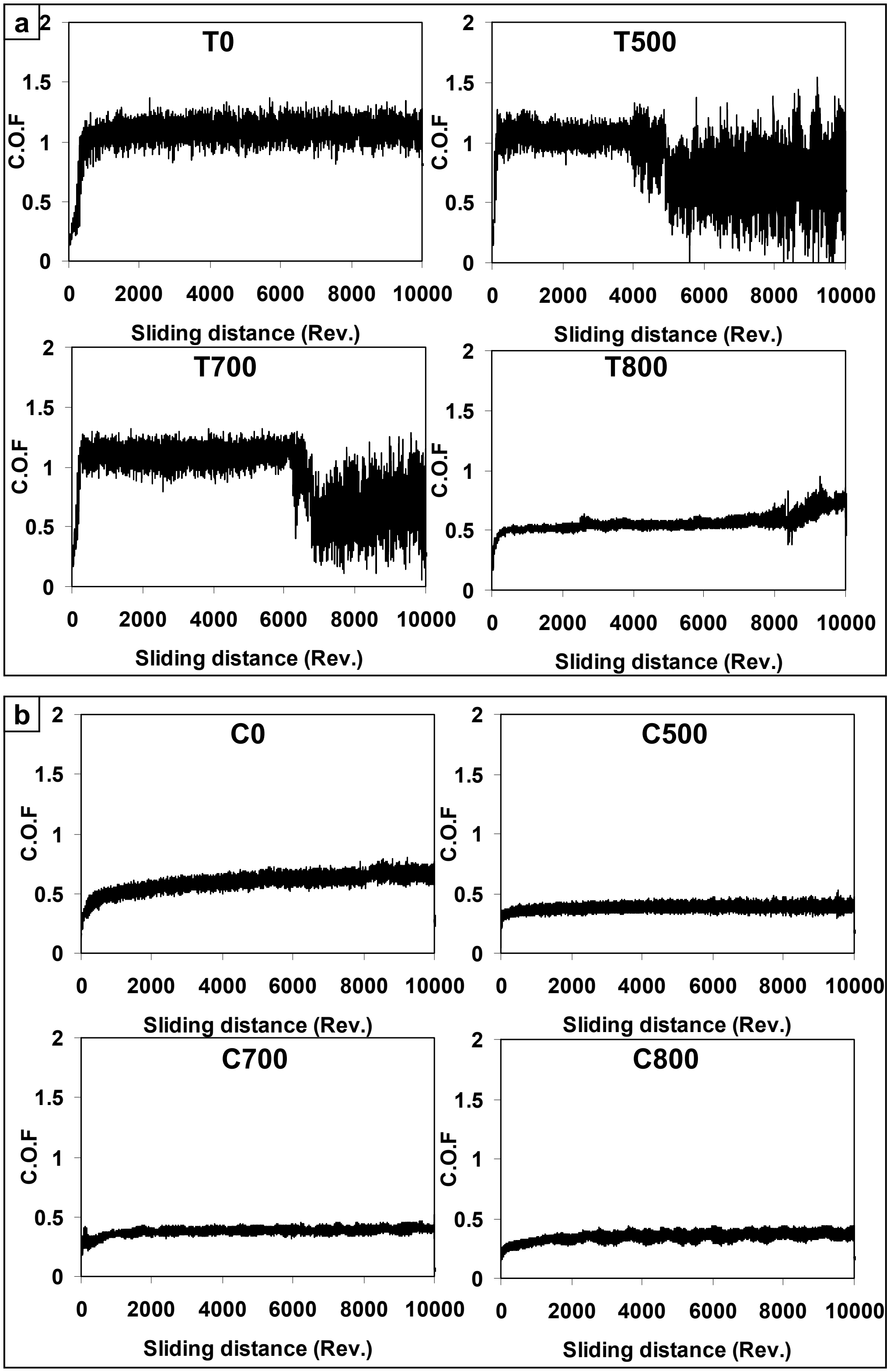
a
T0
T500
T700
T800
b
C0
C500
C700
C800
C.O.F
0
0.5
1
1.5
2
0
2000
4000
6000
8000
10000
Sliding distance (Rev.)

Fig. 4.8(a, b)

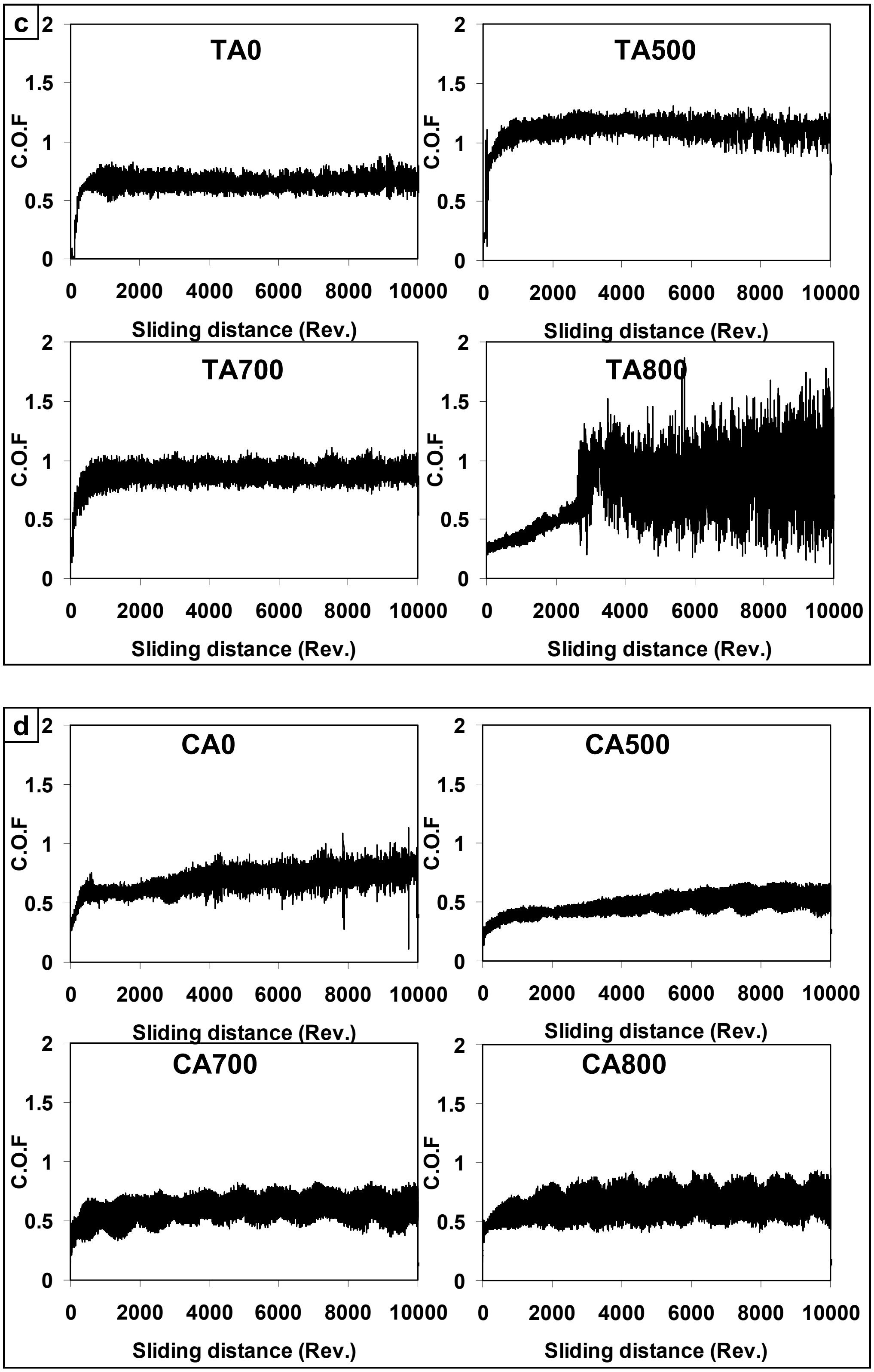

Fig. 4.8 Coefficient of friction (C.O.F.) curves of original and annealed coatings (a) TiN, (b) CrN, (c) TiAlN and (d) CrAlN during the dry sliding tests against ceramic Al_2O_3 balls.

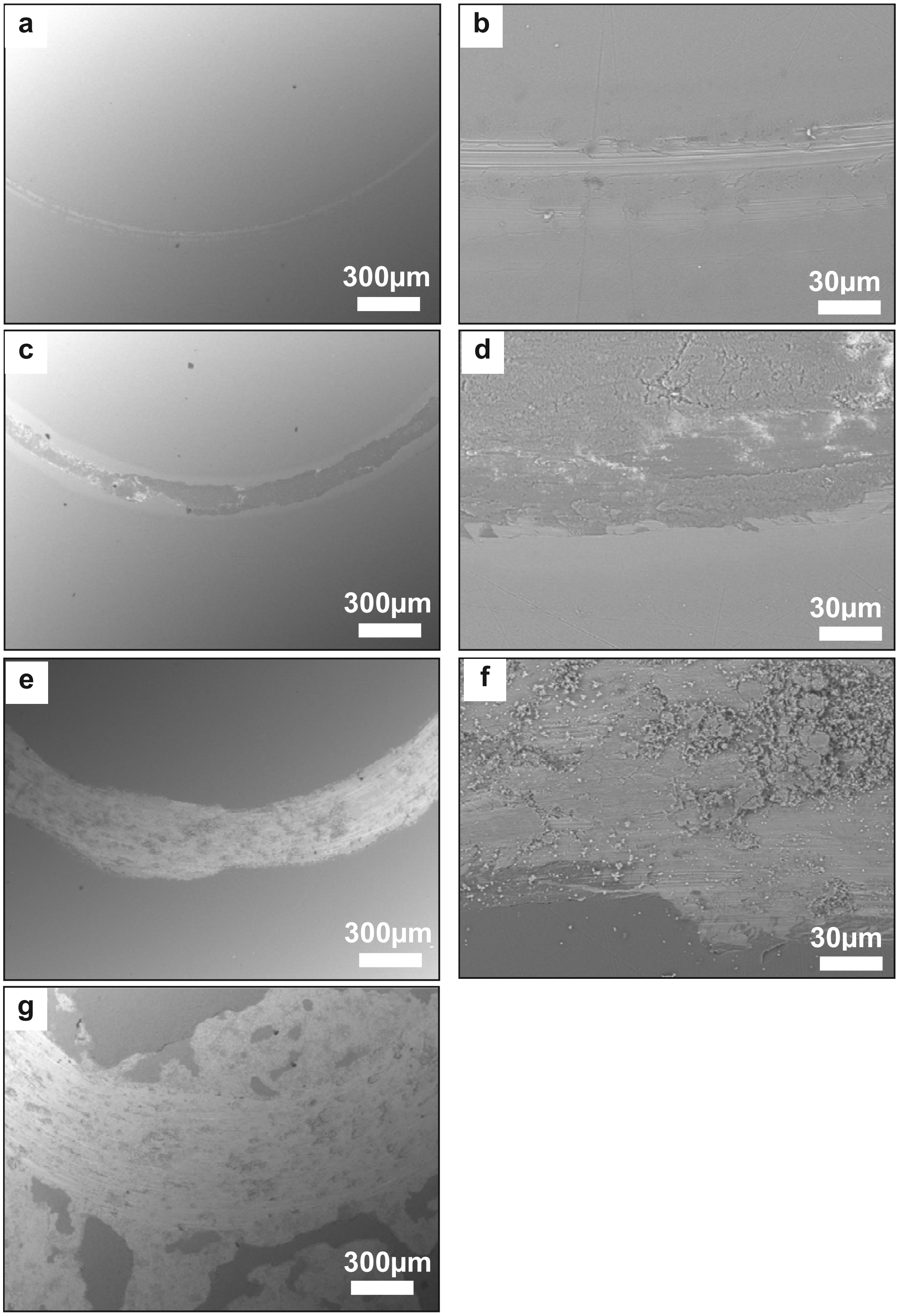

Fig. 4.9 SEM micrographs of wear tracks of (a, b) T0, (c, d) T500, (e, f) T700 and (g) T800 after the dry sliding tests against ceramic Al_2O_3 balls. (b, d, f) are the corresponding magnified images of (a, c, e).

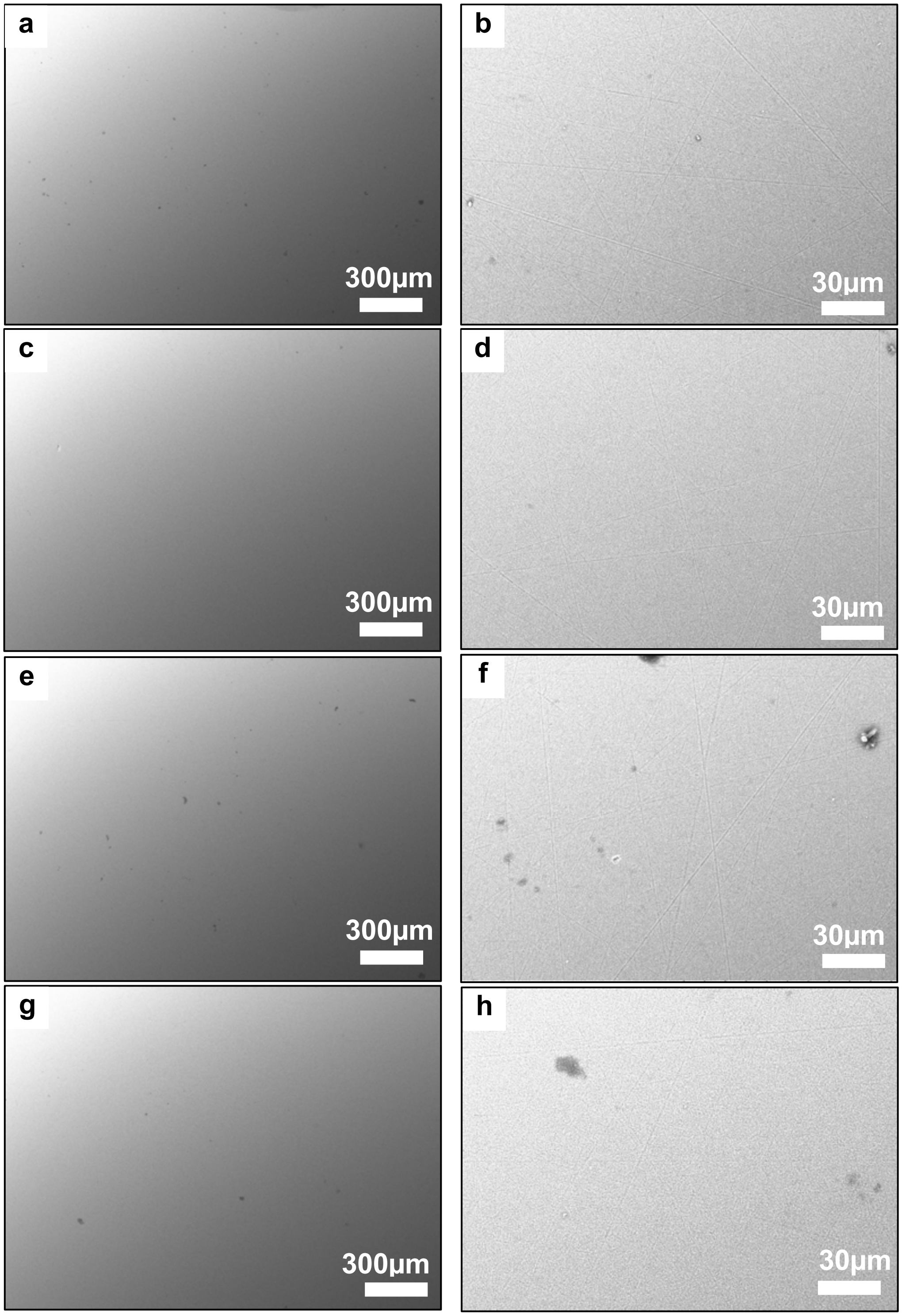

Fig. 4.10 SEM micrographs of wear tracks of (a, b) C0, (c, d) C500, (e, f) C700 and (g, h) C800 after the dry sliding tests against ceramic Al_2O_3 balls. (b, d, f, h) are the corresponding magnified images of (a, c, e, g).

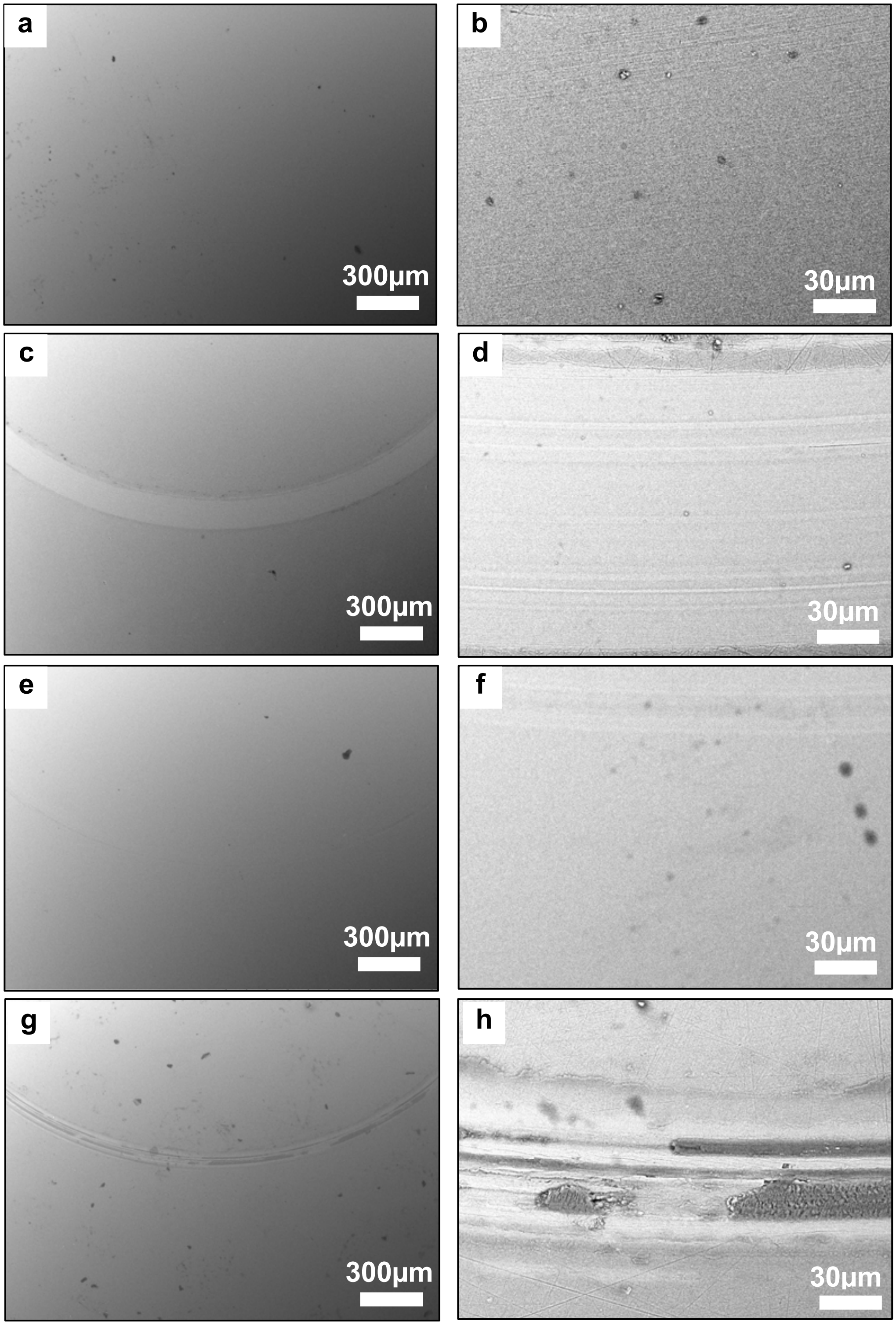

Fig. 4.11 SEM micrographs of wear tracks of (a, b) TA0, (c, d) TA500, (e, f) TA700 and (g, h) TA800 after the dry sliding tests against ceramic Al_2O_3 balls. (b, d, f, h) are the corresponding magnified images of (a, c, e, g).

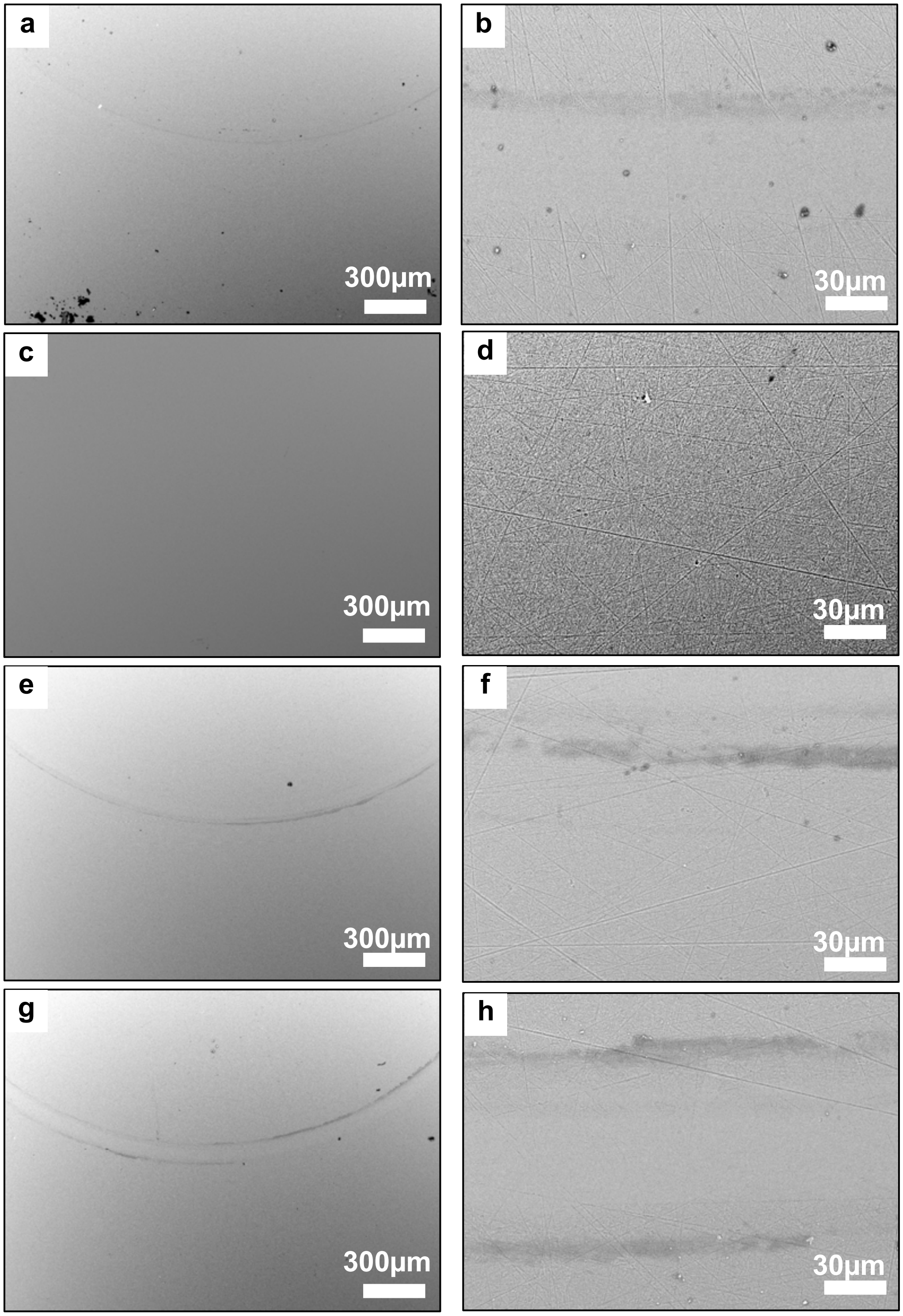

Fig. 4.12 SEM micrographs of wear tracks of (a, b) CA0, (c, d) CA500, (e, f) CA700 and (g, h) CA800 after the dry sliding tests against ceramic Al_2O_3 balls. (b, d, f, h) are the corresponding magnified images of (a, c, e, g).

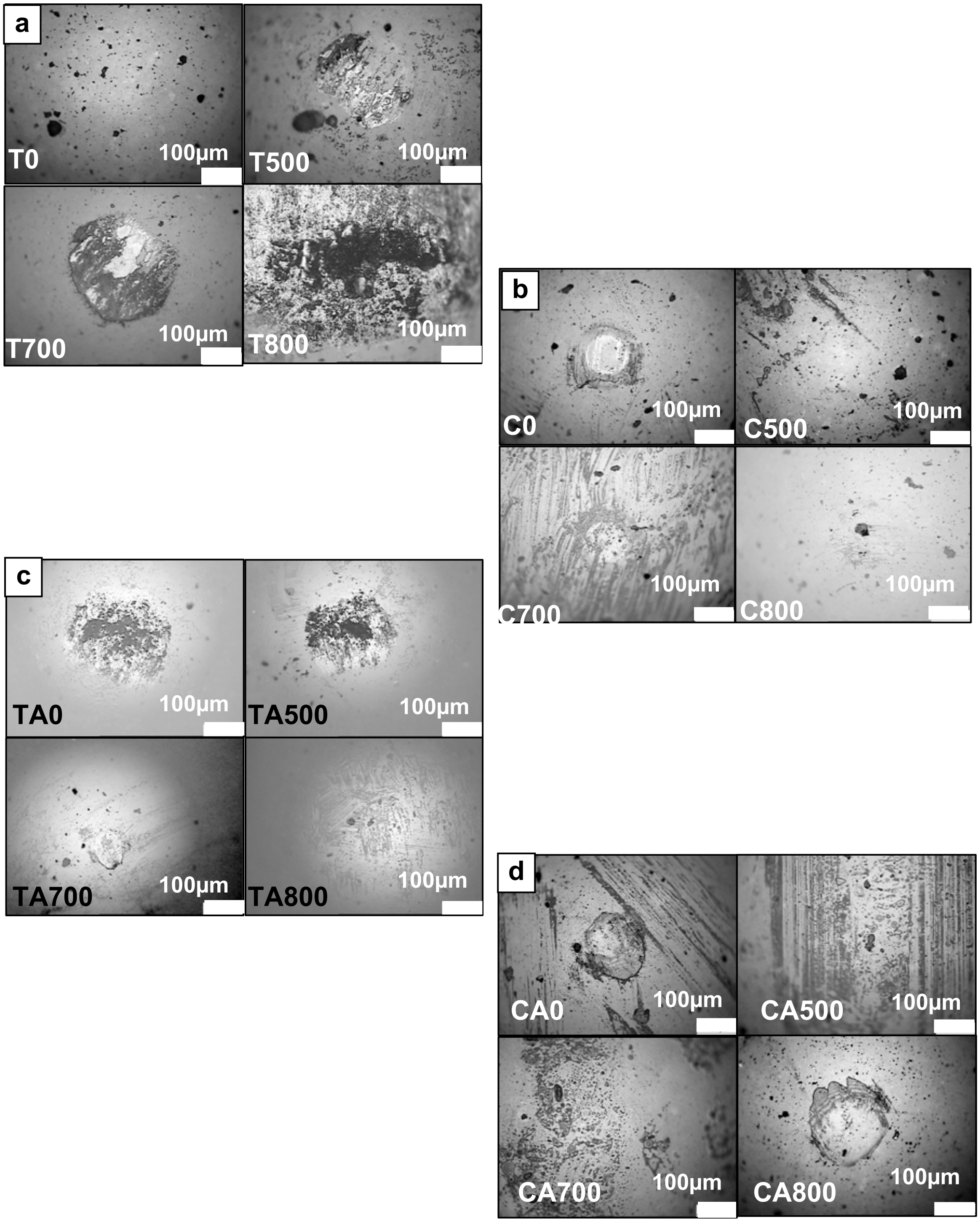

Fig. 4.13 SEM micrographs of counterface Al_2O_3 balls after dry sliding wear tests against original and annealed coatings (a) TiN, (b) CrN, (c) TiAlN and (d) CrAlN at various annealing temperatures.

4.1.3.2 Wear behaviors of coatings against steel balls

Fig. 4.14 shows the curves of coefficient of friction (cof) of original and annealed TiN, CrN, TiAlN and CrAlN coatings during the dry sliding tests against steel balls under 1 N normal load. Fig. 4.14(a) shows the average cofs of original and annealed TiN coatings against steel counterface balls. The cof is about 0.95 for original TiN coating (T0) and first increases to about 1.1 for T500 coating then decreases to about 0.95 for T700 coating. The surface morphology of wear tracks of TiN coatings after dry sliding tests against steel balls are shown on the SEM micrographs in Fig. 4.15 and the 2 D profiles of cross-sections of wear tracks are shown in Fig. 4.16. On the wear track of T0 (Figs. 4.15(a, b)), coating wear is minimum and some materials transferred from steel balls and attached on the coating surface can be observed (Figs. 4.15(b) and 4.16(a)). For T500 coating, both abrasive and adhesive wear occur (Figs. 4.15(c, d)) and from the 2D profile of the wear track cross-section (Fig. 4.16(b)), at the deepest spot, the coating has been penetrated. After sliding tests on T700 coating, at the central wear track, the coating is worn out which can be detected from SEM micrographs (Figs. 4.15(e, f)) and the profile of wear track cross-section (Fig. 4.16(c)). Since there is large sized coating peeling on the T800 coating, the sliding actually occurs between the M2 substrate and steel counterface ball. A large amount of adhesive wear and even seizure have occurred during the sliding test, which can be observed in the SEM micrographs of wear tracks in Figs. 4.15(g, h). Thus, the cof curve of T800 fluctuates in a large range of ±0.3 (Fig. 4.14(a)). Fig. 4.23 shows the optical micrographs of counterface steel ball after the sliding tests against various coatings. Fig. 4.23(a) shows the steel balls after the sliding tests against various TiN coatings. The ball wear loss increases from against T0 to T800 coatings.

Fig. 4.14(b) shows curves of cof during the dry sliding tests against steel balls on CrN coatings, from which it is found that the coatings annealed at various temperatures have similar cof values, 0.85-0.9. The SEM micrographs of wear tracks on CrN coatings against steel balls (Fig. 4.17) illustrate that a large amount of material has transferred and stuck on the surfaces of CrN coatings. The transferred steel material from steel counterface balls covers on the wear tracks and forms a dense transferred material layer. After certain testing time, the sliding activity becomes the steel balls against the steel transferring layer, which can explain the similar cofs of various CrN coatings. The attached material would aggravate the adhesive wear since the transferred material and steel ball could weld together and tear away again and again during the sliding tests. Compared with TiN coatings, CrN coatings have higher hardness and less coating damages after annealing processes, therefore, after sliding tests, less coating wear occurs. From the profiles of wear track cross-sections (Fig. 4.18), the deepest wear spots occurred on C800 is about 0.5 μm. Fig. 4.23 (b) shows that the wear loss of steel balls is similar and for the steel balls against C500, C700 and C800, the wear loss is less than those against the corresponding TiN coatings.

Fig. 4.14(c) shows that the curves of cofs of original and annealed TiAlN coatings are with ups and downs of ±0.5 around the average. The average cof value of TA0 is about 0.8 and similar value of 0.7 for TA500, TA700 and TA800, respectively. The SEM micrographs (Fig 4.19) show that on the four TiAlN coating wear tracks, a large amount of material transferring has occurred. By comparing the profiles of wear track cross-sections, it is found that on TA0 coating (Fig. 4.20 (a)), detached material from steel ball was picked up and formed transferred layer on TA0 coating surface. On the annealed coatings, coating wear begins to occur. The wear track profiles, Figs. 4.20 (b, c, d), show that the coating wear increases with increasing annealing temperature. From the wear track profiles, the deepest spots in the wear tracks of TA500, TA700 and TA800 are 0.8, 1.0 and >2.0 μm, respectively. The counterface steel balls against TiAlN coatings (Fig. 4.23(c)) are worn and the wear loss is similar among those against various TiAlN coatings but higher than those against TiN and CrN coatings in Fig. 4.23 (b).

Fig. 4.21 and Fig. 4.22 show the SEM micrographs and 2D profiles of wear tracks of CrAlN coatings annealed at various temperatures after dry sliding tests against steel balls. On the CA0 coating, some material transferring has occurred. The attached wear debris on the wear track is scattered and does not form continuous transferred layer (Figs. 4.21 (b) and 4. 22(a)) and the cof during the sliding test against steel is about 0.9 (Fig. 14(d)). However, on CA500 and CA700 coatings, there is a continuous transferred layer on the wear track (Figs. 4.21(c, d) and 4.21(e, f)). Meanwhile, the cofs fluctuate severely within ±0.5 (Fig. 4.14(d)) with repeatedly stick-slip behaviors between the steel ball and the transferred layer and the average cof is about 0.75. However, on the CA800 coating (Figs. 4.21(g, h)), the material transferring becomes less than that on CA500 and CA700 (Figs. 4.22(b, c)). From cof curves (Fig. 4.14(d)), the wear behavior and average cof of CA800 are similar to that of CA0. The rank of steel ball wear loss is consistent with the amounts of material transferred to the coatings, i.e., the steel balls against CA0 and CA800 coatings have much less wear loss than those against CA500 and CA700. That indicates that the balls were worn and the released material was picked up by CrAlN coatings and formed a transferred layer. CA0 and CA800 coatings have a better anti-sticking performance than other CrAlN coatings. The less material transferring on CA800 coating could result from the Al_2O_3 layer formation which decreased the shear stress between the coating and steel ball and therefore decreased the adhesion between the counterfaces.

4.1.3.3 Wear behaviors of coatings against aluminium balls

Fig. 4.24 shows the curves of coefficient of friction (cof) of original and annealed TiN, CrN, TiAlN and CrAlN coatings during the dry sliding tests against Al balls under a 1 N normal load. Fig.4.24 (a) shows the cofs of original and annealed TiN coatings against Al counterface balls. The cof is about 0.55 for all the coatings. The SEM micrographs (Fig. 4.25) and 2D profiles (Fig. 4.26) of wear tracks of various TiN coatings against Al balls indicate that on the TiN coatings T0, T500 and T700, after sliding tests, severe material transfer and coating wear have occurred. It is believed that adhesive wear is the dominated wear mechanisms. Since the coating wear and transferred material have piled up in the wear tracks and it is difficult to quantify the wear rate.

Fig. 4.24 (b) shows the average cofs of various CrN coatings during the sliding tests against Al balls. The average cof values of the CrN coatings C0, C500, C700 and C800 are 0.55, 0.55, 0.5 and 0.6, respectively. The SEM micrographs (Fig. 4.27) and 2D profiles (Fig. 4.28) of wear tracks of various CrN coatings against Al balls indicate that on the CrN coatings C0, C500, C700 and C800, after sliding tests, severe material transfer and coating wear have occurred.

Figs. 4.24 (c, d) shows the average cofs of various TiAlN and CrAlN coatings during the sliding tests against Al balls, respectively. The various TiAlN coatings have a similar average cof value of 0.55. For CrAlN coatings, the CA0 coating has an average cof about 0.45 and CA500, CA700 and CA800 coatings have a similar cof value about 0.55. The SEM micrographs and 2D profiles of wear tracks of TiAlN (Figs. 4.29 and 4.30) and CrAlN (Figs. 4.31 and 4.32) coatings after sliding tests against Al balls show that TiAlN and CrAlN coatings do not significantly improve the ability of anti-sticking of Al , even the coatings were prepared by introducing Al into the TiN and CrN crystalline structures. Severe material transferring and adhesive wear have occurred on the TiAlN and CrAlN coatings. With the increase of annealing temperature, the coating hardness decreases and some coating structures degrade due to the annealing process and thus the adhesive wear resistance of TiAlN and CrAlN coating becomes worse. Fig. 4.33 shows the worn Al balls after sliding tests against various coatings. The wear loss of the balls is similar.

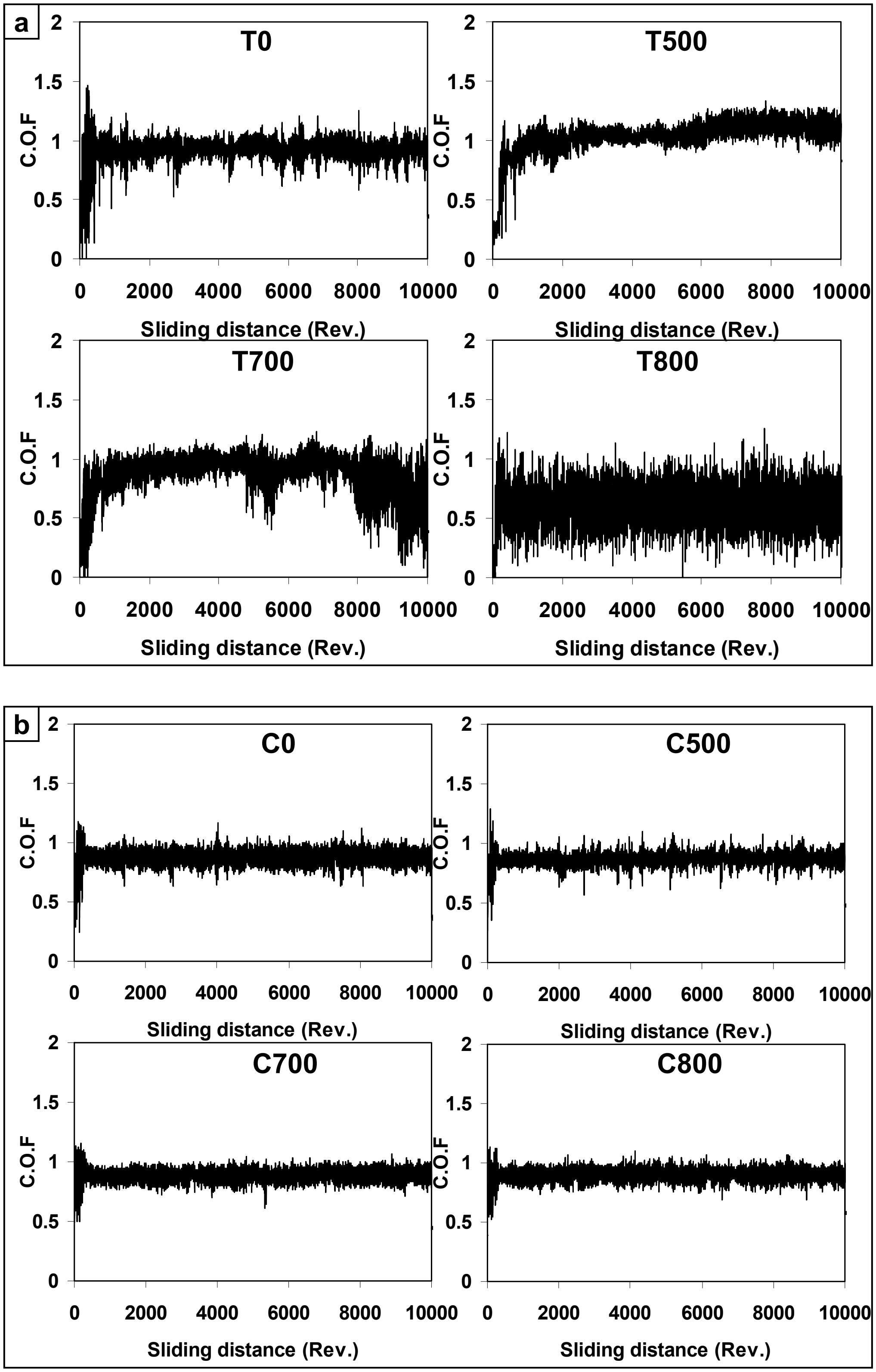
a
b
T0
T500
T700
T800
C0
C500
C700
C800
C.O.F
0
0.5
1
1.5
2
Sliding distance (Rev.)
0
2000
4000
6000
8000
10000

Fig. 4.14 (a, b)

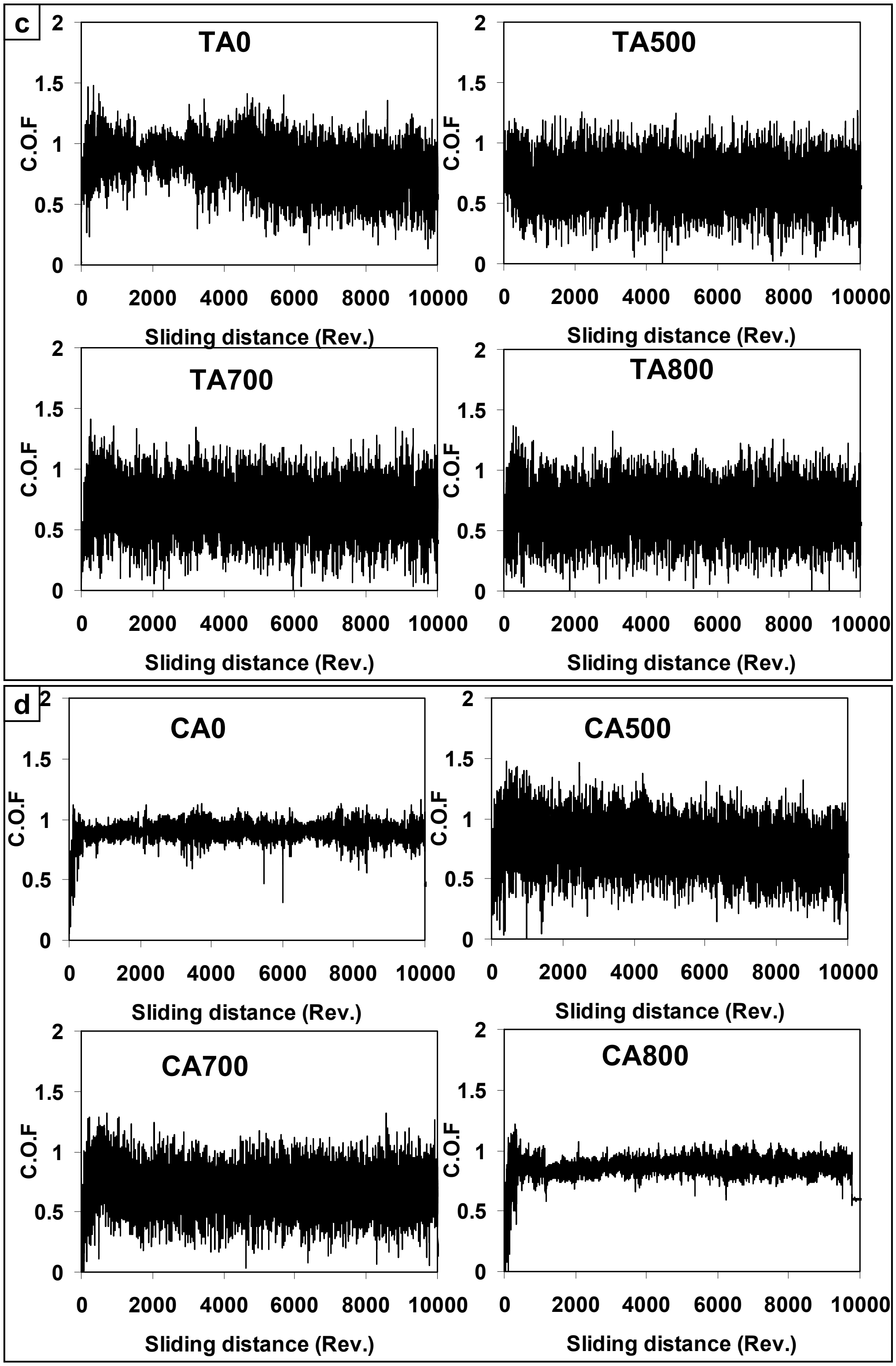

Fig. 4.14 Coefficient of friction (C.O.F.) curves of original and annealed coatings (a) TiN, (b) CrN, (c) TiAlN and (d) CrAlN during the dry sliding tests against steel balls.

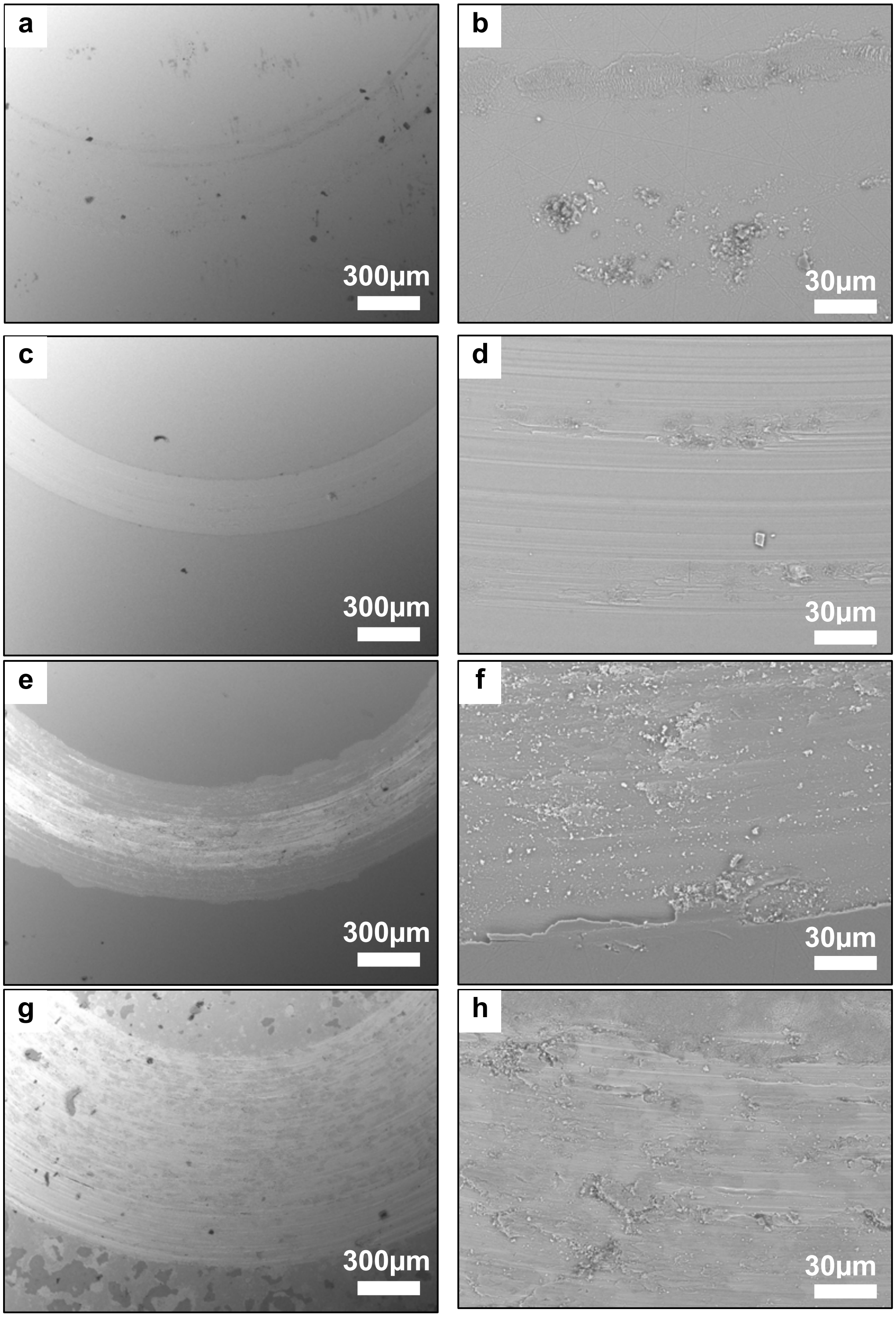

Fig. 4.15 SEM micrographs of wear tracks of (a, b) T0, (c, d) T500, (e, f) T700 and (g, h) T800 after the dry sliding tests against steel balls. (b, d, f, h) are the corresponding magnified images of (a, c, e, g).

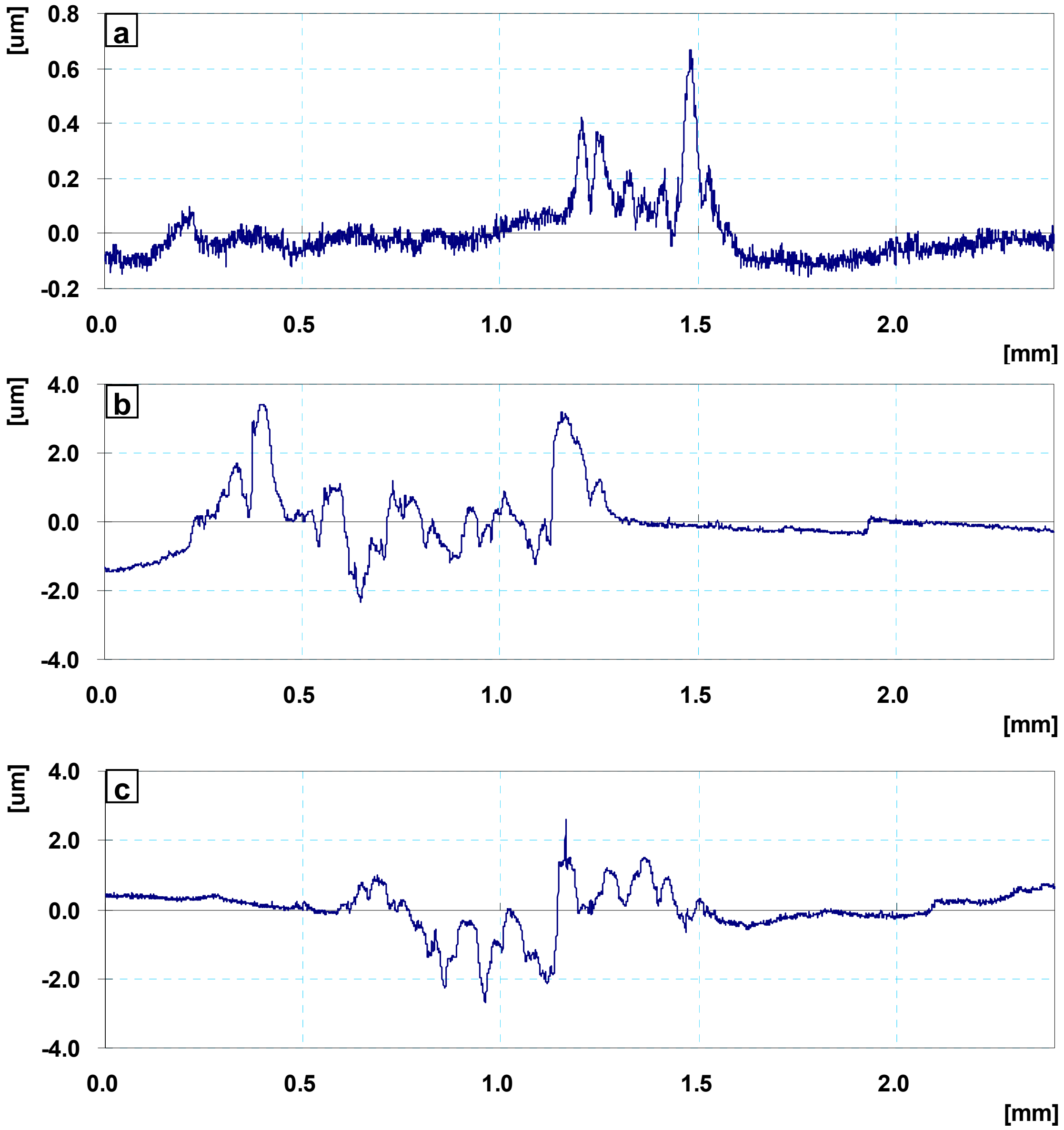

Fig. 4.16 2D profiles of cross-sections of wear tracks of (a) T0, (b) T500 and (c) T700 coatings after the dry sliding tests against steel balls.

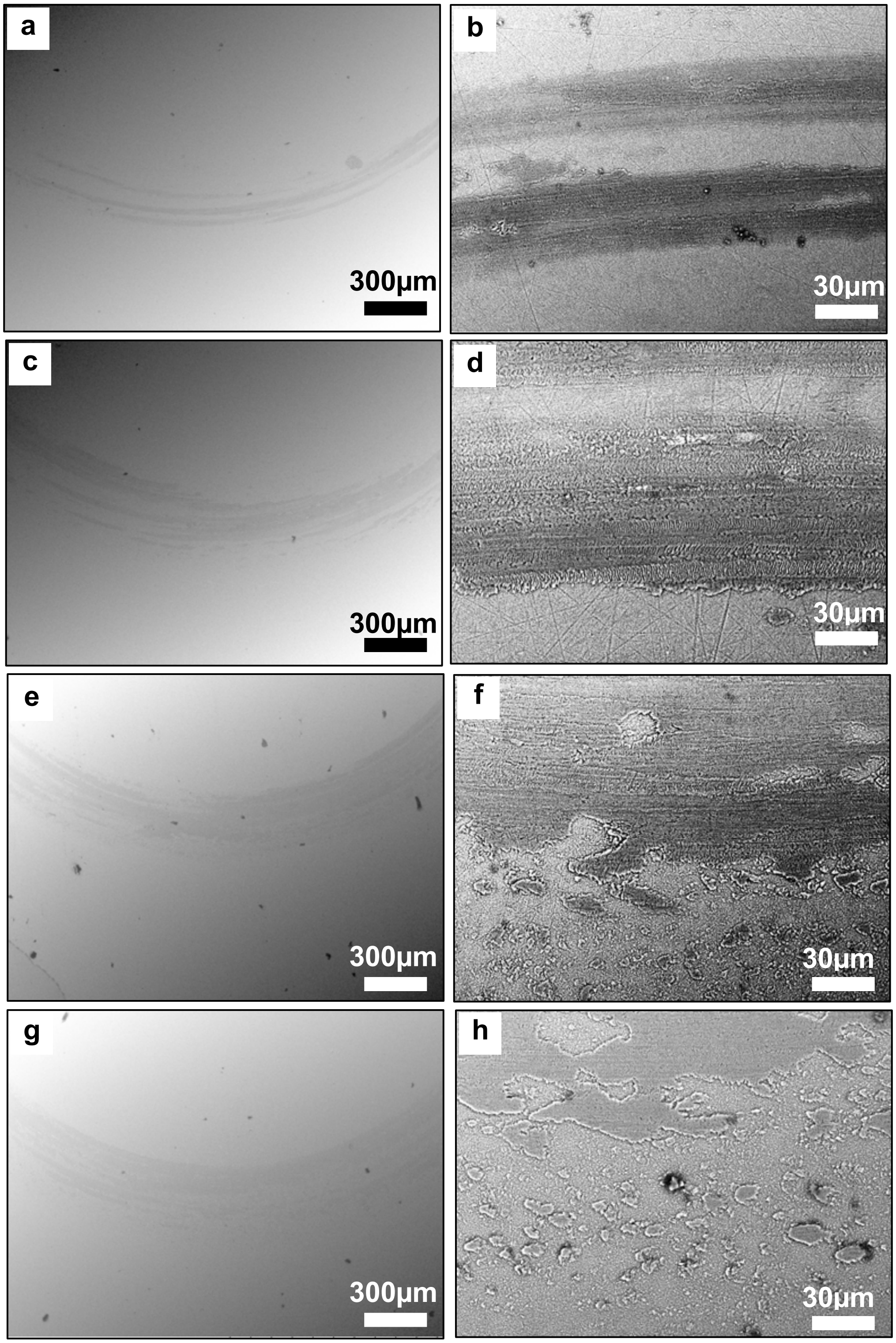

Fig. 4.17 SEM micrographs of wear tracks of (a, b) C0, (c, d) C500, (e, f) C700 and (g, h) C800 after the dry sliding tests against steel balls. (b, d, f, h) are the corresponding magnified images of (a, c, e, g).

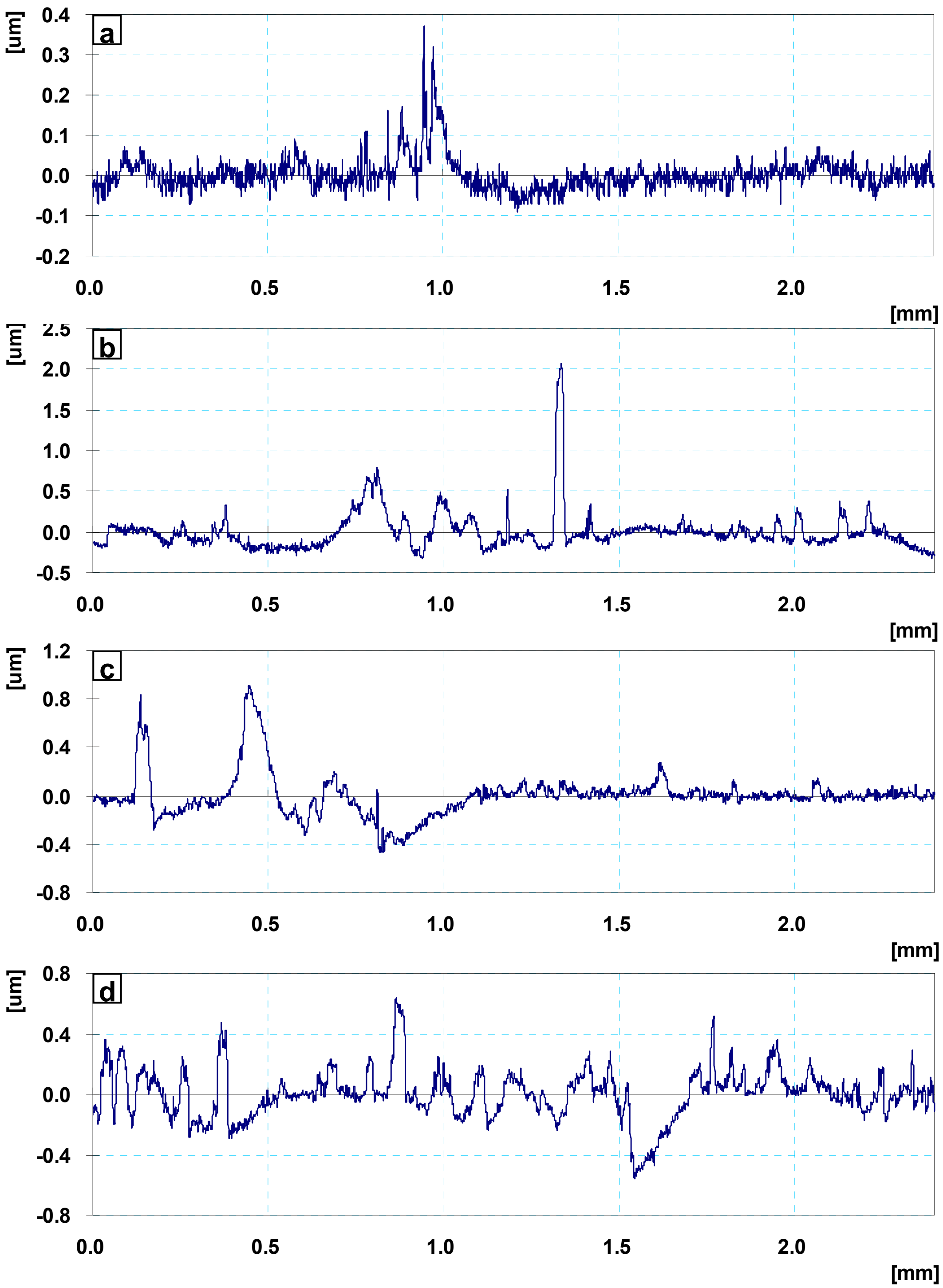

Fig. 4.18 2D profiles of cross-sections of wear tracks of (a) C0, (b) C500, (c) C700 and (d) C800 coatings after the dry sliding tests against steel balls.

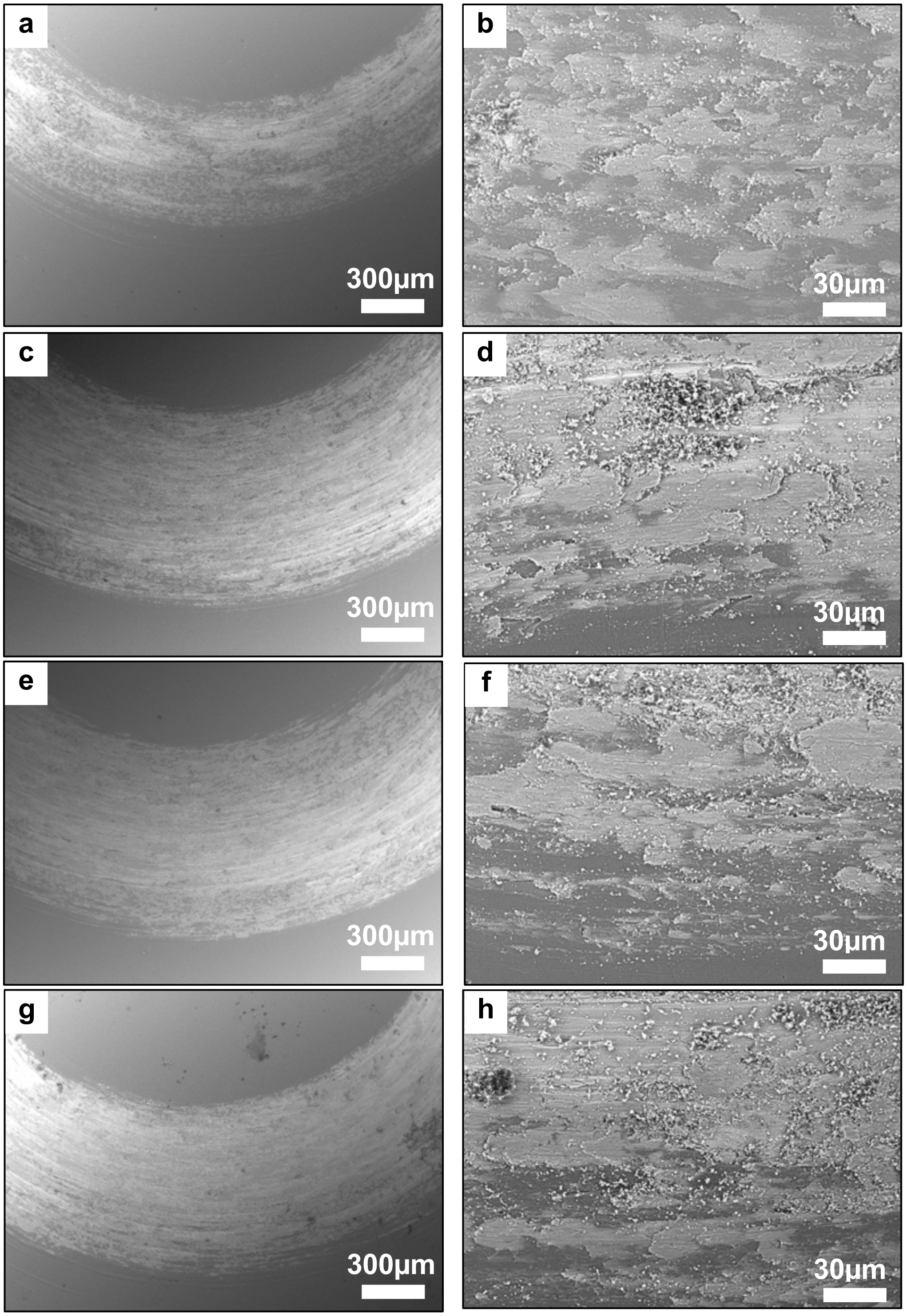

Fig. 4.19 SEM micrographs of wear tracks of (a, b) TA0, (c, d) TA500, (e, f) TA700 and (g, h) TA800 after the dry sliding tests against steel balls. (b, d, f, h) are the corresponding magnified images of (a, c, e, g).

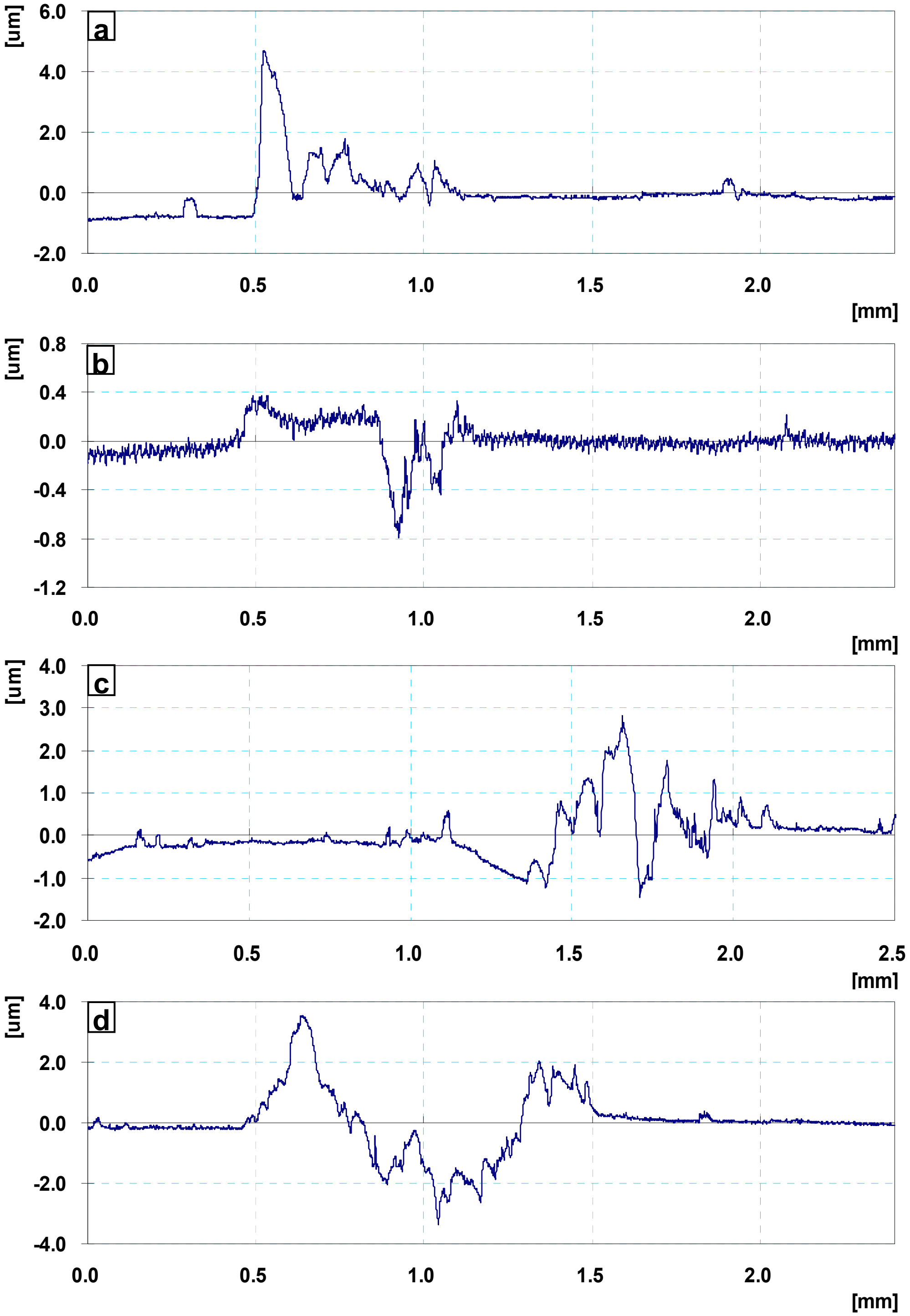

Fig.4.20 2D profiles of cross-sections of wear tracks of (a) TA0, (b) TA500, (c) TA700 and (d) TA800 coatings after the dry sliding tests against steel balls.

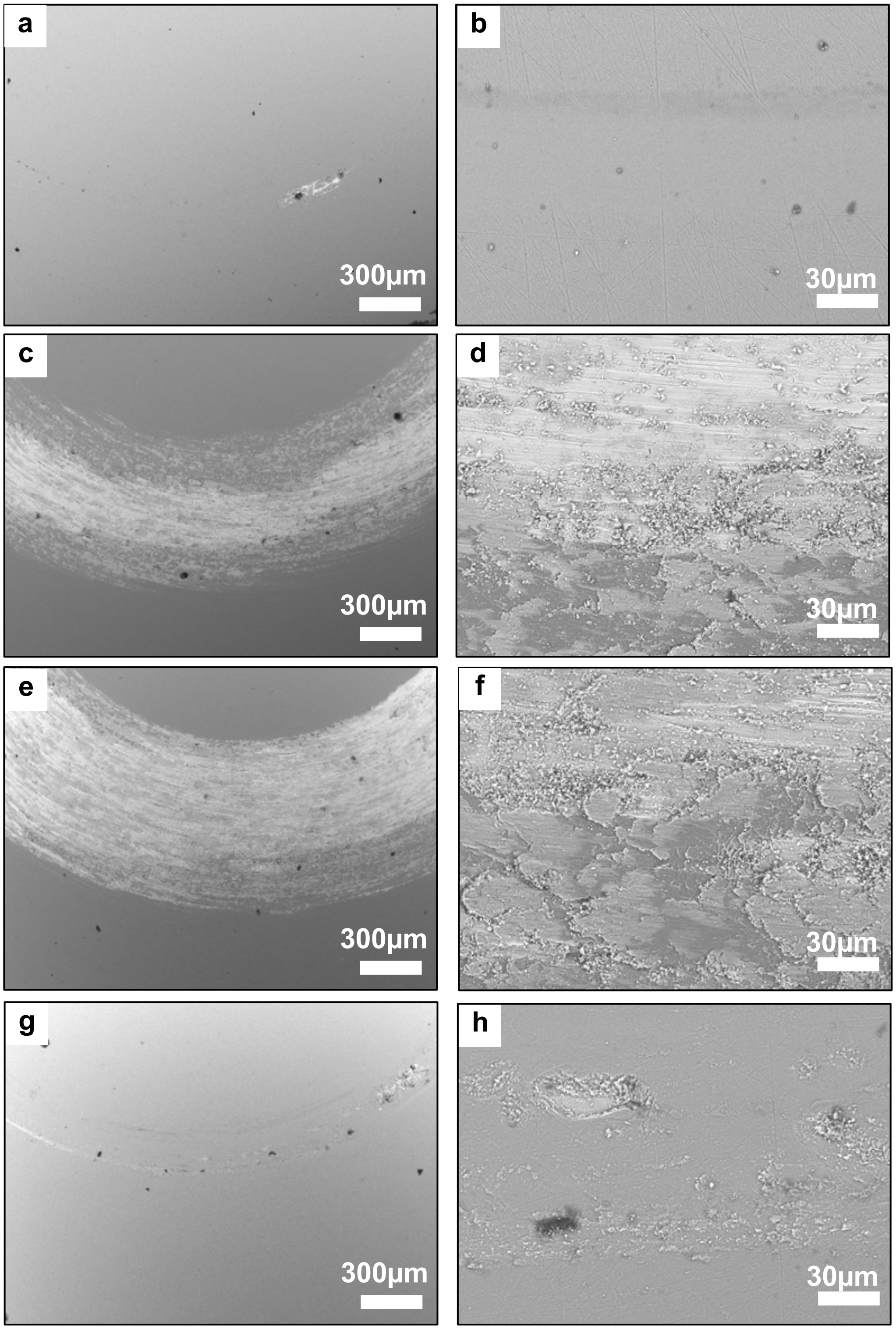

Fig. 4.21 SEM micrographs of wear tracks of (a, b) CA0, (c, d) CA500, (e, f) CA700 and (g, h) CA800 after the dry sliding tests against steel balls. (b, d, f, h) are the corresponding magnified images of (a, c, e, g).

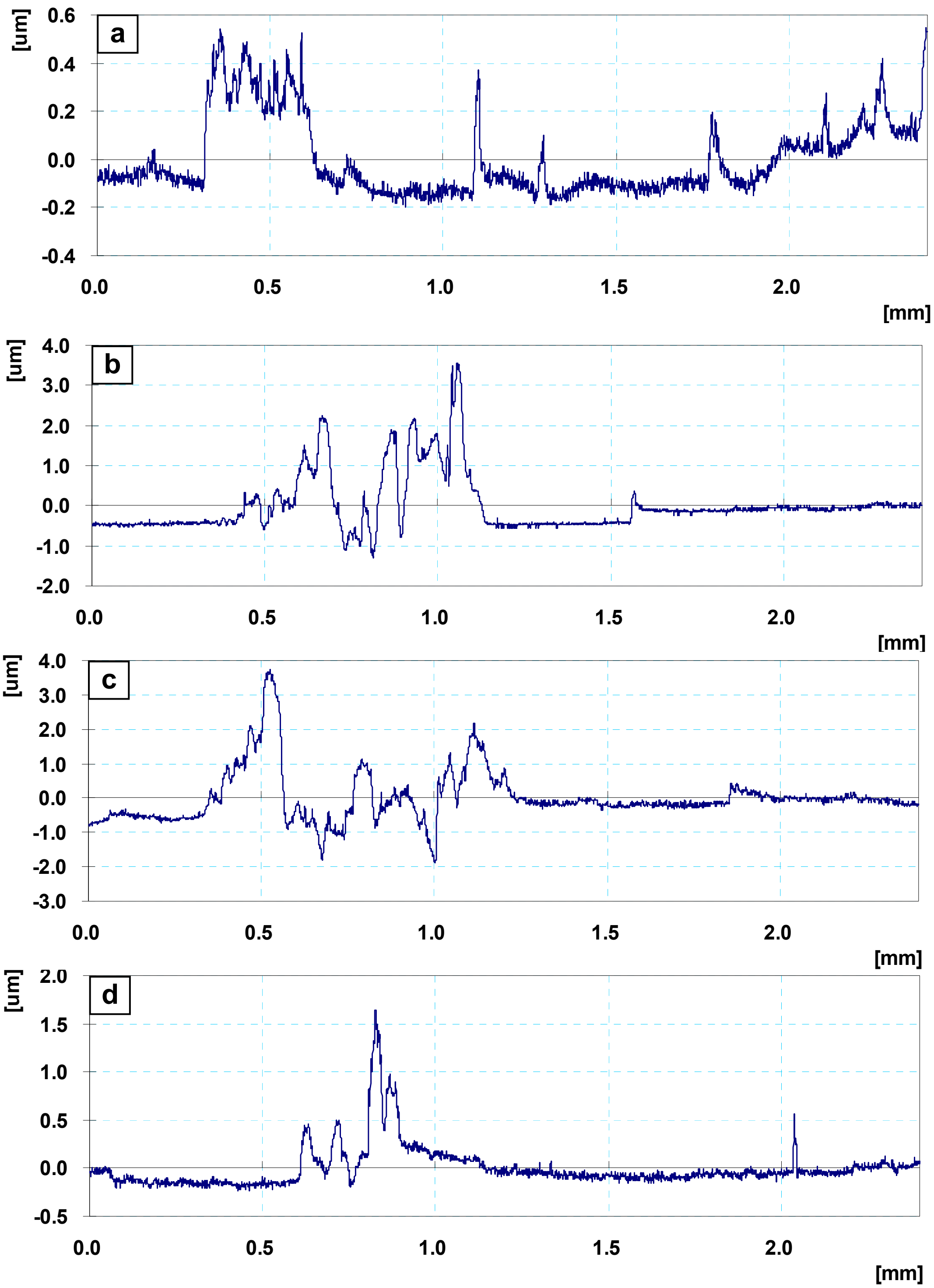

Fig. 4.22 2D profiles of cross-sections of wear tracks of (a) CA0, (b) CA500, (c) CA700 and (d) CA800 coatings after the dry sliding tests against steel balls.

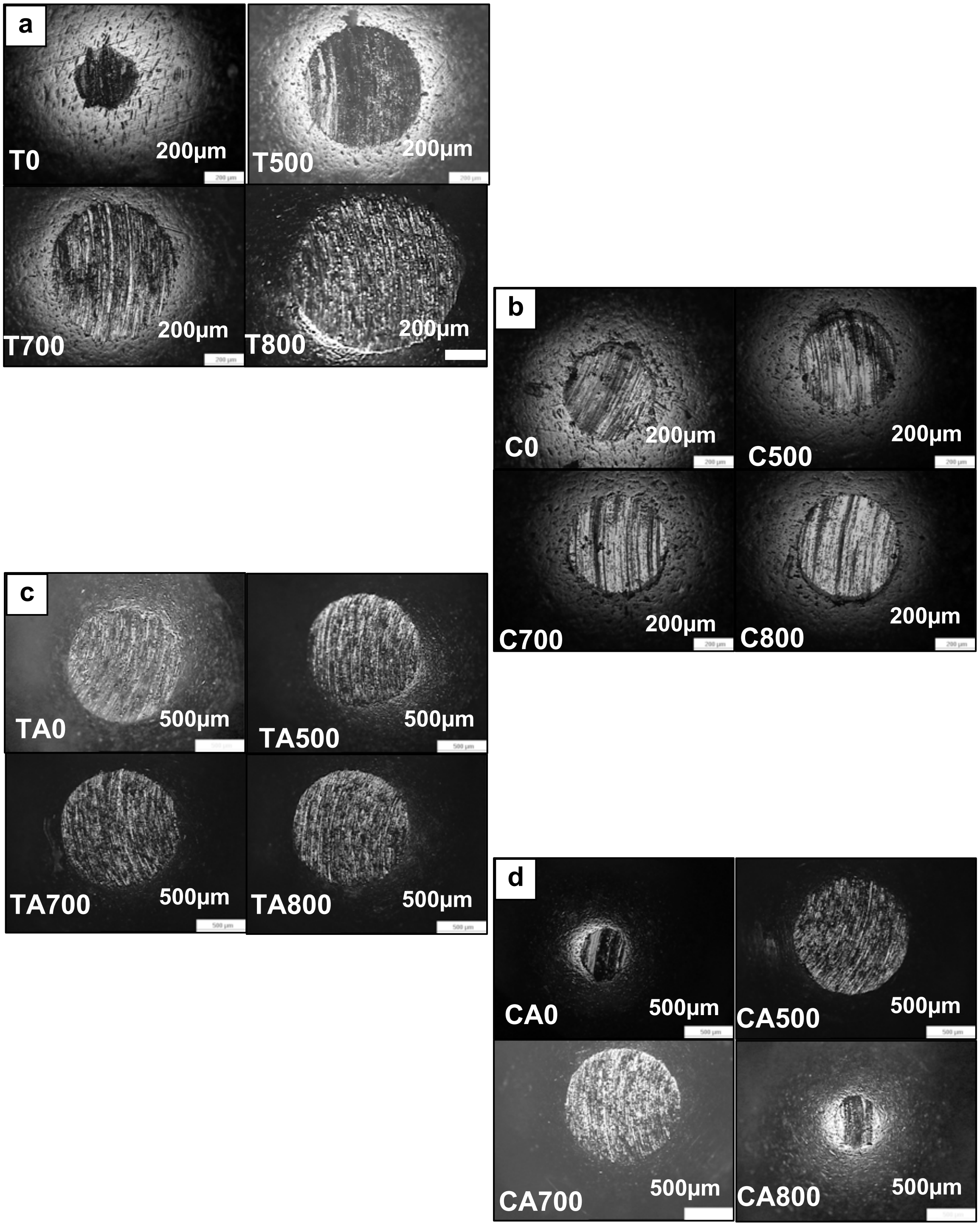

Fig. 4.23 Optical micrographs of counterface steel balls after dry sliding wear tests against original and annealed coatings (a) TiN, (b) CrN, (c) TiAlN and (d) CrAlN at various annealing temperatures.

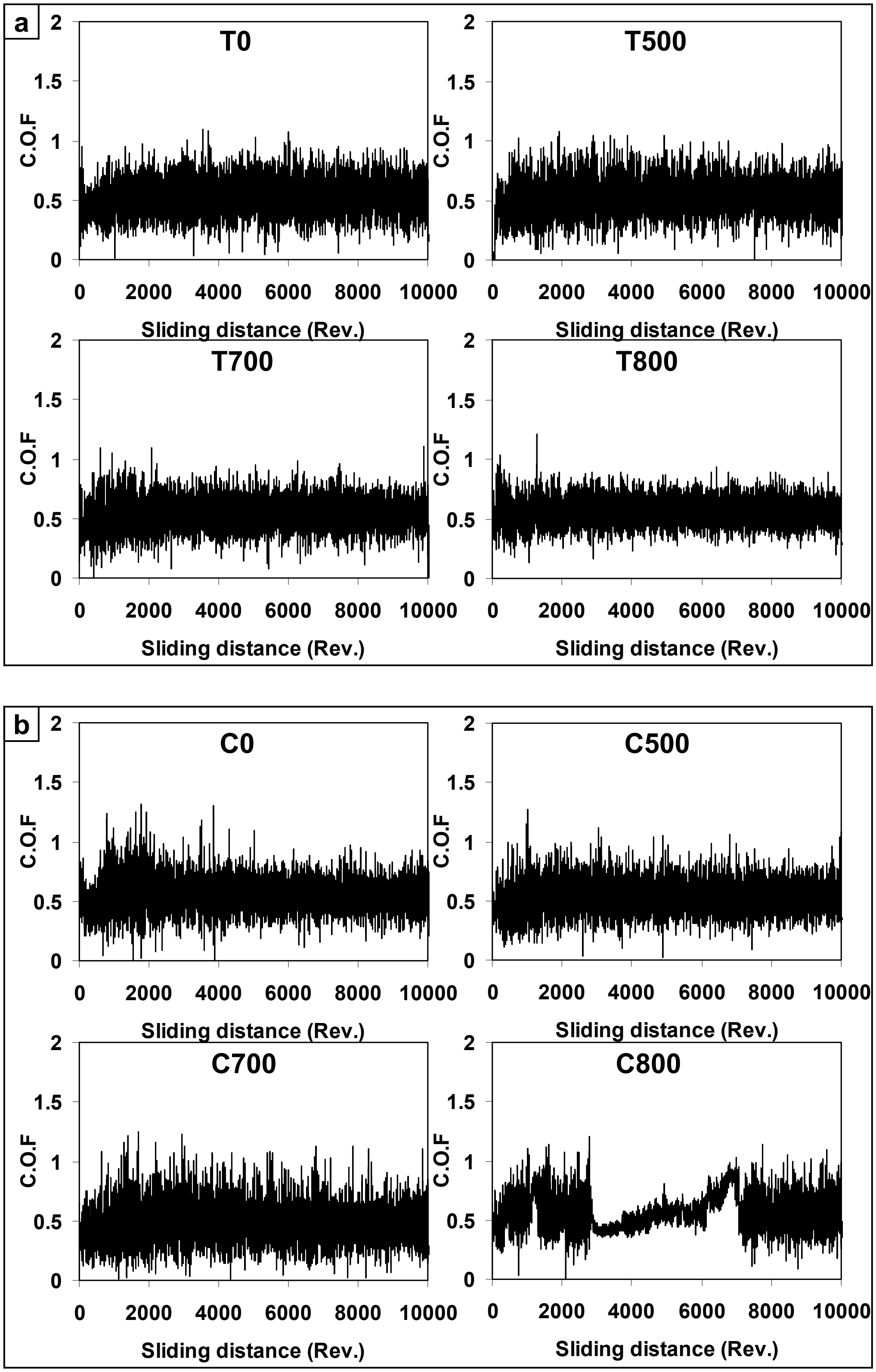
a
T0
T500
T700
T800
b
C0
C500
C700
C800
C.O.F
0
0.5
1
1.5
2
0
2000
4000
6000
8000
10000
Sliding distance (Rev.)

Fig. 4.24(a, b)

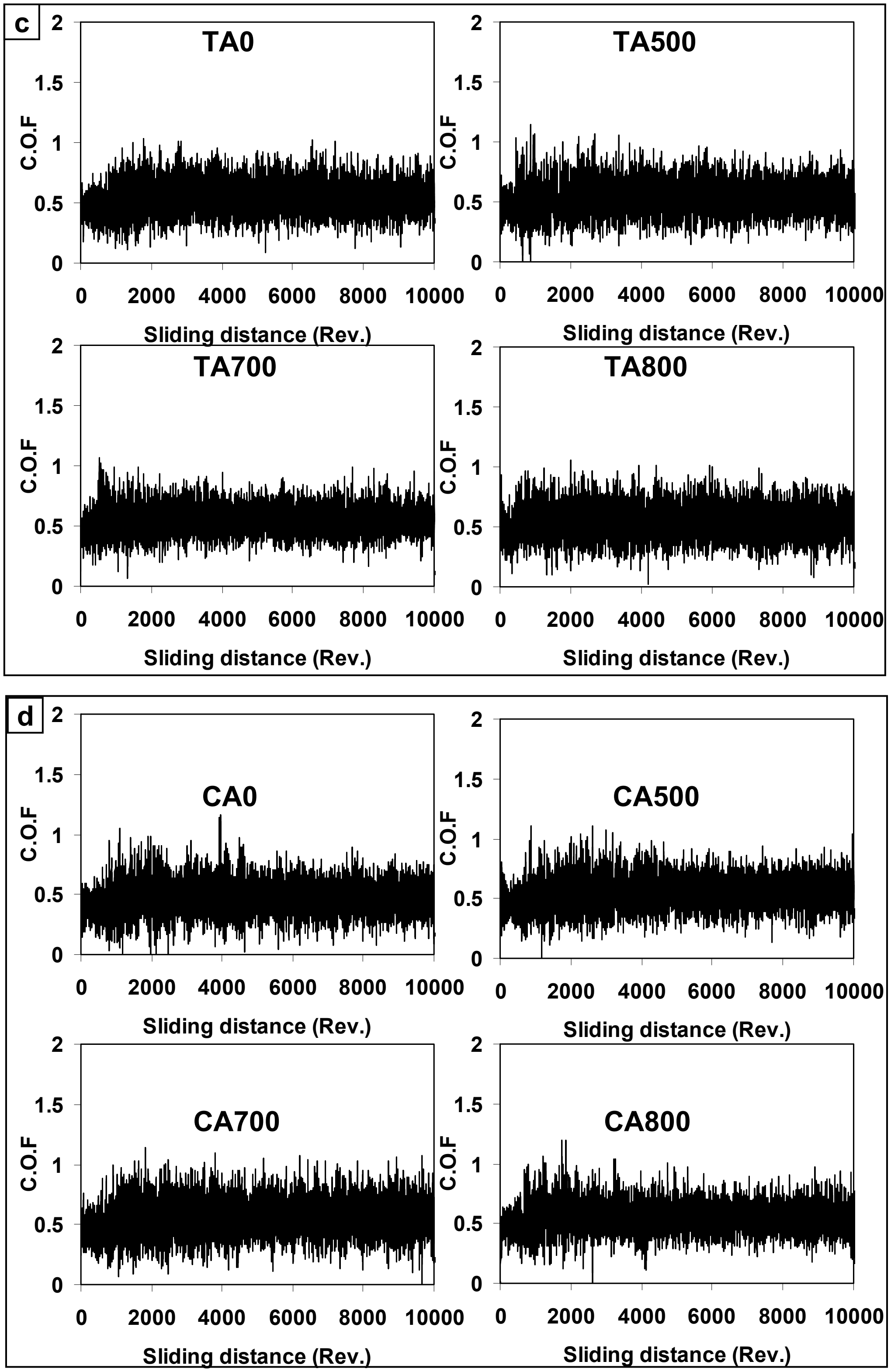

Fig. 4.24 Coefficients of friction curves of original and annealed coatings (a) TiN, (b) CrN, (c) TiAlN and (d) CrAlN after the sliding tests against Al balls.

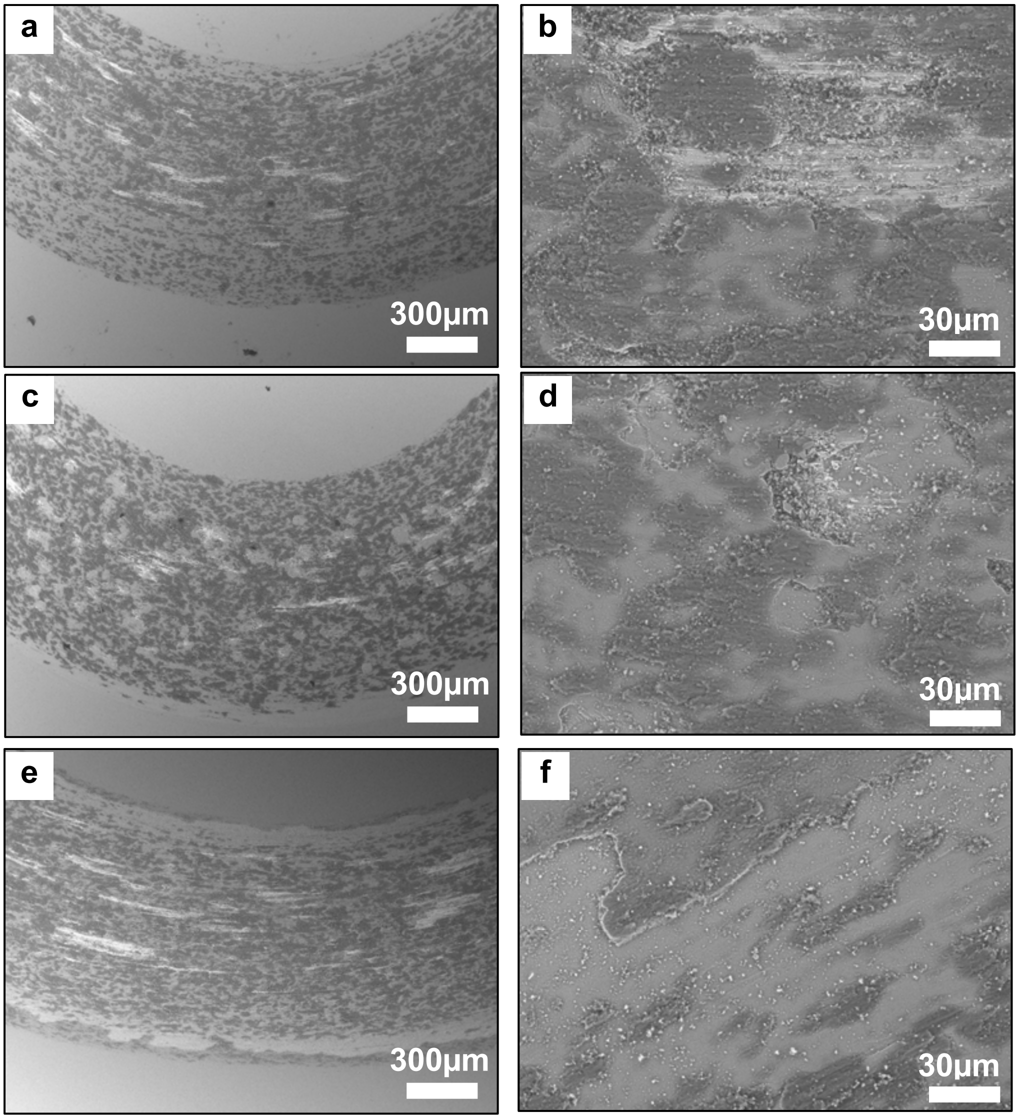

Fig. 4.25 SEM micrographs of wear tracks of (a, b) T0, (c, d) T500 and (e, f) T700 coatings after the dry sliding tests against Al balls. (b, d, f) are the corresponding magnified images of (a, c, e).

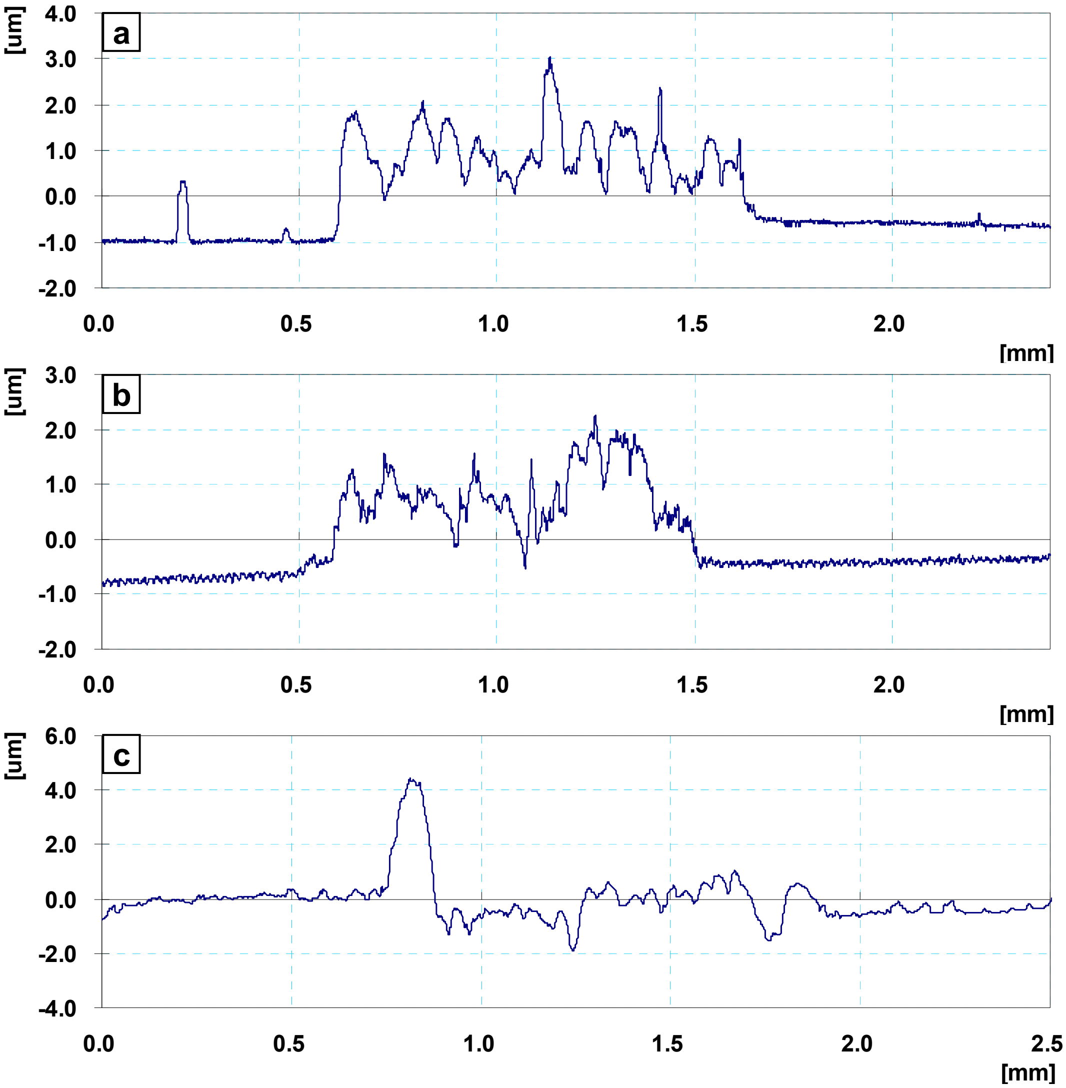

Fig. 4.26 2D profiles of cross-sections of wear tracks of (a) T0, (b) T500 and (c) T700 coatings after the dry sliding tests against Al balls.

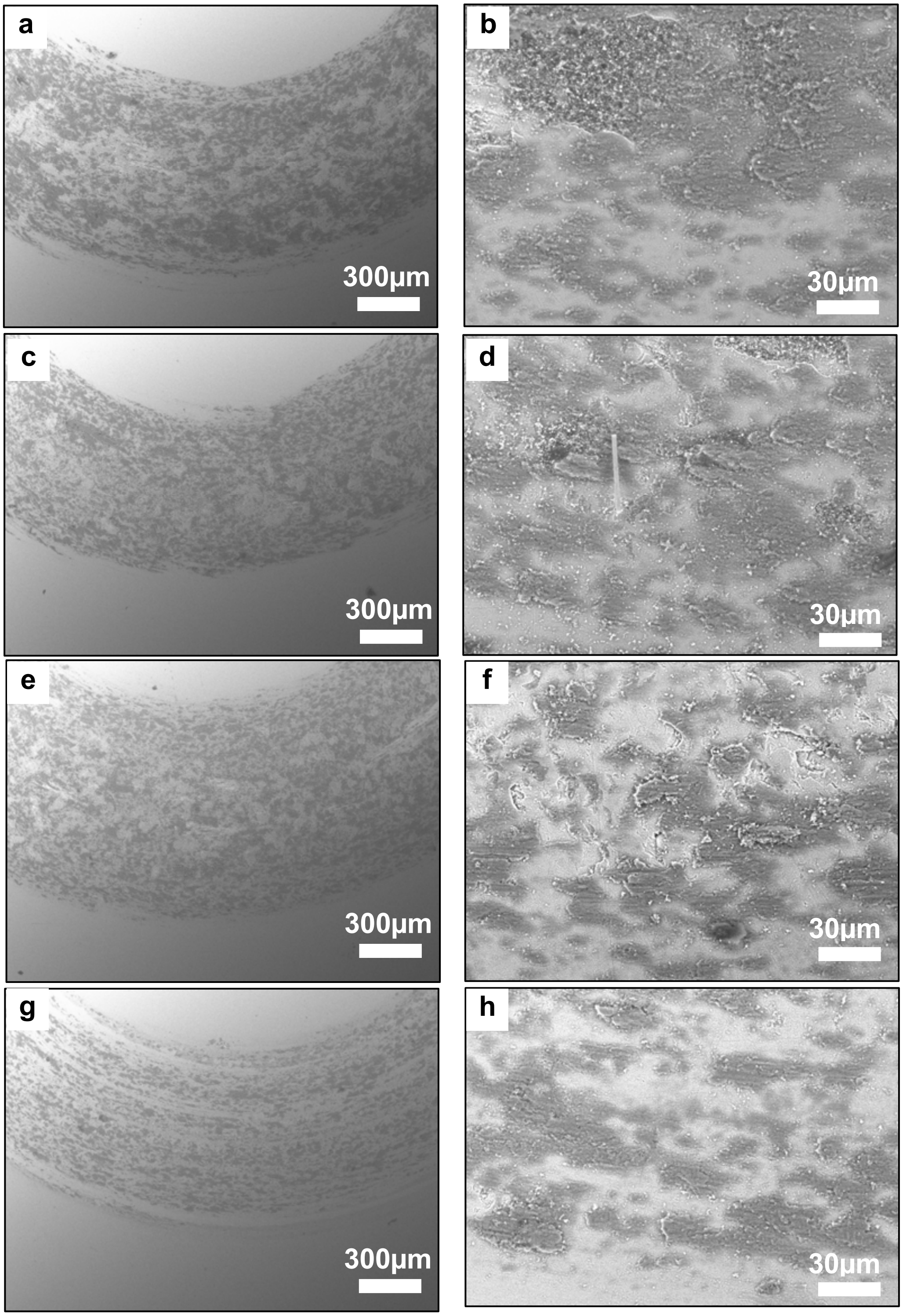

Fig. 4.27 SEM micrographs of wear tracks of (a, b) C0, (c, d) C500, (e, f) C700 and (g, h) C800 coatings after the dry sliding tests against Al balls. (b, d, f, h) are the corresponding magnified images of (a, c, e, g).

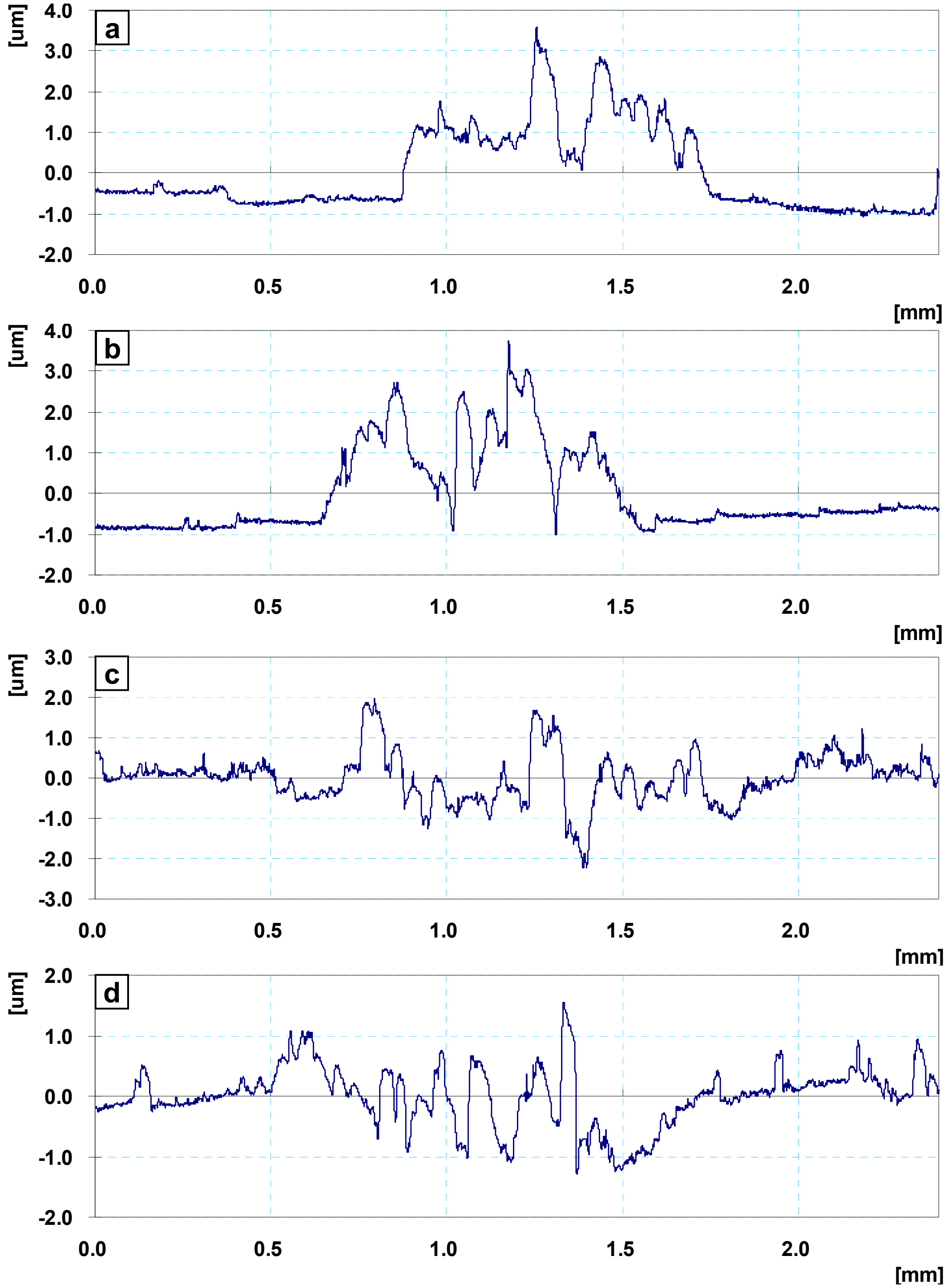

Fig. 4.28 2D profiles of cross-sections of wear tracks of (a) C0, (b) C500, (c) C700 and (d) C800 coatings after the dry sliding tests against Al balls.

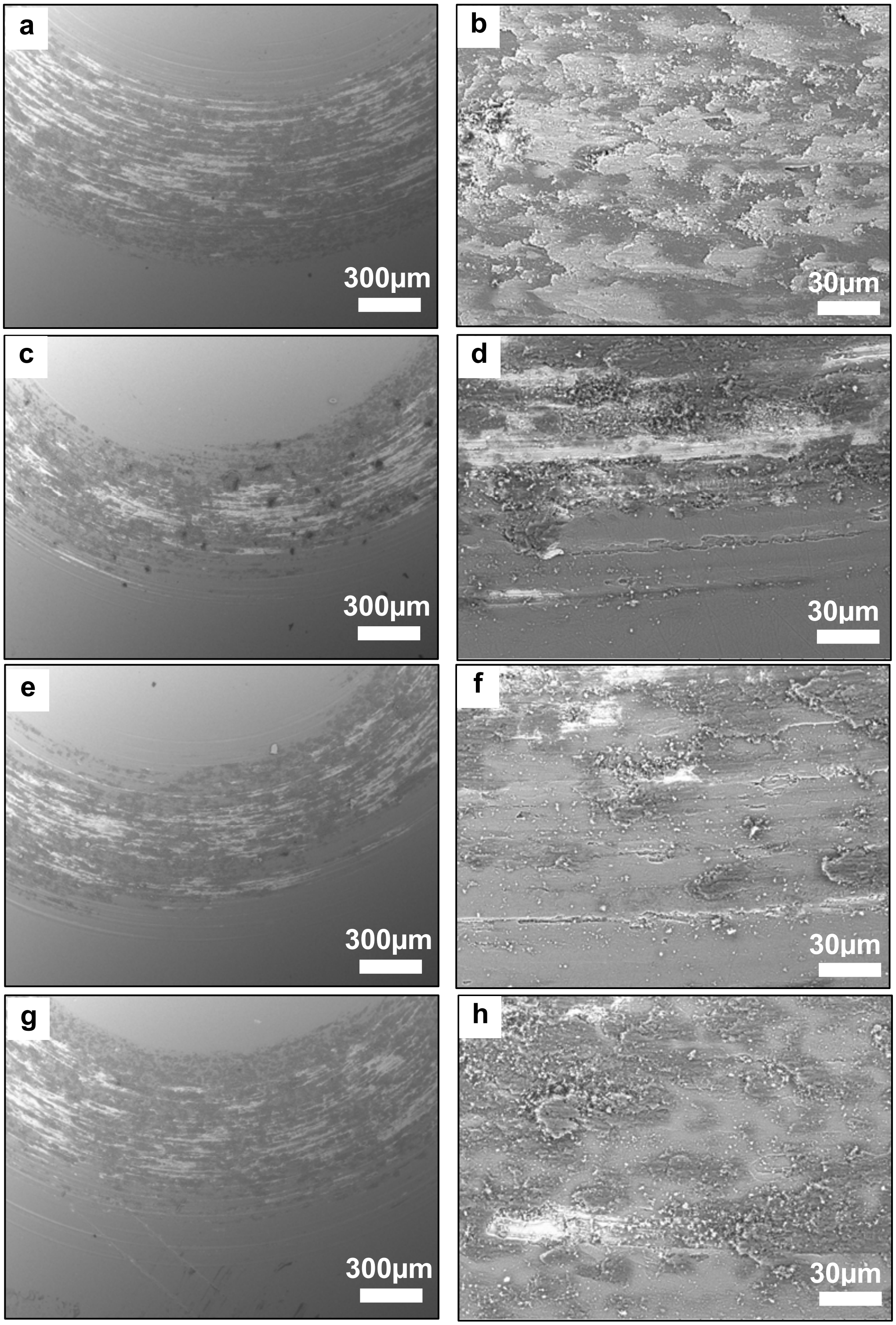

Fig. 4.29 SEM micrographs of wear tracks of (a, b) TA0, (c, d) TA500, (e, f) TA700 and (g, h) TA800 coatings after the dry sliding tests against Al balls. (b, d, f, h) are the corresponding magnified images of (a, c, e, g).

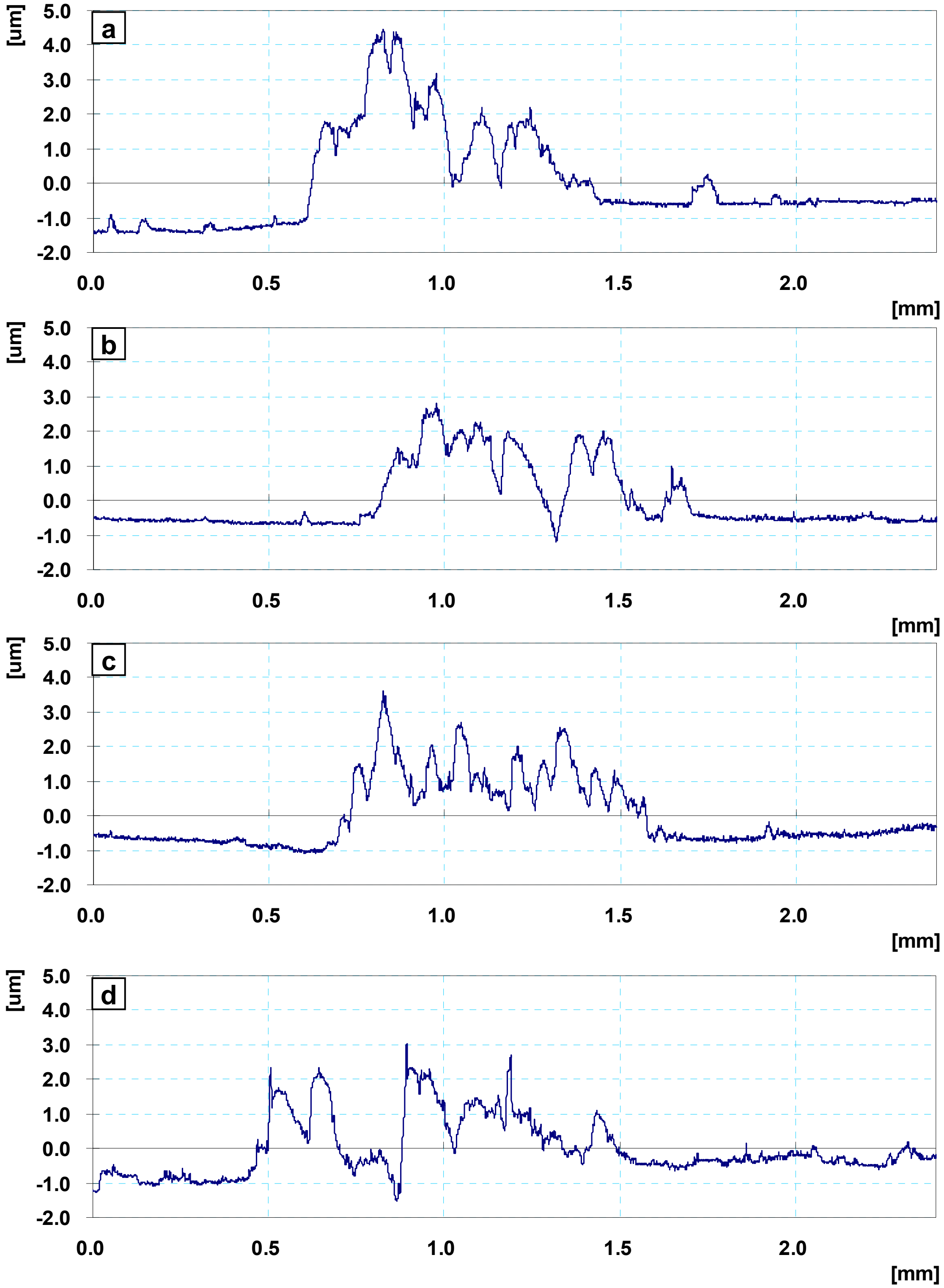

Fig. 4.30 2D profiles of cross-sections of wear tracks of (a) TA0, (b) TA500, (c) TA700 and (d) TA800 coatings after the dry sliding tests against Al balls.

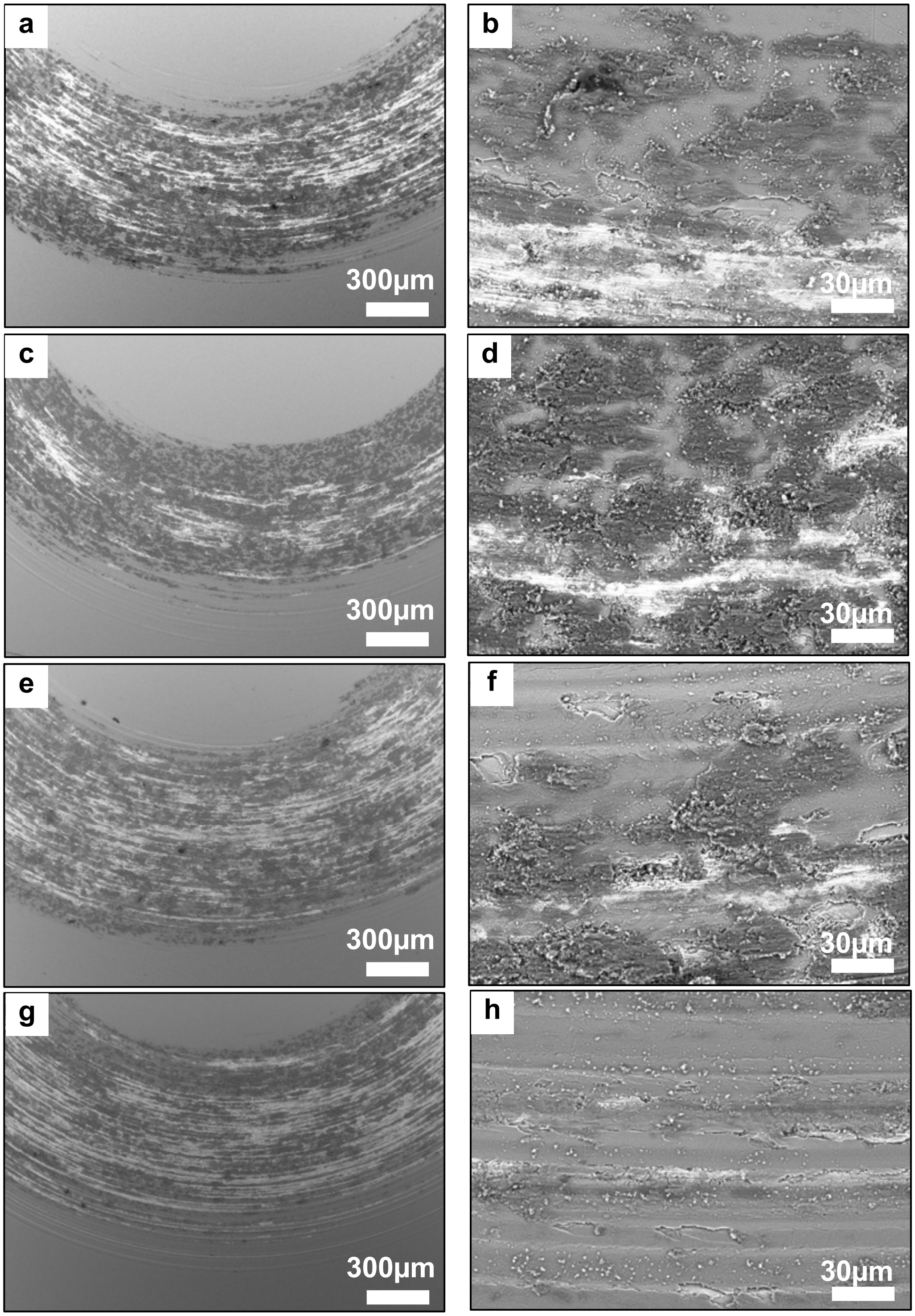

Fig. 4.31 SEM micrographs of wear tracks of (a, b) CA0, (c, d) CA500, (e, f) CA700 and (g, h) CA800 coatings after the dry sliding tests against Al balls. (b, d, f, h) are the corresponding magnified images of (a, c, e, g).

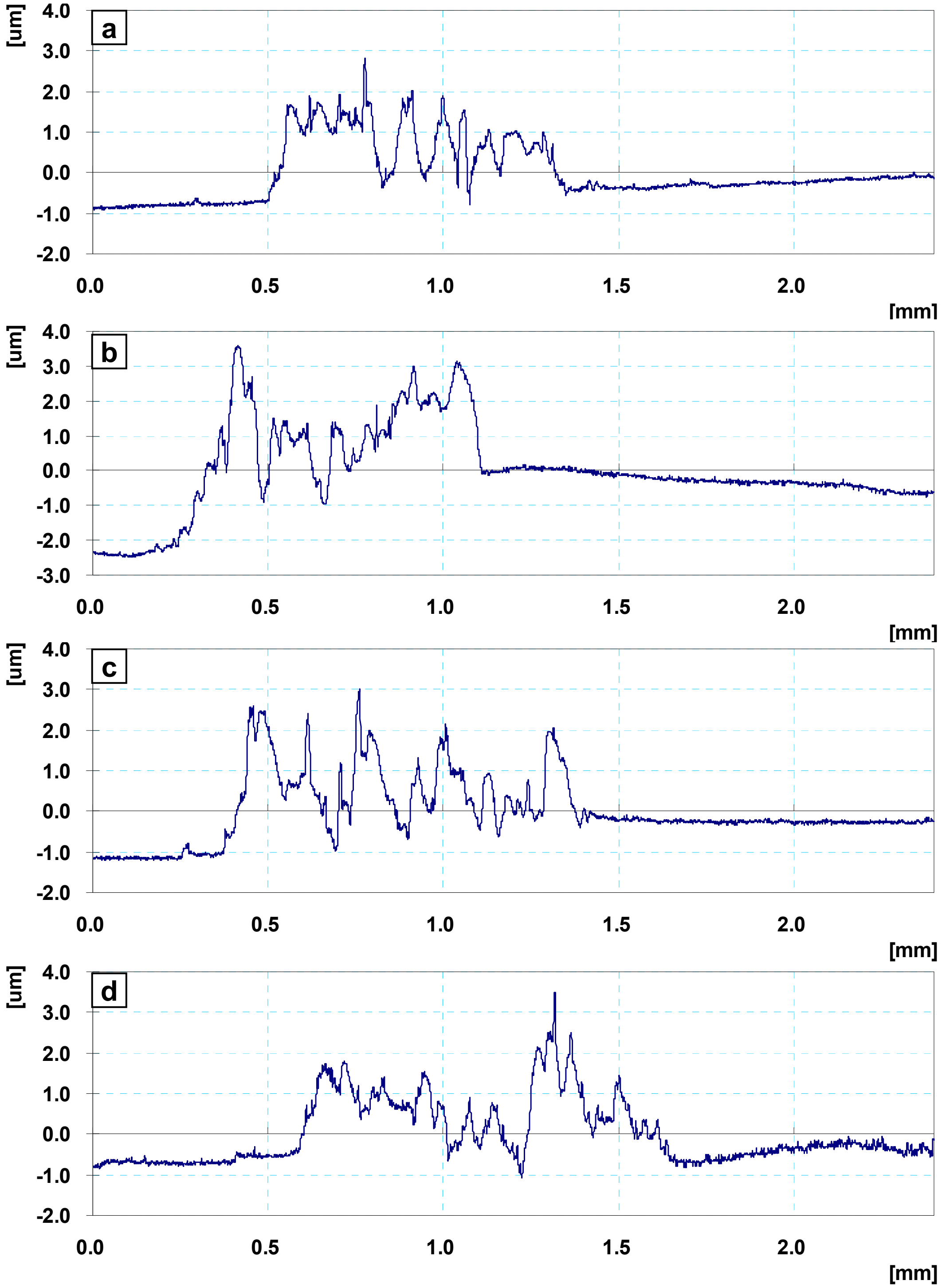

Fig. 4.32 2D profiles of cross-sections of wear tracks of (a) CA0, (b) CA500, (c) CA700 and (d) CA800 coatings after the dry sliding tests against Al balls.

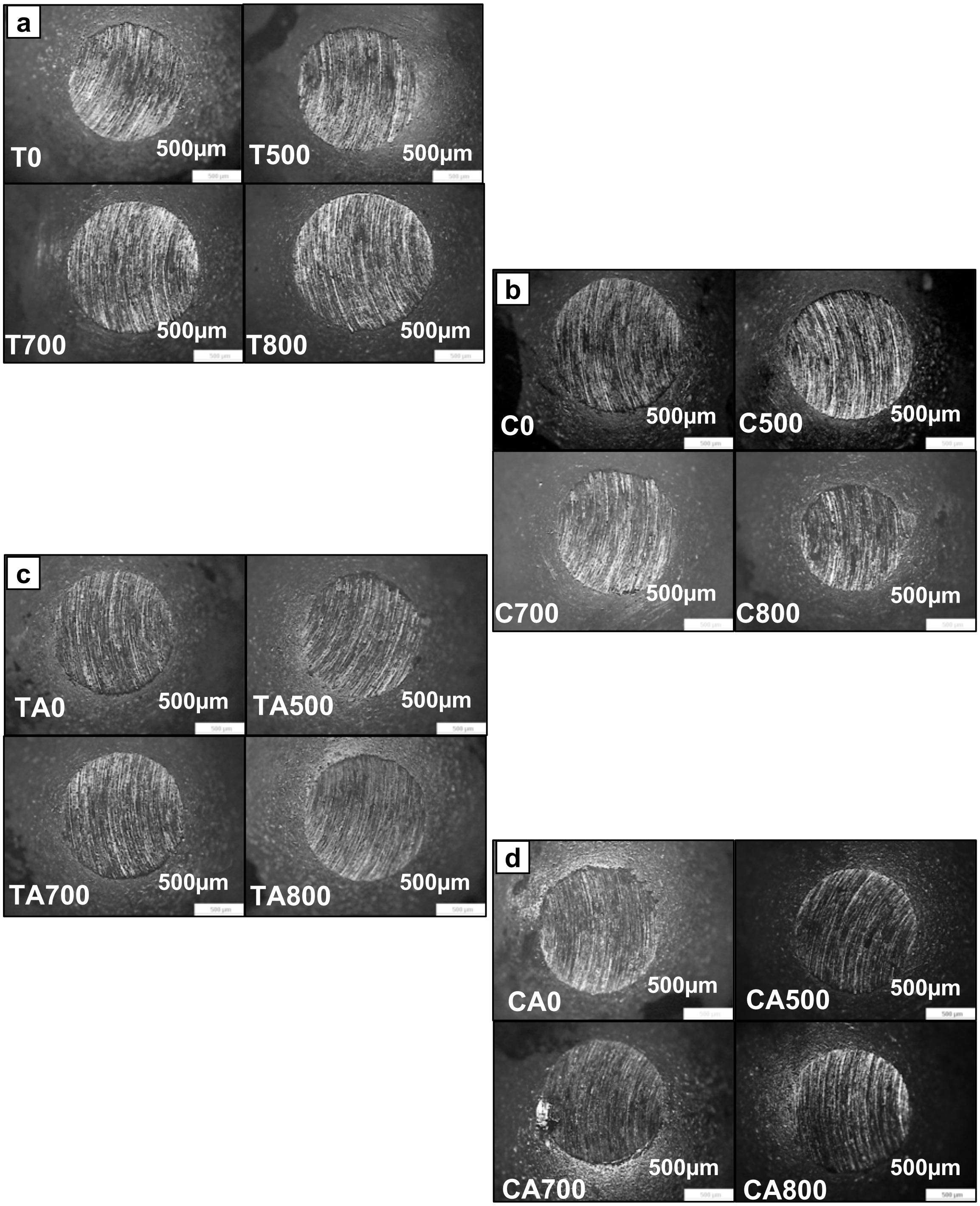

Fig. 4.33 Optical micrographs of counterface Al balls after the dry sliding wear tests against original and annealed coatings (a) TiN, (b) CrN, (c) TiAlN and (d) CrAlN at various annealing temperatures.

4.1.4 Effects of annealing temperature on the tribological property of DLC coating

Fig. 4.34 shows the curves of dynamic cof of original and annealed DLC coatings at 200, 400 and 600 ^{o}C (D0, D300, D400 and D600) against Al_2O_3, steel and Al balls. The cofs of D0, D300 and D400 coatings against steel balls are higher than those against Al_2O_3 and Al balls (Fig. 4.34(a-c)). For D0, the average cof at stable stage is about 0.3 and increases to 0.35 for D300. The D400 has a lower cof about 0.25 compared with D0 and D300. D600 has the lowest cof which is about 0.05 while against the steel ball. Figs. 4.35 and 4.36 show the optical images of wear tracks on the DLC coatings after sliding tests against steel balls and the worn steel balls, respectively. No material transferred from steel balls can be observed on the coating surface but some surface polishing has occurred. On the wear track of D600, the coating has been worn out but from the morphology of wear track (Fig. 4.35(d)) no adhesive wear has occurred. The morphology of steel balls (Fig. 4.36) shows that during the sliding tests, all the steel balls were worn and the wear loss of the ball against D400 was less than other steel balls.

The wear behaviors of original DLC coatings against alumina and aluminum (Fig. 4.34 (a)) are similar. The cofs increase gradually during the sliding tests (10000 revolutions) against the two counterface balls from 0.11 to 0.13. The cof of D300 (Fig. 4.34(b)) against aluminum ball is higher than that of the original coating, with the cof gradual increasing from 0.11 to 0.15 during the sliding. Furthermore, the cof against alumina ball is even higher, which is up to 0.18 at the end of the testing (Fig. 4.34(b)). The cof curves of D400 against alumina and aluminum (Fig. 4.34(c)) are overlapped and the values are from 0.11 to 0.14 which are similar to the original DLC. The D600 coating against alumina ball has the lowest cof at the beginning stage (1800 revolutions), which are less than 0.08, but suddenly increases to 0.2 after 1800 revolutions and the cof curve goes up rapidly to ~0.4 at the end of 10000 revolutions which implies that the coating has been penetrated after 1800 revolutions when sliding against ceramic alumina ball. For the cof of D600 coating against aluminum ball, the cof decreases to 0.07 at the end of sliding.

Compared with the original DLC coating (D0), the D300 coating has a higher cof. The cofs of D400 coating against the three types of counterface balls are lower than the corresponding cofs of D300. The high cof of D300 can be explained by both hydrogen loss and its lower hardness compared to the original coating, resulting in more coating plowing when against the hard alumina ball. Although the hydrogen loss exists at 400 °C, more graphitization also occurs at this temperature and thus the formed graphite at the interface can be used as lubricate to reduce the cofs in somewhat degree. After annealing at 600 °C, the coating possesses both high sp^2 graphite fraction and low hardness, and thus, the relatively low cof but also low wear resistance.

Figs. 4.37(a-d) are the cross-section profiles of the wear tracks against ceramic alumina ball and Fig. 4.38 shows the optical micrographs of the corresponding wear tracks against aluminum ball. No any material transfer and attachment between the coating and alumina ball can be observed on the original, D300 and D400 but some deformation and coating wear occur and the highest wear depth is 0.12, 0.20 and 0.27 μm (Figs. 4.37 (a, b, c)), respectively. For the coating annealed at 600 °C, when against an alumina ball, the coating was penetrated and M2 steel substrate was plowed locally (Fig. 4.37 (d)). Consequently, coating materials together with some steel from substrate were attached on the counterface alumina ball surface (Fig. 4.37(e)).

When against aluminum ball, the wear tracks on original, D300 and D400 coatings (Figs. 4.38 (a-c)) show small deformation, surface polishing and some transferred material in the form of small particles. Those particles are loosened and they do not form wear debris attached on the coating surfaces. D600 illustrates a coating worn out and some adhesive wear on the substrate, which occurred during sliding against aluminum ball (Fig. 4.38 (d)).

The surface morphologies of worn counterface aluminum balls are shown at Fig 4.39. The abrasive wear can be clearly observed for the balls against original, D300 and D400, among which, the wear loss of balls against original and D300 is similar (Figs. 39(a, b)) and less than that of D400 (Fig. 4.39(c)). On the ball against D600 (Fig. 4.39(d)), some transferred materials can be found.

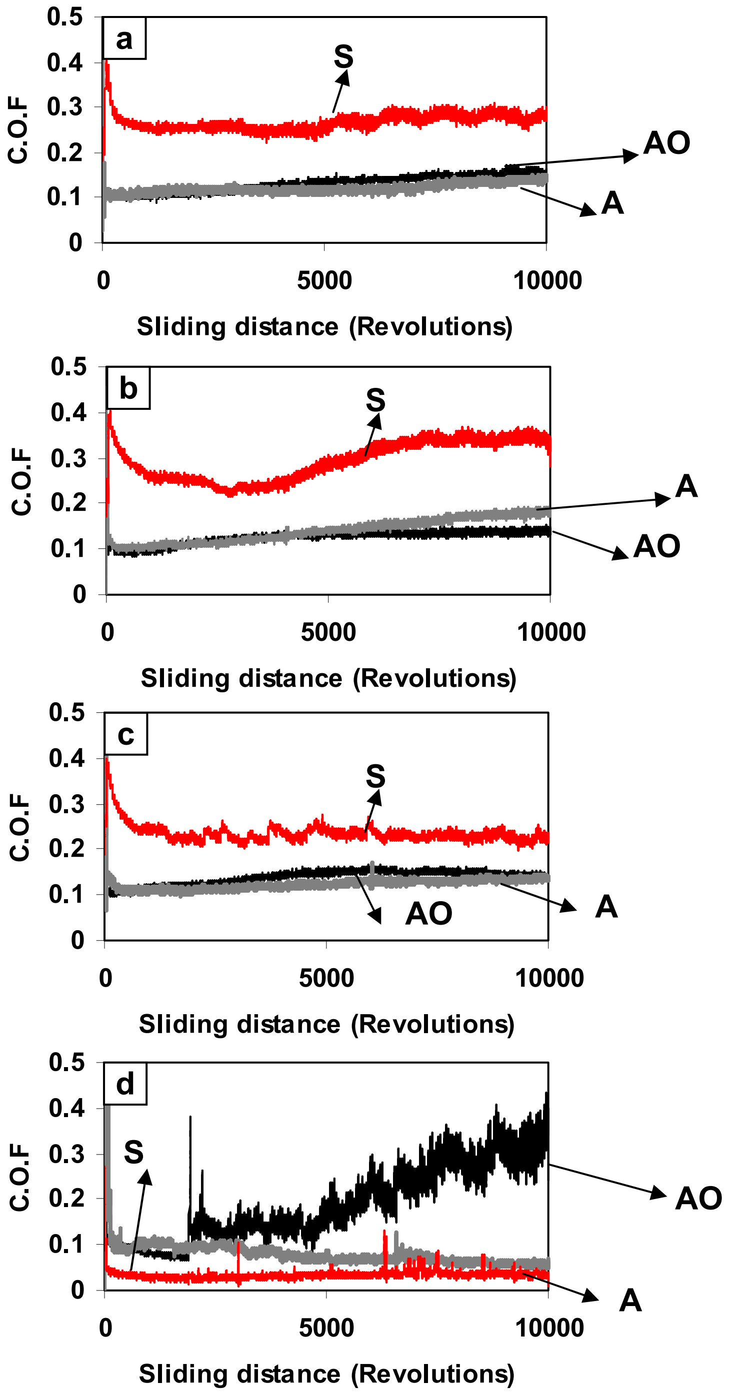

Fig. 4.34 COF curves of (a) D0, (b) D300, (c) D400 and (d) D600 coatings during the dry sliding tests against ceramic Al_2O_3 (AO), steel (S) and aluminium (A) balls.

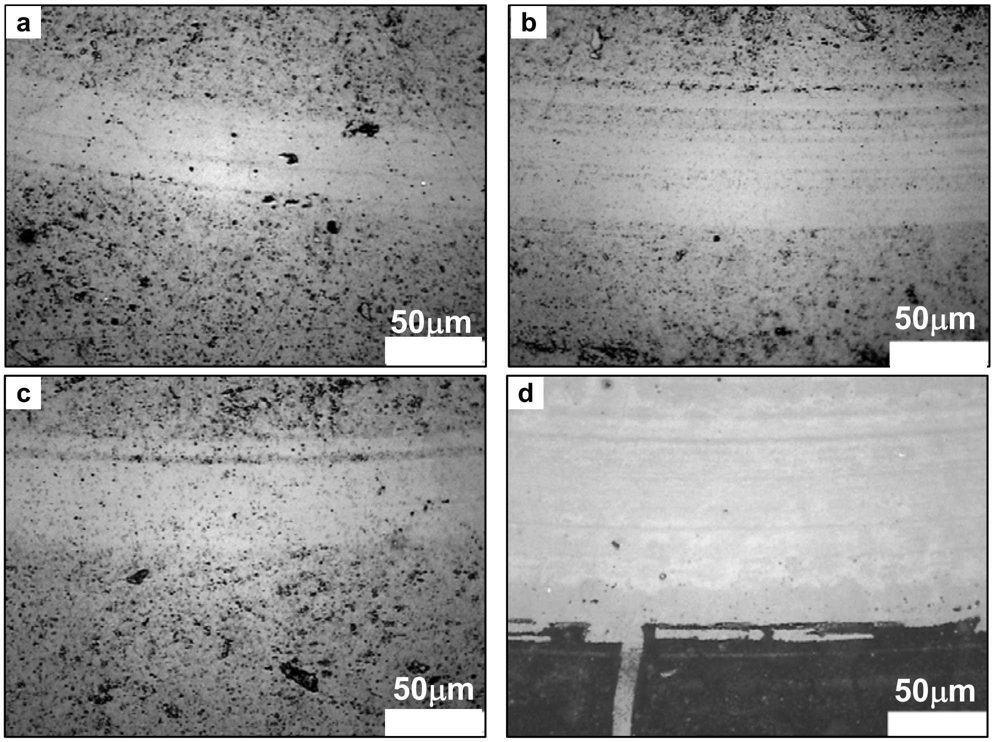

Fig. 4.35 Optical microscope micrographs of wear tracks on (a) original DLC coating and annealed DLC coatings at (b) 300, (c) 400 and (d) 600 ^{o}C after the dry sliding tests against steel counterface balls.

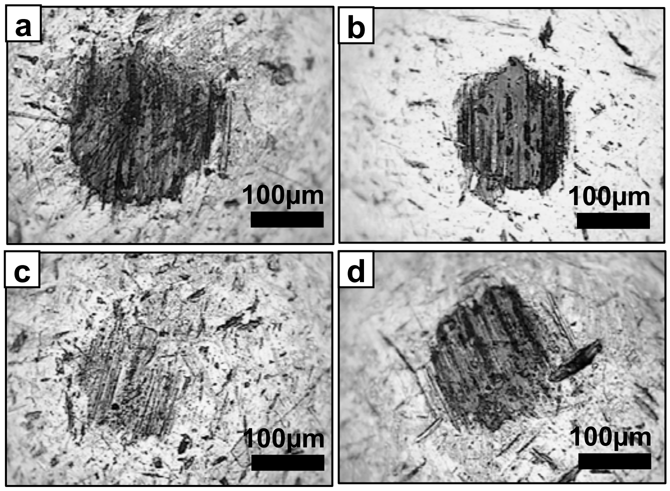

Fig. 4.36 Optical microscope micrographs of wear scars of steel counterface balls after the dry sliding tests against (a) original DLC coating and annealed DLC coatings at (b) 300, (c) 400 and (d) 600 ^{o}C.

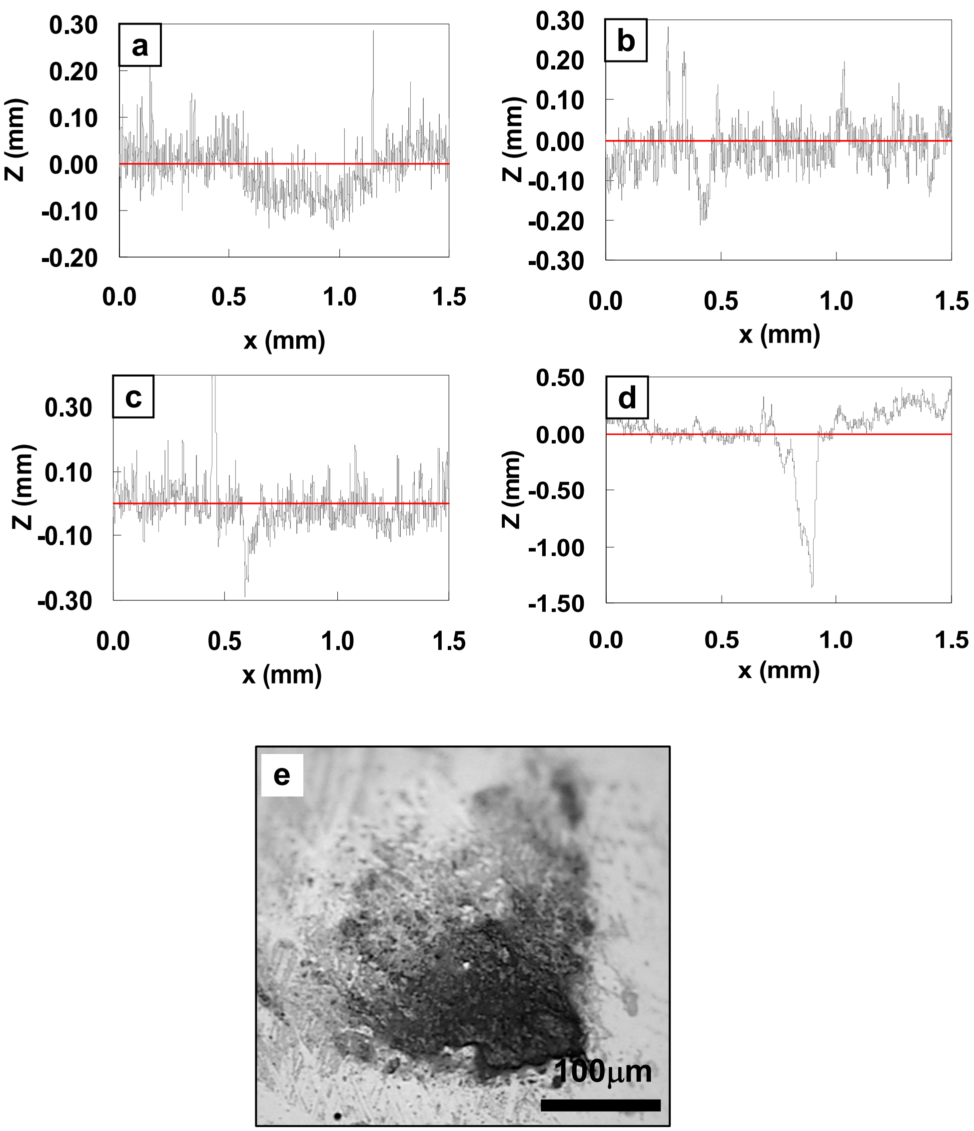

Fig. 4.37 Cross-section profiles of wear tracks after the dry sliding tests against alumina counterface balls on DLC coatings of (a) original and annealed conditions at (b) 300, (c) 400 and (d) 600 ^{o}C. (e) The optical micrograph of the ceramic Al_2O_3 ball after sliding test against D600.

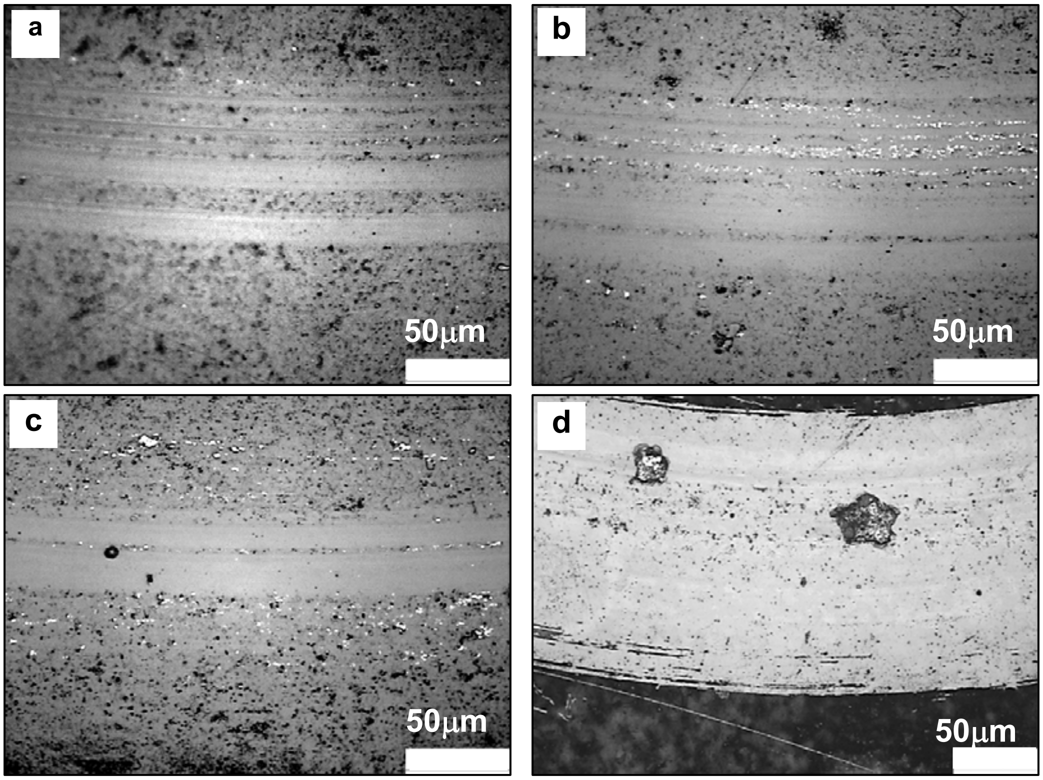

Fig. 4.38 Optical microscope micrographs of wear tracks on (a) original and annealed DLC coatings at (b) 300, (c) 400 and (d) 600 ^{o}C after dry sliding tests against aluminium counterface balls.

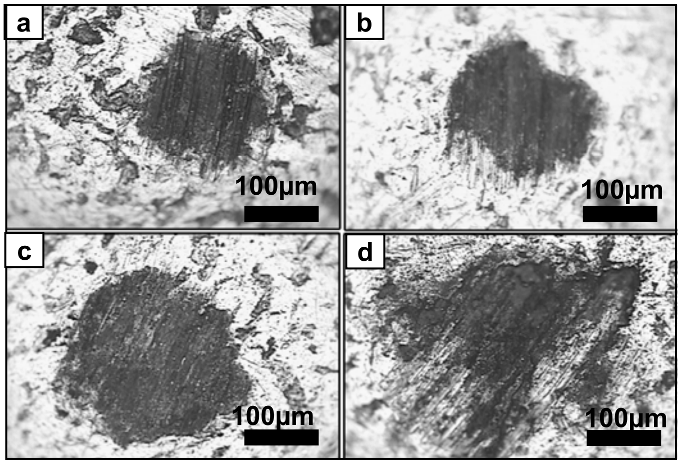

Fig. 4.39 Optical microscope micrographs of wear scars on aluminium counterface balls after the dry sliding tests against (a) original and annealed at (b) 300 (c), 400 and (d) 600 ^{o}C DLC coatings.

4.2 An industrial trial of TiN and CrAlN coatings in an actual stamping plant

The laboratorial pin-on-disc tribological testing results in section 4.1 indicated that CrAlN coating had the best thermal stability. In this section, an industrial trial of TiN and CrAlN coated punches in an actual stamping plan has been conducted to evaluate the coating performance under actual application conditions.

4.2.1 Lifetime of uncoated and coated stamping punches

Whenever severe burrs occur on the perforated sheet, punches would be judged as failed. Fig. 4.40 shows the schematic and the actual appears of the edge of the blanked pieces. The edge of the blanked pieces is consisted of roll-over, sheared, fracture edge and burr (Fig. 40(a)). The actual edge of the blanked pieces (Figs. 4.40(b, c)) shows that severe burrs occur after the punch fails, where the height of burr (H_b) is around ½ thickness of perforated sheet. The number of holes blanked prior to failure is used to express their lifetimes.

The lifetimes of three punch tools are presented in Fig. 4.41. The industrial trials show that the CrAlN-coated M2 steel punch has a lifetime of 450,000 hits against high strength steels, which is more than 2.5 and 5 times higher than that of the TiN-coated (160,000 hits) and uncoated punch (78,000 hits), respectively. The increased tool life can significantly reduce machine downtime and manufacturing costs.

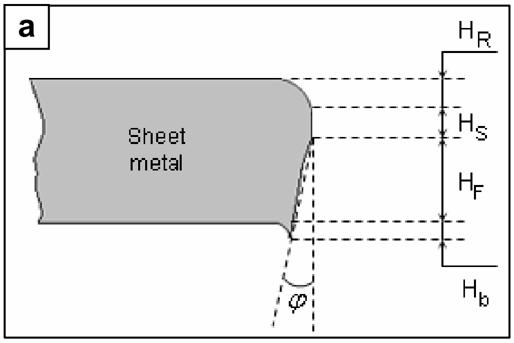

H_R : Roll-over depth.

H_S : Sheared edge.

H_F : Fracture depth.

H_b : Burr height.

Fig. 4.40 (a)

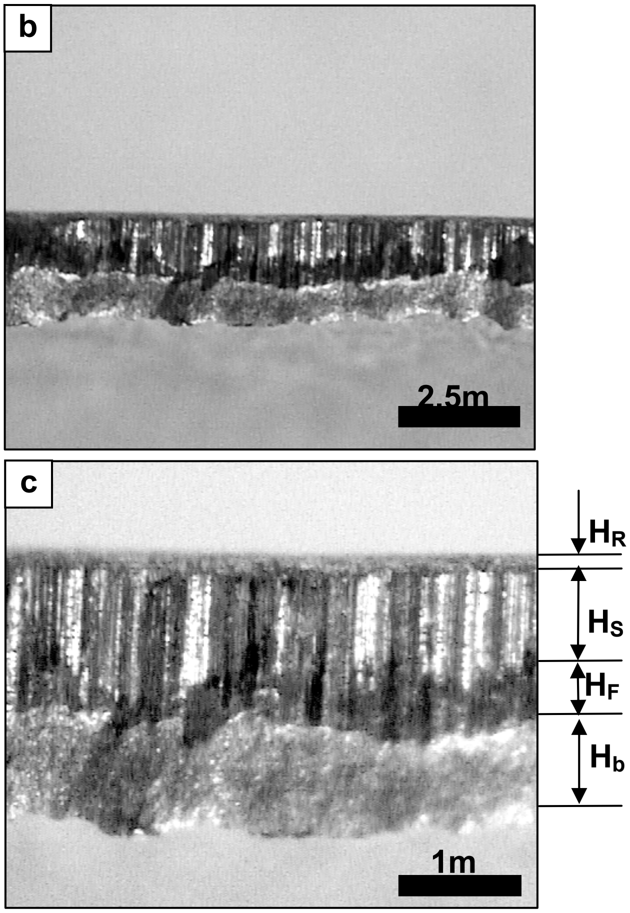

Fig. 4.40 (a) Schematic of geometry of the blanking edge, where H_R, H_s, H_f, H_b are roll-over depth, sheared edge, fracture depth and burr height [158]. (b) and (c) are the optical micrographs of actual blanking edge and its magnified image.

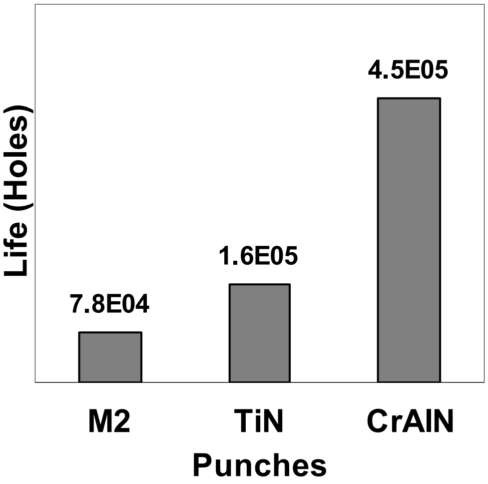

Fig. 4.41 Lifetimes of uncoated and coated stamping punches after the industrial trials.

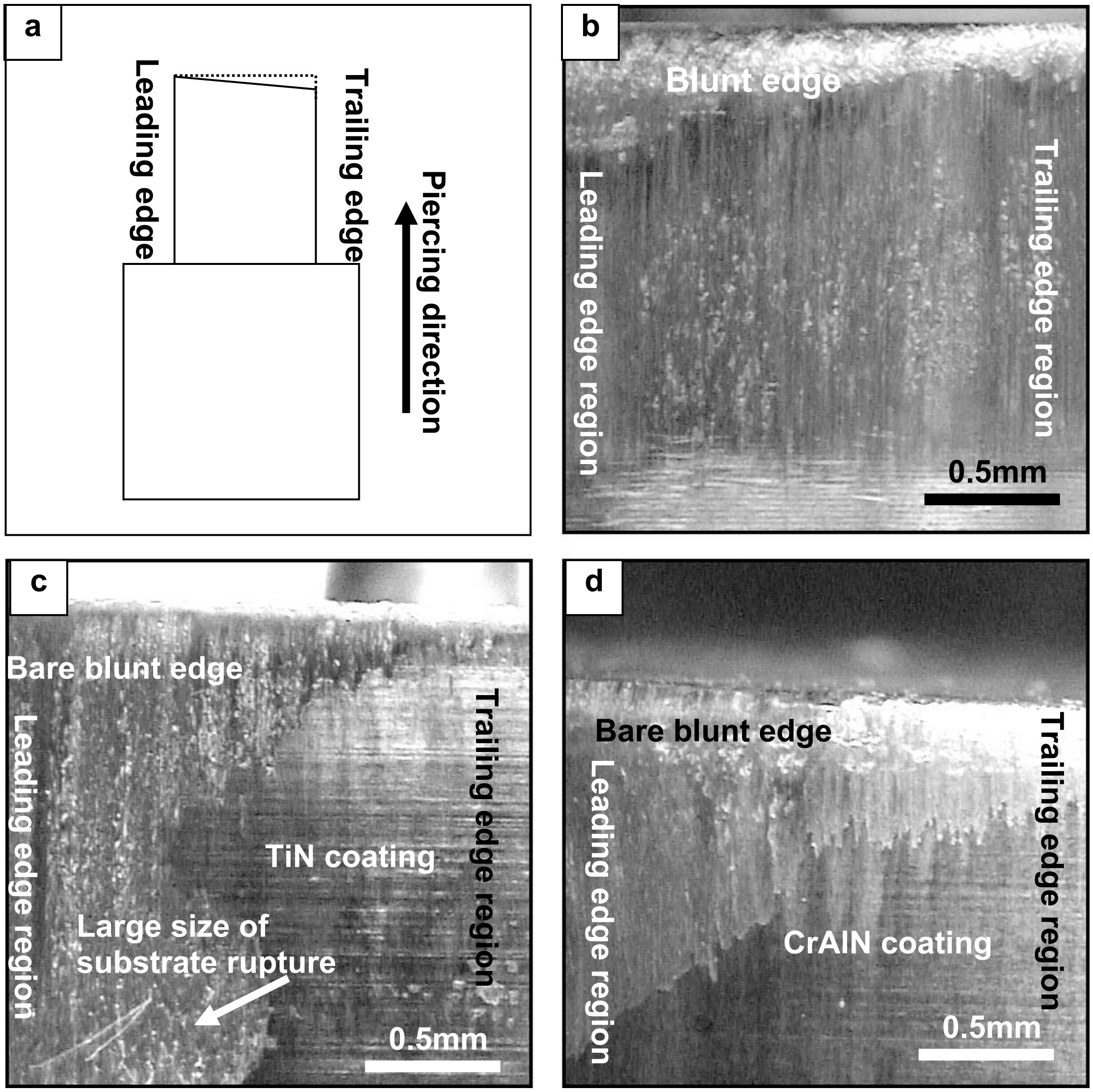

Fig. 4.42 (a) Schematic of leading edge, trailing edge and piercing direction. (b, c, d) are optical micrographs of failed uncoated, TiN-, and CrAlN-coated punches, respectively.

4.2.2 Failure mechanisms of uncoated and coated punches in the industrial trials.

Fig. 4.42 shows optical micrographs of the edge regions on the failed punch tools after industrial trials. Because of the angled assembly of the punch tools, the blanking is a bevel shear process. As a result, the severity of the wear on the punch tools decreases gradually from the leading edge to the trailing edge of the punch. These phenomena can be clearly observed from the optical micrographs (Figs. 4.42(b-d)).

To investigate failure mechanisms, SEM with EDX was used to observe the leading edge and trailing edge regions of uncoated, TiN- and CrAlN-coated punches (shown in Figs. 4.43, 4.44 and 4.45, respectively). The leading edge region of the uncoated M2 punch (Fig. 4.43(a)) shows a scored or grooved surface, parallel to the blanking direction. The surface is very uneven with craters and projections along the grooving direction, which could be related to continuous and repeated plastic flow of the uncoated punch at edge regions during the stamping process. During stamping, the punch was abraded by the high strength steel sheet and meanwhile, small particles of wear debris agglomerated and grew, to generate larger particles stuck on the worn punch surface (i.e., projections on the surface) accompanied by repeated deformation and possible work hardening. EDX analysis of the blunt leading edge region shows an amount of elemental O. This suggests that oxidization had occurred during the sliding contact, which could be attributed to abrupt temperature rising at the contacting faces during piercing. Counterface scuffing is believed to happen in this process since the accumulation, deformation and hardening of wear debris during the sliding under a very high stamping force often cause this kind of surface damage. At the trailing edge of the M2 punch (Fig. 4.43(b)), however, only scratches can be observed without severe plastic deformation.

On the leading edge regions of TiN-coated punches (Fig. 4.44(a)), the coatings were worn out and bare blunt edges were left after the industrial trials. The bare edges regions were divided into two zones, i.e. A and B by white dash line, which have different morphology (Fig. 4.44(a)). The bare regions in Zone A have a surface morphology similar to that of the failed uncoated punch and have more projections on the surface compared with Zone B. At the interface between the exposed bare substrate and the remaining TiN coating at the leading edge, a relatively large amount of coating peeling (Fig. 4.44(a)) and even locally substrate rupture (Fig. 4.42(c)) could be observed. By comparing the EDX analysis results, it is found that Zone B have more elements of Mo, V which is from M2 substrate and Ti from the remaining TiN coating than Zone A. That indicates that zone B is the area of bared M2 substrate which is left after TiN coating delaminated and in the region of the top edge (zone A), the bared substrate is not only abraded but also some material transferred from perforated sheet has been adhered to this region. From a SEM image of the trailing edge of the TiN-coated punch (Fig. 4.44(b, c)), a large amount of transferred material and extensive coating peeling can be observed. EDX analysis of the transferred material (spectrum C) indicates a chemical composition comprising Zn, O and Fe. The Zn element is from the high strength steel which has a galvanized Zn coating on its surface.

At the leading edge of the CrAlN-coated punch (Fig. 4.45(a)), the coating seemed to be worn away more gradually, with less peeling of the coating. From a SEM image of the trailing edge of the CrAlN-coated punch (Fig. 4.45(b)), little material transfer could be observed at the corresponding position on the CrAlN-coated punch surface. However, small-scale coating chipping and peeling were also locally present in the trailing edge region (Fig. 4.45(b)). The EDX analysis indicated that steel sheet materials Fe/Zn (spectrum D in Fig. 4.45) could be smeared and trapped into some of those peeling pits on the CrAlN coating surface. It demonstrated that the TiN coating had a higher Zn and Fe pick-up tendency than the CrAlN coating under the industrial trial conditions.

Due to the fact that industrial M2 steel punches do not normally exhibit a very smooth surface finish (unlike the polished surface of the laboratory test coupons), the coatings on industrial punches had a rough surface due to replication of machining grooves on the substrate surfaces (Figs. 4.44 and 4.45)). It was noticed by SEM observations (Figs. 4.44 and 4.45) that the borderlines (vertical to stamping direction) of flaking and peeling regions tended to be on those machining-caused grooves. Similar coating wear phenomena were reported in [159], where premature failure occurred on a coated tool with a machined surface but coatings on well-finished tools showed little wear after extended stamping tests. The local coating on the top of the grooves could have a non-uniform, less dense structure, and thus less integration into the substrate due to atom shadowing effects [160]. During the stamping process, those sites were subjected to stress concentration. It is believed that ruptures occurred at the grooved regions first, and then the cracks propagated along the piercing direction with successive stamping operations. Consequently, small peelings at groove regions became interconnected, forming larger areas of coating delamination. Compared with the CrAlN coating, the adhesive wear on the TiN coating caused by Zn-coated high strength steels would also play a role in the coating peeling, leading to a shorter lifetime. The size of peelings on the CrAlN coating (Figs. 4.45(b)) was smaller than that on the TiN coating (Figs. 4.44(b, c)), which may be attributed to the higher H/E ratio of CrAlN than TiN, allowing the CrAlN to deflect and recover under repetitive loading.

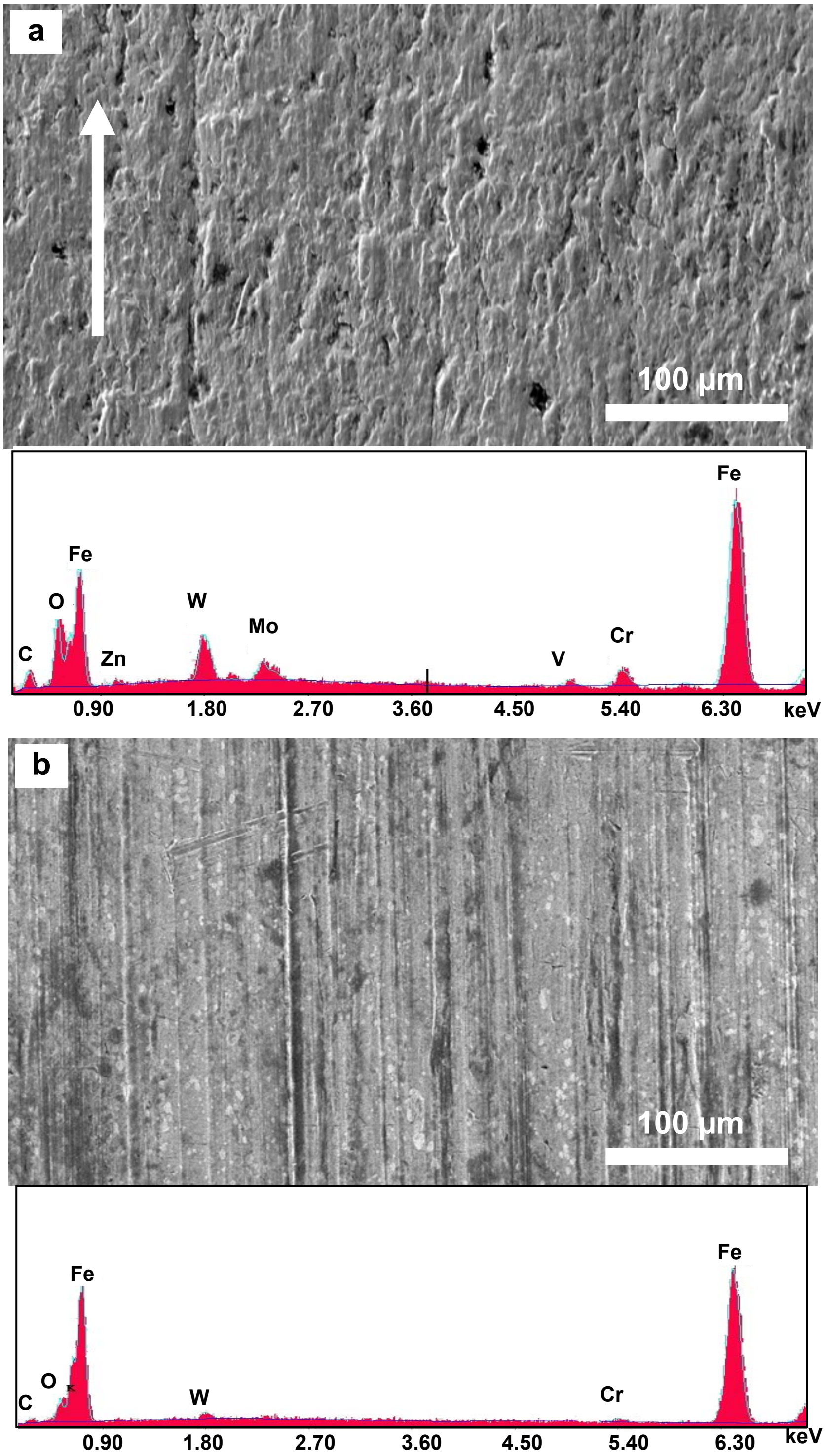

Fig. 4.43 SEM micrographs and corresponding EDX spectra of the top edge of uncoated punch after industrial trials, showing (a) the leading and (b) trailing edge regions. Piercing direction is as shown in (a).

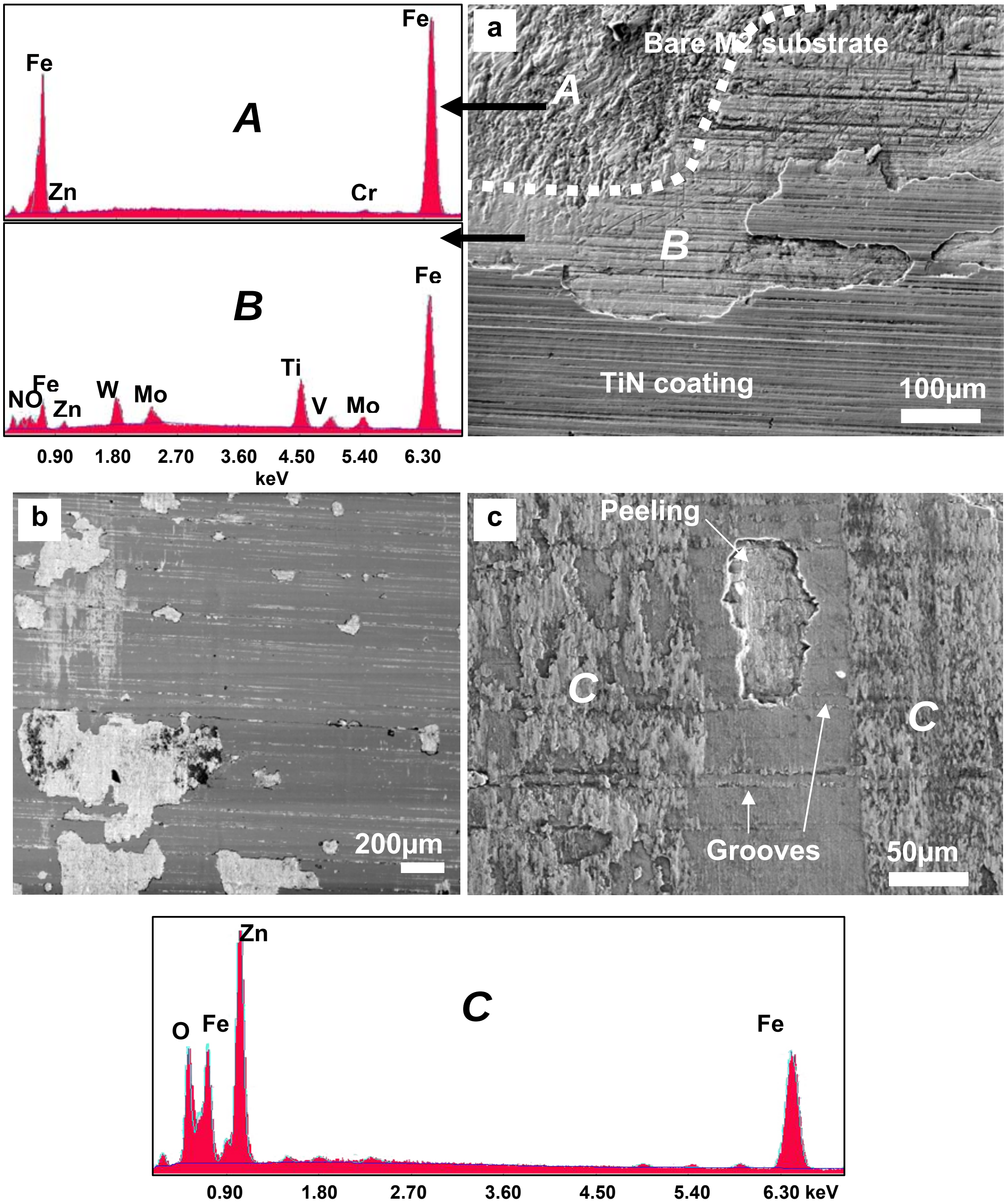

Fig. 4.44 SEM micrographs and corresponding EDX spectra of the top edge of TiN-coated punch after industrial trials, showing (a) the leading and (b, c) trailing edge regions. (c) is the magnified image of (b) to show the grooves and coating peeling. The EDX spectra (A, B, C) are collected from regions of A and B in (a) and C in (c).

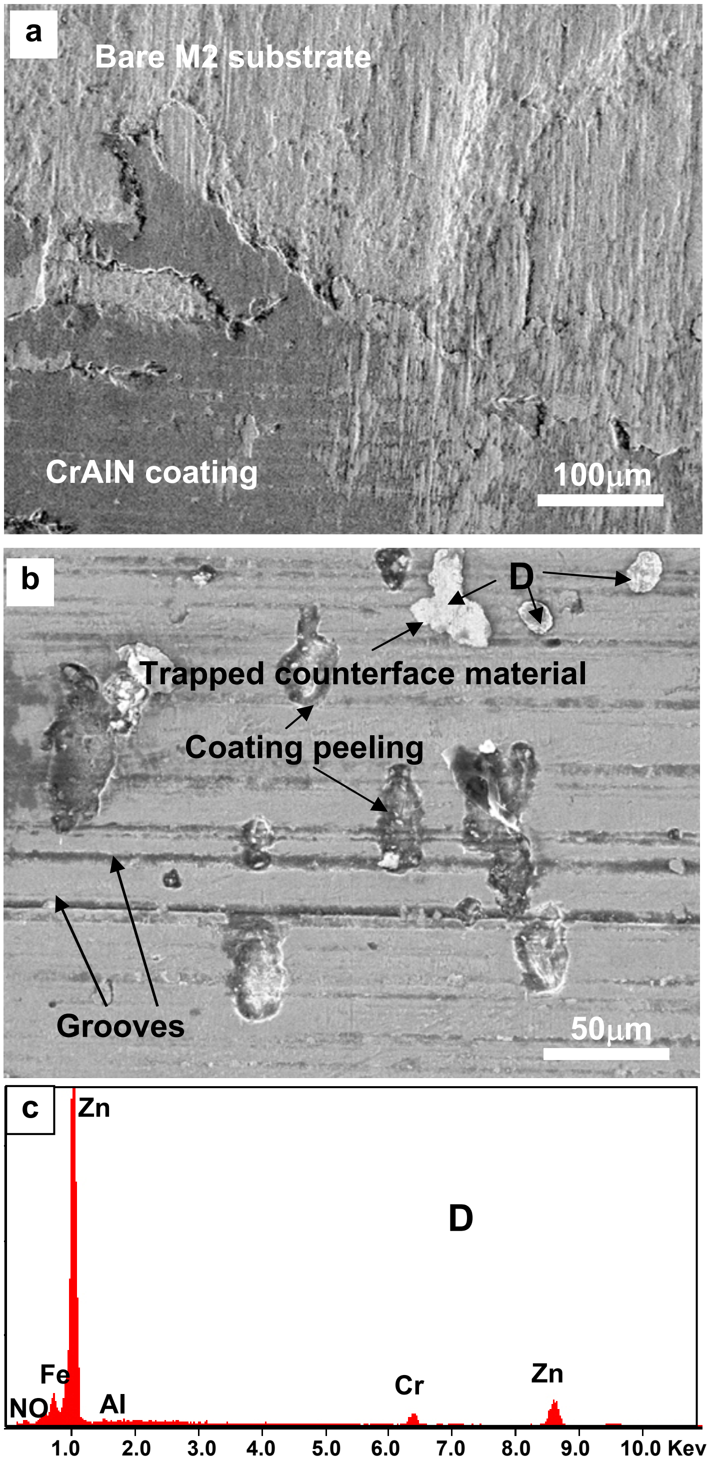

Fig. 4.45 SEM micrographs of the top edge of CrAlN-coated punch after industrial trials, showing the leading (a) and trailing (b) edge regions. (c) is the EDX spectrum collected from region D.

4.3 Development and characterization of Cr(CrN)/C(DLC) multilayered coating system used for dry machining aluminum alloys

The results of sections 4.1 and 4.2 indicated that carbon based coating had a better anti-sticking of steel and Al materials than the TiN based or CrN based coatings. However, above 400 ^{o}C, due to the hydrogen loss and graphitization effects, the coating structure has degraded and the coating lost the superior wear performance such as good wear resistance and low friction. Thus, in this section of this dissertation, a Cr(CrN)/C(DLC) multilayered coating system are attempted to develop by using unbalanced magnetron sputtering PVD method. This coating is expected to combine the properties of hard CrN and DLC based coatings to achieve both high wear resistance and low friction.

4.3.1 Coating bilayer thickness determination

The low-angle XRD pattern can be used to calculate the bilayer thickness according to the Bragg's law equation: $\sin^2\theta = (\frac{n\lambda}{2\Lambda})^2 + 2\delta$, where 2θ is the peak position of the *n*th order to reflection, λ is the X-ray wavelength (0.156 nm), δ is the deviation of the average refractive index of the film, and Λ is the bilayer period.

Fig. 4.46 shows the low-angle XRD data collected from multilayer coatings R1, R2, R3 and R4. The Bragg's peaks of multilayers, which are a result of scattering from the chemical modulation of the layers, are clearly observed. By plotting $\sin^2\theta$ vs n^2 and fitting to a straight line with a constant slope $\left(\frac{\lambda}{2\Lambda}\right)^2$ (Fig. 4.47), the Λs could be determined. Thus, the average Λs are gained and presented in Table 4.5.

The bilayer period can also be measured directly from XPS depth profiling. Fig. 4.48 is an illustration of the elemental profiles as a function of depth for coating R2 based on the Ta_2O_5 thin film (standard) etching rate 11.1 nm/min. It indicates coating R2 contains elements Cr, N and C. The average bilayer thickness of R2 is 7 nm, which is slightly different from the XRD analysis due to the different sputtering rate between the standard Ta_2O_5 and the coating R2.

Fig. 4.49 is the cross-section TEM images of coatings R3 and R4. Uniform multilayers are observed and the bilayer thicknesses of R3 and R4 are 4.5 nm and 3.5 nm respectively. The dark layers are Cr(CrN) layers and the bright layers are C(DLC) layers. The values of bilayer thickness obtained by these three methods are listed in Table 4.5. The data in brackets were calculated based on the sample holder rotation speed related to the studied coatings. The comparison of the measured and deduced bilayer thickness values demonstrates the similarity of three methods though some errors exist.

4.3.2 Nanomechanical properties

Fig. 4.50 is the load-displacement curves of four coatings with maximum load 1 mN. The hardness (H), reduced elastic modulus (E_r) and ratio of H/E_r are tabulated in Table 4.6. The hardness increases with the bilayer period Λ decreasing, reaches the maximum value 12.76 GPa at $\Lambda\sim$ 4.5 nm (R3). Further increase in period reduces the hardness. The same phenomenon was also early observed by Barnett and his coworkers [144, 161].

Several models have been proposed including dislocation blocking by layer interfaces[162], Hall-Petch strengthening[163], strain effects at layer interfaces[164] and the supermodulus effect [165] to explain the hardness enhancement with decreasing bilayer thickness (Λ).According to the elastic modulus (Table 4.6), there is no supermodulus effect. Generally, the hardening mechanism is related to the effect of interface between layers which may impede dislocation motion giving rise to a large increase in strength. However when the layer below a critical value, the interface layer does not appear, a hardness drop can be seen.

Table 4.5 Bilayer thickness values determined by XRD, XPS and TEM methods

	Bilayer thickness in nm			
	XRD		*XPS*	*TEM*
	$(\frac{\lambda}{2\Lambda})^2$	Λ		
R1	0.00003	14.2	(14)	(14)
R2	0.0001	7.8	7	(7)
R3	0.0003	4.5	(4.7)	4.5
R4	0.0005	3.5	(3.5)	3.5

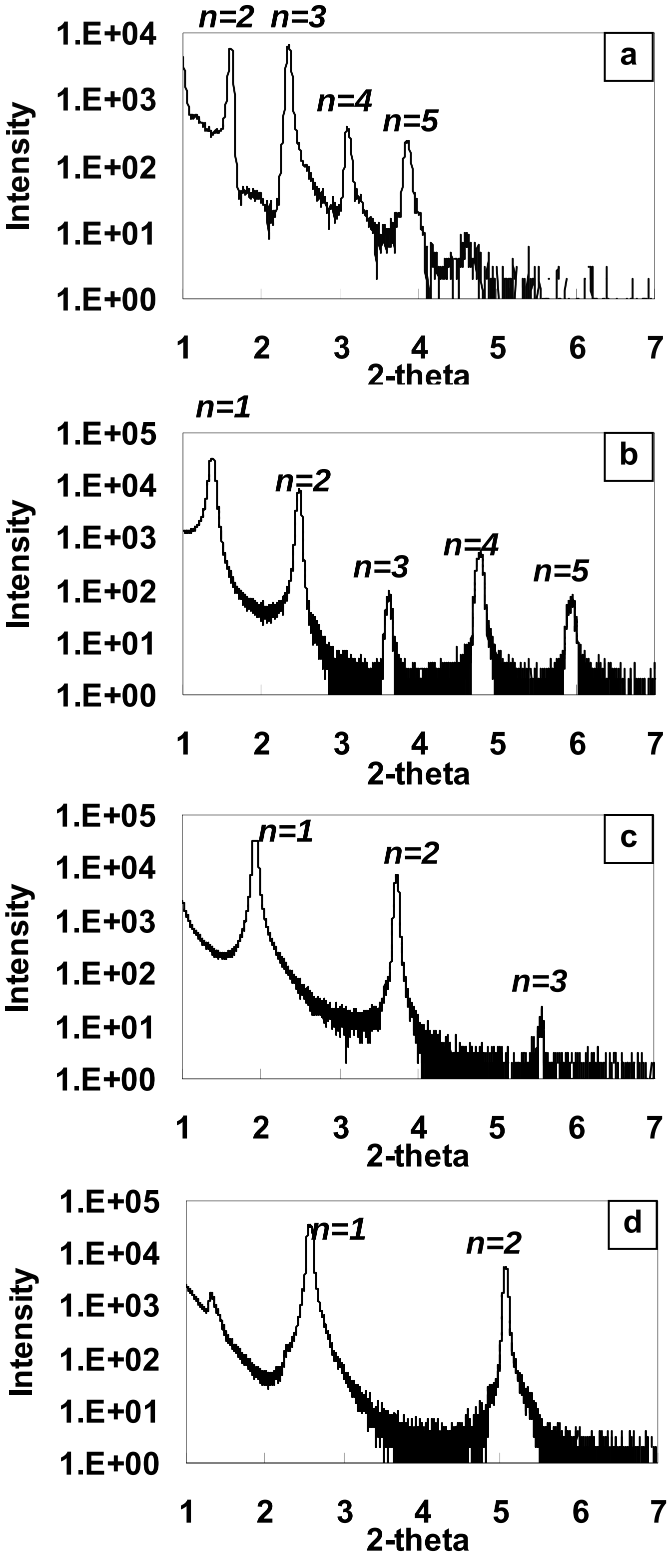

Fig. 4.46 The low-angle XRD patterns of coatings (a) R1, (b) R2, (c) R3 and (d) R4.

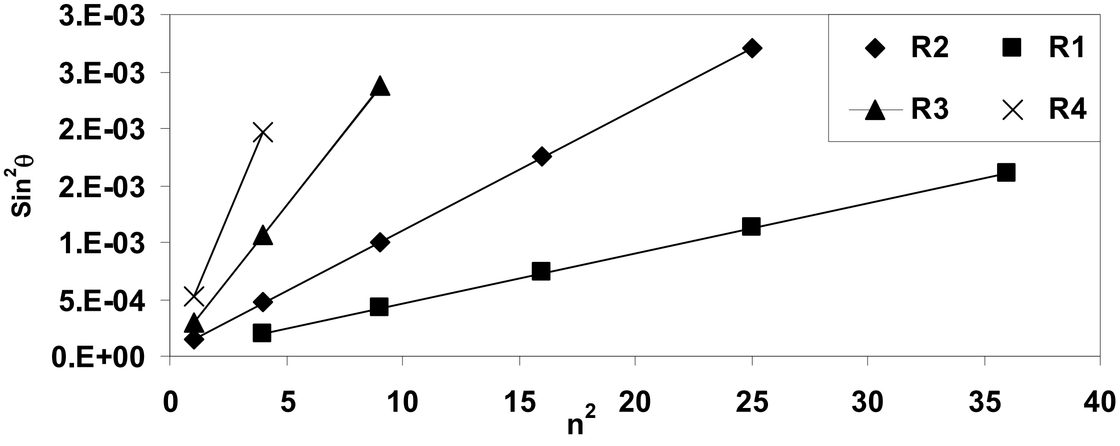

Fig. 4.47 Plots of $Sin^2\theta$ as function of n^2 for coatings R1, R2, R3 and R4.

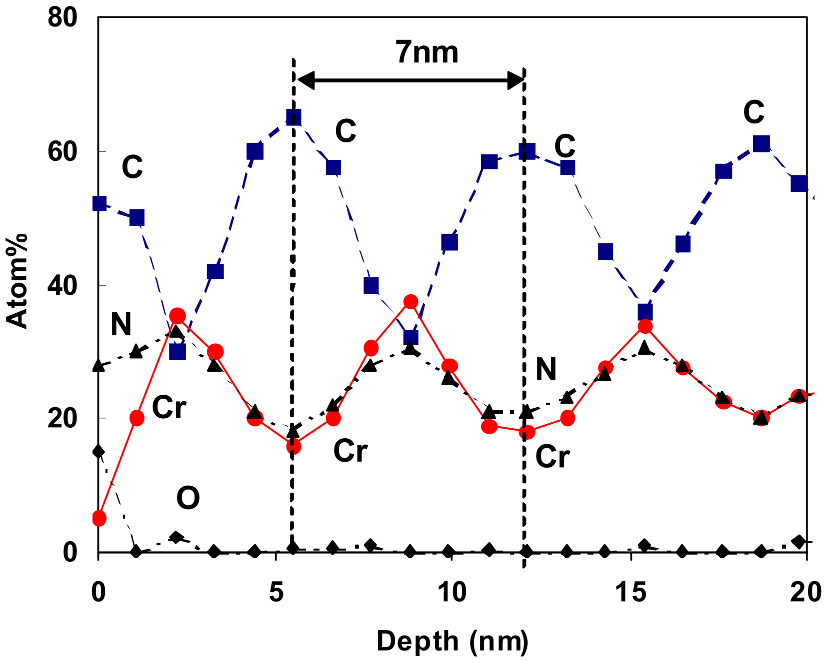

Fig. 4.48 XPS depth profiling of a Cr(CrN)/C(DLC) nano-multilayered coating R2.

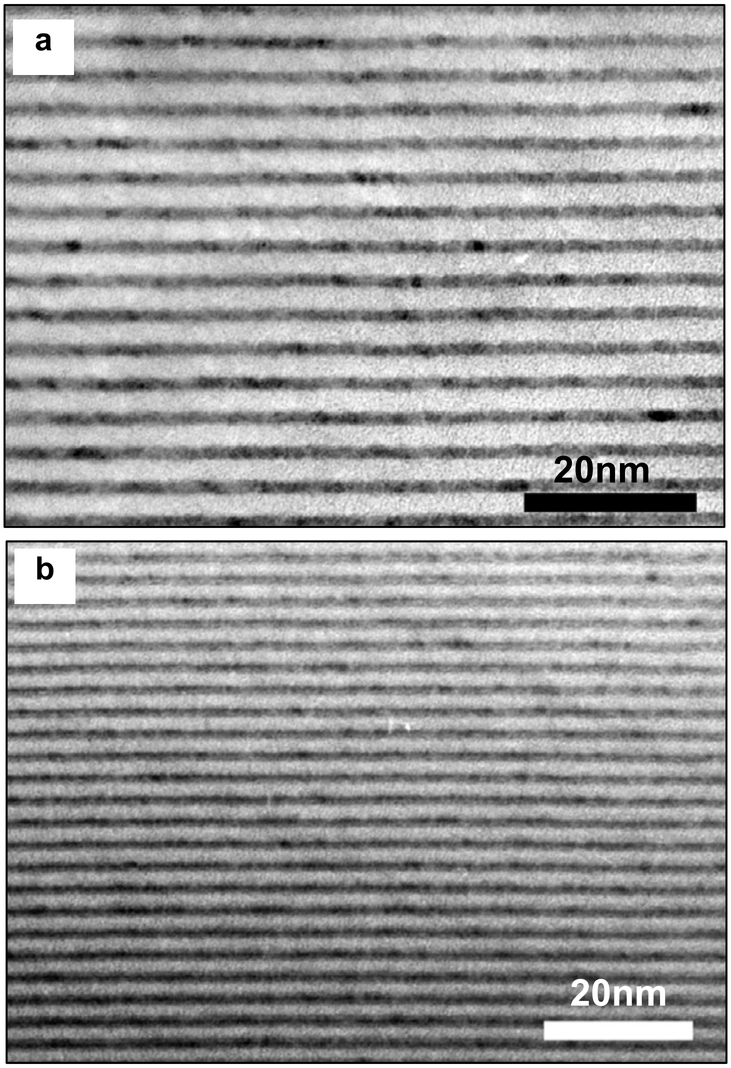

Fig. 4.49 TEM cross-sections of coatings (a) R3 and (b) R4.

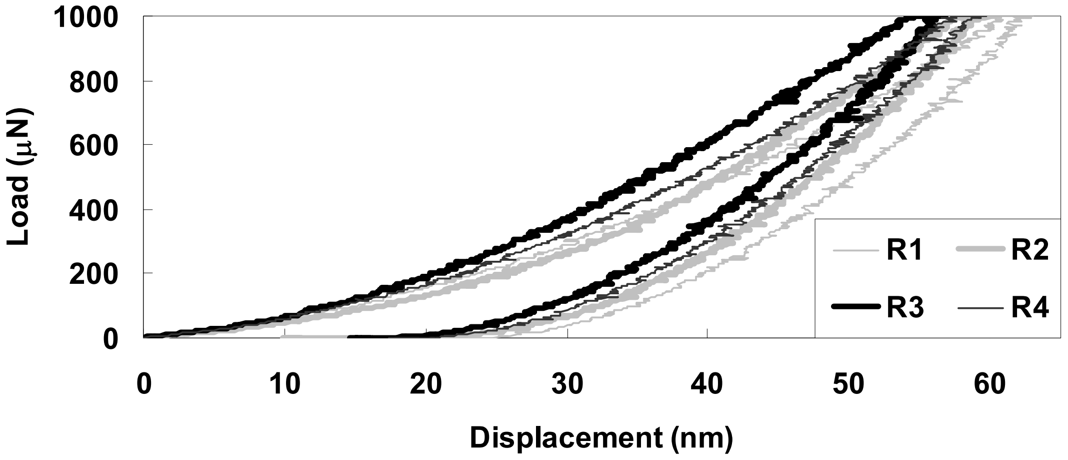

Fig. 4.50 Load vs. displacement curves of various Cr(CrN)/C(DLC) coatings with four different bilayer thickness

Table 4.6 Hardness (H), reduced elastic modulus (E_r), maximum penetration depth (h_{max}), and residual depth (h_f).

	R1	R2	R3	R4
H (GPa)	10.14	11.67	12.76	12.04
E (GPa)	128.99	147.71	149.92	140.3
h_f (nm)	26.09	19.39	17.32	17.82
h_{max} (nm)	62.39	59.84	57.9	58.69
H/E	0.0786	0.0790	0.0851	0.0858
h_f / h_{max}	0.4182	0.3240	0.2991	0.3036
H^3/E^2	0.0627	0.0728	0.0924	0.0887

4.3.3 Tribological properties in nano-scale

The nanoscale wear testing was performed on the coatings R1, R2, R3 and R4 which are deposited on the silicon wafers. According to the mechanical property test results (Table 4.6), R3 is expected to have the lowest wear rate. Fig. 4.51 presents the scanning images of wear track for all coatings. The wear scar depth was obtained by the roughness measurement, counted automatically by the scanning software. The wear rate (k) was calculated by the following equation: $k = \frac{h}{n}$ where h and n are the wear scar depth and number of sliding cycles. Wear rate for each coating is illustrated in Fig. 4.52. Same as the assumption, R3 has the best wear resistance, as well as the best mechanical properties mentioned above. It seems that there is a connection between the mechanical and tribological properties. A. Matthews and A. Leyland established that relationship [166-168]. It has been pointed out that the ratio of Hardness (H) over Elastic modulus (E), which is inversely proportional to plasticity index, could be used to evaluate the wear performance of materials. Since the material removal results from plastic deformation for wear, the material with high H/E, indicating the good resistance to plastic deformation, consequently has excellent wear resistance. In the same way, the ratio of residual depth (h_f) over maximum depth (h_{max}) during the nanoindentation test, representing the unrecoverable strain, and yielding strength, proportional to H^3/E^2, could also be applied to judge the anti-wear ability of materials. The values of these standards are listed in Table 4.6. Apparently, all criterions match with the wear test well, except for coating R2. Its high wear rate is mainly due to the peeling, suggesting strong internal stress, which is not occurred for coating R2 deposited on the M2 substrate.

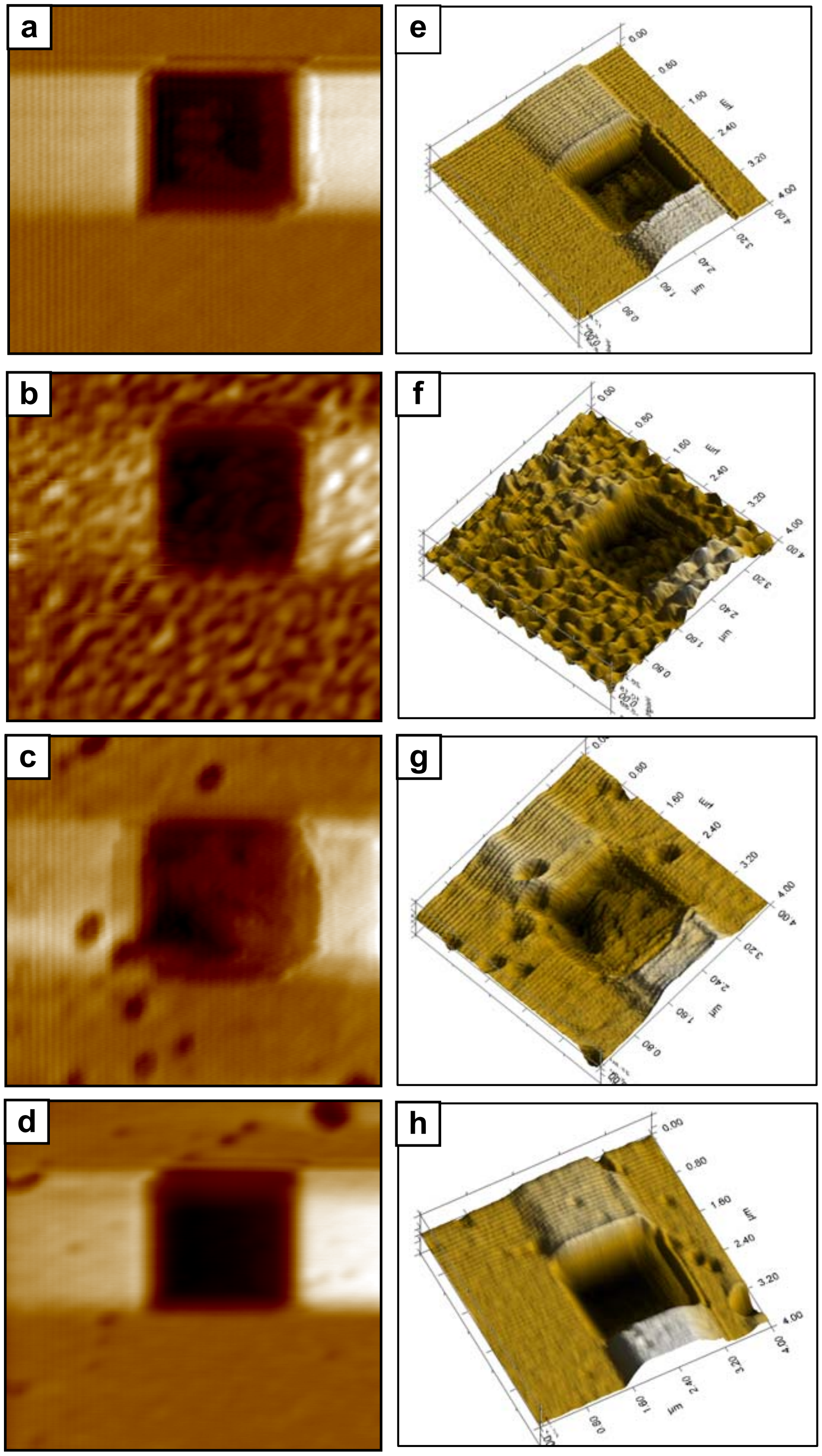

Fig. 4.51 (a, b, c, d) 2D and (e, f, g, h) 3D AFM images of wear tracks on coatings (a, e) R1, (b, f) R2, (c, g) R3 and (d, h) R4, respectively.

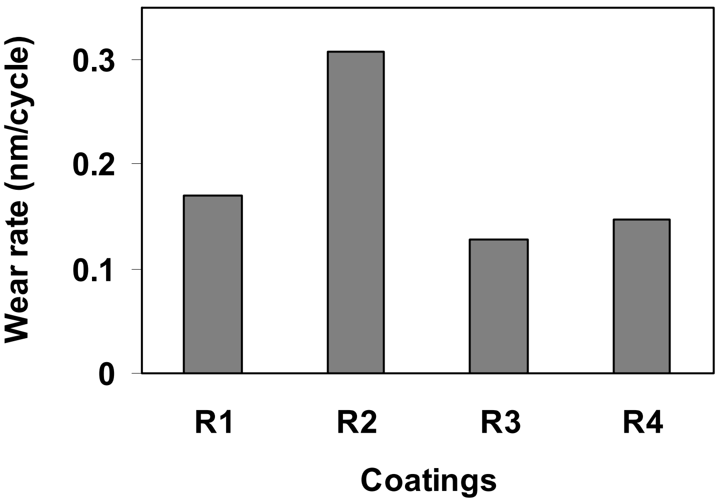

Fig. 4.52 Wear rate of coatings in nano-scale wear tests.

4.3.4 Tribological properties in microscaled pin-on-disc sliding wear tests

The tribological properties were characterized by microscale pin-on-disc sliding wear tests on the four coatings deposited on M2 steel substrates. Fig. 4.53 is the cof curves of the four coatings during the dry sliding tests against Al counterface pins and Fig. 4.57 summarizes the average cof values during the dry and with-lubricate sliding tests. Under the dry sliding conditions, coatings R1 and R2 have a similar friction coefficient about 0.7, while the friction coefficient reduces greatly when the bilayer thickness decreases to < 5 nm. The friction coefficients of coatings R3 and R4 (bilayer thickness 4.5 nm and 3.5 nm) are 0.46 and 0.43, respectively. The values of wear rate of the four coatings after dry sliding tests are $2.30\times10^{-7}mm^{-3}/(m.N)$, $1.61\times10^{-7}mm^{-3}/(m.N)$, $1.72\times10^{-7}mm^{-3}/(m.N)$, and $1.72\times10^{-7}mm^{-3}/(m.N)$, respectively. However, it should be mentioned that due to amounts of Al material transferring to coating surface during dry sliding tests, the wear rate may not reflect the actual wear resistance of coatings accurately. Thus, close observation and detailed analysis using SEM would be beneficial to better understanding of their wear mechanism.

Fig. 4.54 is the SEM micrographs of wear tracks on the coatings after dry sliding wear tests. Although coatings R1 and R2 have the similar friction coefficient in the dry sliding tests, the morphologies of the wear tracks on the two coatings are quite different. On the wear track of coating R1 (Figs. 4.54 (a)), cracks and flaking can be observed. No cracks or flaking occurred on the wear track of coating R2 (Figs. 4.54(b)) after the dry sliding test, but abrasive wear exhibited and some Al material was attached in the wear scar, which was transferred from the A319 counterface pin. Due to the transferred material in the wear scar, the actual wear loss of coatings R2 should be larger than the measured data. With the bilayer thickness less than 5nm, only a slight polishing can be observed on the wear tracks of coating R3 (Fig. 4.54(c)) and R4 (Fig. 4.54(d)). The material adhesion and transferring to wear tracks are negligible. The formation of flaking during sliding wear could be the combination of adhesive wear (Al sticking) and fatigue cracking. A progressive damage initiated at the interfaces between layers and propagated due to fluctuating stresses and strains on the material. When adhesive wear (Al sticking) occurred at the fracture regions, the localized material was torn off and the crack and flaking formed in situ. Increased layer interface number (i.e., thinner bilayer thickness) in the coating would perform more effective energy dissipation and stress relieving through absorbing more energy due to a longer cracking path caused by detouring at layer interfaces.

The morphologies of wear tracks shown in Fig. 4.54 also showed less Al transferring to the coatings with thinner bilayer thickness (R3 and R4). The Cr, Al and C mixed debris would exist at the interface between the tribological counterfaces. From naked eye observation of the wear debris formed on coatings R1 – R4 during testing in air, the coating R1 has a large number of debris particles, but coating R4 has very little of them. The thicker bilayered coating such as R1 exhibits a high friction coefficient, behaving more like a metallic coating. The thinner bilayered coatings R3 an R4 (with less wear debris) seem to allow graphite debris to perform a solid lubricate. Thus, the coatings R3 and R4 exhibit a low friction coefficient.

Fig. 4.55 shows the morphologies of counterface pins against the four coatings after dry sliding tests. The morphologies of the pins worn against coating R1 (Fig. 4.55(a)) and R2 (Fig. 4.55(b)) exhibited a combination of adhesive wear and abrasive wear where Al with some oxidation was worn away and some wear debris would be re-stuck on the pins surface in the subsequent sliding pass. With the decrease in coating bilayer thickness, the pin wear became limited. On the pin against coating R4 (Fig. 4.55(d)), just a small scar could be observed. This phenomenon indicates that the improved lubrication effect of the coating with thinner bilayer could prevent Al alloy material from being adhered to coating surfaces and reduce abrasion between wear counterfaces so that a low friction can be achieved by thinner layer coating.

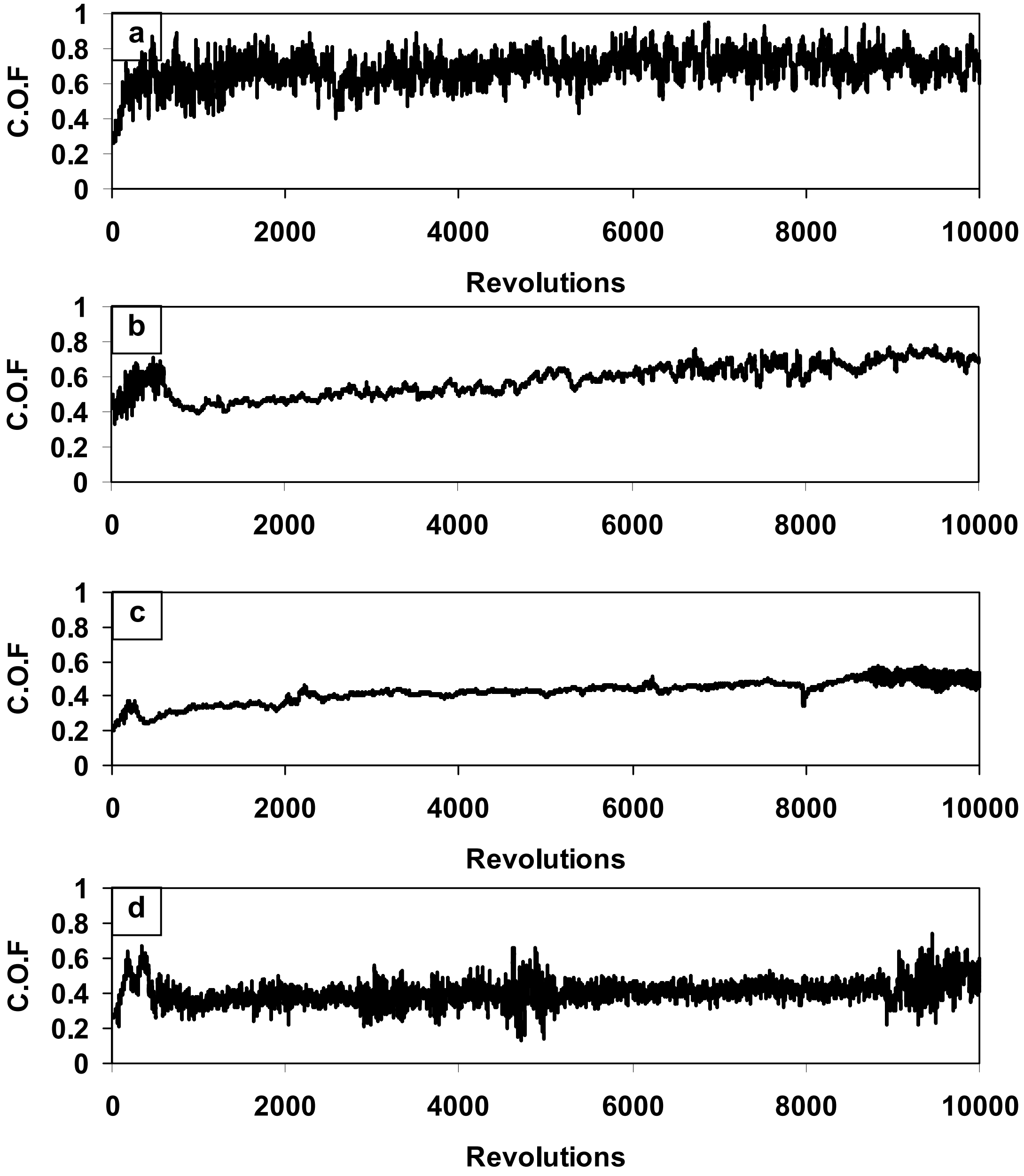

Fig. 4.53 Coefficient of friction (C.O.F) vs. sliding distance of coatings (a) R1, (b) R2, (c) R3 and (d) R4 during the dry sliding tests against aluminum counterface pins.

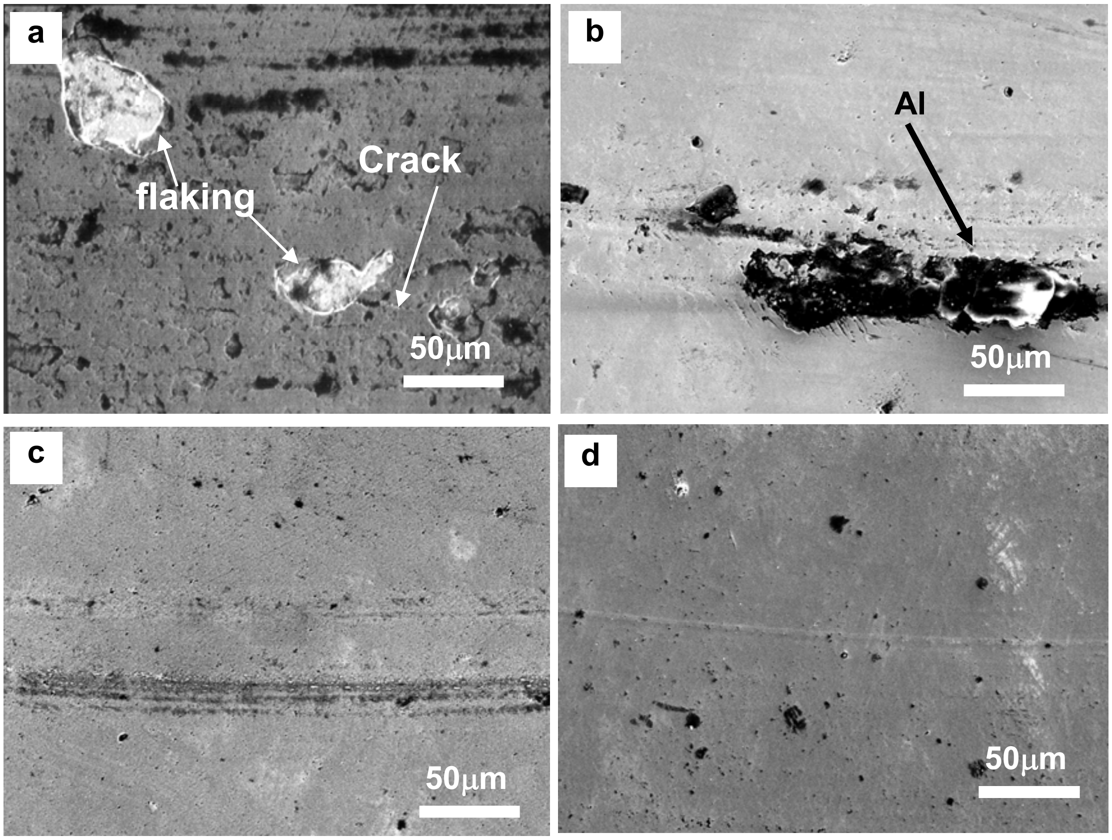

Fig. 4.54 SEM micrographs of wear track morphologies on coatings (a) R1, (b) R2, (c) R3, and (d) R4 after dry sliding tests against aluminum counterface pins.

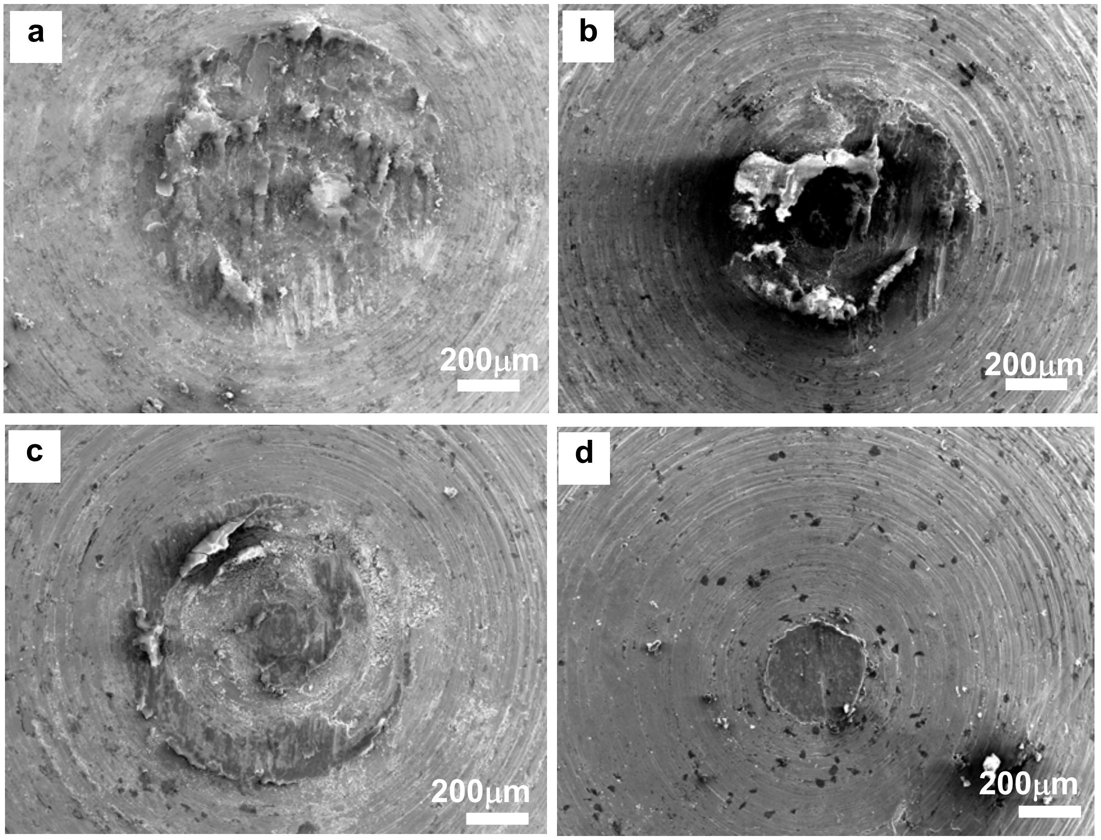

Fig. 4.55 SEM micrographs of the worn Al pins after dry sliding wear tests against coatings (a) R1, (b) R2, (c) R3, and (d) R4.

The cof curves during the wear test with coolant as lubricant are shown in Fig. 4.56 and average cof values are summarized in Fig. 4.57. The friction coefficient in the wear test with coolant as lubricant was much lower for all the four coatings, less than 0.2. Fig. 4.58 shows the SEM micrographs of wear tracks on the coatings after wear tests in the coolant. Slightly abrasive wear can be observed on coatings R1, R2 and R4 (shown in Figs. 4.58(a, b, d), respectively). On the wear track of coating R3 (Fig. 4.58(c)), no abrasion but a little polishing can be observed. On worn counter pin surfaces after the wear tests in coolant, slightly abrasive scars can be observed. Under the coolant lubricate condition, the counterface Al pins showed little wear (Fig. 4.59).

The coolant used in this research is a solution of concentrated water soluble oil (S500 produced by Hangsterfer Laboratories) which is generally comprised of 60-90% petroleum or mineral oil, emulsifiers and other additives. Soluble oils offer good lubrication due to the blending of oil and water. However, a number of precipitate particles were observed on both counterface pins and wear tracks. The precipitates probably were formed when the concentrated coolant mixed with water during the diluting. Those particles would act as three-body abrasive particles between the Al pin and coating material. Due to its higher hardness, coating R3 exhibited a better abrasive wear resistance than other coatings. It should be noted that the abrasive scar on coating R4 (with the thinnest layer thickness) was obviously deeper than that of on the others, which implies that the tribo-eletrochemical reaction might also occur during the wear process in the coolant. Thus, a caution on tribo-electrochemical reaction should be taken during the coating material selection and multilayer thickness design.

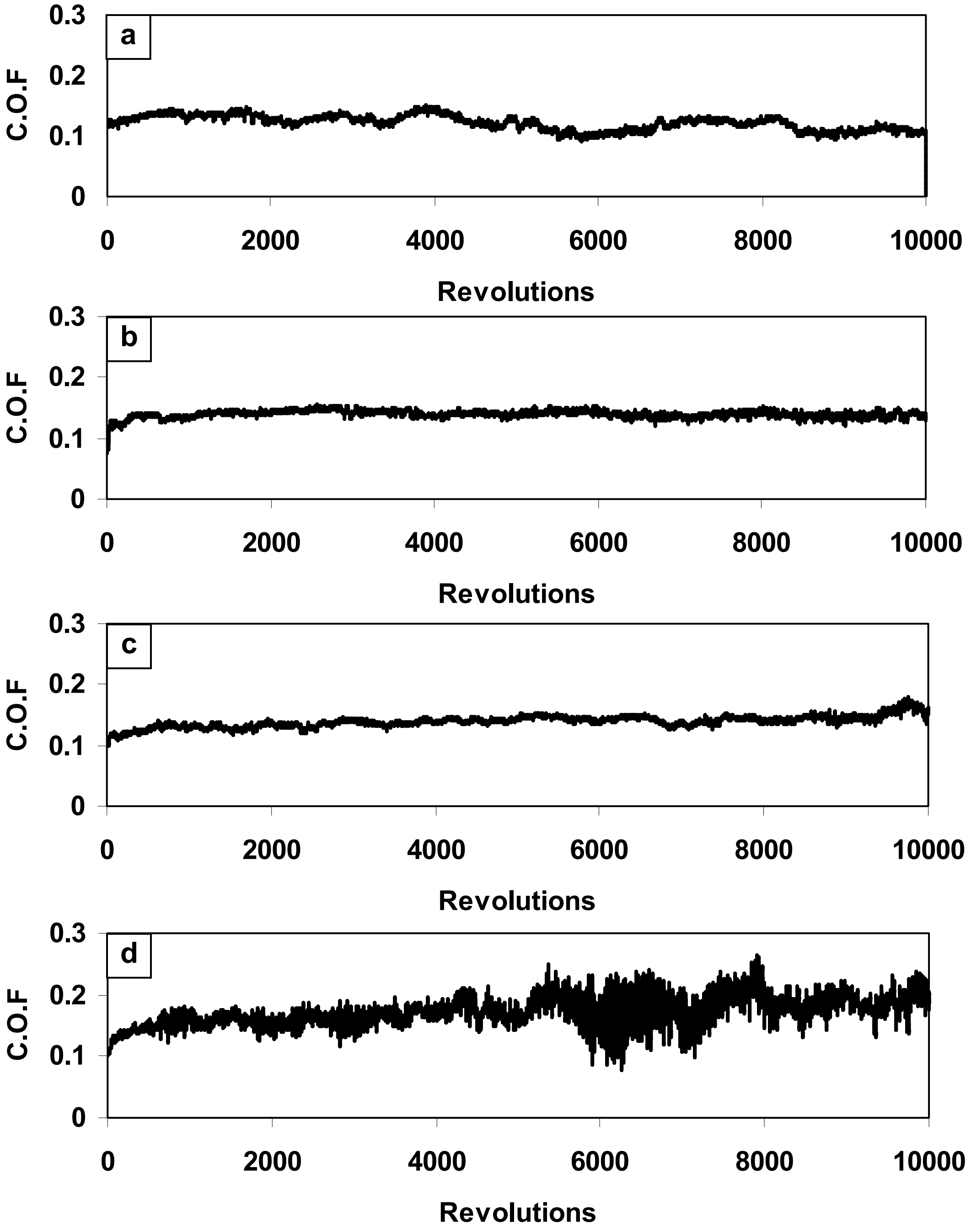

Fig. 4.56 Coefficient of friction (C.O.F) vs. sliding distance of coatings (a) R1, (b) R2, (c) R3 and (d) R4 during sliding tests with the coolant against aluminum counterface pins.

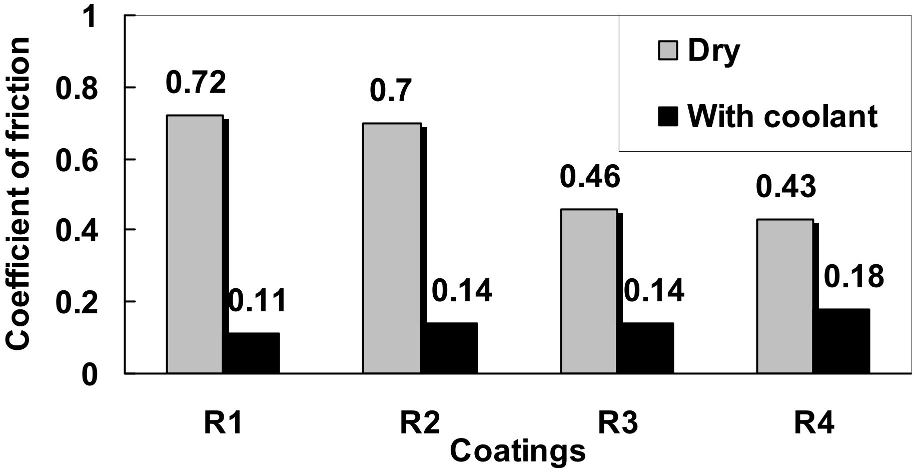

Fig. 4.57 Average friction coefficients of coatings at the stable stage of dry and wet sliding tests.

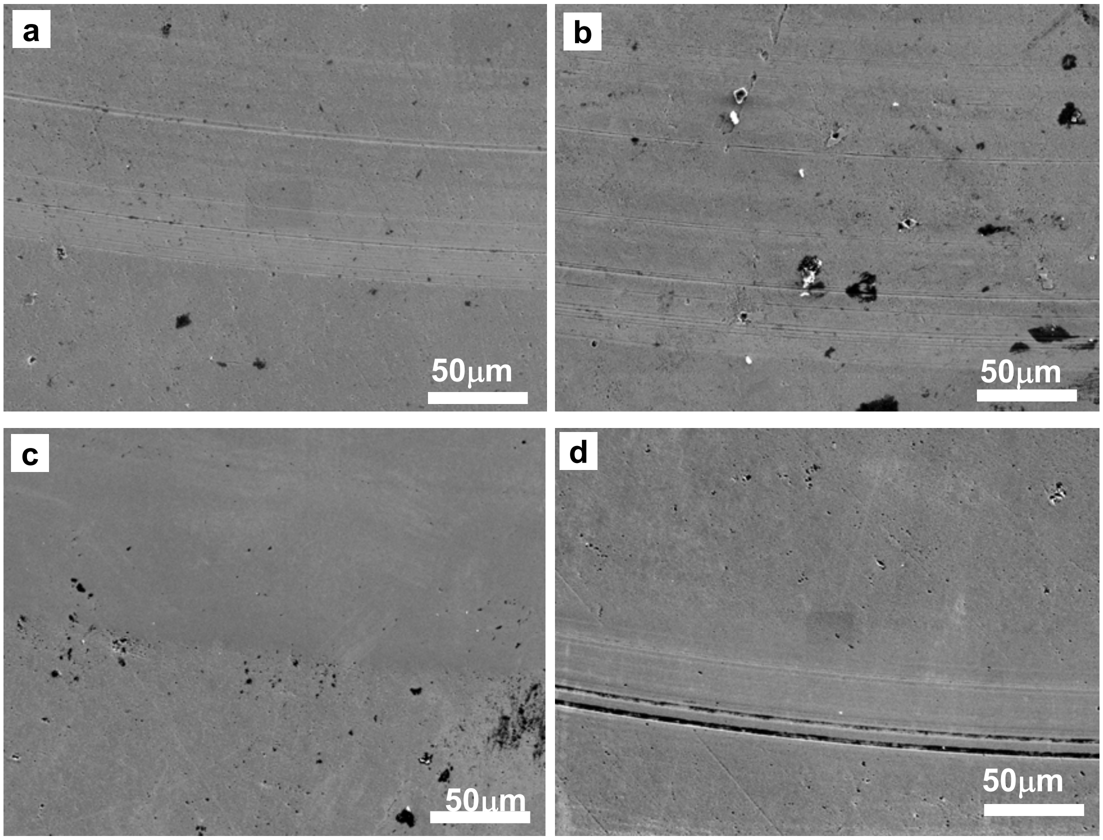

Fig. 4.58 SEM micrographs of wear tracks on coatings (a) R1, (b) R2, (c) R3, and (d) R4 after sliding tests with S500 coolant.

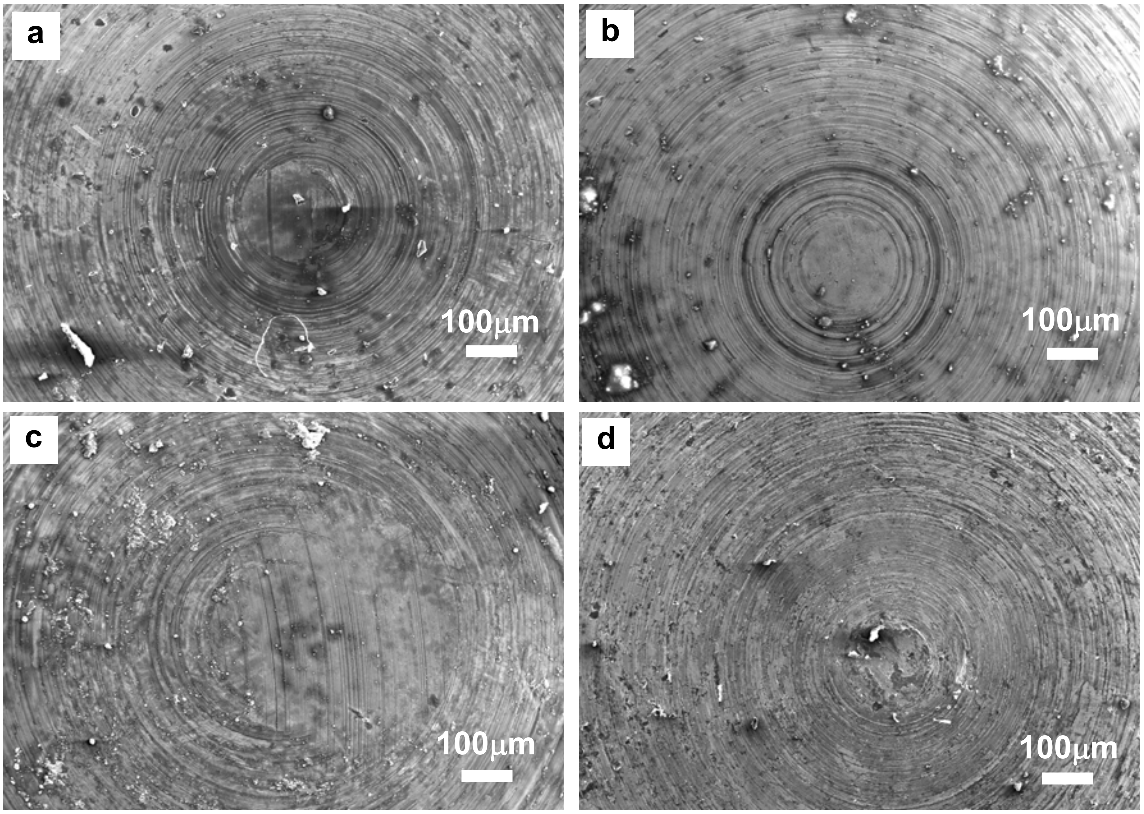

Fig. 4.59 SEM micrographs of the worn Al pins after sliding wear tests with S500 coolant against coatings (a) R1, (b) R2, (c) R3, and (d) R4.

4.4 Summaries of Chapter 4

4.4.1 Effects of annealing temperature on the coating structure and mechanical properties

The coating damages resulting from the annealing occurred at 800 ^{o}C, 1000 ^{o}C and 900 ^{o}C for TiN, CrN and TiAlN coatings. At the annealing tempertures up to 1000 ^{o}C, CrAlN coating can still keep an intact surface morphology though some oxidization has occurred. DLC coating delaminating occurred beyond 400 ^{o}C annealing temperature.

For the TiN coating, the rutile structure TiO_2 begins to be detected after annealing at 600 ^{o}C by XRD and the TiO_2 phase increases with increasing annealing temperature. After 800 ^{o}C, little TiN phase was left. For the CrN coating, when annealing temperature $\leq$ 700 ^{o}C, no any Cr oxides can be detected. The Cr_2O_3 phase occurred above 700 ^{o}C and above 700 ^{o}C, the phase compositions of coatings are CrN, Cr_2O_3 and Cr_2N. Relative intensity of Cr_2O_3 generally increases with rising temperature. A rutile TiO_2 structure begins to exist in the TiAlN coating after 700 ^{o}C annealing. Besides formation of more TiO_2 phase, an aluminum titanium oxide nitride compound, $Al_{0.54}Ti_{2.46}N_{0.28}O_{4.58}$ can be detected on the TiAlN coating after annealing at 800 ^{o}C. After annealing at 600 ^{o}C, a weak Al_2O_3 peak was observed. No other evident oxide peaks could be detected. When the annealing temperature was even increased up to 900 ^{o}C, the CrAlN phase was still very strong.

Due to the change of coating structure, the mechanical properties of coatings are correspondingly changed as follows in Fig. 4.60.

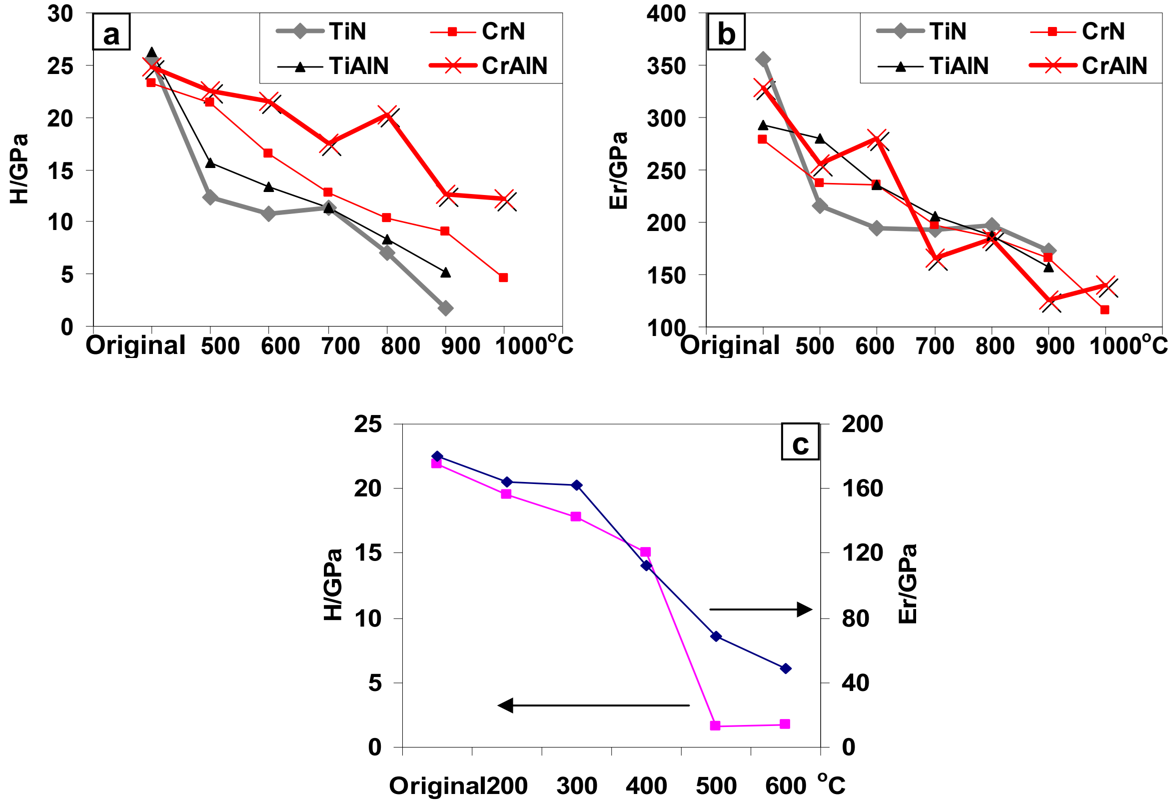

Fig. 4.60 Hardness (H) and reduced elastic modulus (E_r) change with annealing temperature of (a, b) TiN, CrN, TiAlN, CrAlN and (c) DLC coatings.

At the same annealing temperature conditions, the CrAlN and TiN coatings always exhibits the highest and lowest hardness, respectively, among the coatings after the annealing treatments. For the DLC coatings, the large extend hardness drop occurred when the annealing temperature is above 400 °C which is from 15 GPa for D400 (400 °C) to less than 2 GPa for D500 and D600 (500 °C and 600 °C).

4.4.2 Effects of annealing temperature on the tribological properties and material transfer phenomena of TiN, CrN, TiAlN and CrAlN coatings under pin-on-disc testing conditions

Against ceramic Al_2O_3 balls. During the sliding wear tests against ceramic Al_2O_3 balls, little material transferred from Al_2O_3 balls to the coating surfaces but some detached coating and M2 substrate material attached on the balls surface. Thus, the abrasive wear is the dominated wear mechanism. The coating wear phenomena are listed in Table 4.7. The results of wear performance against Al_2O_3 balls indicate that for TiN, CrN, TiAlN and CrAlN, the oxide on the coatings resulted from annealing processes has served as a lubrication layer and thus the coatings exhibited a lower friction, while the hardness of annealed coatings plays a determinative role in the wear rate of coatings. Although TiAlN coating has an improved wear performance, CrN and CrAlN coatings are still superior to TiN and TiAlN coatings in this matter based on therein testing conditions.

Against steel balls. During the sliding wear tests against steel balls, the relatively soft steel balls were worn and the released materials were picked up and stuck on the coating surfaces. A large amount of material transferring occurs and it is believed that adhesive wear is the main wear mechanisms. Due to the low hardness, severe adhesive wear occurred on TiN coating annealed at 500 ^{o}C. On the CrN coatings, though a large amount of material transferring occurred, much less adhesive wear took place compared with the corresponding TiN coatings. The Al introduction into TiN did not improve the anti-sticking of steel properties significantly. Compared with TiAlN coating, less material transferring occurred on original CrAlN coating but severe material transferring happened on annealed CrAlN coatings. The coating CA800 (800 °C) has less material transferring than CA500 and CA700 (500 °C and 700 °C) which could be related to the formation of Al_2O_3 film that retards the adhesion between coating and Fe.

Against aluminium balls. During the sliding wear tests against aluminium balls, severe material transferring and adhesive wear occurred on all the un-annealed and annealed coatings TiN, CrN, TiAlN and CrAlN.

4.4.3 Effects of annealing temperature on the tribological properties and material transfer phenomena of DLC coatings under pin-on-disc testing conditions

The DLC coating has a very good properties of anti-sticking of steel and aluminum materials. However, above 400^{o}C annealing, the coating structure transforms to sp^2 graphite and the coating loses the strength and structure and thus the coating is not suitable for load bearing application.

4.4.4 Industrial trials of TiN and CrAlN coatings in an actual stamping plant

Industrial trials showed that the CrAlN-coated punch had a lifetime of more than 2.5 and 5 times longer than that of the TiN-coated and uncoated punches, respectively. Under the high shear force and stress during the stamping, peeling on the coatings initiated locally from the regions where machining grooves existed underneath. Compared with the CrAlN coating, the TiN coating had a higher Zn and Fe pick-up tendency, suggesting that adhesive wear could also be one of the mechanisms contributing to failure for the TiN coating. Improvement of the tool substrate surface finish is a way to further increase lifetime of the coated tools.

4.4.5 Development and characterization of Cr(CrN)/C(DLC) multilayered coating system used for dry machining of aluminium alloys

The bilayer thicknesses of four Cr(CrN)/C(DLC) coatings were determined by low-angle XRD, XPS plotting with an etch depth method and TEM cross-section observations. Similarity of three analysis methods in bilayer thickness determination was demonstrated. The nano-scale mechanical and wear property test results indicated that the coating with a 4.5 nm bilayer thickness had the best wear resistance and mechanical properties. In dry sliding tests, decreasing bilayer thickness structure achieved a lower friction. The coating with a thinner bilayer thickness exhibited a less intendancy in formation of fatigue cracks during sliding wear tests. The coolant as a lubricant provided a lower friction. The precipitates in the coolant could cause a significant scratching on the coatings. However, the thinnest bilayered coating (R4), which has the best anti-wear performance in the dry testing condition, exhibited the worst wear resistance in coolant environment.

Table 4.7 Wear phenomina of coatings against Al_2O_3 balls

Anneal.temp. (^oC)	Original	500	700	800
TiN	Abrasive wear	Penetrated	Penetrated	penetrated
CrN	No visible wear	No visible wear	No visible wear	No visible wear
TiAlN	No visible wear	A little abrasive wear	A little abrasive wear	Partially penetrated
CrAlN	Surface polishing	Surface polishing	Surface polishing	Surface polishing
Anneal. temp (^oC)	Original	300	400	600
DLC	A little abrasive wear	A little abrasive wear	A little abrasive wear	penetrated

CHAPTER 5 PERFORMANCE OF COATINGS AT THE SIMULATED PEM FUEL CELL ENVIRONMENT

5.1 Contact resistance (CR)

The preliminary electrical resistance screening test results indicated that DLC and multilayered CrAlN coatings had very high electrical resistance which is about 100 times higher than the SS316. Thus, these two coatings are not suitable for the application in bipolar plates in PEM fuel cells and the study in this section focuses on TiN, CrN and TiAlN coatings. Besides the high electrical resistance of diamond phase (sp^3) in the DLC coating, hydrogen in DLC also plays an important role: hydrogencarbon (H-C) bonds in DLC produce large free spaces in the structure, which inhibit conductive routes and lead to high electrical resistivity [59]. The reason of the high electrical resistance of CrAlN coating is not clear so far and it could be related to the interface effect in the multilayered structure.

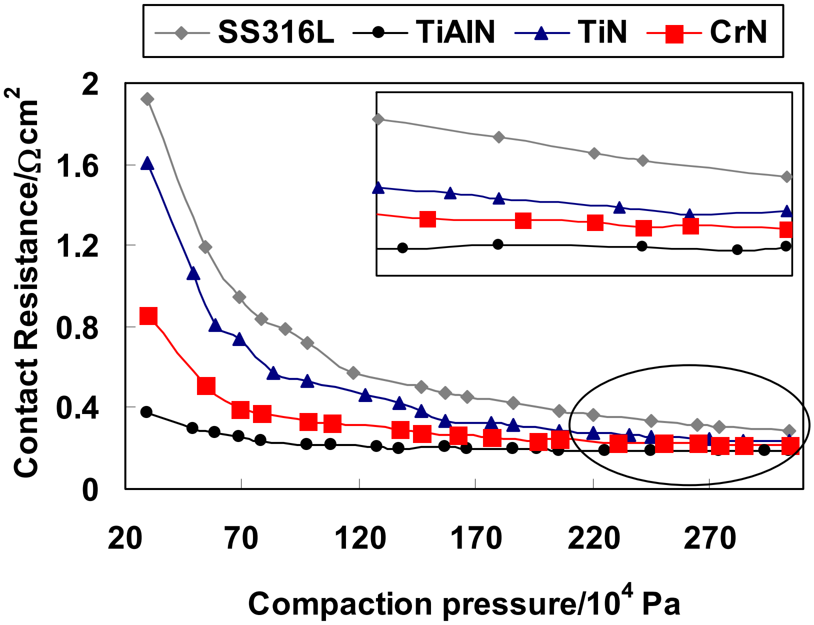

Fig. 5.1 Contact resistances for the coated and uncoated stainless steel samples.

The results of comparative contact resistances of the coated and uncoated samples are shown in Fig. 5.1. The insert in Fig. 5.1 is an expanded plot at compacting pressures in the range 2.2 to 3.0 MPa. With increasing compaction pressure, the contact resistance of the sample materials decreases rapidly at low compaction pressures (<0.7 MPa) and then decreases gradually at higher compaction pressures. At a given compaction pressure, the contact resistance increases in the order of TiAlN< CrN< TiN< SS316L. For example, at a compaction pressure of 2.0 MPa, the contact resistance of TiAlN, CrN, TiN and uncoated SS316L are 191.1, 241.6, 289.5 and 385.5 $m\Omega.cm^2$, respectively. The uncoated stainless steel sample has a higher CR than all the coated samples, which can be attributed to the natural oxide layer on the steel surface. The contact resistance of the CrN coating is slightly lower than TiN coating. The TiAlN coating has the lowest contact resistance. Given the fact that these deposited coatings have a similar surface roughness (R_a<0.1 μm), coating thickness and the same substrate material, the comparative contact resistance (Fig.5.1) is determined by the interfacial contact resistances (ICR) between flat carbon papers and the surface of tested specimen ($R_{cp}/_{Rs}$) plus the electrical resistance of coatings (R_{film}). According to the band structure, strongly hybridized N 2p and Ti 3d orbitals contribute nine valence electrons to the electrical conductivity of TiN [19]. The Al atoms introduced into the TiN structure could generally give a polar interphase resulting in metallic bonding between Ti-Al or covalent bonding (Ti-N and Al-N) [169] and therefore, lead to an increase in the electrical conductivity of the TiAlN coating compared with the TiN coating. It has been reported that the electrical resistance of TiN and TiAlN coatings are significantly affected by the phase, N content and the defect density in the coatings [19, 169, 170]. For example, since AlN is a good electrical insulator, the electrical conductivity of a TiAlN coating should be significantly decreased if the hexagonal AlN (B4 wurtzite) structure is present in a TiAlN coating. However, there was no AlN phase formed in the TiAlN coating deposited in this study.

5.2 Potentiodynamic polarization behavior

Fig.5.2 shows the potentiodynamic polarization curves for TiN-, CrN-, TiAlN-coated, and uncoated SS316L specimens in the simulated anodic and cathodic environments of a fuel cell, i.e., with H_2 purging (Fig. 5.2(a)) and O_2 purging (Fig. 5.2(b)). The corrosion potential (E_{corr}), current density (i_{corr}) and polarization resistance (R_p) obtained by Tafel calculations for uncoated and coated SS316L are given in Table 5.1. The corrosion resistances in anodic and cathodic environments increase in the order of TiAlN<SS316L<CrN<TiN and TiAlN<TiN<CrN<SS316L, respectively.

Regarding the effect of H_2 or O_2 on the corrosion properties of uncoated and coated samples, Figs. 5.3-5.6 are presented to show the comparative polarization curves in H_2 and O_2 environments and the surface morphologies of the corresponding corroded areas. The SS316L substrate exhibits a typical polarization curve in either H_2 or O_2 (Figs. 5.3 (a)) bubbled environments. The corrosion potential (E_{corr}) in the O_2 bubbled environment (-0.24 V) is higher than that in the H_2 bubbled environment (-0.27 V) and corrosion current density is about 10 times lower in the former environment than in the latter one. This is not unexpected, because stainless steel is more readily passivated in an O_2-containing environment and the passive layer formed is more stable and thicker than in a H_2-containing environment [97]. Figs. 5.3(b, c) show the micrographs of the surfaces of both uncoated samples after the potentiodynamic polarization tests under H_2 and O_2

environments, respectively. Pits and etched grain boundaries can be observed in both micrographs.

Table 5.1 Potentiodynamic polarization parameters of uncoated and coated SS316L in a 1 M H_2SO_4 solution with either H_2 or O_2 purging

		β_a (V/dec)	β_c (V/dec)	E_{corr}/V	$i_{corr}/\mu Acm^{-2}$	R_P (Ωcm^2)
SS316L	H_2	0.075	0.093	-0.27	20.20	893.63
	O_2	0.048	0.064	-0.24	1.90	6276.56
TiN	H_2	0.14	0.11	-0.38	4.07	6580.49
	O_2	0.057	0.036	-0.34	31.50	304.55
CrN	H_2	0.011	0.0096	-0.32	1.41	1580.70
	O_2	0.021	0.025	-0.34	1.31	3787.93
TiAlN	H_2	0.027	0.032	-0.36	317.00	20.09
	O_2	0.018	0.020	-0.36	18.60	221.45

* βa, βc, E_{corr}, i_{corr}, and R_p are the Tafel slopes of the anodic and cathodic reactions, the corrosion potential, corrosion current density and polarization resistance, respectively.

For the TiN coated sample (Fig. 5.4(a)), the corrosion potential is higher in the O_2 bubbled environment (-0.34 V) than in the H_2 bubbled environment (-0.38 V) but corrosion current density is higher in the former environment. The corrosion resistance of TiN in the H_2 purged environment is 20 times higher than that in the O_2 purged environment. No pits or corrosion products could be found on the surface of the TiN-coated sample after tested in the same conditions (Figs. 5.4(b, c)). The potentiodynamic polarization curves of TiN coating in H_2 and O_2 environments (Figs. 5.4(a)) show that at the final testing potential (1.2 V vs. Ag/AgCl electrode), the curves have not yet reached a transpassive state of the coating and therefore no pitting corrosion can be detected by SEM observation and EDX analysis. This characteristics may allow the TiN-coated bipolar plate to be used in a PEMFC system operating at a high cathodic potential (> 0.6V) with a less transpassive corrosion susceptibility compared to the SS316L plate.

The effect of gas purging is not significant for the CrN coating (Fig. 5.5(a)) and the corrosion current density and corrosion potential are similar in both environments. Figs. 5.5(b, c) are the micrographs of CrN surface after potentiodynamic corrosion tests in the anodic and cathodic environments, respectively. Both surfaces are quite smooth. However, one pit can be found on the CrN coating after potentiodynamic corrosion tests (the inserts in Figs 5.5(b, c)). Some corrosion product can be observed in cathodic condition (the inserts in the Fig. 5.5(c)). From the EDX analysis, the corrosion product is shown to be Cr-N-O-Fe compounds.

The TiAlN-coated SS316L (Fig. 5.6(a)) has a similar corrosion potential in either a H_2 or O_2 environment but a higher corrosion current density in H_2 environment than in O_2 environment (Table 5.1). For the CrN and TiAlN coatings, the corrosion resistances in the simulated cathodic environment are 2 and 11 times higher than those in an anodic environment. The TiAlN coating has been corroded severely in both anodic and cathodic environments (Figs. 5.6(b, c)) and had an uneven corroded surface which could be observed even by the naked eye.

From the potentiodynamic polarization curves (Fig. 5.2(a)), at the anode application potential (E_{ap}), i.e., -0.1 V vs. Ag/AgCl electrode, the SS316L is in the passive state. However, since the primary passive potential (E_{pp}) is -0.15V which is close to the anode potential, the current density of SS316L at -0.1 V is still very high at 1.53 ×

10^{-4} A/cm^2. The E_{pp} in the anodic environment of TiN, CrN and TiAlN coatings are -0.26, -0.23 and -0.17 V, respectively. Thus, at the E_{ap}, the TiN-, CrN- and TiAlN-coated materials are all in a passive state, with corrosion current densities of 1.04× 10^{-5}, 2.10× 10^{-5}, and 3.96 × 10^{-2} A/cm^2, correspondingly. At the cathodic environment (Fig. 5.2(b)) and cathodic application potential (E_{cp}= +0.6 V vs. Ag/AgCl electrode), the uncoated and TiN-, CrN-, TiAlN-coated specimens are all in the passive state (Fig. 5.2(b)), the current density are 1.0× 10^{-5}, 1.16× 10^{-4}, 5.24× 10^{-5}, and 1.69× 10^{-2} A/cm^2, respectively. At the simulated anodic conditions, the current density of CrN is lower than that of TiN but in the same order of magnitude (10^{-5} A/cm^2), which is 1 order magnitude lower than that of uncoated SS316L. In the simulated cathodic conditions (Fig. 5.2(b)), uncoated SS316L has the lowest corrosion current density and the CrN coating has a lower current density than the TiN coating.

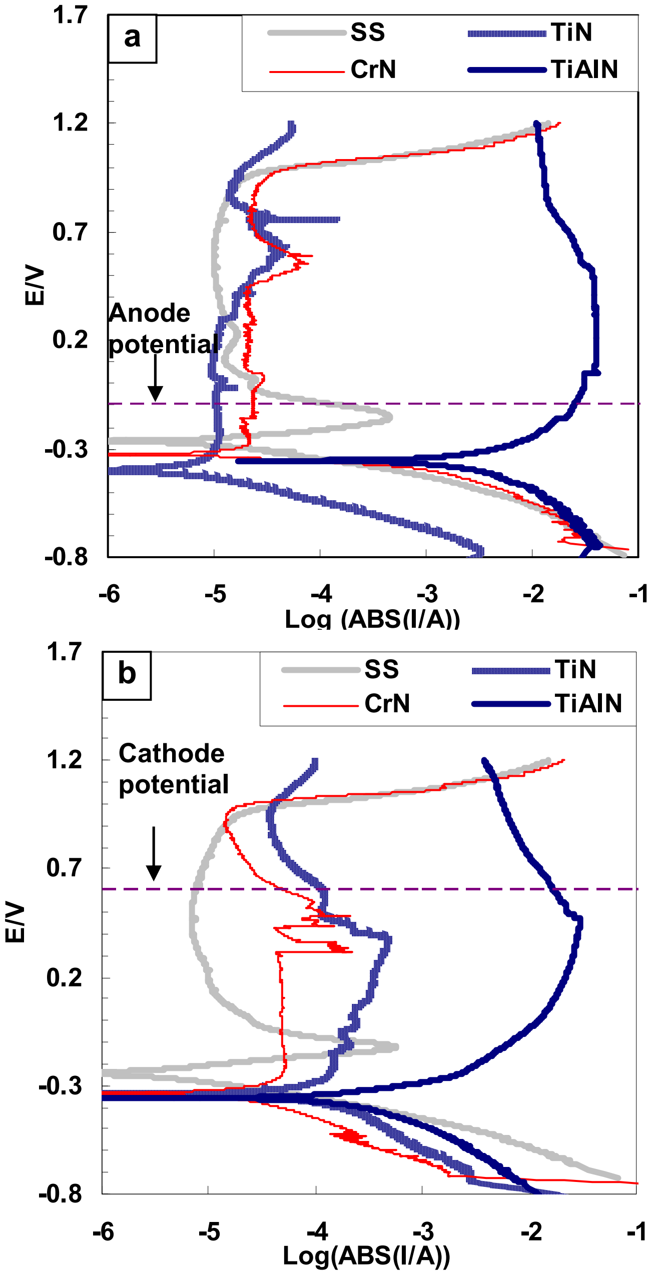

Fig. 5.2 Potentiodynamic polarization curves for TiN-, CrN-, TiAlN-coated and uncoated stainless steel 316L samples in a 1 M sulphuric acid solution at 70 °C with (a) H_2 purging and (b) O_2 purging.

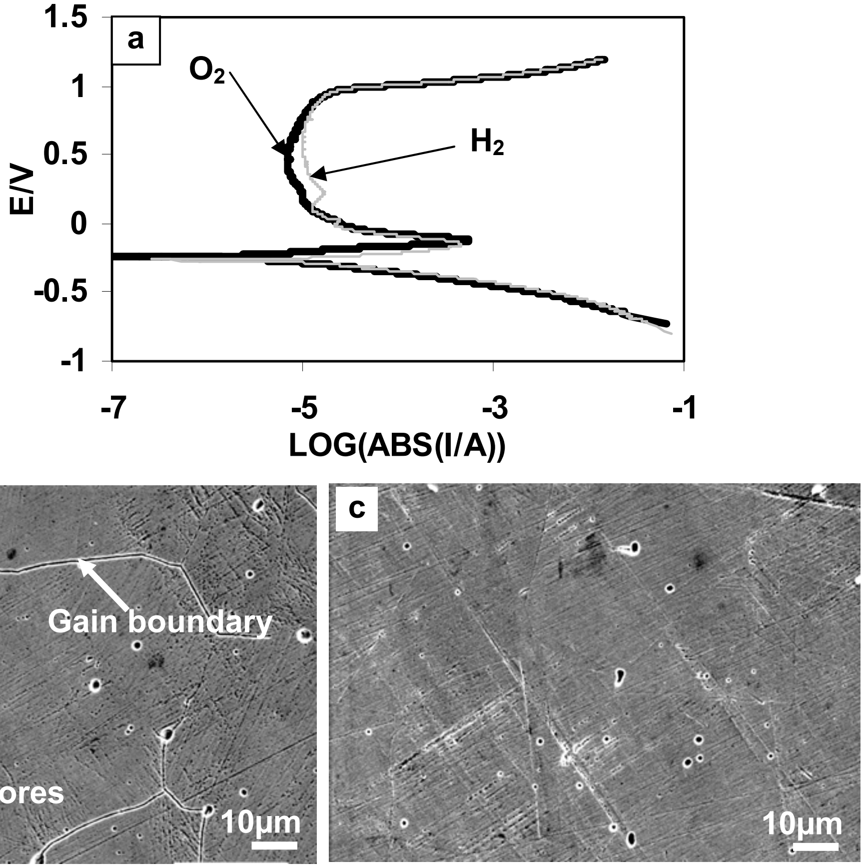

Fig. 5.3 (a) Comparative potentiodynamic polarization curves for uncoated SS316L samples in a 1 M sulphuric acid solution at 70 ^{o}C with either H_2 purging or O_2 purging. (b, c) are the SEM micrographs of corroded area after the potentiodynamic corrosion tests with (b) H_2 and (c) O_2 purging.

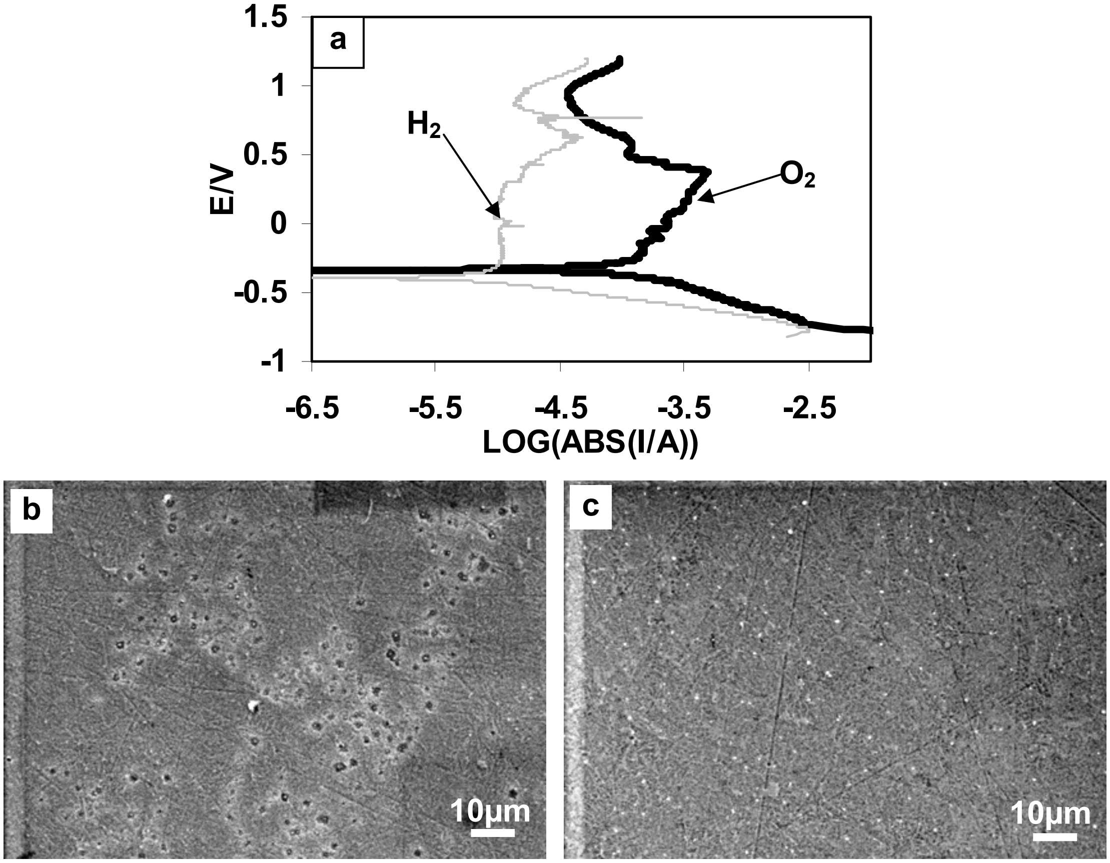

Fig. 5.4 (a) Comparative potentiodynamic polarization curves for TiN-coated samples in a 1 M sulphuric acid solution at 70 °C with either H_2 purging or O_2 purging. (b, c) are the SEM micrographs of the corroded area after the potentiodynamic corrosion tests with (b) H_2 and (c) O_2 purging.

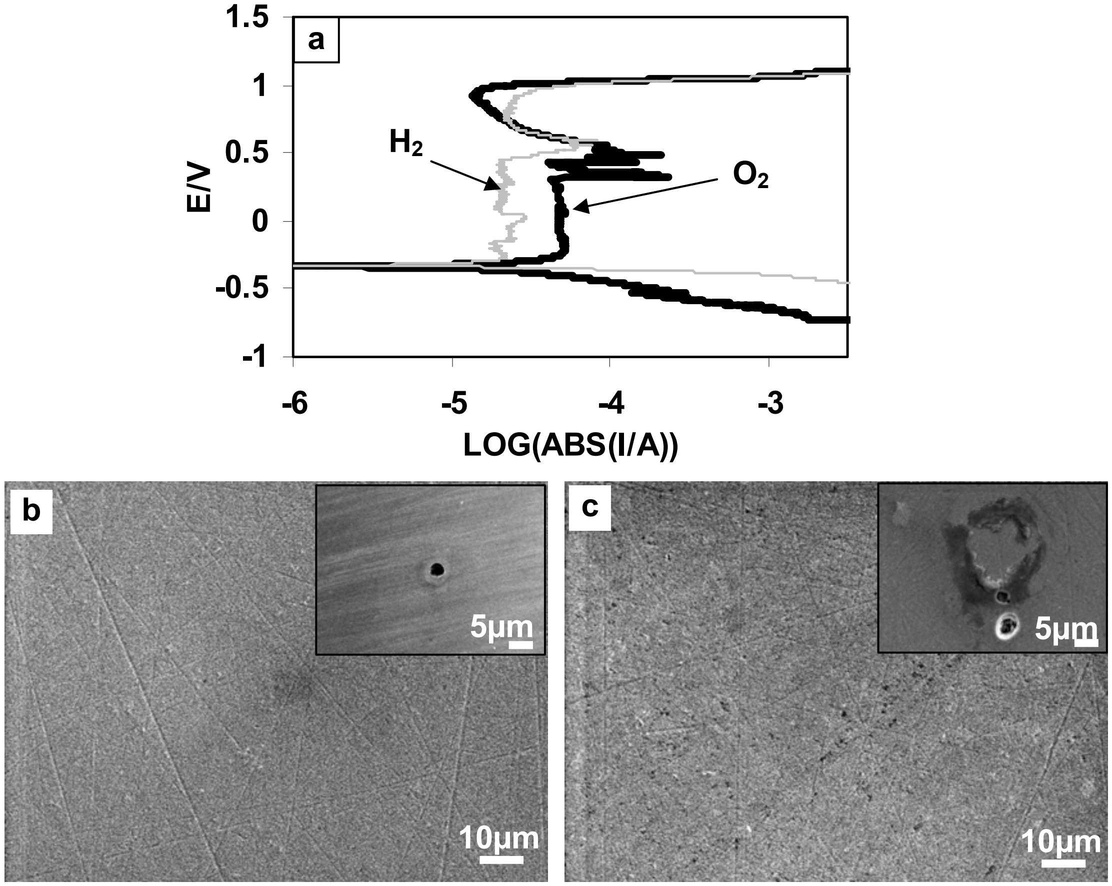

Fig. 5.5 (a) Comparative potentiodynamic polarization curves for CrN-coated samples in a 1 M sulphuric acid solution at 70 ^{o}C with either H_2 purging or O_2 purging. (b, c) are the SEM micrographs of the corroded area after the potentiodynamic corrosion tests with (b) H_2 and (c) O_2 purging.

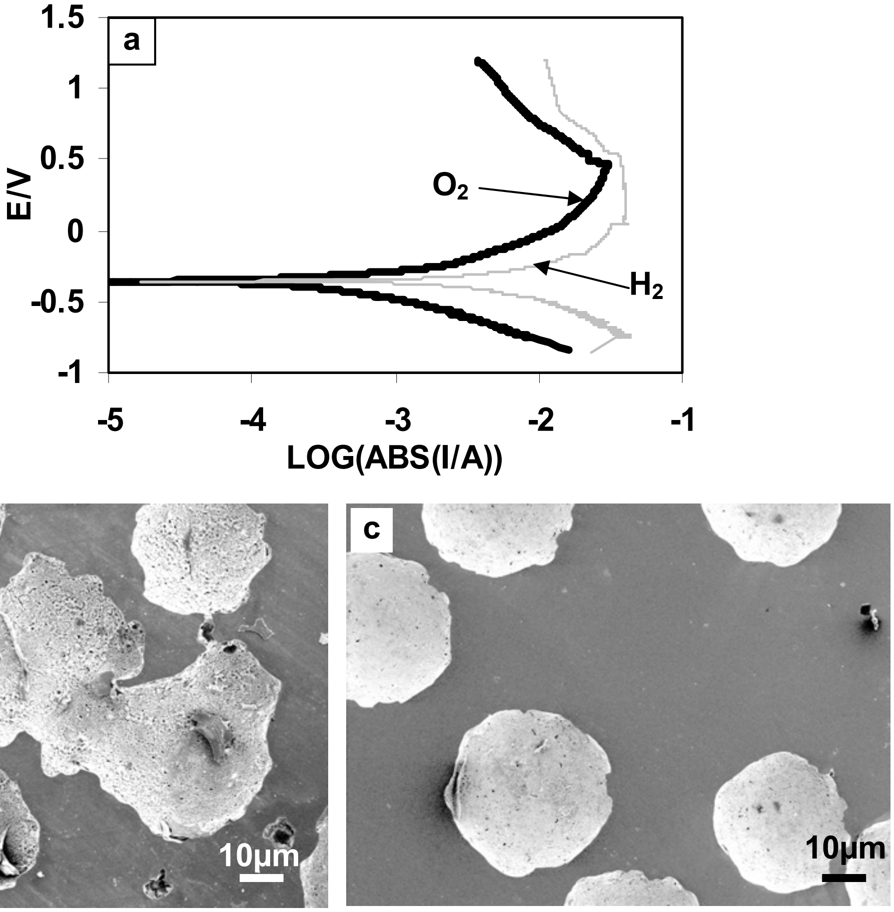

Fig. 5.6 (a) Comparative potentiodynamic polarization curves for TiAlN-coated samples in a 1 M sulphuric acid solution at 70 °C with either H_2 purging or O_2 purging. (b, c) are the SEM micrographs of the corroded area after the potentiodynamic corrosion tests with (b) H_2 and (c) O_2 purging.

5.3 Potentiostatic corrosion tests

Figs. 5.7(a) and 5.7(b) show the potentiostatic polarization curves at -0.1 V vs. Ag/AgCl electrode in a H_2-purged solution (anodic environment) and +0.6 V vs. Ag/AgCl electrode in an O_2-purged solution (cathodic environment), respectively.

In the anodic environment, SS316L (Fig. 5.7(a)) shows a slight increase in the anodic current density during the first 0.5 hours then becomes stable and finally reaches 145 $\mu A/cm^2$ at the end of the test. At the beginning stages, the TiN- and CrN-coated materials show lower polarization current densities than the stainless steel (Fig. 5.7(a)) at -0.1V vs. Ag/AgCl electrode which is consistent with the potentiodynamic polarization curves (Fig. 5.2(a)). For example, at the 10 minute test time, the polarization current densities of TiN, CrN and SS316L are 1.04×10^{-5}, 1.79×10^{-5} and 5.18×10^{-5} A/cm^2, respectively. However, after about 35 minutes test time, the current densities of the TiN- and CrN-coated specimen are higher than that of stainless steel and reach up to $0.01 A/cm^2$ magnitude. The TiAlN coating is rapidly corroded in the simulated anodic testing environment and the current density increases from 10^{-4} to 10^{-2} A/cm^2 magnitude.

In the simulated cathodic environment, i.e., +0.6 V application potential and oxygen purging, the potentiostatic polarization curves are shown in Fig. 5.7(b). Compared with the curves for tests in the anodic environment (Fig. 5.7(a)), the current densities of all the samples in the cathodic environment are much lower. At the early period (about 45 minutes), the current densities increase in the order of SS316L<CrN<TiN<TiAlN which is consistent with the potentiodynamic corrosion test results (Fig. 5.2(b)). After 45 minutes test time, the polarization current density of CrN-coated and uncoated SS316L are similar which is about 1.1 $\mu A/cm^2$. The current density

of TiN (18.0 μA/cm^2) is higher than those of CrN coating and SS316L. The TiAlN coating, in the initial stages, has a current density similar to the CrN coating; however, the current density gradually increases with time and reaches 0.001 A/cm^2 at the end of test which is 2 and 3 orders of magnitude higher than that of the CrN and TiN coatings.

To investigate the corrosion performance under anodic and cathodic conditions, Figs. 5.8-5.11 show the comparative potentiostatic polarization curves of uncoated and coated SS316L samples under simulated anodic and cathodic conditions, and the SEM micrographs and EDX spectra on the corroded surfaces.

The comparative potentiostatic polarization curves of SS316L indicate that SS316 presents a much higher current density in anodic condition than in cathodic condition (Fig. 5.8(a)). The SEM micrograph in Fig. 5.8(b) shows that in the anodic environment, on uncoated SS316L surface, pits and etched grain boundaries can be clearly observed. After testing in the cathodic environment (Fig. 5.8(c)), corrosion occurs not only at the grain boundaries but also over the entire surface and some brown corrosion products are presented. The EDX spectra (Figs. 5.8(d, e)) indicate that under the both conditions, after corrosion tests, some oxide can be detected.

Although the TiN coating under an anodic condition at the beginning stage of the testing time presented a lower current density than under a cathodic condition, the current density under the anodic condition became much higher than that under the cathodic condition with the increase of testing time (Fig. 5.9(a)). Also, CrN and TiAlN coatings (Figs. 5.10(a) and 5.11(a)) presented a lower current density under cathodic conditions than anodic conditions.

For both the TiN and CrN coatings after potentiostatic polarization testing in the anodic environment (Figs. 5.9(b) and 5.10(b) respectively), there was a large pit in their corroded areas though no corrosion or corrosion deposits were observed at the other regions of the corrosion test areas. However, for the TiN and CrN coatings in the cathodic environments (Figs. 5.9(c) and 5.10(c)), no pits or corrosion deposits were observed but general overall corrosion had taken place. Thus, the TiN and CrN coatings can protect the stainless steel from corrosion and the corrosion current density is indeed lower at the anode potential condition for the test of the early stage compared with uncoated stainless steel. These observations imply that in the anodic conditions, the corrosion initiated at some specific location, such as a pinhole in the coating structure, which were formed during the PVD deposition processes. Around the initial corrosion spot, the coating cracked and spalled off due to the adhesion failure along the coating/substrate interface. With an increase in exposure time, a large pit gradually formed. For the TiN and CrN coatings in the cathodic environment (Figs. 5.9(c) and 5.10(c)), no pits or corrosion deposits were observed but general overall corrosion had taken place. Thus, the TiN and CrN coatings can protect the stainless steel from corrosion at the anode application potential since the corrosion current density of the coatings is lower than that of the uncoated stainless steel as shown in both the potentiodynamic polarization test (Fig. 5.2(a)) and at the early stages of the potentiostatic corrosion tests (Fig. 5.7(a)). However, any pinholes existing in the corrosion test area of TiN and CrN coatings can provide a site for enhanced local corrosion. After some period of testing, the stainless steel substrate began to corrode at the pinhole site. Based on the potentiodynamic polarization corrosion curves (Fig. 5.2(a)), the stainless steel substrate exhibited a higher current density than the TiN- and CrN-coated materials in the anodic environment (anode application voltage: -0.1 V vs. reference electrode in H_2 bubbled environment). Thus, in the anodic environment, accelerated and localized corrosion would occur in pinhole sites due to the small exposed surface area of the stainless steel substrate within the pinholes. However, in the cathodic environment (cathode application voltage: +0.6 v vs. reference electrode in O_2 bubbled environment), the substrate stainless steel had a lower corrosion current density than the TiN and CrN coatings based on the potentiodynamic polarization corrosion tests at simulated cathodic conditions (Fig. 4.2(b)). The large surface areas of the coatings, which have less corrosion resistance than stainless steel in the cathodic environment, would exhibit general corrosion instead of the localized corrosion. Thus, at the cathodic conditions, the negative effect of pinholes in the coatings on the corrosion resistance is minor. Moreover, the cathodic environment also provided the coatings with better passivation ability compared with the anodic environment. Since a passive Cr oxide layer on the CrN coating is believed denser than a passive Ti oxide layer on the TiN coating [171], the CrN coating is superior to the TiN coatings in both anodic and cathodic environments.

Figs. 5.11(b, c) show that the TiAlN coating has the worst corrosion resistance under the potentiostatic test conditions. In the simulated anodic conditions (Fig. 5.11(b)), after about 40 mins potentiostatic testing, the current density reaches $0.1A/cm^2$ and the TiAlN coating almost disappears in the corroded area and the stainless steel substrate is exposed. In the cathodic conditions (Fig. 5.11(c)), after 4 hours potentiostatic testing several large pits could be observed even by the naked eye.

The TiAlN coating exhibits a number of large corroded areas. At the TiAlN coating surface, a Ti-Al-O passive layer existed naturally which may readily dissolved in sulfuric acid solution. Therefore, unlike the situation for cutting tool applications, where the TiAlN coating has a higher hardness and improved high temperature oxidation resistance compared to a TiN coating, the partial replacement of Ti with Al in the cubic TiN structure likely degrades the corrosion resistance of the coating in the simulated PEMFC conditions. It should be noted that the chemical composition of the TiAlN coating in this study is Ti:Al:N=35:15:50 (at.%) and no the AlN phase exists in the coating. TiAlN coatings with different chemical composition and phase structure could exhibit different electrochemical behavior.

Compared with the stainless steel 316L, the CrN coated material has a better corrosion resistance in the anode environment in potentiodynamic polarization corrosion tests and a similar corrosion resistance in longer time potentiostatic corrosion tests in the cathode environment. Given that the contact resistance of the CrN coated SS316L is significantly lower than that of the uncoated SS316L reference material, the PVD CrN coated SS316L could be used as an alternative bipolar plate material since it would have both a lower contact resistance and higher corrosion resistance.

Generally speaking, this study provided a better understanding of PVD coatings performance in simulated anodic and cathodic environments of PEMFCs and as a result, some new directions for future research on PVD coatings can be suggested. As well as developing new coating materials, eliminating pinholes will be among the most critical tasks, particularly for the coatings applied to the anode bipolar plates. EBPVD is usually considered as a better coating deposition process than either magnetron sputtering or cathodic arc PVD in terms of coating smoothness and density. Fewer pinholes are also produced in EBPVD coatings, compared to the coatings prepared by magnetron sputtering and cathodic arc deposition processes [172]. More attention should be paid to the cleanliness of the substrates before coating and the contamination in the vacuum chamber to help avoid pinhole formation. An interrupted coating process, or multilayered coatings, may "disconnect" the pinholes and prevent through-coating pinholes. A CrN/TiN multilayered coating may be able to synergistically combine their advantages (i.e., TiN is better as an anode and CrN is better as a cathode material) for a universal coating that has superior performance as both anodic and cathodic electrodes.

5.4 Summaries of Chapter 5

The ranking for the electrical contact resistance (CR) is TiAlN < CrN < TiN < SS316L.

The potentiodynamic polarization test results showed that the O_2 and H_2 environments significantly affected the polarization characteristics of the TiN-based coatings and SS316L, but less influenced that of the CrN coating. The TiAlN-coated and SS316L samples had a higher corrosion resistance in the cathodic environment (with O_2 purging) than in the anodic environment (with H_2 purging). On the other hand, the TiN coating had a higher corrosion resistance in the anodic environment than in the cathodic environment. The ranking for corrosion resistance in H_2 and O_2 bubbled environments is TiAlN<SS316L<CrN<TiN and TiAlN<TiN<CrN<SS316L, respectively.

The potentiostatic corrosion tests show that in the simulated anodic conditions (-0.1 V vs. Ag/AgCl electrode), both TiN and CrN have a lower corrosion current density than SS316L, but with increasing test time, the current density increases because corrosion has been initiated at pinholes in the coatings. In the simulated cathodic conditions, since the SS316L substrate at the pinhole sites can be readily passivated, and thus provide higher corrosion protection, the negative effect of pinholes in the coatings is minor. TiN has a higher corrosion current density than SS316L in the cathodic test conditions, whereas, the CrN coating shows a similar value to SS316L. The electrochemical test results indicate that the TiAlN coating prepared in this work has the poorest corrosion resistance in environments simulating operations in PEM fuel cells.

Since the EBPVD CrN coating has a low contact resistance and high (in the anodic environment) or similar (in the cathodic environment) corrosion resistance, compared with the SS316L, the CrN coated material can be used as an alternative bipolar plate material. The EBPVD process greatly reduced number of pinholes existing in the coatings compared to more conventional PVD processes but more research work is required to help eliminate pinholes for the long-term durability of such coatings for PEM fuel cell applications.

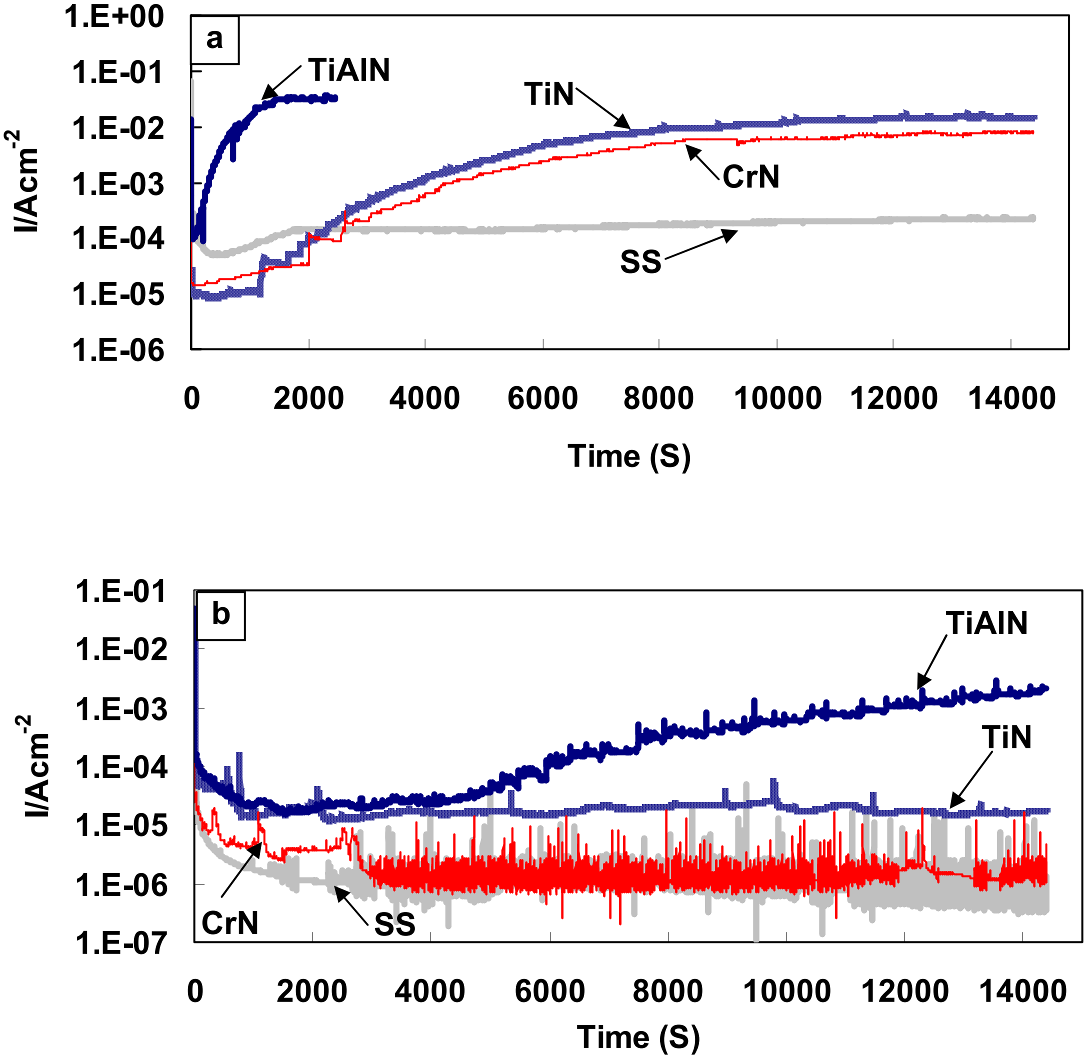

Fig. 5.7 Potentiostatic polarization behaviours of TiN-, CrN-, TiAlN-coated and uncoated stainless steel 316L at (a) -0.1 V vs. Ag/AgCl reference electrode with H_2 purging and (b) +0.6 V vs. Ag/AgCl reference electrode with O_2 purging in a 1 M sulphuric acid solution at 70 ^{o}C for 4 hours.

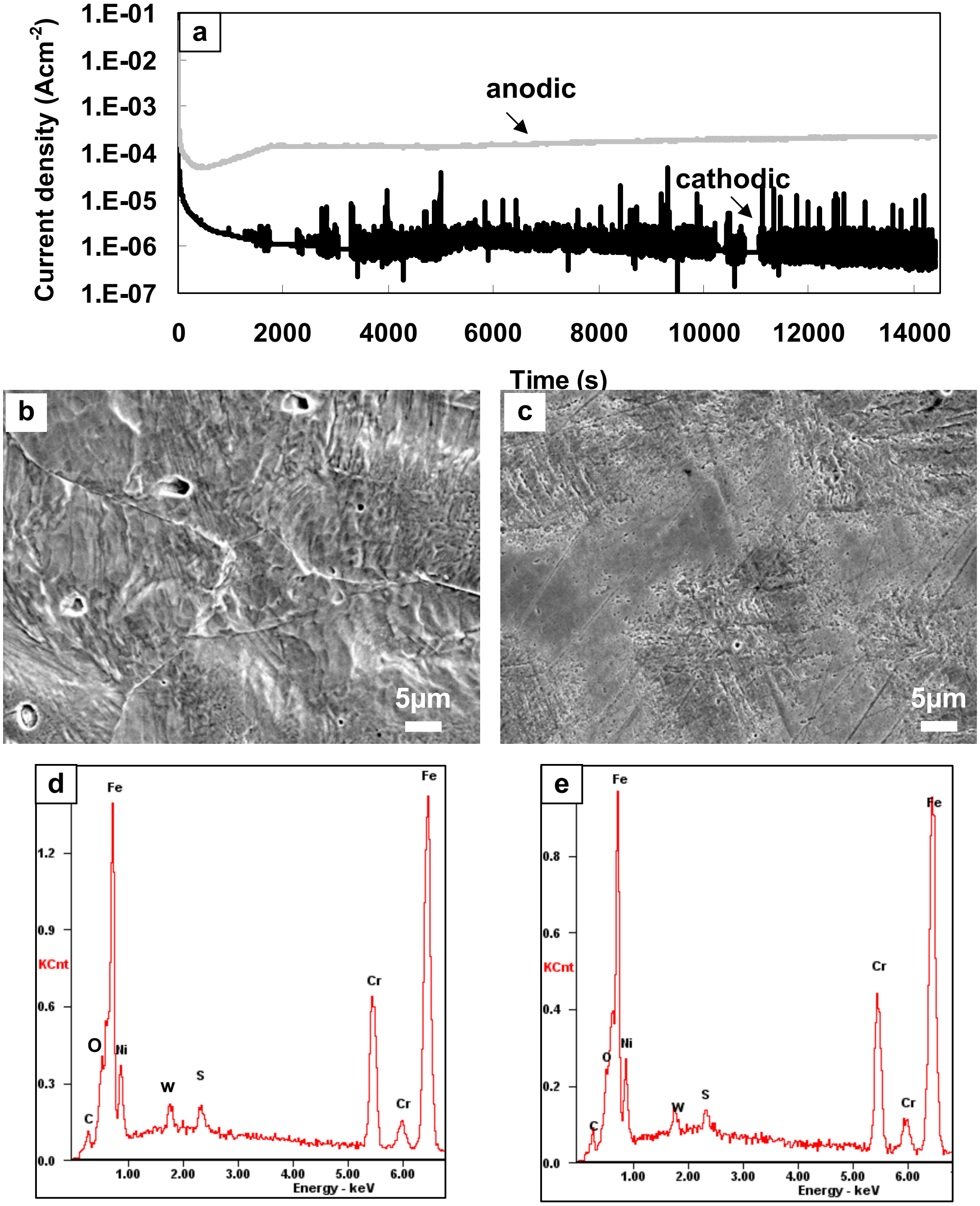

Fig. 5.8 (a) Comparative potentiostatic polarization curves and (b, c) SEM micrographs of uncoated SS316L samples under simulated anodic and cathodic conditions, respectively, in a 1 M sulphuric acid solution at 70 ^{o}C with H_2 purging and O_2 purging. (d, e) are the EDX spectria collected from (b, c).

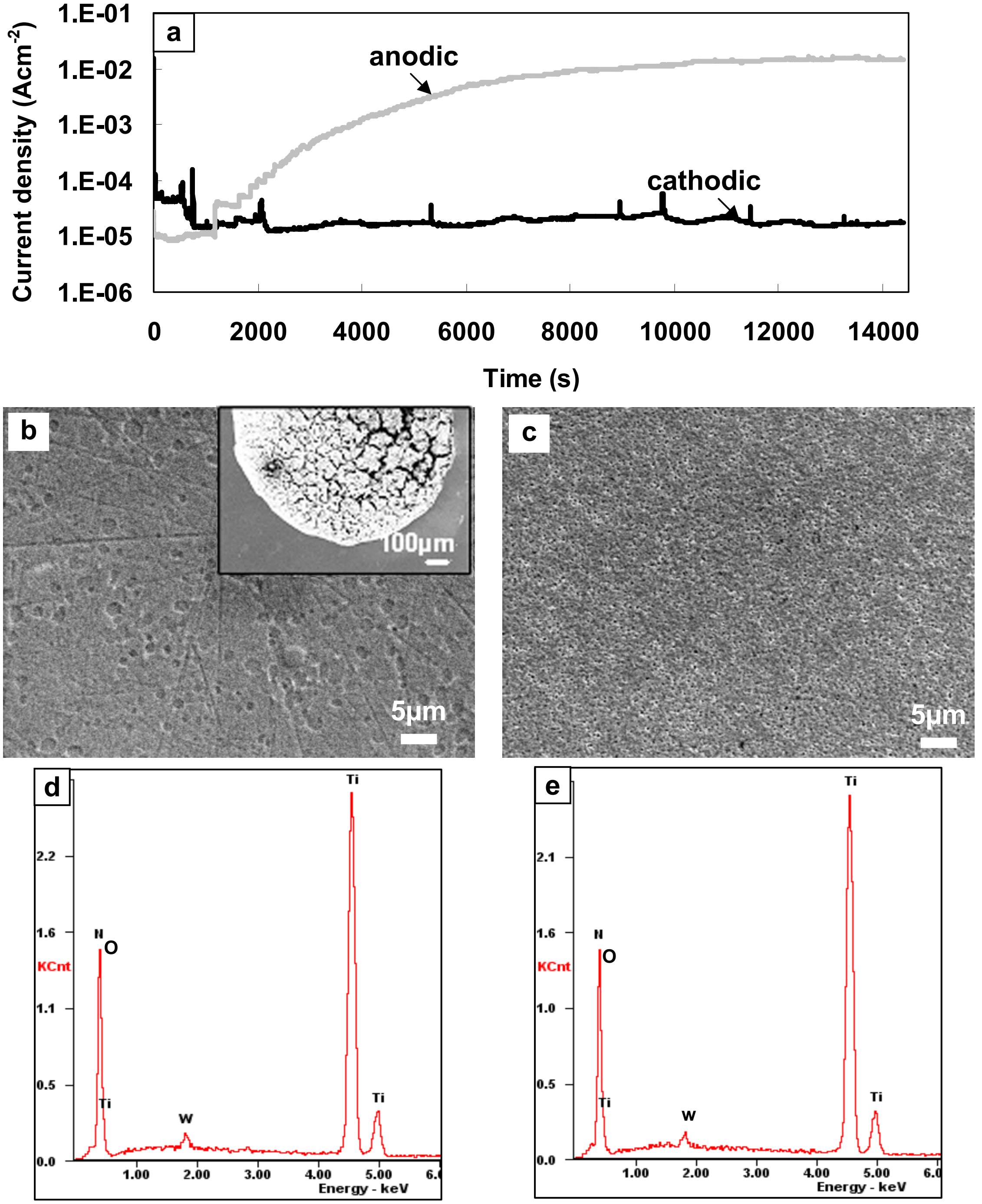

Fig. 5.9 (a) Comparative potentiostatic polarization curves and (b, c) SEM micrographs of TiN-coated SS316L samples under simulated anodic and cathodic conditions, respectively, in a 1 M sulphuric acid solution at 70 °C with H_2 purging and O_2 purging. (d, e) are the EDX spectra collected from (b, c), respectively.

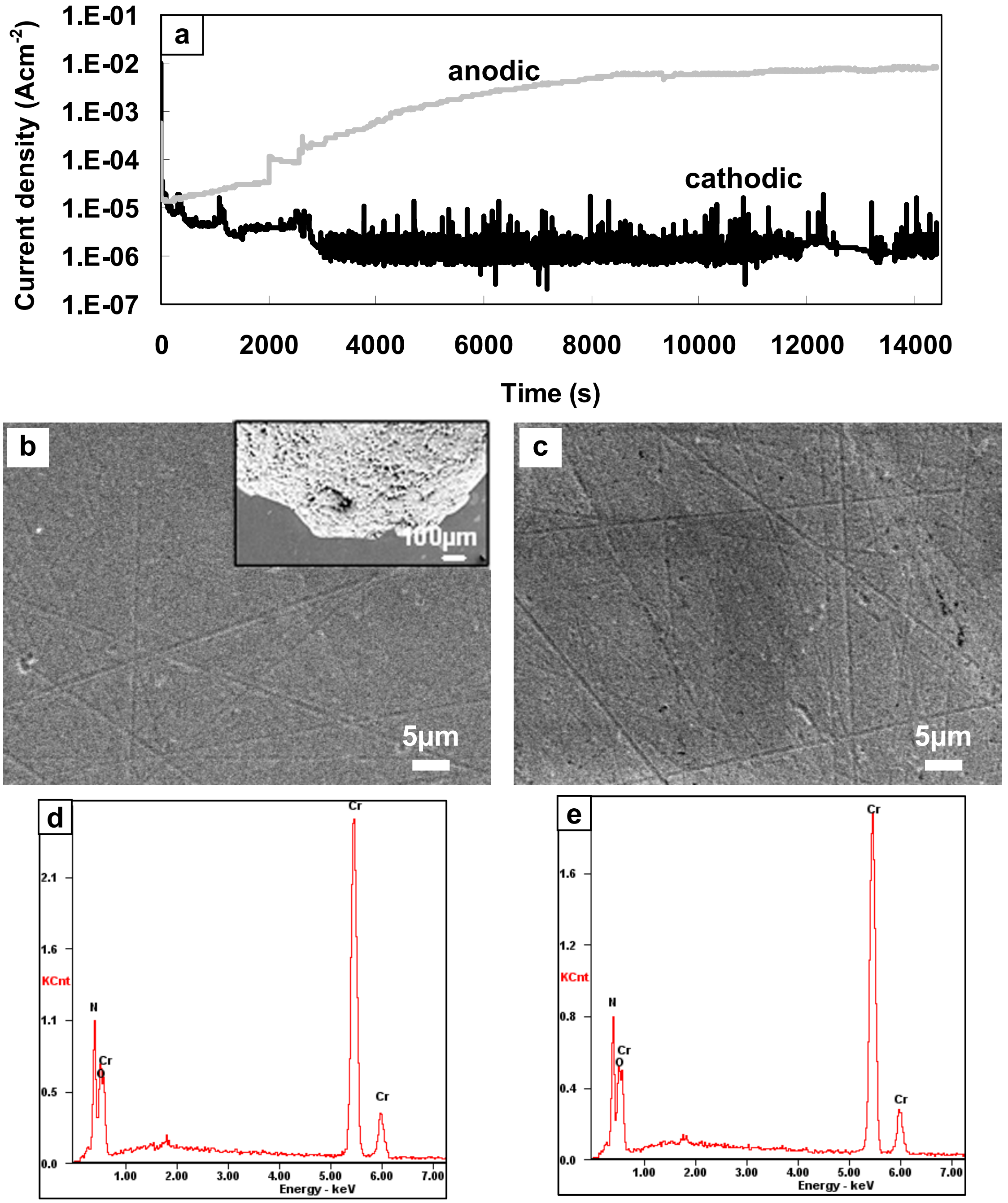

Fig. 5.10 (a) Comparative potentiostatic polarization curves and (b, c) SEM micrographs of CrN-coated SS316L samples under simulated anodic and cathodic conditions, respectively, in a 1 M sulphuric acid solution at 70 ^{o}C with H_2 purging and O_2 purging. (d, e) are the EDX spectria collected from (b, c), respectively.

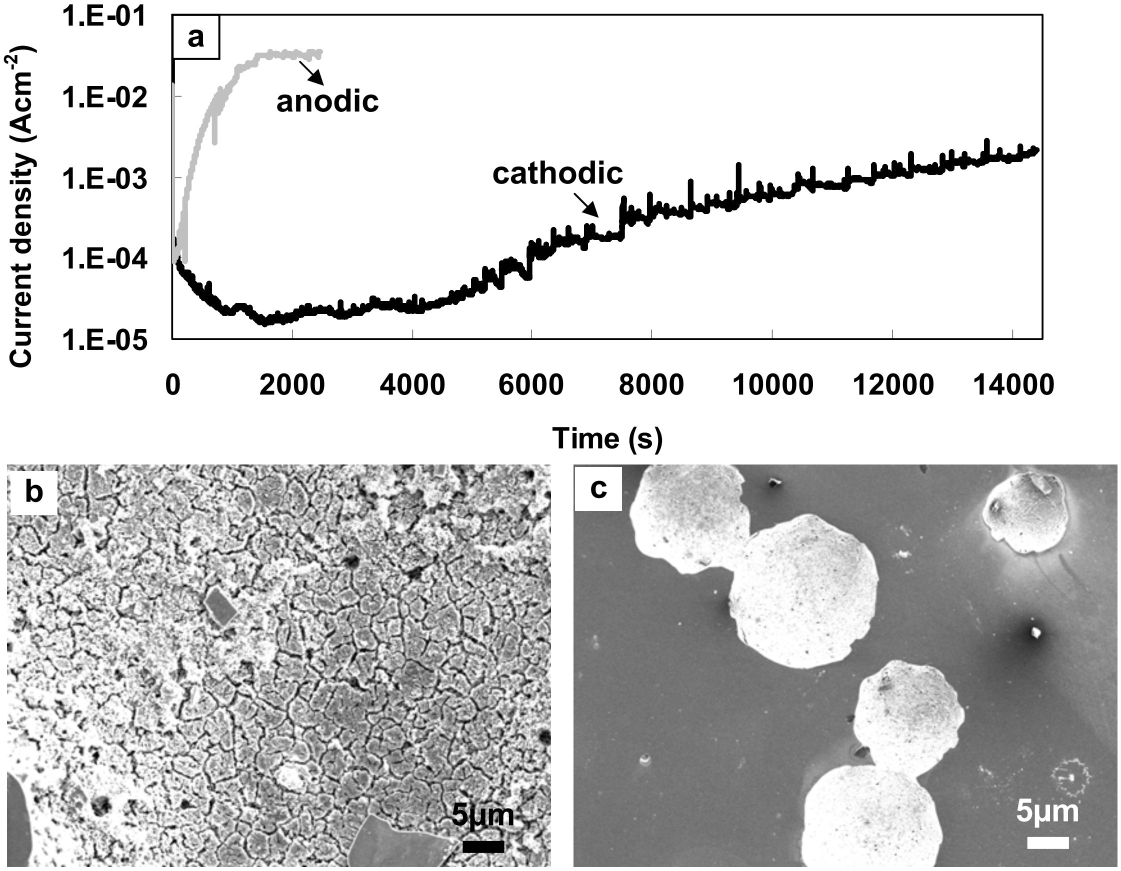

Fig.5.11 (a) Comparative potentiostatic polarization curves and (b, c) SEM micrographs of TiAlN-coated SS316L samples under simulated anodic and cathodic conditions, respectively, in a 1 M sulphuric acid solution at 70 ^{o}C with H_2 purging and O_2 purging.

CHAPTER 6 CORROSION AND TRIBOLOGICAL PROPERTIES OF COATINGS IN SIMULATED BIOMEDICAL ENVIRONEMNTS

6.1 Corrosion properties of coatings in simulated body fluid

Fig. 6.1 shows the potentiodynamic polarization curves of uncoated and coated stainless steel 316L samples in SBF solution at 37 °C. The polarization parameters are listed in Table 6.1. The corrosion test results showed that the TiN, CrN and DLC coated samples could achieve a higher corrosion resistance (R_p) compared with uncoated SS316L. DLC coating had the highest R_p, ~1544 kΩ.cm^2, which is 10 times higher than that of TiN and CrN (~145 kΩ.cm^2). However the R_p of TiAlN and CrAlN coated samples was much lower than that of uncoated SS316L (R_p=7.63 kΩ.cm^2). i.e. TiAlN and CrAlN had the R_p of 3.95 and 0.6 kΩ.cm^2, respectively.

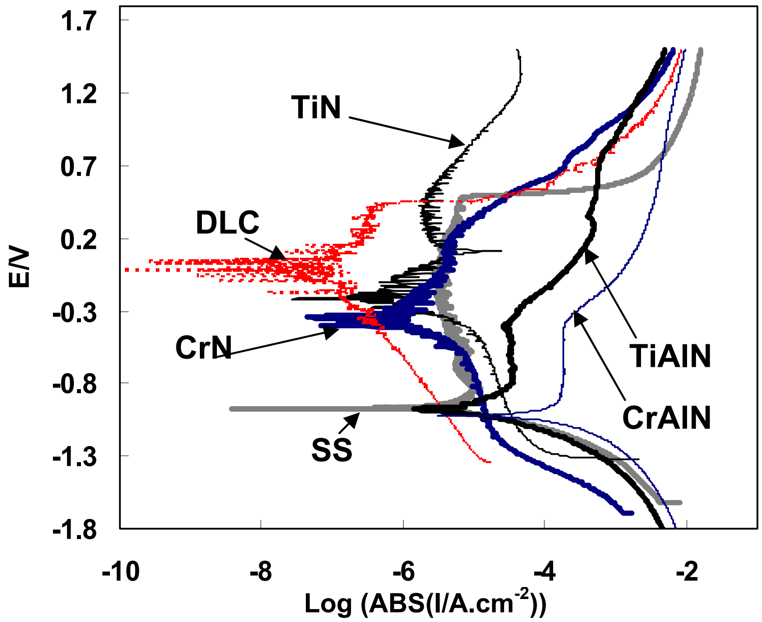

Fig. 6.1 Potentiodynamic polarization curves of uncoated and coated stainless steel 316L samples in SBF solution at 37 °C.

Table 6.1 Potentiodynamic polarization corrosion parameters of uncoated and coated samples in a simulated body fluid

	E_{corr} (mV)	I_{corr} (μA/cm^2)	β_a(mV/dec)	β_c(mV/dec)	R_p(kΩ.cm^2)
SS	-929.6	5.359	275.4	142.8	7.63
TiN	-158.6	0.256	176.0	155.9	140.40
CrN	-333.2	0.261	199.2	157.0	146.26
TiAlN	-980.5	13.200	440.5	164.7	3.95
CrAlN	-1034.2	127.140	1372.6	208.5	0.62
DLC	+4.4	0.0550	334.6	469.2	1543.99

Fig. 6.2 shows the curves of corrosion potential (E_{corr}) vs. testing time for various uncoated and coated samples in simulated body fluids. Fig. 6.2(a) shows the E_{corr} change behavior of the uncoated SS 316L during the testing time. The corrosion potential is less than -0.1 V at the first 2-hours-testing time, then increases gradually to positive value. After that, the curve fluctuates with testing time within a range from -0.03 V to +0.03 V. After 10 hours testing time, the E_{corr} becomes positive. The SEM micrographs, Figs. 6.3(a, b), show the surface morphology after corrosion test. No obvious pitting corrosion can be observed on the uncoated SS316L surface. The EDX spectrum (Fig. 6.3(c)) demonstrates that a large amount of element O is detected from the corroded surface. It can be believed that the fluctuation of E_{corr} vs. time curves (Fig. 6.2(a)) is related to the forming and dissolving of the passive oxide film on the stainless steel surface. When the film forming process is faster than the dissolving process, the E_{corr} increases, otherwise, drops. The oxide forming and dissolving process lead to release metal ions, such as Fe and Cr, which have negative effects on the performance of stainless steel in the biomedical application.

For the TiN coating, in the E_{corr} vs. time curve (Fig. 6.2(b)), at the first half hour, the E_{corr} increases gradually to +0.085 V, then the curve is relatively stable compared to that of uncoated SS316L. The curve of the CrN coating (Fig. 6. 2(c)) presents a similar shape to that of TiN coating but the E_{corr} value at stable stage is about 0.15 V which is higher than that of TiN coating. The SEM micrographs of the TiN (Fig. 6.4) and CrN (Fig. 6.5) coatings show no visible corrosion. The EDX spectra collected from the TiN and CrN coatings are shown at Figs. 6.4(c) and 6.5(c), respectively. Compared with the TiN coating after corrosion tests, more amount of element O can be detected from the CrN coating surfaces. This may be an evidence showing that the Cr-O film on the CrN coating surface can be attributed to the corrosion protection. The result is in good agreement with previous reports [153, 154, 173] that the thin oxide passive film, Cr-O film, has a denser structure than porous Ti-O film and thus CrN afforded a better corrosion resistance than TiN.

The E_{corr} values of the TiAlN and CrAlN coatings are negative from curves in Figs. 6.2(d) and 6.2(e). With the increase of testing time, the E_{corr} decreases from -0.05 V to -0.45 V, for the TiAlN coating during the whole testing process though some ups and downs. For the CrAlN coating, the E_{corr} changes from -0.36 V to -0.52 V. The E_{corr} of the CrAlN coating is lower than that of the TiAlN coating at any corresponding testing time. The low E_{corr} of the TiAlN and CrAlN coatings could be related to the Al introduction into the coating structure. As an active metal, Al could react with the ions in simulated body fluids such as PO_4^{-3} and CO_3^{-2}, which contributes the low value of the E_{corr}. Due to the fact that more Al presents in the top layer of the CrAlN coating than TiAlN coating, the CrAlN shows lower E_{corr} than the TiAlN coating. On both surfaces, the SEM micrographs (Figs. 6.6 and 6.7) still show no visible corrosion. The EDX spectra (Figs. 6.6(c) and 6.7(c)) indicate that element O can be detected on both surfaces.

At the beginning stage of corrosion test, the DLC coating has a E_{corr} of +0.1 V then the E_{corr} increases very slowly during the test process and finally reaches up to +0.15V at the end of corrosion testing. This E_{corr} value is similar to that of CrN coating. The E_{corr} vs. time curve of the DLC has many ups and downs at a fluctuation rang of ±0.02 V (Fig. 6.2(f)). No visible corrosion can be observed on the DLC coating surface (Figs. 6.8 (a, b)) and no any resultants as corrosion products can be detected by EDX analysis (Fig. 6.8(c)).

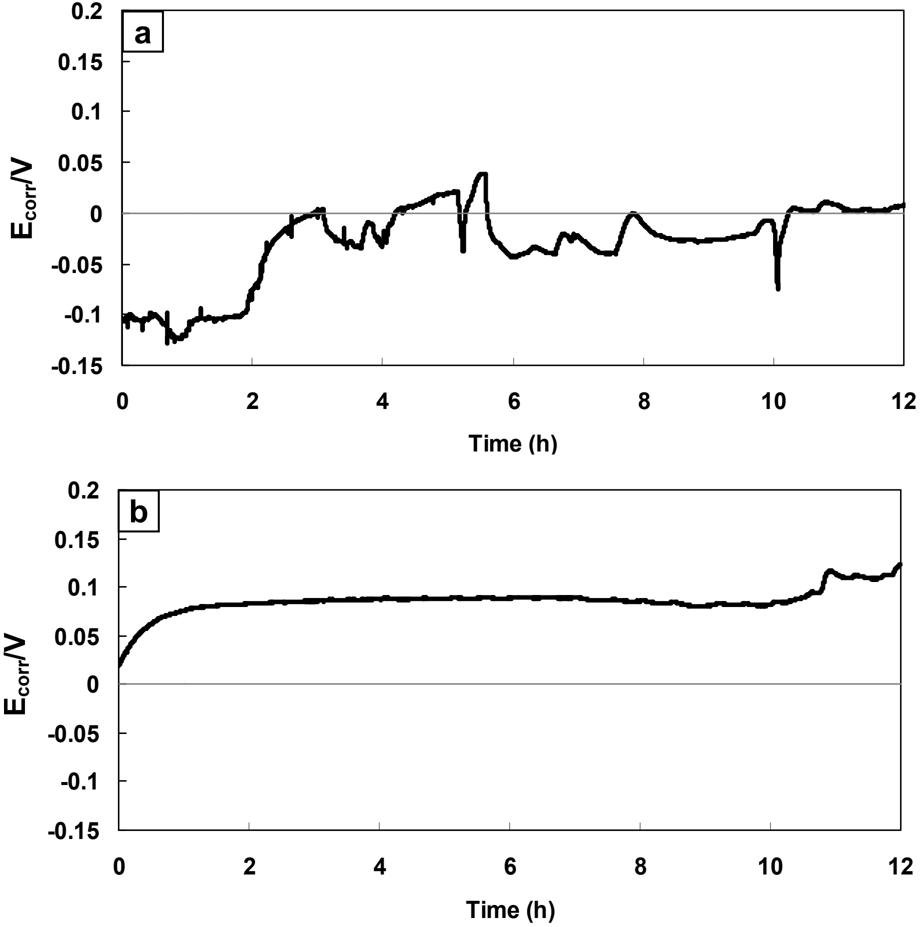

Fig. 6.2 (a, b)

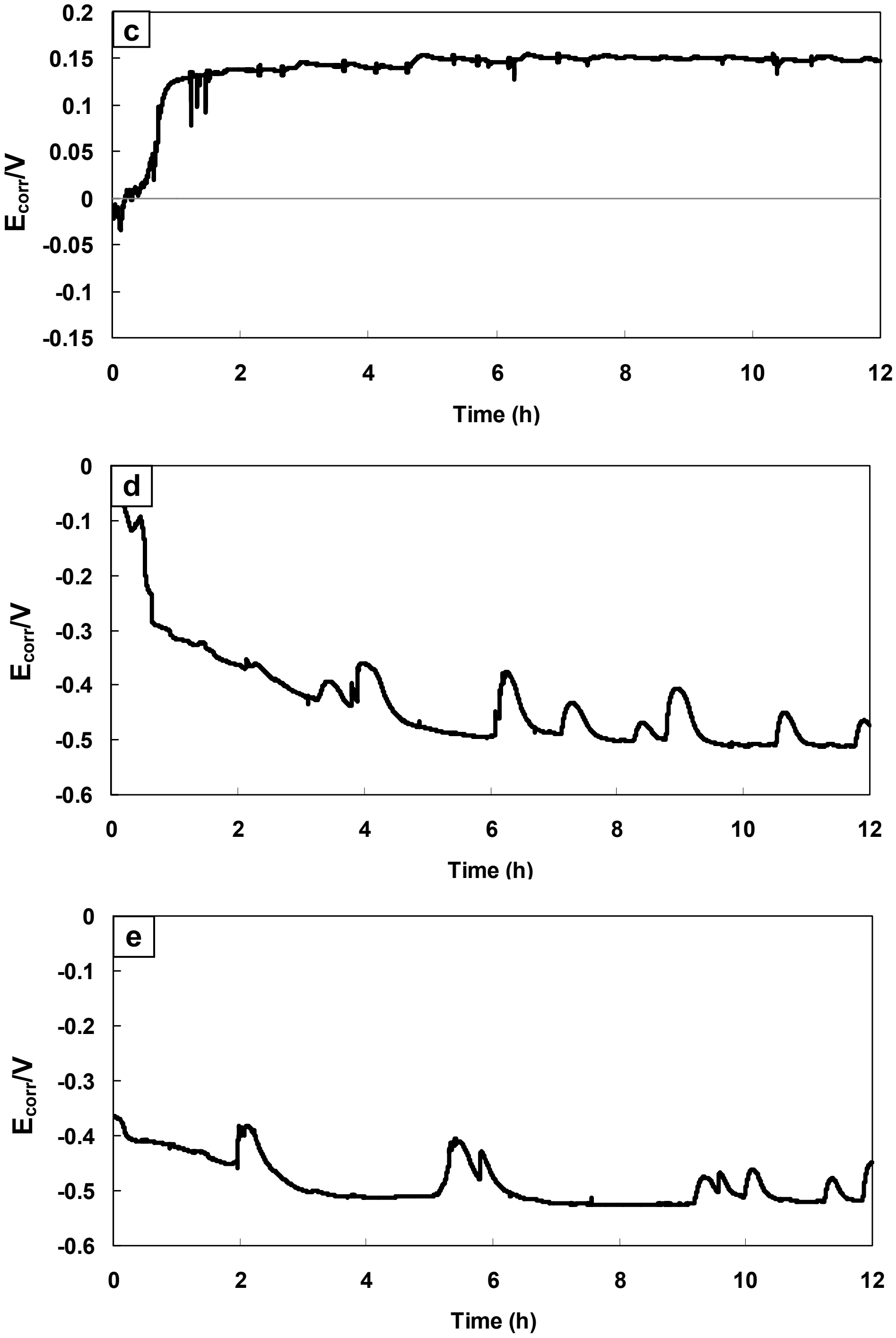
c
0.2
0.15
0.1
0.05
0
-0.05
-0.1
-0.15
E_{corr}/V
0
2
4
6
8
10
12
Time (h)
d
0
-0.1
-0.2
-0.3
-0.4
-0.5
-0.6
E_{corr}/V
0
2
4
6
8
10
12
Time (h)
e
0
-0.1
-0.2
-0.3
-0.4
-0.5
-0.6
E_{corr}/V
0
2
4
6
8
10
12
Time (h)

Fig. 6.2 (c, d, e)

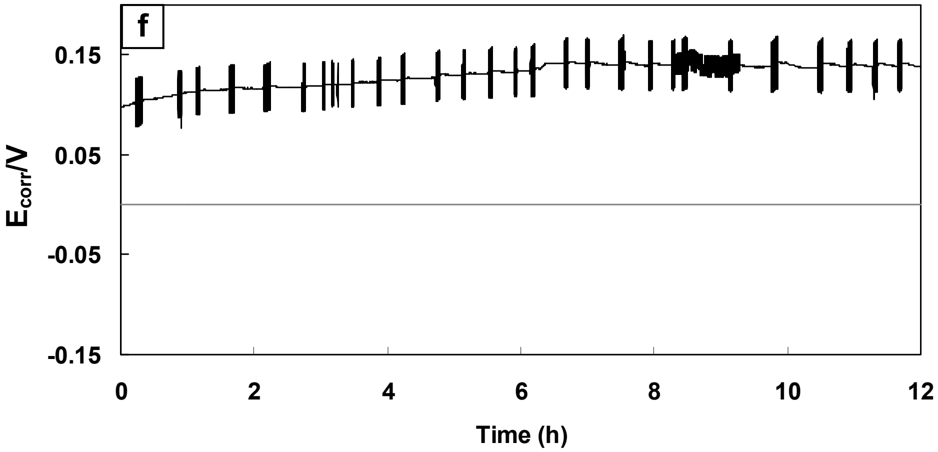

Fig. 6.2 E_{corr} vs. time curves of (a) uncoated SS 316L, (b) TiN, (c) CrN, (d) TiAlN, (e) CrAlN and (f) DLC coatings during a 12-hour testing period in a simulated body fluid.

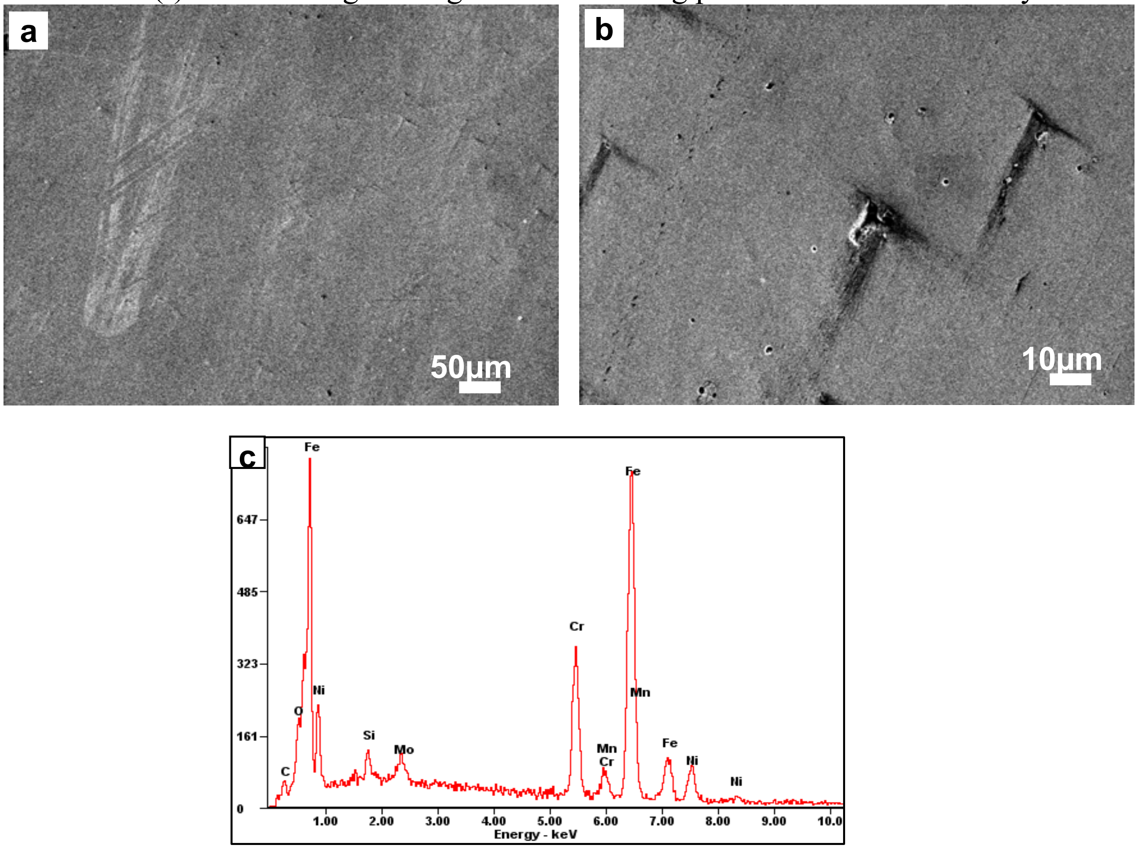

Fig. 6.3 (a, b) SEM micrographs of the uncoated SS316L sample after a 12-hours corrosion test and (c) EDX spectrum collected from the corroded area. (b) is the magnified image of (a).

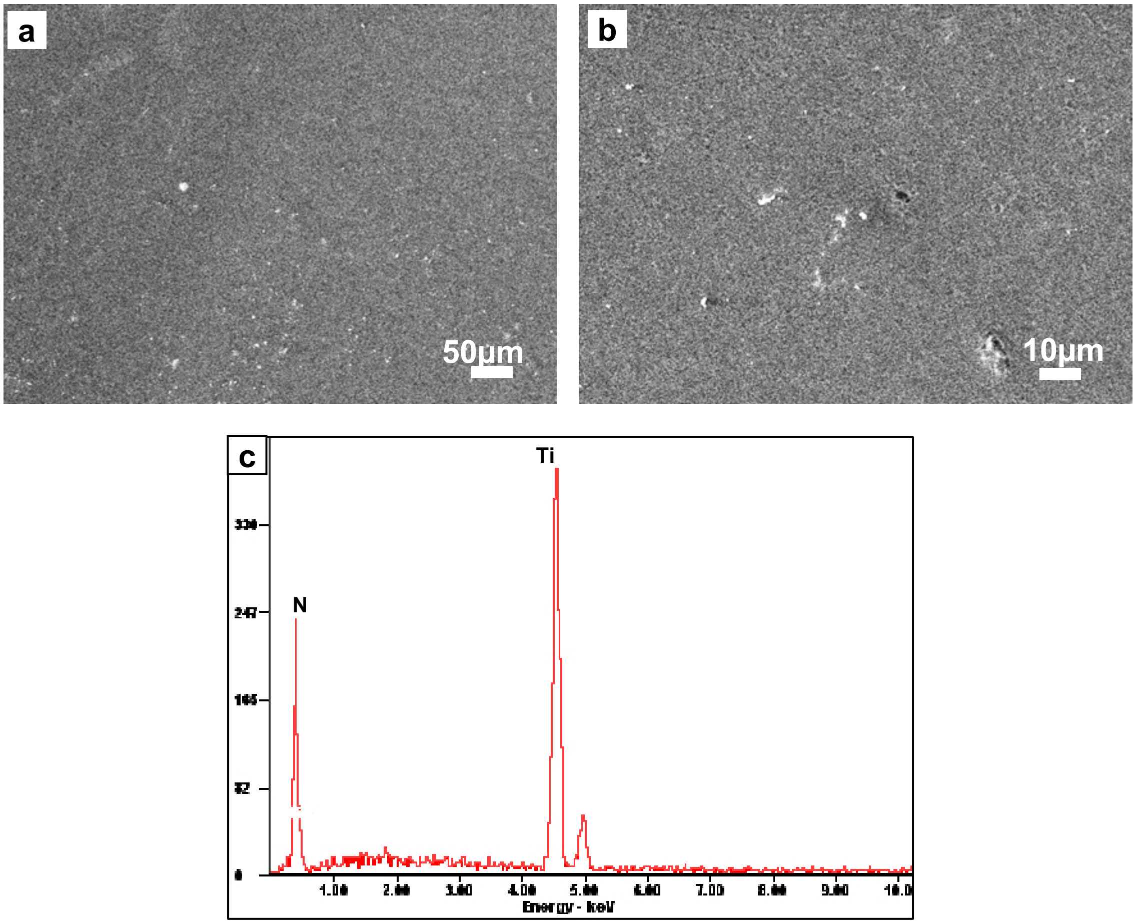

Fig. 6.4 (a, b) SEM micrographs of the TiN-coated SS316L sample after a 12-hours corrosion test and (c) EDX spectrum collected from the corroded area. (b) is the magnified image of (a).

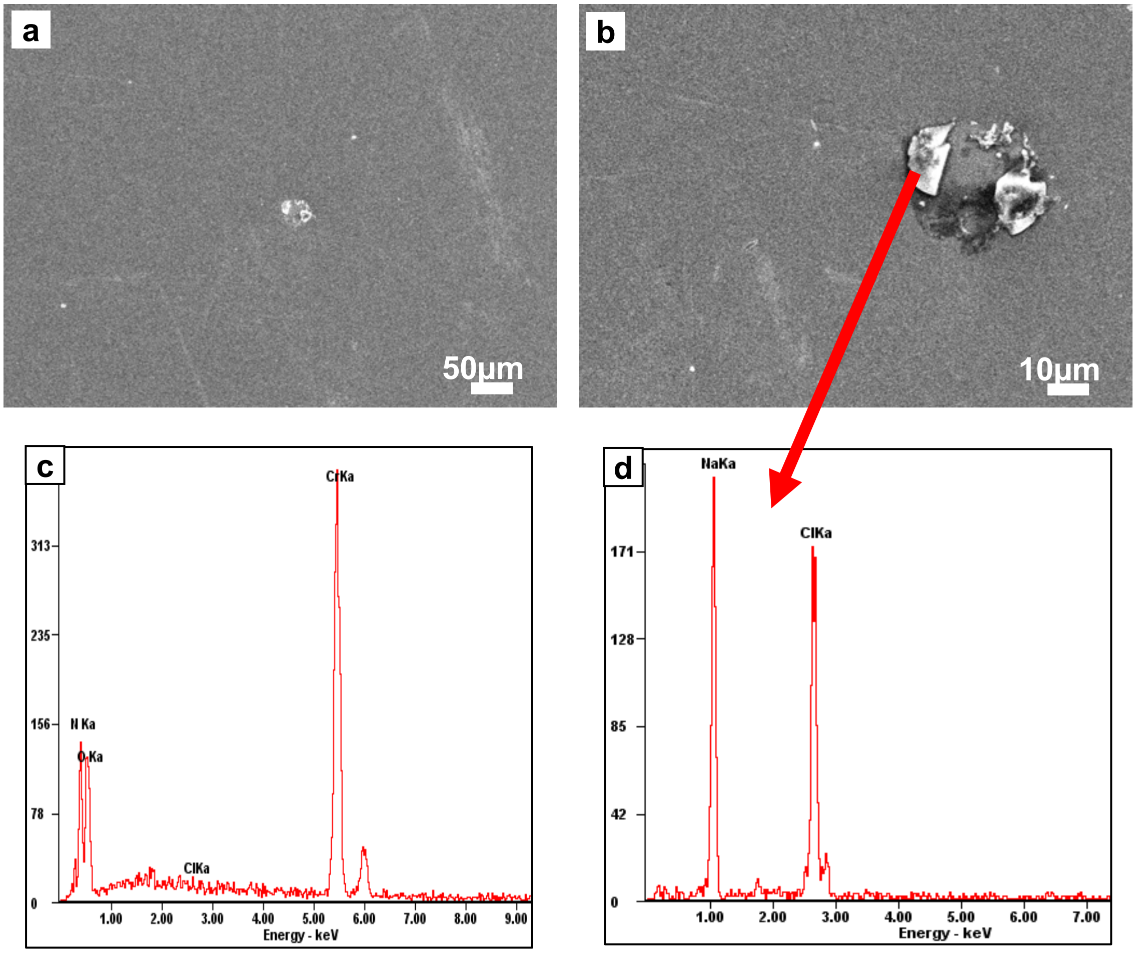

Fig. 6.5(a, b) SEM micrographs of the CrN-coated SS316L sample after a 12-hours corrosion test and (c, d) EDX spectra collected from the corroded area and the particle, respectively. (b) is the magnified image of (a).

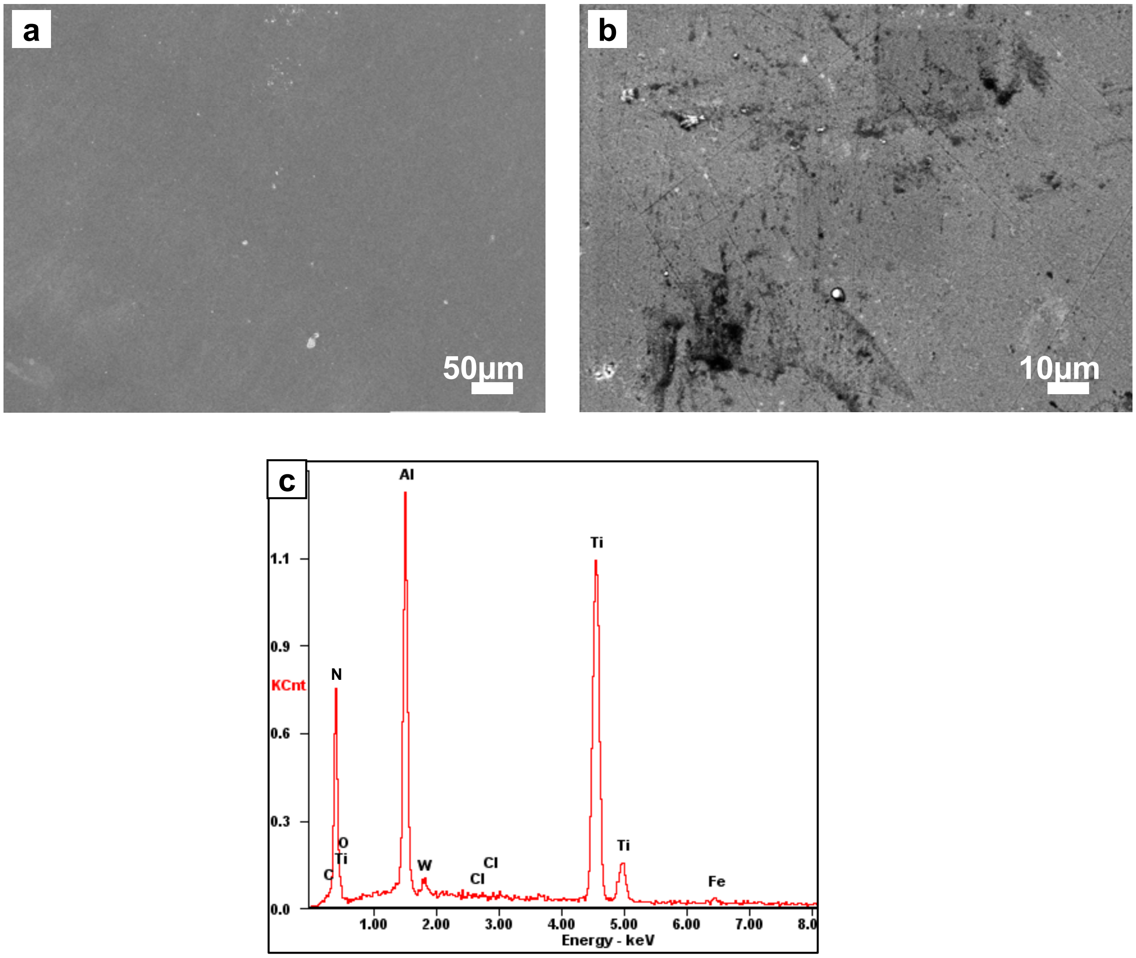

Fig. 6.6 (a, b) SEM micrographs of the TiAlN-coated SS316L sample after a 12-hours corrosion test and (c) EDX spectrum collected from the corroded area. (b) is the magnified image of (a).

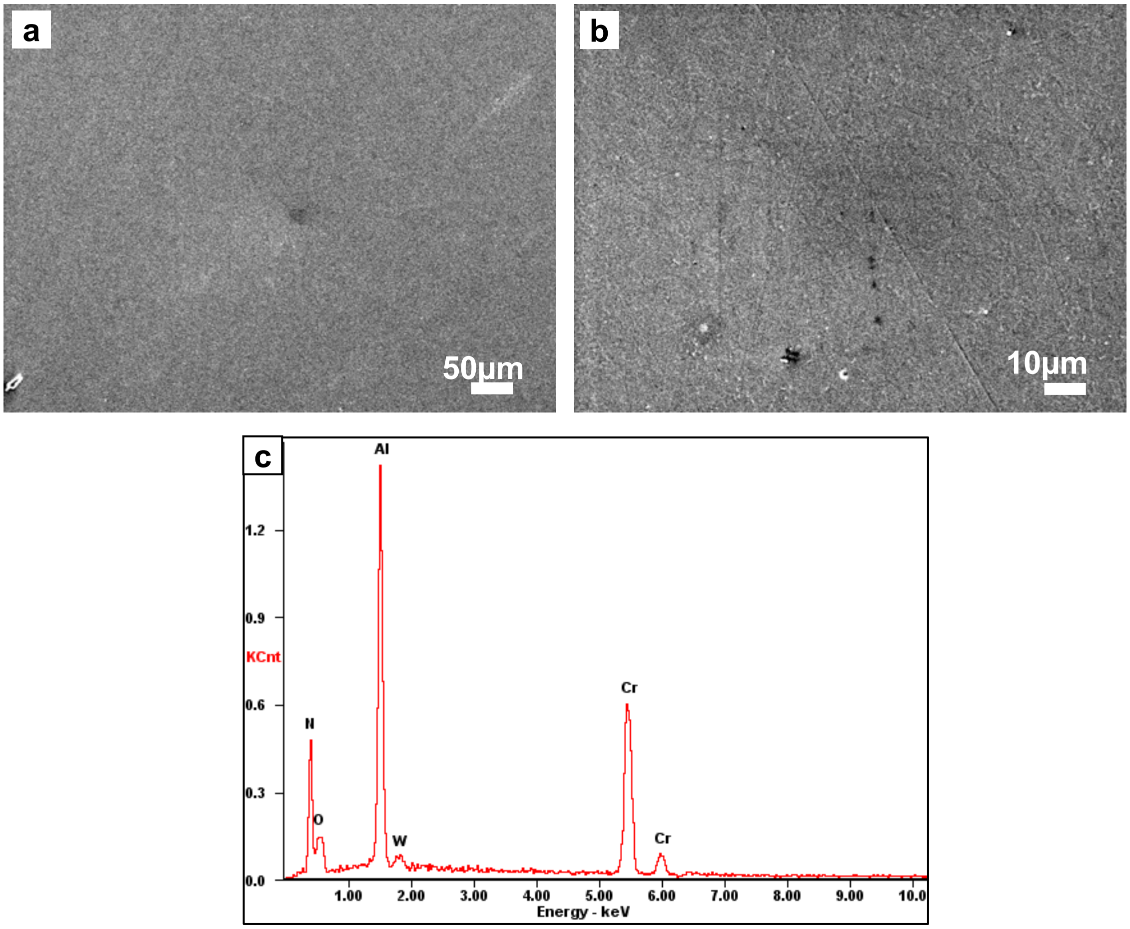

Fig. 6.7 (a, b) SEM micrographs of the CrAlN-coated SS316L sample after a 12-hours corrosion test and (c) EDX spectrum collected from the corroded area. (b) is the magnified image of (a).

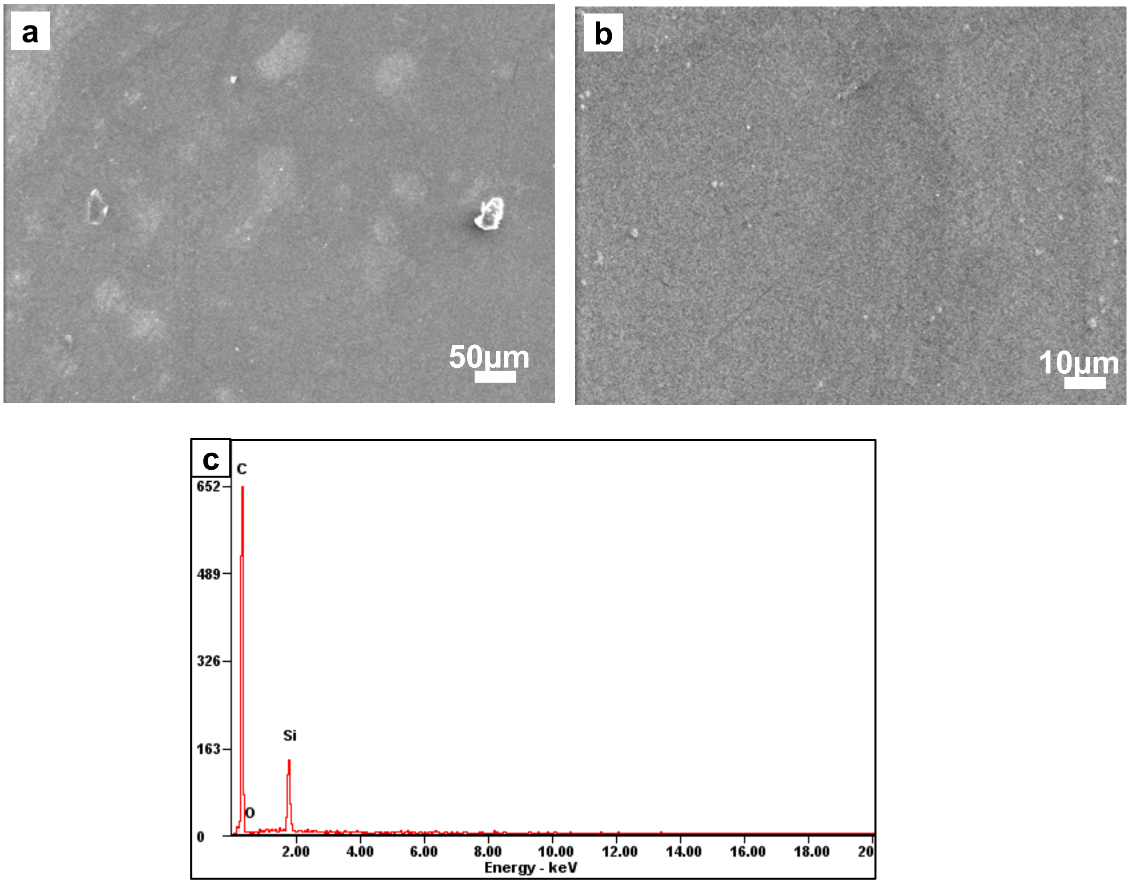

Fig. 6.8 (a, b) SEM micrographs of the DLC-coated SS316L sample after a 12-hours corrosion test and (c) EDX spectrum collected from the corroded area. (b) is the magnified image of (a).

6.2 Tribological properties of coatings against polyethylene biomaterial

To investigate the tribological properties of coatings against polyethylene biomaterial, the pin-on-disc sliding tests have been conducted on uncoated and coated SS316L, under dry and boundary lubrication conditions with either distilled water or simulated body fluid (SBF). From the corrosion tests, the TiAlN and CrAlN coatings have relatively worse corrosion properties, thus only the TiN, CrN and DLC coatings are chosen as the materials of interest to perform pin-on-disc tests.

Fig. 6.9 shows the dynamic cofs of uncoated SS316L samples during the sliding wear tests against high density polyethylene (HDPE) counterface balls under dry, distilled water and SBF boundary lubrication conditions. After a running-in stage, the uncoated SS316L has an average cof of 0.40 under dry condition (Fig. 6.9(a)). With the lubrication/cooling of distilled water, the cof curve (Fig. 6.9(b)) presents a slip-stick behavior and the average cofs is about 0.16. The average cofs of SS316L under the lubrication of SBF is about 0.14 but the cof curve (Fig. 6.9(c)) fluctuates more severely than the other two conditions and the up and down range is up to ±0.15.

Figs. 6.10 and 6.11 show the SEM micrographs of wear tracks on uncoated SS316L samples and the counterface HDPE balls, respectively, after sliding tests under various conditions. On the wear tracks of uncoated SS316L, a little abrasion occurred under dry condition (Figs. 6.10(a, b)), and on the corresponding counterface ball (Figs. 6.11(a, b)), obvious adhesive wear and some abrasive wear were observed. It should be mentioned that although the HDPE ball used in the tests are made of pure original polyethylene, some small pumice stone particles existed on the ball surface which was induced from the ball surface polishing vibratory media. Those particles are generally 1-2 μm in size and not readily noticeable since they are embed into the ball surface. Fig. 6.11(g) gives an example of pumice stone particle (bright spot pointed by the arrow) embedded into a scratch scar of the ball after sliding test against SS316L under dry condition. Fig. 6.11(h) is the EDX spectrum of the particle area which shows that the main chemical compositions of this particle are K, Mg, Al, Si, and O. The hard pumice stone particles abraded the wear couple surfaces during the sliding tests which can explain the minor abrasion on the steel surface during the dry sliding tests (Figs. 6.10(a, b)). With the lubrication of distilled water, the average cof decreases to 0.16 and wear track (Figs. 6.10(c, d)) has a similar morphology to that of under dry condition. Comparing the EDX spectrum i and ii in Fig. 6.10 which are collected from the corresponding area on the wear tracks on SS316L under dry and distilled water conditions, respectively, wear track after sliding in water has a higher O/Fe ratio which implies that with water, more oxide has formed on SS316L surface. In the wear track of SS316L after the sliding with SBF (Figs. 6. 10(e, f)), there is a large amount of accumulated materials but no severe discharging could be observed from SEM observation. The main elements of these materials are C, O and some elements from steel alloy and SBF, which were detected by the EDX and the spectrum shown in Figs. 6.10 (spectrum iii). When sliding with SBF, more corrosion likely occurred at the steel surface compared with the dry and water lubrication conditions. The accumulated material is the corrosion products with some polymer material transferred from the counterface ball. The corroded surface of wear track has accelerated the wear of counterface ball and therefore the ball after sliding against SS316L with SBF (Figs. 6.11(e, f)) has the most wear loss among those three testing conditions.

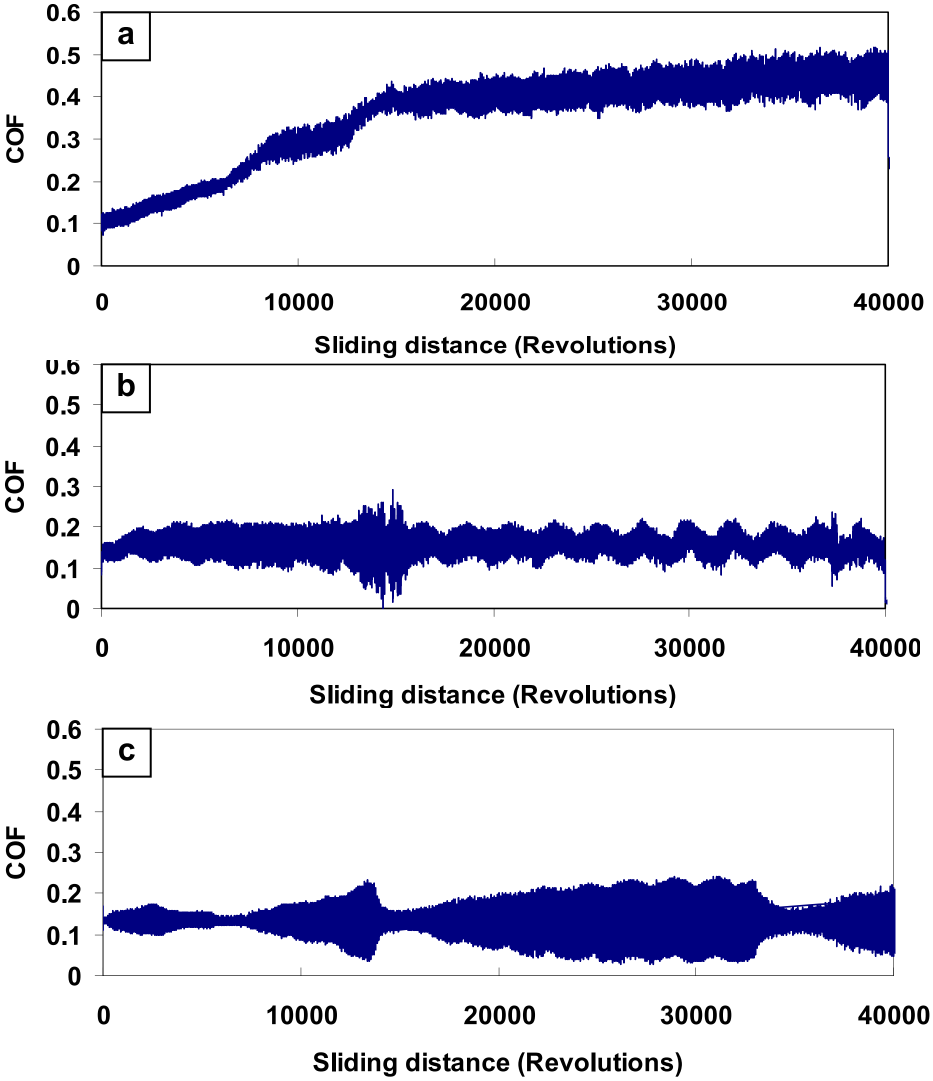

Fig. 6.9 Dynamical cof curves of uncoated SS316L samples during the sliding wear tests against HDPE balls under (a) dry and boundary lubrication conditions with with (b) distilled water and (c) SBF.

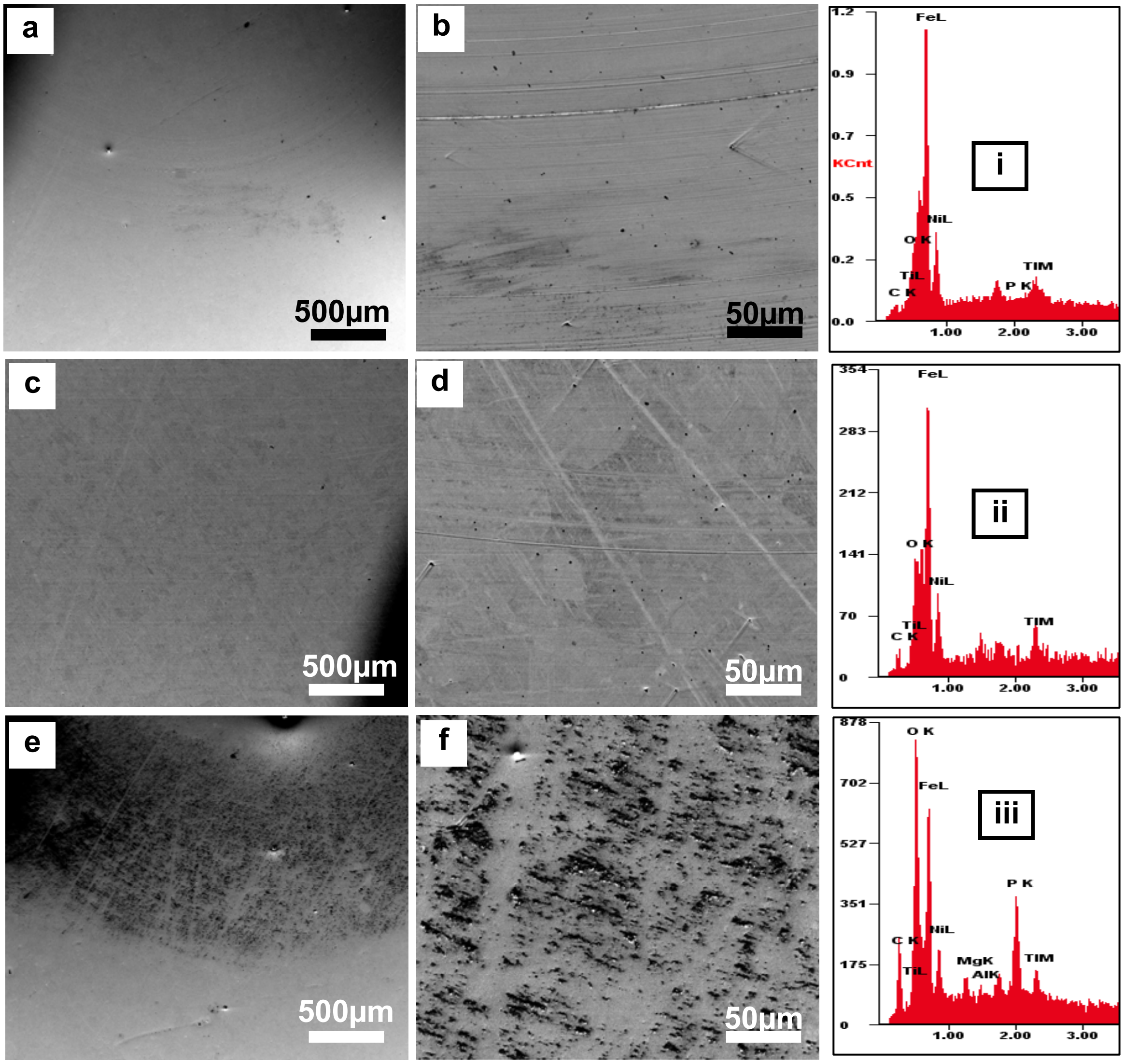

Fig. 6.10 SEM micrographs of the wear tracks on uncoated SS316L samples after the sliding wear tests against HDPE balls under (a, b) dry and boundary lubrication conditions with (c, d) distilled water and (e, f) SBF. (b, d, f) are the corresponding magnified images of (a, c, e). Spectra i, ii and iii are the EDX spectra collected from the corresponding areas in (b, d, f).

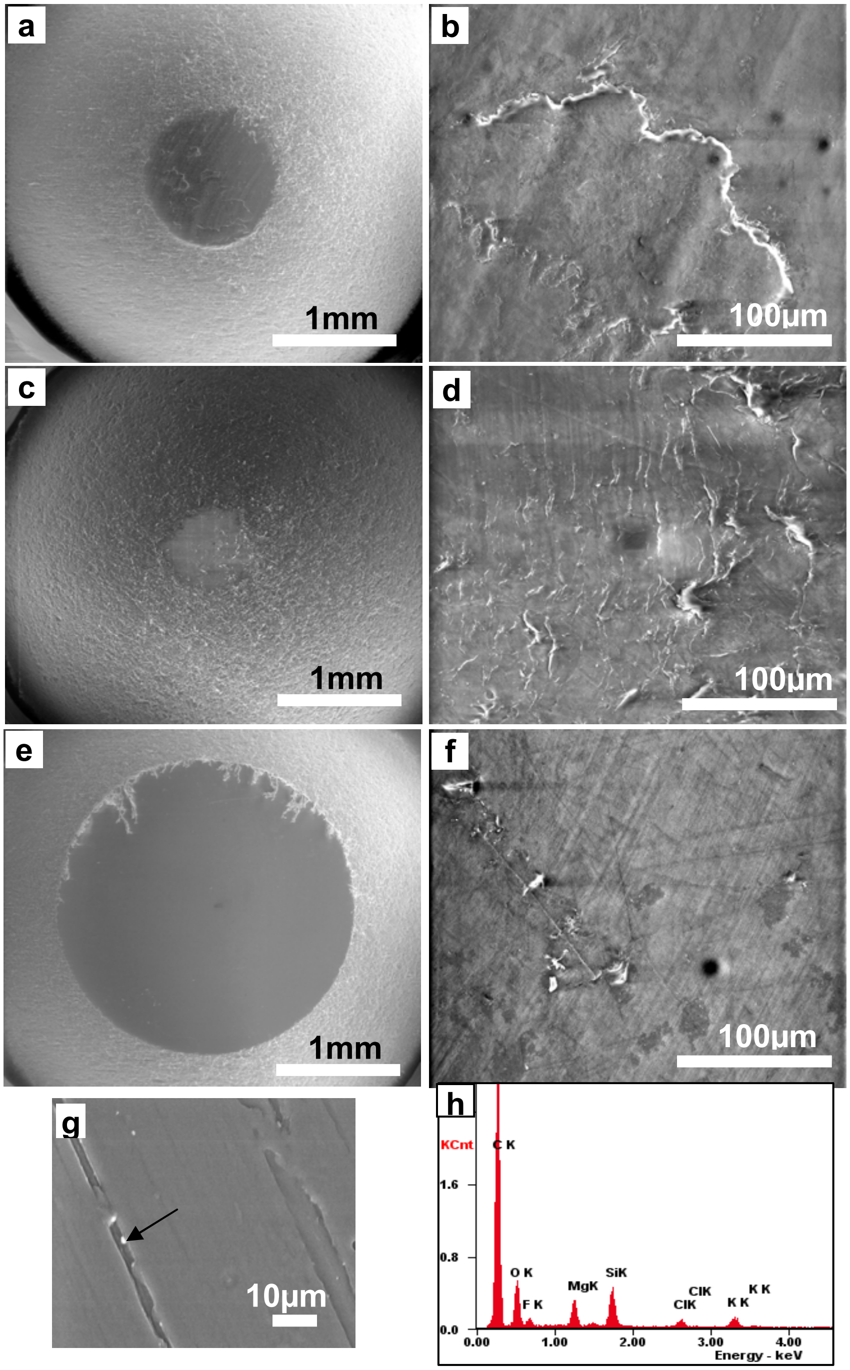

Fig. 6.11 SEM micrographs of worn PE balls after sliding tests against uncoated SS316L samples under (a, b) dry and boundary lubrication conditions with (c, d) distilled water and (e, f) SBF. (b, d, f) are the corresponding magnified images of (a, c, e). (g) is the SEM of small pumice stone particles embedded into the ball surface and (h) is the EDX spectrum of the particle.

Fig. 6.12 shows the dynamic cofs of the TiN-coated SS316L samples during the sliding wear tests against HDPE counterface balls under the same conditions as the tests for the uncoated steel sample. After a running-in stage, the cof curve of TiN-coated SS316L under a dry testing condition enters a stable stage where the average cof is about 0.45 (Fig. 6.12(a)). With distilled water and SBF, both cof curves (Figs. 6.12(b, c), respectively) show a slip-stick behaviour and the average cof values are similar which is about 0.1. No obvious scratch on the TiN coating surface after the dry sliding wear test can be observed from the SEM micrographs on the wear tracks (Figs. 6.13(a, b)). The SEM observation of wear tracks on the TiN coating after sliding tests with distilled water and SBF (Figs. 6.13(c, d) and Figs. 6.13(e.f)) indicates that both wear tracks have a similar morphology and under both conditions, no obvious wear but some HDPE material smears exist on the wear tracks. The counterface ball after the dry sliding test (Figs. 6. 14(a, b)) has a higher wear loss than those with lubrication conditions. The balls under lubrication of distilled water and SBF (Figs. 6.14(c, d) and Figs. 6.14(e, f), respectively) have a similar wear loss which indicates that the TiN coating is relatively stable in SBF and besides the lubricating/cooling effect of water, the effect of chemical compositions in SBF on the TiN coating's tribological properties is limited.

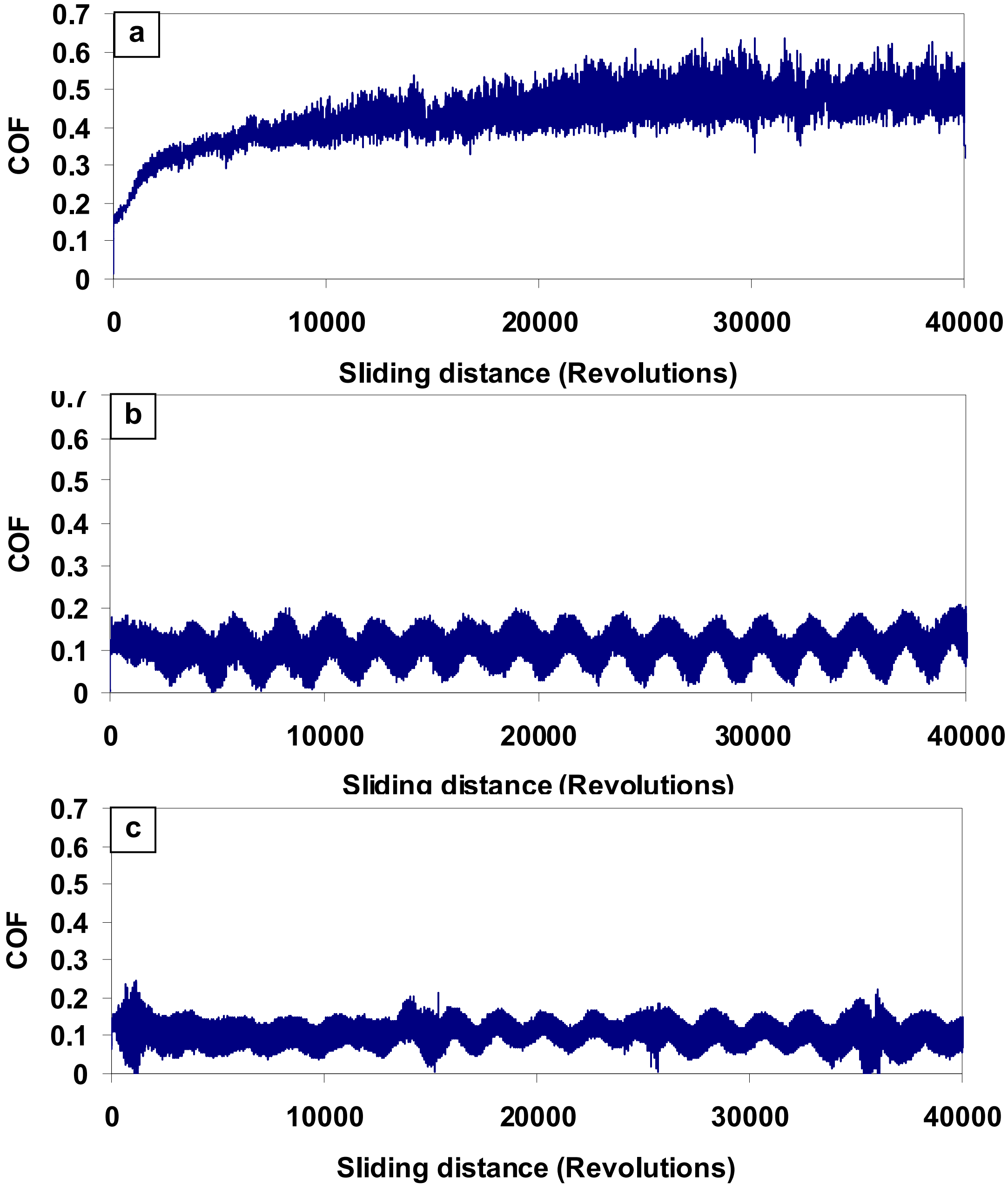

Fig. 6.12 Dynamical cof curves of the TiN-coated SS316L samples during the sliding wear tests against HDPE balls under (a) dry and boundary lubrication conditions with with (b) distilled water and (c) SBF.

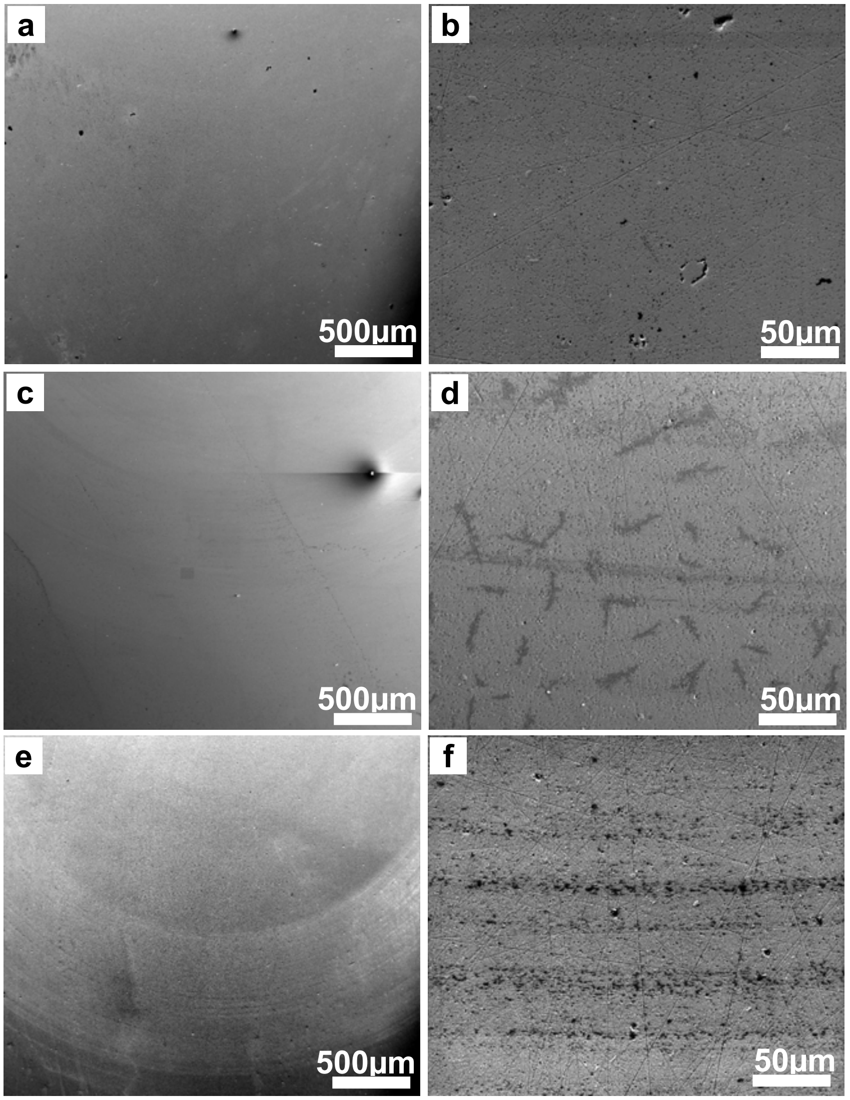

Fig. 6.13 SEM mcirographs of wear tracks on the TiN-coated SS316L samples after the sliding wear tests against HDPE balls under (a, b) dry and boundary lubrication conditions with (c, d) SBF and (e, f) distilled water. (b, d, f) are the corresponding magnified images of (a, c, e).

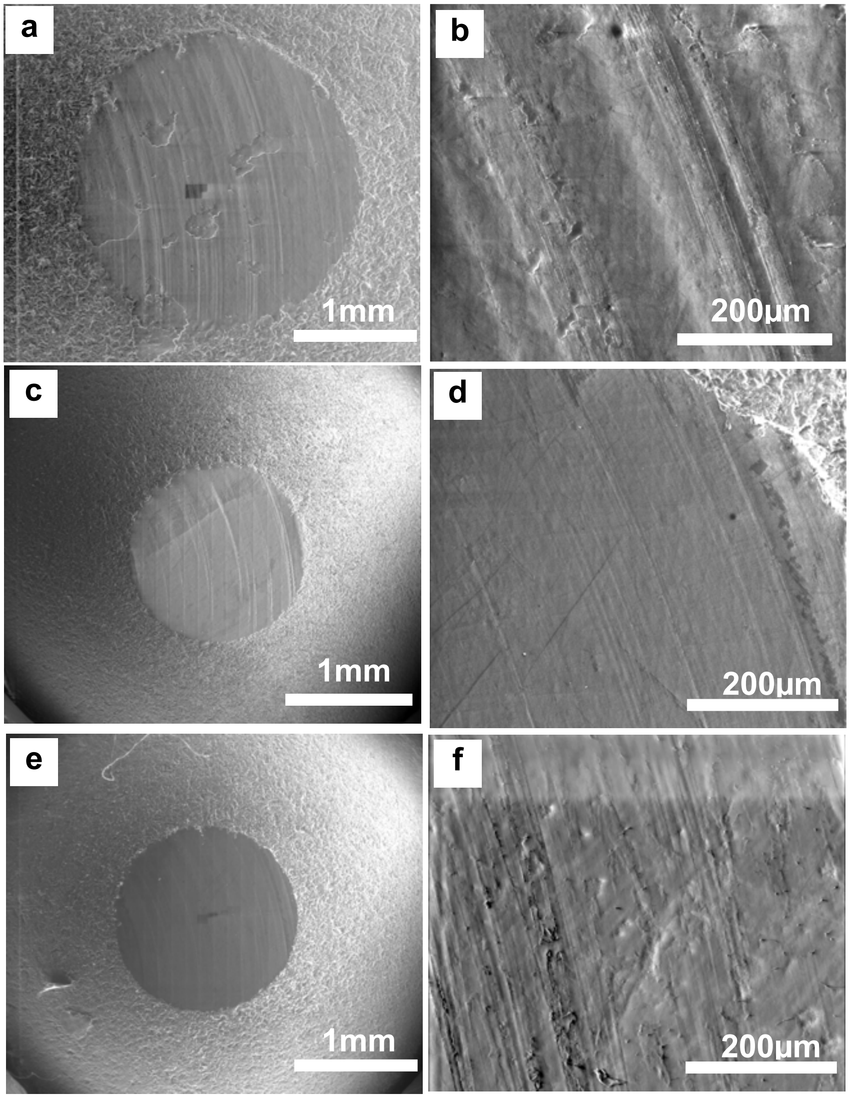

Fig. 6.14 SEM micrographs of the worn HDPE balls after sliding tests against the TiN-coated SS316L samples under (a, b) dry and boundary lubrication conditions with (c, d) distilled water and (e, f) SBF. (b, d, f) are the corresponding magnified images of (a, c, e).

Fig. 6.15 shows the dynamic cofs of the CrN-coated SS316L samples during the sliding wear tests against HDPE counterface balls under same conditions as last two samples. All the cof curves present a slip-stick behaviour and the average cofs are 0.48, 0.27 and 0.28 for those under dry condition, with distilled water and SBF lubrications, respectively. On the wear tracks after sliding tests between the CrN coating and HDPE balls under various conditions (Fig. 6.16), more material accumulation can be observed compared with the TiN-coated and uncoated samples. EDX analysis (spectra i, ii and iii in Fig. 6.16) shows that relatively high O fraction exists in the wear tracks which indicates an oxygen-rich tribofilm forming during the sliding tests. Furthermore, the counterface balls (Fig. 6.17) have been abraded during the sliding against the CrN coating. The ball tested in distilled water (Figs. 6.17(c, d)) and SBF (Figs. 6.17(e, f)) has the lowest and highest wear loss, respectively.

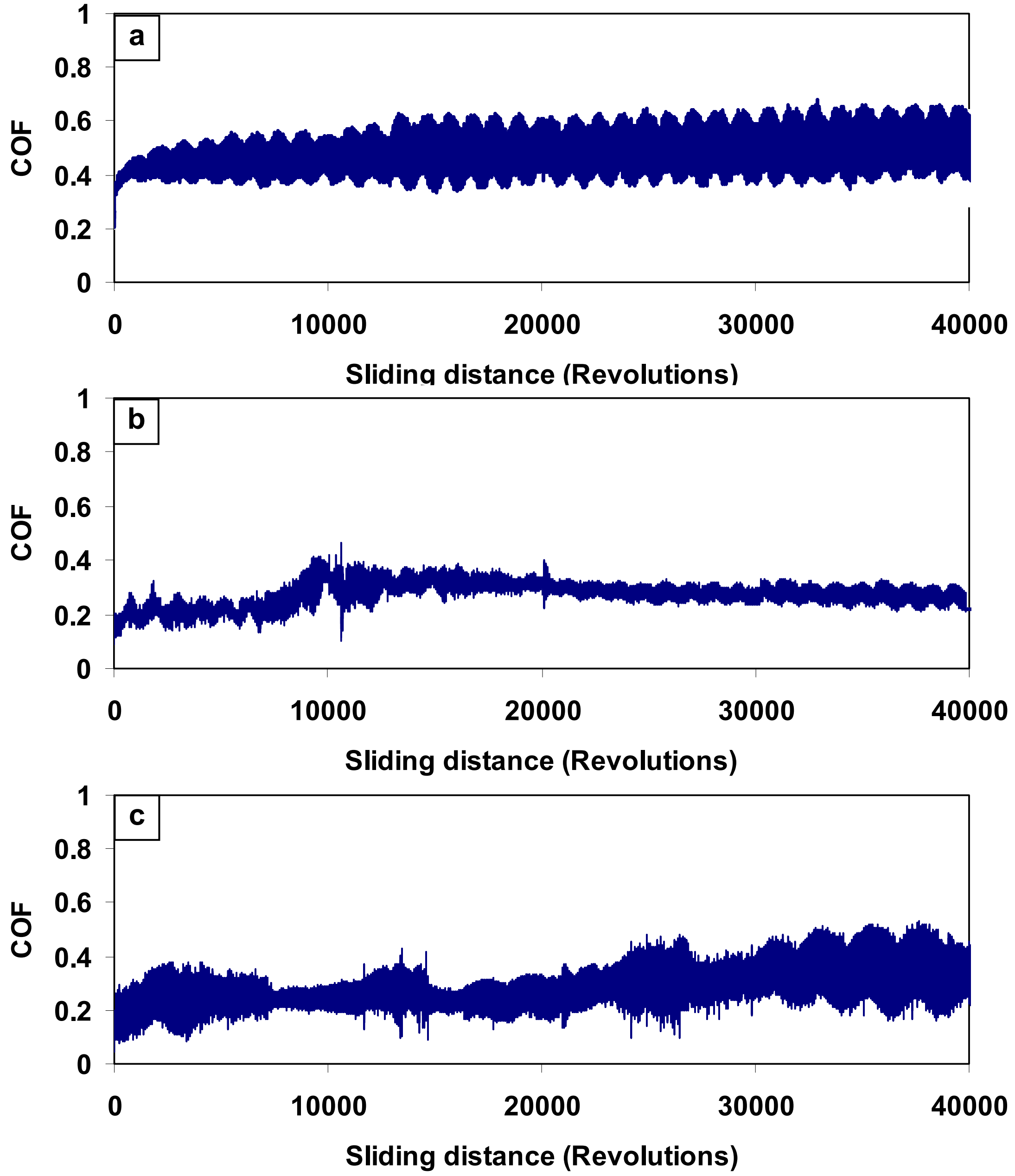

Fig. 6.15 Dynamical cof curves of the CrN-coated SS316L samples during the sliding wear tests against HDPE balls under (a) dry and boundary lubrication conditions with (b) distilled water and (c) SBF.

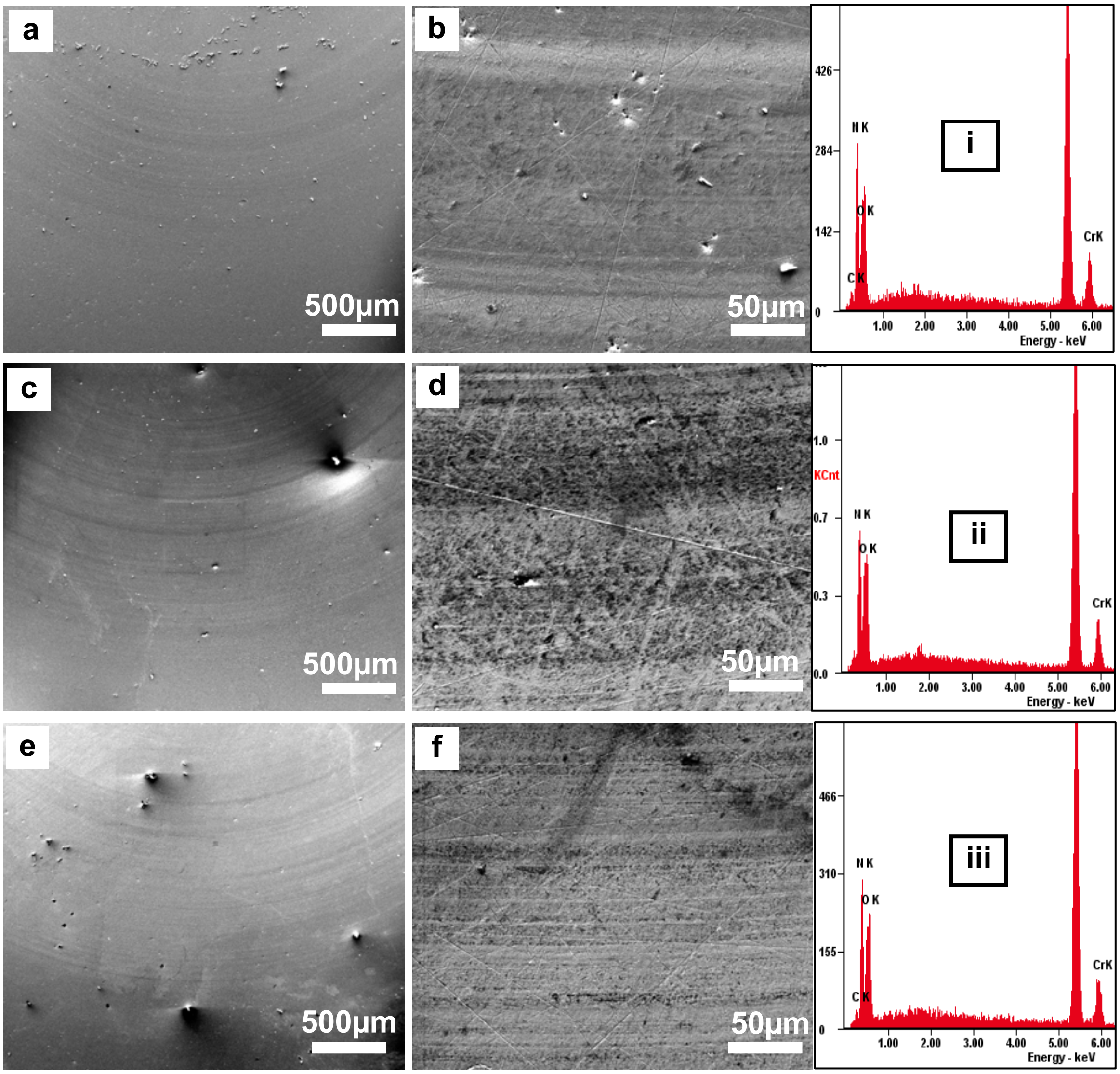

Fig. 6.16 SEM micrographs of wear tracks on the CrN-coated SS316L samples after the sliding wear tests against HDPE balls under (a, b) dry and boundary lubrication conditions with (c, d) distilled water and (e, f) SBF. (b, d, f) are the corresponding magnified images of (a, c, e). Spectra i, ii and iii are the EDX spectra collected from the corresponding areas in (b, d, f).

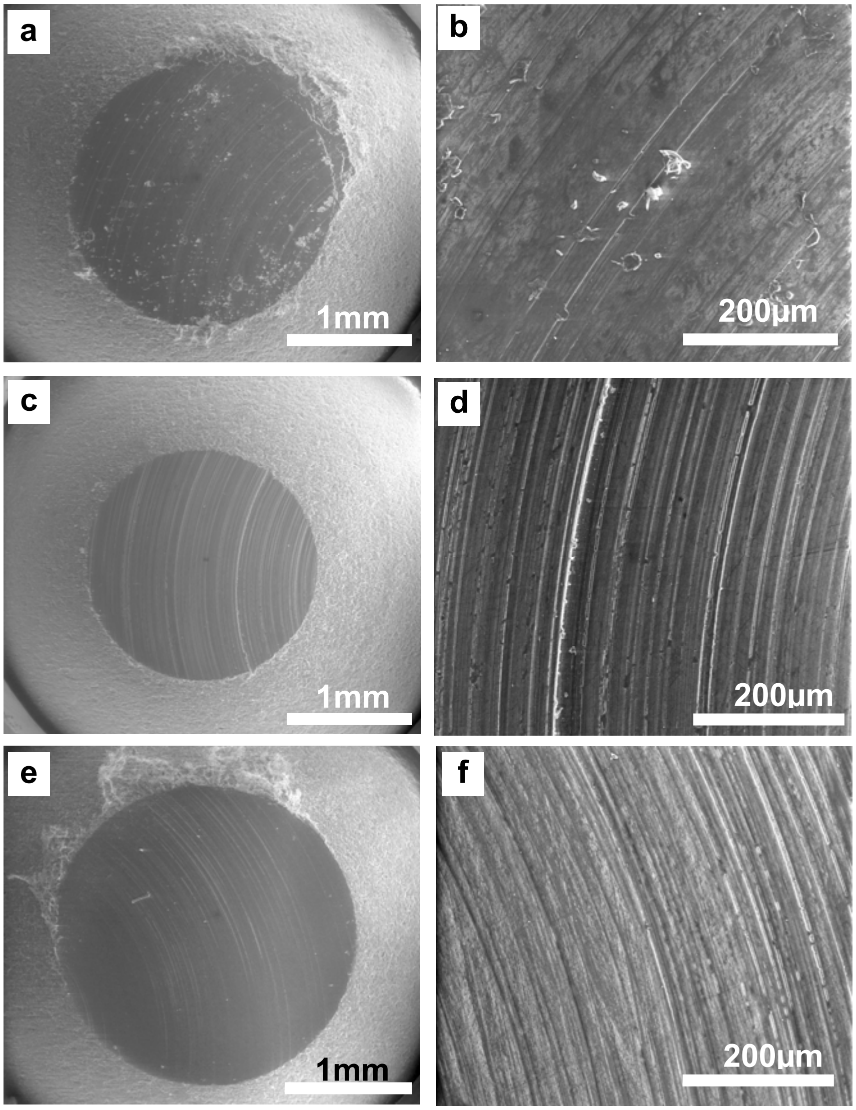

Fig. 6.17 SEM micrographs of the worn HDPE balls after sliding tests against the CrN-coated SS316L samples under (a, b) dry and boundary lubrication conditions with (c, d) distilled water and (e, f) SBF. (b, d, f) are the corresponding magnified images of (a, c, e).

Fig. 6.18 shows the dynamic cofs of the DLC-coated SS316L samples during the sliding wear tests against HDPE counterface balls under dry and boundary lubrication conditions with SBF and distilled water. When sliding under dry condition, the cof curve (Fig. 6.18(a)) is relatively smooth and with lubrications of either distilled water or SBF, the curves have a lot of ups-and-downs. However, the average cofs under the three conditions are similar i.e. about 0.35. Fig. 6.19 shows the SEM micrographs of wear tracks on DLC coatings after sliding tests against polymer balls. The three wear tracks are very smooth and some loosen polymer particles released from balls can be observed. The magnified images of the wear tracks (Figs. 6.19(b, d, f)) also show no visible wear. However, obvious imprints under SEM observation can be found, which is due to the uniform and thin transferring layer from the counterface ball. The SEM micrographs of counterface balls against the DLC coatings are shown in Fig. 6.20. With lubrication of distilled water and SBF, the wear losses of the balls are similar (Figs. 6.20 (c, d) and 6.20(e, f)) which is a little bit lower than that of under dry condition (Figs. 6.20 (c, d)). The cof curves and SEM morphology observation of wear tracks and counterface balls indicate that the DLC coating is stable under water or SBF and the lubrication effect of aqueous solution on the tribological properties is trivial.

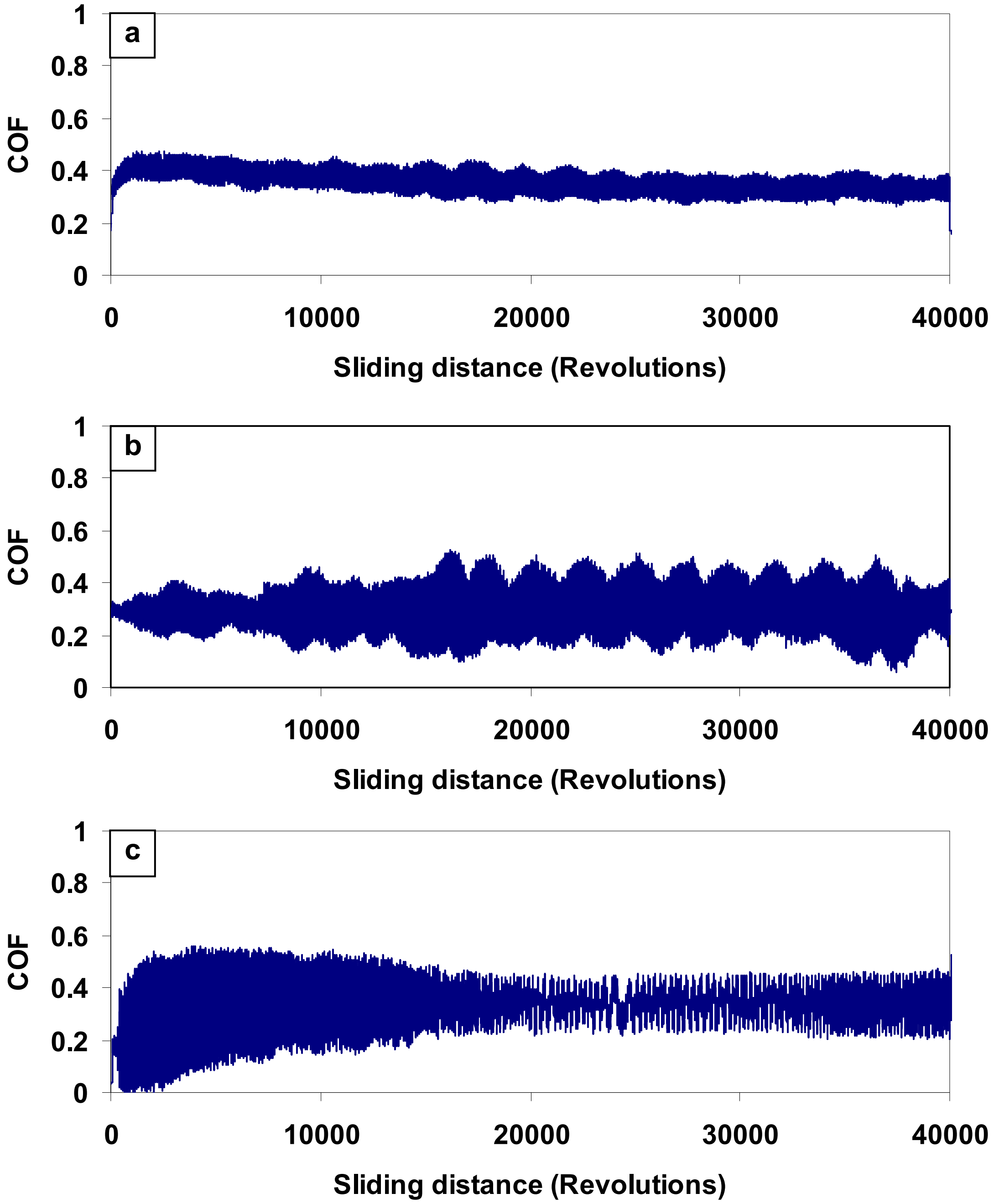

Fig. 6.18 Dynamical cof curves of the DLC-coated SS316L samples during the sliding wear tests against HDPE balls under (a) dry and boundary lubrication conditions with (b) distilled water and (c) SBF.

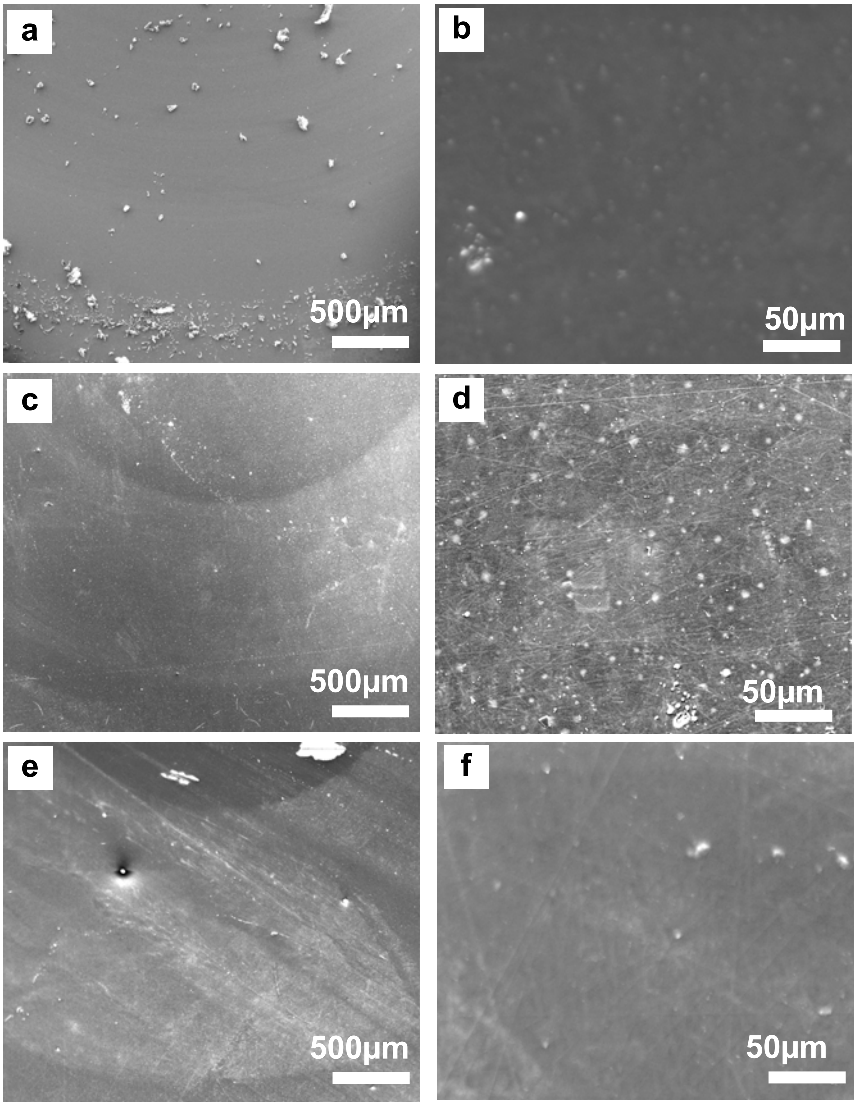

Fig. 6.19 SEM micrographs of wear tracks on the DLC-coated SS316L samples after the sliding wear tests against HDPE balls under (a, b) dry and boundary lubrication conditions with (c, d) distilled water and (e, f) SBF. (b, d, f) are the corresponding magnified images of (a, c, e).

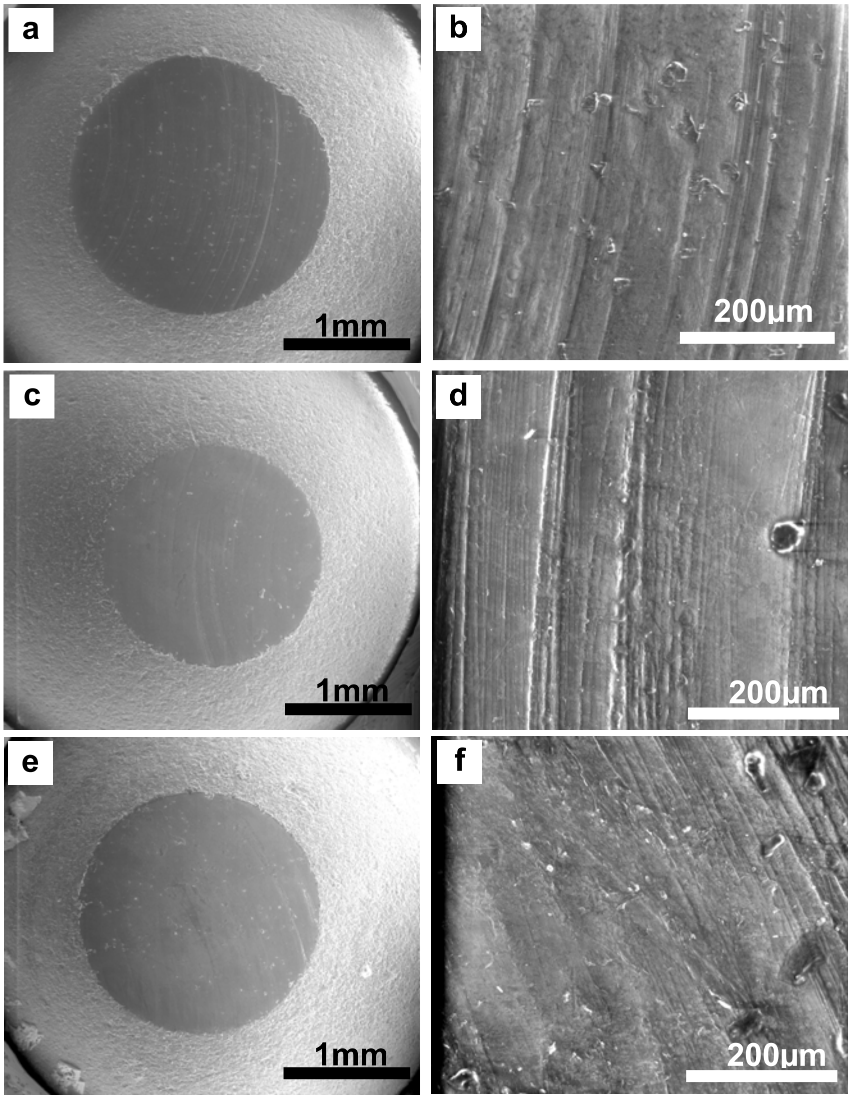

Fig. 6.20 SEM micrographs of the worn HDPE balls after sliding tests against the DLC-coated SS316L samples under (a, b) dry and boundary lubrication conditions with (c, d) distilled water and (e, f) SBF. (b, d, f) are the corresponding magnified images of (a, c, e).

6.3 Summaries of Chapter 6

The results of potentiodynamic polarization tests and corrosion potential vs. testing time (12-hours) indicate that the TiN, CrN and DLC coatings can achieve higher corrosion polarization resistance and corrosion potential in SBF environment than the uncoated SS316L, which means the low corrosion rate and reduced metal ions release from the coatings and substrate materials. However, both the TiAlN and CrAlN coatings have a much lower corrosion polarization resistance and corrosion potential, i.e., less corrosion protection than the uncoated stainless steel. The superior corrosion protection performance of the CrN and TiN could be due to the Cr-O and Ti-O passive layer formation on the coating surfaces which protect the coating from further corrosion. However, the good corrosion property of the DLC coating is due to its chemical inertness under the SBF condition.

Figs. 6.21 and 6.22 show the average cofs during the pin-on-disc sliding tests and the volumetric wear loss of counterface balls against the uncoated and coated-SS316L after the sliding tests under the various environments under 10 N normal loads, respectively.

During the dry sliding tests, the coated samples give higher wear loss on HDPE ball than uncoated steel sample. The ball against the TiN coating has a higher wear loss than the CrN and DLC coatings. The DLC coating has the lowest cof than other uncoated and coated samples.

With the lubrication/cooling effect of distilled water, the cof becomes lower compared to the corresponding dry sliding condition except for the DLC coating which has a similar cof between under dry and lubricated conditions (Fig. 6.21). With lubrication of distilled water, the cofs of uncoated and coated samples increase in the order of TiN<SS<CrN<DLC and the ball wear loss is SS<TiN< CrN < DLC.

In the SBF environment, the uncoated steel was corroded to some extent and the corrosion products accelerated the wear of counterface balls and the material transferring. Thus the ball against the SS316L sample has the highest wear loss in the SBF environment. The DLC gives a higher wear loss on HDPE ball than TiN under the medium of SBF. The trend of HDPE balls wear loss in SBF against the uncoated, TiN- and DLC-coated samples are consistent with the previous research results reported by Hoseini et. al.[130]. For the CrN coating tested in SBF, the counterface ball has a high wear loss which is similar to that for uncoated SS316L under the sliding test in SBF. The interaction between Cr-O and HDPE balls during the tests of CrN and SS316L in the SBF may be the reason for the similarity.

In term of material transferring phenomena, more material transferring and accumulation occurred on the CrN and DLC coatings under dry condition compared with other samples. A thin transferred film on the DLC coatings were formed under all the three conditions but the effect of sliding condition on the material transferring is not significant. After sliding with SBF, the CrN- and uncoated SS316L samples have much more material accumulation on the wear tracks than other samples. For steel sample, the accumulation could be the corrosion product mixing with some PE materials which are easy to stick on the steel surface. However, the exact mechanisms that control the material transferring onto the CrN coating are not well-understood yet. It may be related to the Cr-O passive film on the CrN coating surface. The oxide film could have high chemical affinity to polymer materials. Another possible reason could be the oxidation of polyethylene under the oxygen-rich environment [174] on the CrN coating surface with SBF. The oxidation increased brittleness and diminished mechanical properties of the polyethylene ball and therefore the wear of polyethylene increased. The SBF environment can accelerate the Cr-O forming and therefore the oxidation of polyethylene and degradation of its mechanical properties.

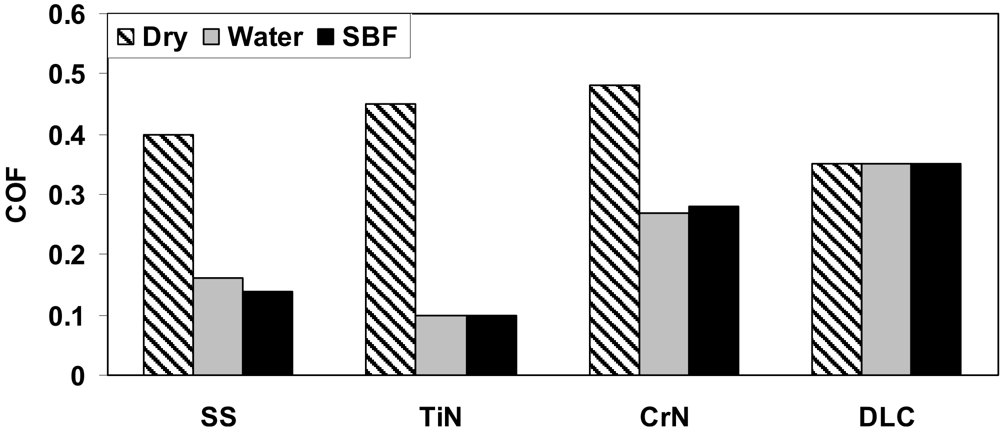

Fig. 6.21 Average cofs of uncoated and coated-SS316L during the sliding tests under the various environments.

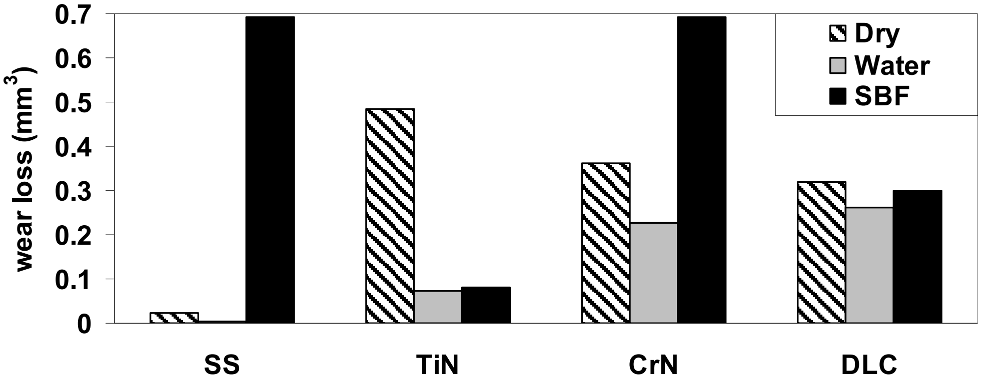

Fig. 6.22 Wear loss of polyethylene balls after sliding tests against uncoated and coated-SS316L under the various environments.

CHAPTER 7 CONCLUSIONS AND FUTURE WORK

7.1 Summaries

In this dissertation, three parts of experiments were reported. Wear and corrosion properties of PVD and CVD hard coatings were characterized under simulated dry machining, fuel cell and biomedical application conditions which were reported in chapters 4, 5 and 6, respectively. The test results were analyzed, and potentials of the coatings for the targeted applications were discussed.

To evaluate the effect of high temperature on the wear performance of various tool coatings, including TiN, TiAlN, CrN, CrAlN and DLC, the phase structures as well as mechanical and tribological properties of un-annealed and annealed coatings were characterized in the first part of chapter 4 (section 4.1). The research results of this part indicated that the CrAlN coating has the best thermal stability among all the coatings. The CrAlN coating can still keep an intact surface morphology at the annealing temperatures up to 1000 ^{o}C, though oxidization has occurred to some extent. At the same annealing temperature conditions, the CrAlN and TiN coatings always exhibit the highest and lowest hardness, respectively, among the nitride coatings after the annealing treatments. For the DLC coatings, the large extended hardness drop occurred when the annealing temperature is above 400 ^{o}C which is from 15 GPa for D400 (400 ^{o}C) to less than 2 GPa for D500 and D600 (500 ^{o}C and 600 ^{o}C). The tribological properties of un-annealed and annealed coatings were examined by pin-on-disc sliding tests against various counterface materials, i.e., ceramic Al_2O_3, steel and Al alloys. The results of wear performance of TiN, CrN, TiAlN and CrAlN coatings against Al_2O_3 balls indicate that the oxide on the coatings resulted from annealing processes has served as a lubrication layer and thus the coatings exhibited a lower friction, while the hardness of annealed coatings plays a determinative role in the wear rate of coatings. Although TiAlN coating has an improved wear performance, CrN and CrAlN coatings are still superior to TiN and TiAlN coatings in this matter based on therein testing conditions. During the sliding wear tests of the coatings against steel counterfaces, the relatively soft steel balls were worn and the released materials were picked up and stuck on the coating surfaces. It is believed that adhesive wear is the main wear mechanisms. Due to the low hardness, severe adhesive wear occurred on the TiN coating annealed at 500 ^{o}C. On the CrN coatings, though a large amount of material transferring occurred, much less adhesive wear took place compared with the TiN coatings. The Al introduction into TiN did not improve the anti-sticking of steel properties significantly. Compared with TiAlN coating, less material transferring occurred on the original CrAlN coating but material transferring still happened on annealed CrAlN coatings. The coating CA800 (800 ^{o}C) has less material transferring than CA500 and CA700 (500 ^{o}C and 700 ^{o}C) which could be related to the formation of Al_2O_3 film that retards the adhesion between coatings and Fe. During the sliding wear tests against aluminium balls, severe material transferring and adhesive wear occurred on all the un-annealed and annealed coatings TiN, CrN, TiAlN and CrAlN. The DLC coating has a very good properties of anti-sticking of steel and aluminum materials. However, above 400 ^{o}C annealing, the coating structure started to transform to sp^{2} graphite and the coating lost the strength and structure and thus the coating is not suitable for load bearing application in the high temperature.

The excellent anti-wear performance of the CrAlN coating when sliding against ceramic alumina and steel counterface materials was verified by industrial trial results which were reported in the second part of chapter 4 (section 4.2). In the industrial trial, CrAlN- and TiN-coated punches were installed into a stamping die in an automotive manufacturer's stamping plant. Industrial trials showed that the CrAlN-coated punch had a lifetime more than 2.5 and 5 times longer than the TiN-coated and uncoated punches, respectively. Under the high shear force and stress during the stamping, peeling on the coatings initiated locally from the regions where machining grooves existed underneath. Compared to the CrAlN coating, the TiN coating had a higher Zn and Fe pick-up tendency from galvanized high strength steels, suggesting that adhesive wear could also be one of the mechanisms contributing to failure for the TiN coating. Improvement of the tool substrate surface finish is a way to further increase lifetime of the coated tools.

Based on the findings derived from sections 4.1 and 4.2 of chapter 4 that CrN based coatings have a better thermal stability and wear resistance than the TiN- and C-based coatings when sliding against ceramic alumina and steel materials, whereas DLC is the best in terms of anti-sticking of some soft materials (steel and aluminium), a multilayered Cr(CrN)/C(DLC) coating system was developed in the third part of chapter 4 (section 4.3) with attention of combining both wear resistance and anti-sticking properties. The bilayer thicknesses of four Cr(CrN)/C(DLC) coatings were determined by low-angle XRD, XPS plotting with an etch depth method and TEM cross-section observations. Similarity of three analysis methods in bilayer thickness determination was demonstrated. In dry sliding tests, decreasing bilayer thickness structure achieved a lower friction. The coating with a thinner bilayer thickness exhibited a less intendancy in formation of fatigue cracks during sliding wear tests. The coolant as a lubricant provided a lower friction. The precipitates in the coolant could cause a significant scratching on the coatings. However, the thinnest bilayered coating (R4), which had the best anti-wear performance in the dry testing condition, exhibited the worst wear resistance in coolant environment.

In the second part of experimental studies (i.e., chapter 5), the contact resistance and electrochemical properties of uncoated, TiN-, CrN- and TiAlN-coated SS316L substrates were investigated in a simulated proton exchange membrane (PEM) fuel cell environment. The ordering of the electrical contact resistance (CR) is TiAlN<CrN<TiN<SS316L. The potentiodynamic polarization test results showed that the O_2 and H_2 environments significantly affected the polarization characteristics of the TiN-based coatings and SS316L, but less influenced that of the CrN coating. The TiAlN-coated and SS316L samples had a higher corrosion resistance in the cathodic environment (with O_2 purging) than in the anodic environment (with H_2 purging). On the other hand, the TiN coating had a higher corrosion resistance in the anodic environment than in the cathodic environment. The ranking for corrosion resistance in H_2 and O_2 bubbled environments is TiAlN<SS316L<CrN<TiN and TiAlN<TiN<CrN<SS316L, respectively. The potentiostatic corrosion tests showed that in the simulated anodic conditions (-0.1 V vs. Ag/AgCl electrode), both the TiN and CrN had a lower corrosion current density than SS316L, but with increasing the testing time, the current density increased and finally reached over $0.01 A/cm^2$ since corrosion has been initiated at pinholes in the coatings after a long hours' testing. In the simulated cathode conditions, TiN had a higher corrosion current density than SS316L, whereas the CrN coating showed a similar value to SS316L. The electrochemical test results indicated that the tested TiAlN coating had the poorest corrosion resistance and was not suitable for

application in PEM fuel cells. It was concluded that both TiN- and CrN-coated SS316L could potentially be used as bipolar plate materials in the PEM fuel cell environment. However, the pinholes existing in the PVD TiN and CrN coatings are sites for enhanced corrosion, and therefore the long-term durability of such coatings is questionable. Thus, more research work is needed to find way of eliminating pinholes resulting from the PVD deposition process.

In the final part of experimental investigations (Chapter 6), the corrosion property of coatings was investigated in a simulated body fluid (SBF) environment, and the tribological property against polyethylene biomaterial was characterized in order to exam the feasibility of those coatings for load-bearing medical devices and implants. The results indicated that the TiN, CrN and DLC coatings can achieve higher corrosion polarization resistance and corrosion potential in the SBF environment than the uncoated SS316L. However, both TiAlN and CrAlN coatings have a much lower corrosion polarization resistance and corrosion potential (even worse than the uncoated stainless steel). The superior corrosion protection performance of the CrN and TiN could be due to the Cr-O and Ti-O passive layer formation on the coating surfaces which protect the coating from further corrosion. The good corrosion property of the DLC coating is likely due to its chemical inertness under the SBF condition. The TiN and DLC coatings presented a good wear resistance and chemical stability during the sliding tests with SBF. The uncoated and CrN-coated stainless steel samples were not compatible with polyethylene materials in terms of their tribological properties in the tested SBF condition.

7.2 Conclusions

Based on the summary described above, the dissertation can be concluded as follows:

The tests results on the performance of coatings for dry machining applications indicated that the conventional CrN and developing CrAlN coatings had a better thermal stability than the TiN and TiAlN coatings. The CrAlN coating had the highest thermal stability and could keep phase structure after annealed at 1000 ^{o}C. CrAlN coating had a superior wear performance under both dry sliding pin-on-disc test and industrial stamping conditions in this study when against ceramic and steel counterface materials but no improvement in anti-sticking property has been presented against aluminum counterface material. H:DLC coating was the best in term of anti-sticking of aluminum but its low thermal stability at above 400 ^{o}C limited its application for dry machining. Thus, the CrN/DLC nanostructured composite coating could be the future research direction to develop tool coatings used for this application.

The research on the performance of the TiN, CrN and TiAlN coatings at a simulated PEM fuel cell environment revealed that they achieved a lower contact resistance than uncoated 316L. The TiAlN coating used in this study was not suitable for applying in the PEM fuel cell conditions. The CrN coated material could be used as an alternative bipolar plate material since it had a low contact resistance and high (in the anodic environment) or similar (in the cathodic environment) corrosion resistance, compared to the SS316L. The pinhole existing in the PVD coatings deteriorated the long-term corrosion performance of coatings especially at the anode condition.

For the applications of coatings at biomedical environment, TiN, CrN and DLC coatings were able to supply corrosion protection to SS316 but TiAlN and CrAlN coatings had poor corrosion properties under this condition. The DLC coating showed the highest corrosion resistance and the best chemical stability in the simulated body fluid. In the term of reduction of polyethylene wear loss, TiN showed the best compatibility with polyethylene material.

7.3 Future Work

In this study on PVD/CVD coatings for manufacturing applications, the post-annealing treatment was adopted to simulate the high temperature resulting from dry machining processes and a relative pure aluminum alloy AA6061 was used as counterface material in the pin-on-disc tests. In the future work, to better simulate the condition of actual dry machining processes, tribological tests using high-temperature pin-on-disc tribometers are recommended. In addition, the Al-Si alloys should be employed as the counterface materials due to their widely uses at various industrial applications. Further investigations on the thermal stability of Cr (CrN)/ C (DLC) coating systems developed in this part of experiment and optimization of the deposition parameters are still needed to achieve a wonderful wear performance against Al alloys during dry machining.

In the future work of PVD/CVD coatings for fuel cell applications, longer time corrosion tests are suggested to conduct on CrN-coated SS316L in a simulated PEMFC conditions to determine the leaching and lifetime of this material. Moreover, the compact resistance after the long-term tests should also be performed to have an insight into the effect of corrosion on the contact resistance.

In the actual application as biomaterial in implants, some more complicated types of movements could be encountered such as climbing, running, jumping and stumbling. Thus, besides pin-on-disc sliding tests, some other mechanical loading tests should be performed on the coatings, for example the impact tests under various static and dynamic loading are highly recommended in the future study.

REFERENCES

[1] J. Singh, D.E. Wolfe, Journal of Materials Science 40 (2005) 1.

[2] H.O. Pierson (Ed.), Handbook of Chemical Vapor Deposition (CVD) - Principles, Technology and Applications (2nd Edition), William Andrew Publishing, 1999, p. 26.

[3] D.M. Mattox, Handbook of Physical Vapor Deposition (PVD) Processing, William Andrew Publishing, 1998, p. 31.

[4] R.F. Bunshah (Ed.), Handbook of Hard Coatings, William Andrew Publishing, 2001, p. 426.

[5] R.F. Bunshah (Ed.), Handbook of Hard Coatings, William Andrew Publishing, 2001, p. 16.

[6] R.F. Bunshah (Ed.), Handbook of Deposition Technologies for Films and Coatings - Science, Technology and Applications (2nd Edition), William Andrew Publishing, 1994, p. 33.

[7] M. Ohring, Materials Science of Thin Films Second Edition, Academic press, A division of Harcourt, Inc., San Diego, 2002, p. 216-257.

[8] R.F. Bunshah (Ed.), Handbook of Hard Coatings, William Andrew Publishing, 2001, p. 61.

[9] K.L. Choy, Progress in Materials Science 48 (2003) 57.

[10] I. Petrov, P.B. Barna, L. Hultman, J.E. Greene, Journal of Vacuum Science & Technology A 21 (2003) S117.

[11] J.P. Bars, E. Etchessahar, J. Debuigne, Journal of the Less-Common Metals 52 (1977) 51

[12] S.Y. Zhang, W.G. Zhu, Journal of Materials Processing Technology 39 (1993) 165.

[13] S.Y. Zhang, Materials Science and Engineering a-Structural Materials Properties Microstructure and Processing 163 (1993) 141.

[14] R.F. Bunshah (Ed.), Handbook of Hard Coatings, William Andrew Publishing, 2001, p. 377.

[15] H. Bomas, P. Mayr, B. Kurth, Materials and Manufacturing Processes 12 (1997) 17.

[16] R. Hubler, Surface and Coatings Technology 116-119 (1999) 1111.

[17] V.K.W. Grips, H.C. Barshilia, V.E. Selvi, Kalavati, K.S. Rajam, Thin Solid Films 514 (2006) 204.

[18] T. Polcar, T. Kubart, R. Novak, L. Kopecky, P. Siroky, Surface & Coatings Technology 193 (2005) 192.

[19] Y.H. Cheng, B.K. Tay, S.P. Lau, Journal of Vacuum Science & Technology B 20 (2002) 2000.

[20] J.C.A. Batista, C. Godoy, A. Matthews, Tribology International 35 (2002) 363.

[21] S. Veprek, S. Reiprich, Thin Solid Films 268 (1995) 64.

[22] K. Kawabata, T. Muto, Electrocomponent Science and Technology 8 (1981) 249.

[23] G.L. Zhao, T.B. Zhang, T. Zhang, J.X. Wang, G.R. Han, Journal of Non-Crystalline Solids 354 (2008) 1272.

[24] J.E. Sundgren, Thin Solid Films 128 (1985) 21.

[25] G. Berg, C. Friedrich, E. Broszeit, C. Berger, Surface and Coatings Technology 86-87 (1996) 184.

[26] A. Aubert, R. Gillet, A. Gaucher, J.P. Terrat, Thin Solid Films 108 (1983) 165.

[27] Z.P. Huang, Y. Sun, T. Bell, Wear 173 (1994) 13.

[28] P. Hones, R. Sanjines, F. Levy, Surface and Coatings Technology 94-95 (1997) 398.

[29] J.W. Seok, J.H. Li, R.Y. Lin, Surface Engineering 18 (2002) 188.

[30] B. Navinsek, P. Panjan, A. Cvelbar, Surface and Coatings Technology 74-75 (1995) 155.

[31] I. Milosev, H.H. Strehblow, B. Navinsek, Thin Solid Films 303 (1997) 246.

[32] M. Oden, J. Almer, G. Hakansson, Surface & Coatings Technology 120-121 (1999) 272.

[33] M. Oden, J. Almer, G. Hakansson, M. Olsson, Thin Solid Films 377-378 (2000) 407.

[34] M. Oden, C. Ericsson, G. Hakansson, H. Ljungcrantz, Surface & Coatings Technology 114 (1999) 39.

[35] J.A. Sue, T.P. Chang, Surface and Coatings Technology 76-77 (1995) 61.

[36] M. Urgen, A.F. Cakir, Surface & Coatings Technology 96 (1997) 236.

[37] H. Ichimura, Y. Ishii, Surface & Coatings Technology 145 (2001) 94.

[38] A. Conde, C. Navas, A.B. Cristobal, J. Housden, J. de Damborenea, Surface & Coatings Technology 201 (2006) 2690.

[39] W. Ernst, J. Neidhardt, H. Willmann, B. Sartory, P.H. Mayrhofer, C. Mitterer, Thin Solid Films 517 (2008) 568.

[40] J.N. Tu, J.G. Duh, S.Y. Tsai, Surface & Coatings Technology 133-134 (2000) 181.

[41] C. Rebholz, H. Ziegele, A. Leyland, A. Matthews, Surface and Coatings Technology 115 (1999) 222.

[42] A.E. McHale (Ed.), Phase Equilibria Diagrams, The American Ceramic Society, Westerville, OH, 1994.

[43] K. Tonshoff, A. Mohlfeld, T. Leyendecker, H.G. Fu, G. Erkens, R. Wenke, T. Cselle, M. Schwenck, Surface and Coatings Technology 94-95 (1997) 603.

[44] C.W. Kim, K.H. Kim, Thin Solid Films 307 (1997) 113.

[45] K.H. Kim, S.H. Lee, Thin Solid Films 283 (1996) 165.

[46] A. Kimura, H. Hasegawa, K. Yamada, T. Suzuki, Surface and Coatings Technology 120-121 (1999) 438.

[47] M. Kawate, A. Kimura, T. Suzuki, Journal of Vacuum Science & Technology a-Vacuum Surfaces and Films 20 (2002) 569.

[48] Y.C. Chim, X.Z. Ding, X.T. Zeng, S. Zhang, Thin Solid Films 517 (2009) 4845.

[49] J. Robertson, Materials Science & Engineering R-Reports 37 (2002) 129.

[50] S.V. Hainsworth, N.J. Uhure, International Materials Reviews 52 (2007) 153.

[51] W. Jacob, W. Moller, Applied Physics Letters 63 (1993) 1771.

[52] Y. Liu, A. Erdemir, E.I. Meletis, Surface and Coatings Technology 82 (1996) 48.

[53] A. Grill, Wear 168 (1993) 143.

[54] D.R. Tallant, J.E. Parmeter, M.P. Siegal, R.L. Simpson, Diamond and Related Materials 4 (1995) 191.

[55] Z.L. Akkerman, H. Efstathiadis, F.W. Smith, Journal of Applied Physics 80 (1996) 3068.

[56] Z.J. Zhang, K. Narumi, H. Naramoto, Journal of Physics: Condensed Matter 13 (2001) L475.

[57] H. Li, T. Xu, C. Wang, J. Chen, H. Zhou, H. Liu, Thin Solid Films 515 (2006) 2153.

[58] R. Wahter, A. Cordery, Diamond and Related Materials 8 (1999) 504.

[59] S. Takabayashi, K. Okamoto, H. Sakaue, T. Takahagi, K. Shimada, T. Nakatani, Journal of Applied Physics 104 (2008) 043512.

[60] H. Ito, K. Yamamoto, M. Masuko, Thin Solid Films 517 (2008) 1115.

[61] D. Dudzinski, A. Devillez, A. Moufki, D. Larrouquere, V. Zerrouki, J. Vigneau, International Journal of Machine Tools & Manufacture 44 (2004) 439.

[62] P.S. Sreejith, B.K.A. Ngoi, Journal of Materials Processing Technology 101 (2000) 287.

[63] M. Lahres, G. Jorgensen, Surface & Coatings Technology 96 (1997) 198.

[64] M. Sokovic, K. Mijanovic, Journal of Materials Processing Technology 109 (2001) 181.

[65] A.E. Diniz, R. Micaroni, International Journal of Machine Tools and Manufacture 42 (2002) 899.

[66] Y. Ozcatalbas, Materials & Design 24 (2003) 215.

[67] J.M. Dasch, C.C. Ang, C.A. Wong, Y.T. Cheng, A.M. Weiner, L.C. Lev, E. Konca, Surface & Coatings Technology 200 (2006) 2970.

[68] M.S. Carrilero, R. Bienvenido, J.M. Sanchez, M. Alvarez, A. Gonzalez, M. Marcos, International Journal of Machine Tools and Manufacture 42 (2002) 215.

[69] P. Roy, S.K. Sarangi, A. Ghosh, A.K. Chattopadhyay, International Journal of Refractory Metals and Hard Materials 27 (2009) 535.

[70] C.H. Che-Haron, Journal of Materials Processing Technology 118 (2001) 231.

[71] M.S. Dargusch, M.X. Zhang, S. Palanisamy, A.J.M. Buddery, D.H. StJohn, Advanced Engineering Materials 10 (2008) 85.

[72] A. Ginting, M. Nouari, International Journal of Machine Tools & Manufacture 49 (2009) 325.

[73] A. Devillez, F. Schneider, S. Dominiak, D. Dudzinski, D. Larrouquere, Wear 262 (2007) 931.

[74] W.S. Miller, L. Zhuang, J. Bottema, A. Wittebrood, P. De Smet, A. Haszler, A. Vieregge, Materials Science & Engineering A 280 (2000) 37.

[75] A. Heinz, A. Haszler, C. Keidel, S. Moldenhauer, R. Benedictus, W.S. Miller, Materials Science & Engineering A-Structural Materials Properties Microstrucure and Processing 280 (2000) 102.

[76] M. Nouari, G. List, F. Girot, D. Coupard, Wear 255 (2003) 1359.

[77] H.K. Tonshoff, A. Mohlfeld, Surface and Coatings Technology 93 (1997) 88.

[78] T. Leyendecker, O. Lemmer, S. Esser, J. Ebberink, Surface and Coatings Technology 48 (1991) 175.

[79] V. Derflinger, H. Brandle, H. Zimmermann, Surface and Coatings Technology 113 (1999) 286.

[80] E. Konca, Y.T. Cheng, A.M. Weiner, J.M. Dasch, A. Erdemir, A.T. Alpas, Surface and Coatings Technology 200 (2005) 2260.

[81] J.L. Mo, M.H. Zhu, B. Lei, Y.X. Leng, N. Huang, Wear 263 (2007) 1423.

[82] I. Reineck, M.E. Sjostrand, J. Karner, M. Pedrazzini, International Journal of Refractory Metals & Hard Materials 14 (1996) 187.

[83] H. Hanyu, Y. Murakami, S. Kamiya, M. Saka, Surface & Coatings Technology 169 (2003) 258.

[84] S. Bhowmick, A.T. Alpas, International Journal of Machine Tools & Manufacture 48 (2008) 802.

[85] V. Mehta, J.S. Cooper, Journal of Power Sources 114 (2003) 32.

[86] C.Y. Wang, Chemical Reviews 104 (2004) 4727.

[87] J. Wind, R. Spah, W. Kaiser, G. Bohm, Journal of Power Sources 105 (2002) 256.

[88] J. Larminie, A. Dicks (Eds.), Fuel Cell Systems Explained (2nd Edition), John Wiley & Sons, 2003, p. 1-16.

[89] A.J. Appleby, Energy 21 (1996) 521.

[90] A. Hermann, T. Chaudhuri, P. Spagnol, International Journal of Hydrogen Energy 30 (2005) 1297.

[91] H. Tawfik, Y. Hung, D. Mahajan, Journal of Power Sources 163 (2007) 755.

[92] Y.Y. Shao, G.P. Yin, Z.B. Wang, Y.Z. Gao, Journal of Power Sources 167 (2007) 235.

[93] H.L. Wang, J.A. Turner, Journal of Power Sources 180 (2008) 791.

[94] R.J. Tian, J.C. Sun, J.L. Wang, International Journal of Hydrogen Energy 33 (2008) 7507.

[95] N.D.L. Heras, E.P.L. Roberts, R. Langton, D.R. Hodgson, Energy & Environmental Science 2 (2009) 206.

[96] H.L. Wang, M.A. Sweikart, J.A. Turner, Journal of Power Sources 115 (2003) 243.

[97] Y. Wang, O. Northwood, Electrochimica Acta 52 (2007) 6793.

[98] T. Fukutsuka, T. Yamaguchi, S.I. Miyano, Y. Matsuo, Y. Sugie, Z. Ogumi, Journal of Power Sources 174 (2007) 199.

[99] Y. Show, Surface & Coatings Technology 202 (2007) 1252.

[100] M.C. Li, S.Z. Luo, C.L. Zeng, J.N. Shen, H.C. Lin, C.N. Cao, Corrosion Science 46 (2004) 1369.

[101] Y. Wang, D.O. Northwood, International Journal of Hydrogen Energy 32 (2007) 895.

[102] Y. Wang, D.O. Northwood, Journal of Power Sources 165 (2007) 293.

[103] E.A. Cho, U.S. Jeon, S.A. Hong, I.H. Oh, S.G. Kang, Journal of Power Sources 142 (2005) 177.

[104] S.J. Lee, C.H. Huang, Y.P. Chen, Journal of Materials Processing Technology 140 (2003) 688.

[105] B. Cunningham, D.G. Baird, Journal of Materials Chemistry 16 (2006) 4385.

[106] H. Tsuchiya, O. Kobayashi, International Journal of Hydrogen Energy 29 (2004) 985.

[107] C.A. Reiser, L. Bregoli, T.W. Patterson, J.S. Yi, J.D. Yang, M.L. Perry, T.D. Jarvi, Electrochemical and Solid-State Letters 8 (2005) A273.

[108] H.S. Lee, H.J. Kim, S.G. Kim, S.H. Ahn, Journal of Materials Processing Technology 187 (2007) 425.

[109] R.C. Makkus, A.H.H. Janssen, F.A. de Bruijn, R. Mallant, Journal of Power Sources 86 (2000) 274.

[110] H. Wang, J.A. Turner, Journal of Power Sources 128 (2004) 193.

[111] M.J. Kelly, G. Fafilek, J.O. Besenhard, H. Kronberger, G.E. Nauer, Journal of Power Sources 145 (2005) 249.

[112] S. Joseph, J.C. McClure, R. Chianelli, P. Pich, P.J. Sebastian, International Journal of Hydrogen Energy 30 (2005) 1339.

[113] S.J. Lee, C.H. Huang, Y.P. Chen, C.T. Hsu, Journal of Fuel Cell Science and Technology 2 (2005) 290.

[114] Y. Li, L. Qu, F.H. Wang, Corrosion Science 45 (2003) 1367.

[115] X.B. Liu, C. Johnson, C.M. Li, J. Xu, C. Cross, International Journal of Hydrogen Energy 33 (2008) 189.

[116] J.R. Davis (Ed.), Handbook of materials for medical devices, ASM International, 2003, p. 1-19.

[117] C.M. Agrawal, Jom-Journal of the Minerals Metals & Materials Society 50 (1998) 31.

[118] J. Black (Ed.), Biological Performance of Materials, CRC Press, Broken Sound Parkway, 2006, p. 23.

[119] M. Niinomi, Journal of Artificial Organs 11 (2008) 105.

[120] C.V. Vidal, A.I. Munoz, Corrosion Science 50 (2008) 1954.

[121] D. Bombac, M. Brojan, P. Fajfar, F. Kosel, R. Turk, RMZ - Materials and Geoenvironment 54 (2007) 471.

[122] M. Niinomi, Metallurgical and Materials Transactions A-Physical Metallurgy and Materials Science 33 (2002) 477.

[123] A. Balamurugan, S. Rajeswari, G. Balossier, A.H.S. Rebelo, J.M.F. Ferreira, Materials and Corrosion-Werkstoffe Und Korrosion 59 (2008) 855.

[124] H. Behrndt, A. Lunk, Materials Science & Engineering A-Structural Materials Properties Microstrucure and Processing 139 (1991) 58.

[125] J. Zhao, L. Li, D.J. Li, H.Q. Gu, Journal of Adhesion Science and Technology 18 (2004) 1003.

[126] A. Wisbey, P.J. Gregson, M. Tuke, Biomaterials 8 (1987) 477.

[127] O. Knotek, F. Loffler, K. Weitkamp, Surface and Coatings Technology 55 (1992) 536.

[128] P.V. Kola, S. Daniels, D.C. Cameron, M.S.J. Hashmi, Journal of Materials Processing Technology 56 (1996) 422.

[129] A. Kamali, R. Farrar, P. Hatto, M. Stone, J. Fisher, Proceedings of the Institution of Mechanical Engineers, Part J: Journal of Engineering Tribology 219 (2005) 41.

[130] M. Hoseini, A. Jedenmalm, A. Boldizar, Wear 264 (2008) 958.

[131] F.Z. Cui, D.J. Li, Surface & Coatings Technology 131 (2000) 481.

[132] R. Hauert, Diamond and Related Materials 12 (2003) 583.

[133] G. Dearnaley, J.H. Arps, Surface & Coatings Technology 200 (2005) 2518.

[134] R.K. Roy, K.R. Lee, Journal of Biomedical Materials Research Part B-Applied Biomaterials 83B (2007) 72.

[135] M. Vojs, E. Zdravecka, M. Marton, P. Bohac, L. Franta, M. Vesely, Microelectronics Journal 40 (2009) 650.

[136] A. Dorner-Reisel, C. Schurer, C. Nischan, O. Seidel, E. Muller, Thin Solid Films 420-421 (2002) 263.

[137] G. Francz, A. Schroeder, R. Hauert, Surface & Coatings Technology 28 (1999) 3.

[138] D. Sheeja, B.K. Tay, X. Shi, S.P. Lau, C. Daniel, S.M. Krishnan, L.N. Nung, Diamond and Related Materials 10 (2001) 1043.

[139] D. Sheeja, B.K. Tay, S.P. Lau, L.N. Nung, Surface and Coatings Technology 146-147 (2001) 410.

[140] M. Braic, M. Balaceanu, V. Braic, A. Vladescu, G. Pavelescu, M. Albulescu, Surface and Coatings Technology 200 (2005) 1014.

[141] R. Hubler, A. Cozza, T.L. Marcondes, R.B. Souza, F.F. Fiori, Surface and Coatings Technology 142-144 (2001) 1078.

[142] Y.X. Leng, H. Sun, P. Yang, J.Y. Chen, J. Wang, G.J. Wan, N. Huang, X.B. Tian, L.P. Wang, P.K. Chu, Thin Solid Films 398-399 (2001) 471.

[143] W.C. Oliver, G.M. Pharr, Journal of Materials Research 7 (1992) 1564.

[144] P.C. Yashar, W.D. Sproul, Vacuum 55 (1999) 179.

[145] Z.J. Liu, A. Vyas, Y.H. Lu, Y.G. Shen, Thin Solid Films 479 (2005) 31.

[146] B.K. Agrawal, X-ray Spectroscopy, 2nd ed, Springer-Verlag, New York, 1991, p. 337.

[147] E.A. Cho, U.S. Jeon, H.Y. Ha, S.A. Hong, I.H. Oh, Journal of Power Sources 125 (2004) 178.

[148] H.S. Khatak, B. Raj (Eds.), Corrosion of Austenitic Stainless Steels, Woodhead Publishing Limited, Cambridge, 2002, p. 41.

[149] N. Perez (Ed.), Electrochemistry and Corrosion Science, Kluwer Academic Publishers, Norwell, 2004, p. 80.

[150] Product information of Hanks' balanced salts (HBSS) in http://www.sigmaaldrich.com/etc/medialib/docs/Sigma/productinformationsheet2/h1387pis.Par.0001.File.tmp/h1387pis.pdf by Sigma-Aldrich®.Sigma-Aldrich.

[151] S.D.A. Lawes, M.E. Fitzpatrick, S.V. Hainsworth, Journal of Physics D-Applied Physics 40 (2007) 5427.

[152] F.-H. Lu, H.-Y. Chen, Thin Solid Films 398-399 (2001) 368.

[153] X.Z. Ding, A.L.K. Tan, X.T. Zeng, C. Wang, T. Yue, C.Q. Sun, Thin Solid Films 516 (2008) 5716.

[154] P.E. Hovsepian, C. Reinhard, A.P. Ehiasarian, Surface & Coatings Technology 201 (2006) 4105.

[155] P. Hones, M. Diserens, F. Levy, Surface and Coatings Technology 120-121 (1999) 277.

[156] F. Luo, X. Pang, K. Gao, H. Yang, Y. Wang, Surface and Coatings Technology 202 (2007) 58.

[157] M. Urgen, V. Ezirmik, E. Senel, Z. Kahraman, K. Kazmanli, Surface & Coatings Technology 203 (2009) 2272.

[158] M. H., L. Carpentier, G. Monteil, X. Roizard, C. J., P. P., International journal of Material Forming 1 (2008) 1243.

[159] S.J. Dowey, J. Zhang, E.D. Doyle, A. Matthews, Surface and Coatings Technology 116-119 (1999) 654.

[160] D.M. Mattox, Handbook of Physical Vapor Deposition (PVD) Processing, William Andrew Publishing, 1998, p. 497.

[161] U. Helmersson, S. Todorova, S.A. Barnett, J.E. Sundgren, L.C. Markert, J.E. Greene, Journal of Applied Physics 62 (1987) 481.

[162] X. Chu, S.A. Barnett, Journal of Applied Physics 77 (1995) 4403.

[163] P.M. Anderson, C. Li, Nanostructured Materials 5 (1995) 349.

[164] M. Kato, T. Mori, L.H. Schwartz, Acta Metallurgica 28 (1980) 285.

[165] R.C. Cammarata, Scripta Metallurgica 20 (1986) 479.

[166] A. Leyland, A. Matthews, Wear 246 (2000) 1.

[167] A. Leyland, A. Matthews, Surface and Coatings Technology 177-178 (2004) 317.

[168] A. Matthews, A. Leyland, Ttp, Euro Ceramics VII, PT 1-3 206-2 (2002) 459.

[169] L.M. Liu, S.Q. Wang, H.Q. Ye, Acta Materialia 52 (2004) 3681.

[170] A.A. Irudayaraj, P. Kuppusami, S. Kalainathan, Surface Engineering 24 (2008) 28.

[171] S. Rudenja, C. Leygraf, J. Pan, P. Kulu, E. Talimets, V. Mikli, Surface and Coatings Technology 114 (1999) 129.

[172] S. PalDey, S.C. Deevi, Materials Science and Engineering a-Structural Materials Properties Microstructure and Processing 342 (2003) 58.

[173] M. Pakala, R.Y. Lin, Surface & Coatings Technology 81 (1996) 233.

[174] J.P. Garino, P.K. Beredjiklian, Core Knowledge in Orthopaedics: Adult Reconstruction and Arthroplasty, Mosby Elsevier, Philadelphia, 2007, p. 135.

VITA AUCTORIS

NAME: Linlin Wang

PLACE OF BIRTH: Anshan, China

YEAR OF BIRTH: 1975

EDUCATION:

Liaoning University of Science & Technology, Anshan, China
1993-1997 B.Sc.

Liaoning University of Science & Technology, Anshan, China
1998-2001 M.Sc.

University of Windsor, Windsor, Ontario
2004-2005 M.Sc.

University of Windsor, Windsor, Ontario
2005-2009 Ph. D.